University of Nottingham

UK | CHINA | MALAYSIA

Novel Bi-layer Coatings for the Protection and Functionalisation of Magnesium-based Medical Alloys

Jonathan M. A. Wilson

Thesis submitted to the University of Nottingham for the degree of Doctor of Philosophy

Supervisors: Dr. Colin Scotchford, Prof. David Grant, Dr. Matthew Wadge

April 2024

Acknowledgements

I would like to express my thanks to my supervision team; Dr. Colin Scotchford, Prof. David Grant and Dr Matthew Wadge. The guidance of Colin and Matthew during my undergraduate studies were in large part of the reasoning for which I undertook this PhD. With the addition of David, this created a team which pushed and encouraged me through difficult times where I otherwise would not have continued and allowed this work to flourish. I would also like to thank the technical and research staff in the department for their training and expertise. Particularly Louise Briggs for providing training and continual support with cellular assessments; Hannah Constantin for training with XPS & XRD characterization; Zakhar Kudrynski and Jake Greener for profilometry assistance and finally Timothy Cooper for assistance of 3D printing designs for the specimen holder used in the electrodeposition method detailed in this thesis.

A special note to the Final Year Project Students – Gogul Kamalanathan, Joe Hocking and Prashant Giridaran; whose work aided the research into the understanding of Calcium Phosphate electrodeposition by varying parameters of Deposition Time and Electrolyte pH. Working as part of the supervision team for these students and others not listed here, provided me with the opportunity to share my interests into this work and expand upon my skillset into a mentorship role.

In addition, I would like to take this opportunity to thank those who have made my PhD studies at Nottingham a better experience. On top of the aid in my research, Tim, Zakhar and Matthew made the lab workspaces a welcoming place, were great to have a laugh with and were great for understanding any issues I faced and offered solutions to work through them. My housemate Malcolm for all the fun times and laughs when we needed to get a break from both doing Engineering PhDs.

Lastly and most importantly, I want to thank my family for their constant support in all aspects of my life, whether this be achieving sporting goals or completing my PhD studies. Their support has allowed me to balance achieving my sporting goals of representing Ireland on the International Stage at the World Korfball Championships with maintaining progress on my PhD thesis even when it felt like a grind. These successes are dedicated to you all and I hope I have made you proud.

Abstract

Bioresorbable biomaterials represent a revolutionary class of materials in the field of biomedical engineering, offering solutions for various medical applications. Unlike traditional permanent implants, bioresorbable biomaterials are designed to degrade gradually within the body over time, eventually being absorbed and assimilated into the surrounding tissues without the need for surgical removal. Magnesium (Mg) and its alloys are promising candidates for these applications due to their mechanical properties being similar to bone and the biological acceptance in the human body. However, their rapid degradation times are currently not practical for a vast array of clinical applications and as such a way to reduce the corrosion rate or delay the onset of Mg corrosion must be developed.

The work presented in this thesis demonstrates the development of a novel bilayered coating, consisting of an electrodeposited layer of calcium phosphate (CaP) and a layer of radio frequency magnetron sputtered (RFMS) phosphate-based glass (PBG), specifically to protect and functionalise Mg WE43 alloy for bioresorbable biomedical applications. The microstructural development of the CaP layer was assessed as a function of duty cycle, deposition time and electrolyte pH, with the parameters of 0.6 duty cycle, 20 min deposition time and electrolyte pH 4.5 being taken forward for the addition of the PBG layer due to achieving a brushite coating of *ca.* 7 – 8 µm thickness which improved cytocompatibility and corrosion rate of the alloy to 0.57 mm/Y. The PBG layer was varied by P content from 40 mol% to 30 mol% investigating the effects of novel “invert” glasses with the novel P30 glass achieving a significant cytocompatibility improvement over the Mg WE43 alloy and P40 glass whilst improving the corrosion rate. The ca. 0.5 µm thick PBG layer in combination with the CaP layer showed a successful improvement of cytocompatibility and corrosion rate with the P30 CaP coating being the most viable in terms of protection of the Mg WE43 alloy with an annealing effect occurring on the CaP layer during PBG deposition and exhibited corrosion

properties E_{corr} = -0.71 V, i_{corr} = 0.032 mA/cm^2 and corrosion rate 0.74 mm/Y. The coatings were assessed using the combined complementary characterisation methods of scanning electron microscopy (SEM), energy dispersive X-ray spectroscopy (EDX), X-ray diffractometry (XRD), X-ray photoelectron spectroscopy (XPS) and 2D profilometry. Further application testing was performed with an extraction test in Dulbecco's Modified Eagles Medium (DMEM) media and potentiodynamic polarisation (PDP) testing in DMEM.

The novel bilayered coatings developed in this thesis have shown a successful improvement of the cytocompatibility and reduction of the corrosion rate of Mg WE43 alloy. Furthermore, the combination of both deposition methods has shown to be complimentary to each other and both tailorable for a variety of potential orthopaedic applications as bioresorbable biomaterials, providing a promising route for advancement in the biomaterials field.

Table of Contents

Glossary of Abbreviations & Nomenclature

AA/AM	Antibiotics/antimycotics
Ag	Silver
Al	Aluminium
ALP	Alkaline Phosphatase
As	Arsenic
ASTM	American Society for Testing and Materials
Au	Gold
B	Boron
BO	Bridging Oxygens
CaP	Calcium Phosphate
CC	Cobalt-Chrome alloys
Cd	Cadmium
CHA	Carbonated Hydroxyapatite
Co	Cobalt
Cu	Copper
DCPD	Dicalcium Dihydrogen Phosphate
DMEM	Dulbecco's Modified Eagle's Medium
E	Young's Modulus
E^0	Standard Electrode Potential
EDM	Electron Discharge Machining
EDP	Electrodeposition
EDX	Energy Dispersive X-ray Spectroscopy
EGM	Endothelial Growth Medium
EU	European Union
F	Fluorine
Fe	Iron
FWHM	Full Width at Half Maximum
Ge	Germanium
HA	Hydroxyapatite
HCP	Hexagonal Close-Packed
ICDD	International Centre for Diffraction Data
IMS	Industrial Methylated Spirit

KE	Kinetic Energy
LDH	Lactate Dehydrogenase
Li	Lithium
MCP	Monocalcium Phosphate
MEM	Modified Eagle's Medium
Mg	Magnesium
Mn	Manganese
MTT	Methyl Tetrazolium
NBO	Non-Bridging Oxygens
NDE	Negative Differential Effect
NEAA	Non-Essential Amino Acids
Ni	Nickel
NR	Neutral Red
NRU	Neutral Red Uptake
NTM	Non-Treated Media
OCCP	Octacalcium Phosphate
OCP	Open Circuit Potential
OD	Optical Density
P	Phosphorous
PBG	Phosphate-based Glass
PBS	Phosphate-Buffered Saline
PCL	Polycaprolactone
PDP	Potentiodynamic Polarisation
PLGA	Poly(lactic-co-glycolic) acid
PLLA	Polylactic Acid
Pt	Platinum
PVD	Physical Vapour Deposition
Q^0	Orthophosphate
Q^1	Pyrophosphate
Q^2	Metaphosphate
Q^3	Ultraphosphate
RF	Radio-Frequency
RFMS	Radio-Frequency Magnetron Sputtering
SBF	Simulated Body Fluid
SCC	Stress Corrosion Cracking

SCE	Saturated Calomel Electrode
SEM	Scanning Electron Microscopy
SHE	Standard Hydrogen Electrode
Si	Silicon
Sr	Strontium
SS	Stainless-Steel
SU	Simulated Urine
TCP	Tricalcium Phosphate
T_g	Glass Transition Temperature
Ti	Titanium
XPS	X-ray Photoelectron Spectroscopy
XRD	X-ray Diffraction
Y	Yttrium
Zn	Zinc
Zr	Zirconium
ρ	Density

Table of Figures

Table of Tables

Chapter 1 – Introduction

Biomaterials are natural or synthetic materials, suitable for interaction with components of a living system, which are typically used in medical applications to enhance, support or replace damaged tissues in the process of cellular repair [1]. Biomaterial solutions span across a diverse array of applications from tissue engineering to medical devices and dental implants, with each application having specific requirements for the active properties of the materials used such as bioactivity, antibacterial properties and mechanical strength. Biomaterials are commonly used as various components in joint replacements such as plates, screws, pins, rods and fixators [2]. Typically to date biomaterials in joint replacements are composed of non-degradable materials such as Titanium (Ti), Stainless Steel (SS) and Cobalt-Chrome alloys (CC) which may result in effects of stress shielding and wear over time [3].

Currently, in the European Union (EU), it is common practice to perform a secondary surgery for the removal of internal fixations of fractured bones after the healing period. This represents an estimated €3.4bn price tag in the EU per year with cost of treatment included with a 10% annual growth of the industry [4]. To this end, there is a large interest in the development of a biodegradable implant that can maintain its structural properties during the healing process of bone (*ca.* 3 – 6 months) [5] and then degrade within the body without negative effects on patient physiology and health. This means that the materials used must degrade without producing toxic, carcinogenic or mutagenic effects, not block blood vessels by generating particles too large to be adsorbed by cells, must be safe to be adsorbed by cells and should be able to be eliminated through conventional physiological means. This would not only reduce surgical costs, but also reduce the morbidity rate and convalescence for treated patients [6].

In the last two decades, biodegradable metals and degradable polymers have been investigated with polymers often suffering from non-linear degradation and a high inflammatory response

due to autocatalytic effects resulting in acid burst [7, 8]. More recently, research has looked into the biodegradable magnesium (Mg) and its alloys which were first seen in use in 1878 to stop bleeding blood vessels [9] and the last decade has seen the first clinical approval of the Magnezix compression screw for use in 2013 with implementation henceforth [10]. However, the high corrosion rate of Mg alloys has prevented widespread clinical use with other more complex devices, but presents an interesting opportunity for the development of new clinical devices if the corrosion process can either be delayed or slowed. Furthermore, the corrosion products of Mg alloys, such as hydrogen evolution, result in a drastic increase in the localised pH around the implants, causing issues for the cellular processes in that region. The targets set clinically for the corrosion rate of Mg and its alloys of 0.02 mm/Y [11], have not been widely achieved as this would require a drastic improvement from the typical corrosion rate of *ca.* 2.7 mm/Y [12] exhibited within a physiological environment. Some materials have achieved the desired corrosion rate but have concerns due to the mechanical properties exhibited and therefore the solution may be to take a mechanically robust alloy, with a poor corrosion rate to be improved through the deposition of coatings.

Surface modification of the Mg alloys presents an opportunity to reduce or control the degradation rate to meet the required healing times for fractures, although care must be taken as breaches in applied coatings may result in rapid localised degradation of the alloys. Various coating methods have been applied to improve the properties of the implant interface with surrounding tissues such as electrodeposition (EDP) and physical vapour deposition (PVD). A branch of interest has been researching calcium phosphate (CaP) coatings deposited by electrodeposition as these coatings consist of some of the main constituents found in bone and as such have shown beneficial osseointegration effects in many investigations [13, 14, 15, 16]. Hydroxyapatite (HA) is the stable phase of CaP within physiological conditions and according to Clarke [17] HA crystals within bone tend to be of an *ca.* 20 nm, lending themselves to easier

biological resorption. However, the electrodeposition of CaP coatings has shown to leave voids in the coating which expose the underlying alloy, allowing the early onset of corrosion of the Mg alloy. PVD depositions provide an interesting potential for use to complement these CaP coatings as PVD coatings tend to be hard, amorphous and homogenous [18], giving the potential to cover voids left by the EDP process. However, it must be taken into consideration that these coatings must fulfil all the same requirements for a bioresorbable material. PVD coatings of HA have been shown to promote osseointegration but have been known to be structurally weak and delaminate from the surface of implants [19]. This leaves room for new branches of investigation of bioresorbable phosphate-based glass (PBG) coatings which can similarly provide a layer of protection and promote beneficial cytocompatibility effects [20, 21], whilst allowing for controllable resorption profiles by the modification of the PBG composition. Specifically, new research is being conducted into the degradation profiles of "invert" glasses consisting of pyrophosphate (Q^1) and orthophosphate (Q^0) species which have the advantage of slower and more controlled degradation in aqueous solution compared to higher P content glasses [22]. Further benefits of these PBGs are that they can be supplemented with other elements such as Zinc and Strontium, among other ions to enhance certain properties to facilitate proliferation [23], osteogenic gene expression and antimicrobial activity [24], suggesting suitability for bone remodelling applications.

Aim and Objectives

The clinical performance of current Ti implants for bone fracture fixation have proven adequate over the last 100 years. However, there are still shortcomings with this type of treatment to be overcome such as cortical porosis, delayed bridging, bone physiology interference leading to refracture after implant removal and the associated surgery costs to health services for removal. Next generation biomaterials must be explored to provide not only fixation at the bone interface

but the reduction of effects such as stress shielding whilst providing an alternative to implant removal surgeries.

Electrodeposition and magnetron sputtering are suitable methods of producing thin films of calcium phosphate and glass respectively and can be utilized to deposit coatings onto metallic materials such as Mg and its alloys. By understanding the morphologies, compositions and interactions of coatings deposited by these processes, improvements on current bone fracture fixation materials may be achieved.

The aim of this project was to develop a novel bi-layered coating, using CaP electrodeposition and PBG sputtering methods to functionalise and protect a bioresorbable Mg alloy and delay the onset of the corrosion process to prolong resorbable implant life whilst bone remodelling is in progress.

The objectives of the work presented here are to:

1. Survey the literature to determine potential for a novel coating consisting of complimentary layers from separate deposition methods.
2. Determine the structural properties of electrodeposited CaP coating and optimise the coating by observing the similarities/differences of depositions using varied parameters of duty cycle, deposition time and electrolyte pH.
3. Explore the effect of the magnetron sputtered PBG coatings and whether they act as a complimentary layer to the electrodeposited CaP layer and improve biocompatibility by reducing the P content in the bulk PBG target.
4. Assess the corrosion properties of the thin film coatings in physiological media and determine whether the combined coating improves the corrosion response.
5. Determine the potential bioactivity and cell response to the samples through the use of *in vitro* assays such as neutral red uptake.

The following Chapter is a detailed literature review covering the use of Mg and its alloys as a bioresorbable material, CaP coating methods and their use in orthopaedic applications, and the utilisation of magnetron sputtering for the deposition of thin PBG films of varying compositions.

Chapter 2 – Literature Review

2.1 Introduction

Biodegradable materials have attracted much research interest for use as implants due to their potential to provide initial stabilisation and structural support, permit bone healing with sustained stability and mechanical properties, and then gradually degrade (with simultaneous decrease in strength) enabling controlled transferal of physiological force to bone during healing [25]. Magnesium and its alloys are promising materials for this application due to their biocompatible nature and mechanical properties (E=42-45 GPa, ρ=1.7-2.0 g/cm^3) which are similar to those of human bone (E=3-20 GPa, ρ=1.8-2.1 g/cm^3) [26, 27]. However, the main issue with using Mg and its alloys is that their corrosion resistance is too low, and non-linear over time, when in a physiological environment, with a corrosion rate ranging from 0.3 mm/Y to 230 mm/Y [28]. Therefore, a novel method is required that can extend the dissolution time or delay the onset of corrosion until a more appropriate time in the healing process.

This chapter presents a review of the established literature, relevant to the main themes of this thesis. A context is given on Mg and its alloys and their history of use as biomaterials. An emphasis is given to the corrosion mechanisms of Mg in a biological environment, including types of corrosion, methods of measurement and factors which affect corrosion behaviour. Different strategies for protecting Mg and its alloys are also explored, specifically surface coating with a protective phosphate-based glass layer, by physical vapour deposition, as a promising technique and a variety of PBG compositions are reviewed, which are pertinent to the themes within this thesis. Another technique examined is electrochemical deposition of a surface calcium phosphate layer to delay the onset of corrosion. The benefits of performing a variety of biological assays are considered briefly as an aid to selection of biocompatibility measures. Although the literature review will consider a range of Mg-alloys being used in

biomedical application, this thesis will be focussed mainly on the performance of coated Mg-alloy WE43 in a biological environment.

2.2 Introduction to Magnesium and its alloys

2.2.1 Pure Magnesium

In the early 1800s, Sir Humphrey Davy discovered elemental Mg [29]. However, it was not until 1833 that Mg metal could be produced, when Michael Faraday electrolysed fused anhydrous $MgCl_2$ [29]. Since then, much has been discovered about Mg, its properties and as the sixth most abundant element on Earth [26], this has allowed for a wide variety of applications to be developed.

Mg is a light alkaline earth metal with a density of 1.738 g/cm^3 [30] and a Yield Strength which ranges between 65-100 MPa [30] giving it a high strength to weight ratio. It also has a high capacity for alloying and can support a wide range of solute elements with ± 15% difference in atomic size [26]. Therefore, Mg can be used to form a range of alloys with unique properties and can be applied to applications where weight is a constraining factor. Table 2.1 provides a summary of the atomic, physical and mechanical properties of Mg.

The crystal lattice of Mg at ambient temperature adopts a hexagonal close-packed (HCP) structure [31] which, in combination with slip system behaviours, contributes to a strong anisotropy of the Mg lattice [32]. Mg lattice parameters at 25ºC are $a = 0.32094\ nm$, $c = 0.52108\ nm$ and $c/a = 1.6236$; with angles α: 90º, β: 90º and γ: 120º [26]. Due to the critical resolved stress and high c/a ratio, basal slip $(0\ 0\ 0\ 1)\ \langle 1\ 1\bar{2}0\rangle$ is the easiest activated slip system, with prismatic slip $(1\ 0\bar{1}0)\langle 1\ 1\bar{2}0\rangle$ and pyramidal slip systems $(1\ 0\bar{1}1)\langle 1\ 1\bar{2}0\rangle$ and $(1\ 1\bar{2}2)\langle 1\ 1\bar{2}3\rangle$ potentially being active at ambient temperatures as the mechanisms of plastic deformation [32]. Another important mechanism of plastic deformation is twinning due

to c-axis tension $(1\,0\bar{1}2)\langle 1\,0\bar{1}1\rangle$ [32], which is illustrated along with slip mechanisms in Figure 2.1.

Table 2.1 Properties of Pure Magnesium [2, 6]

Properties		**Magnesium**	**Units**
Atomic	Symbol	Mg	-
	Element Classification	Alkaline Earth Metal	-
	Atomic Number	12	-
	Atomic Weight	24.305	amu
	Atomic Volume	14.0	cm^3/mol
	Atomic Radius	0.160	nm
	Ionic Radius	0.072	nm
	Valence (oxidation state)	2+	-
Physical	Density (at 20ºC)	1.738	g/cm^3
	Melting Temperature, T_m	650	ºC
	Boiling Temperature, T_b	1090	ºC
	Thermal expansion coefficient	$26.1x10^{-6}$	$ºC^{-1}$
	Thermal conductivity	157.5	W/mºC
Mechanical	Elastic Modulus	41-45	GPa
	Compressive Yield Strength	65-100	MPa
	Ultimate Tensile Strength (annealed sheet)	160-195	MPa
	Hardness	40-41	-
	Fracture Toughness	15-40	$MPam^{1/2}$

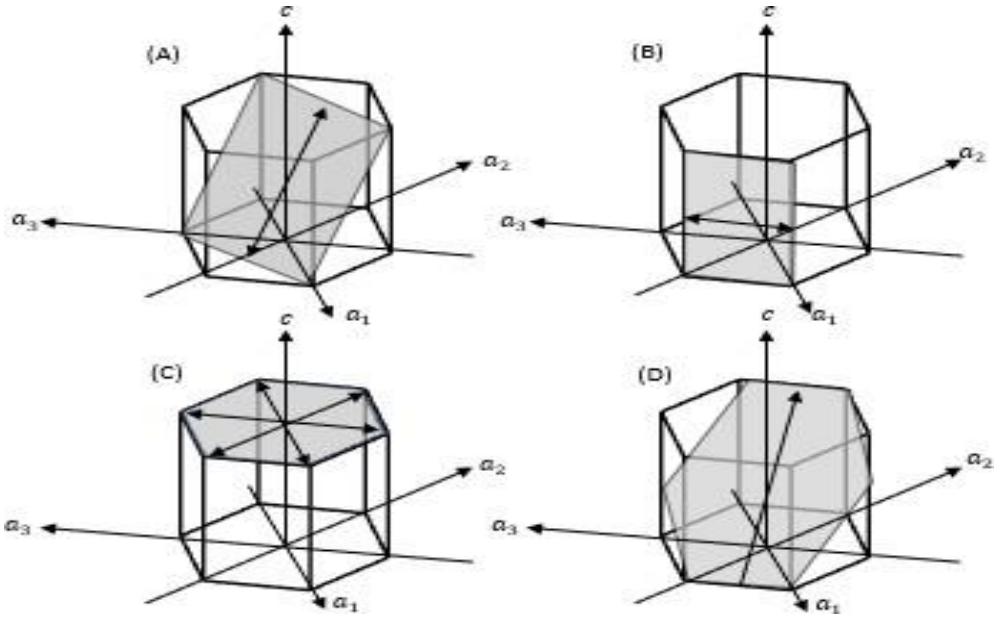

Figure 2.1 Slip and twinning deformation systems of Mg: (A) Pyramidal (B) Prismatic (C) Basal (D) Tensile twinning

2.2.2 Magnesium Alloys

The main issue which arises from using Pure Mg in the body is its poor corrosion resistance as it is one of the most electrochemically active metals [33]. Despite the corrosion products of Mg being beneficial for physiological functions [9], the corrosion occurs too rapidly for use as a biodegradable implant with some corrosion rates being shown as high as 407 mm/y [34] compared to the required 0.5 mm/y [35] and additionally, is not homogenous due to a strong tendency for localised corrosion [36]. This rapid corrosion also gives rise to the issue of hydrogen gas evolution. If the evolution is too rapid, the gas cannot be absorbed and causes a ballooning effect to take place, which subsequently causes an alkaline pH shift [37].

There are generally two ways to improve the corrosion behaviour of Mg:

i. tailor the microstructure (e.g. grain size [38, 39] and texture [40]) and composition of the material through processes such as alloying [41]
ii. perform surface treatments or form coatings [33], to produce an outer, protective layer.

A diverse range of solute elements can be added to Mg to improve its mechanical and corrosion properties. Alloying material selection can be influenced by several factors based on the properties of Mg as a metal. Due to the hexagonal close packed (HCP) structure of Mg, a continuous solid solution can be formed with other hexagonal metals such as zinc (Zn), cadmium (Cd) and zirconium (Zr). However, the formation of a solid solution is restricted by atomic size factors to allow a ± 15% difference. The low electronegativity of Mg also promotes formation of compounds with less electropositive metals such as silicon (Si) [42]. Many of the alloying elements chosen improve corrosion resistance through grain refinement and the development of a more uniform protective layer combined with the removal or passivation of impurities which form a point of weakness for corrosion to nucleate [43].

The American Society for Testing and Materials (ASTM) developed a code system for distinguishing the composition of alloys, which has been adopted for Mg-alloys. The first two letters indicate the principal alloying elements, with the highest proportion in front. The most common letters used in Mg-alloys are shown below in Table 2.2. These letters are followed by the numerical weight composition of the alloy components [26]. Table 2.3 summarises the composition of some common Mg-alloys.

Table 2.2 Letter designation of common alloying elements in Mg-alloys [21]

Designated Letter	Alloying Element
A	Aluminium
B	Bismuth
C	Copper
E	Rare Earth Element
H	Thorium
K	Zirconium
L	Lithium
M	Manganese
Q	Silver
S	Silicon
W	Yttrium
Z	Zinc

Table 2.3 Composition of common alloying elements in Mg-alloys [2, 22, 23, 24, 25]

Magnesium Alloy	Alloying Element Composition (wt%)							
	Al	Zn	Mn	Li	Nd	Zr	Y	Gd
AM60	6.0	0.2	0.2	-	-	-	-	-
AZ31	3.5	1.4	0.3	-	-	-	-	-
AZ61	6.5	1.0	0.15	-	-	-	-	-
AZ91	9.5	0.5	0.5	-	-	-	-	-
LAE442	4.0	-	-	4.0	2.0	-	-	-
WE43	-	-	-	-	3.2	0.5	4.0	-
WE54	-	-	-	-	1.9	-	5.1	2
ZK21	-	6.0	-	-	-	0.8	-	-
ZM21	-	1.2	2.2	-	-	-	-	-

Mg and its alloys have been investigated as biodegradable implants due to their tailorability and similarity in mechanical properties to bone. The section below summarises the history of use of Mg and its alloys as biodegradable implants.

2.2.3 Mg and Mg-alloys as biomaterials

The origins of Mg as a biomaterial are thought to be from the physician, Edward C. Huse, who may have used Mg wires as ligatures to stop the bleeding of a radial artery and in the operation for varicocele in three human patients in 1878 as he also wrote very enthusiastically about the degradable properties of Mg [44]. This work was then followed by Erwin Payr, who started experiments on Mg resorption in 1892 [45] but was limited by the difficulty obtaining filigree fabricated devices until nearly 1900 [46], when he received pure Mg sheets, plates, pins, spheres, wires, pegs, cramps and nails from a company in Austria [45, 46] to pursue his work. His work varied from cardiovascular and musculoskeletal applications to uses in general surgery and tissue responses to corroding Mg [9], providing a basis for the development of biomedical Mg.

2.2.4 Cardiovascular Applications

In research of ligatures, Payr investigated tubular, thin-walled Mg cylinders as connectors for vessel anastomosis – a surgical connection between two structures [45], which he tested in pigs and femoral arteries of dogs [47]. He observed that the connection of the vessel ends solidified with a severely thickened intima layer – innermost layer of an artery or vein, and a fibrous ring on the outer side after 8 days [45]. Research, however, was impeded as the Mg wires available at the time were too brittle to be an effective suture, break immediately upon kinking prevent knot formation [48]. Further research by Höpfner confirmed that thrombosis rarely occurred on extravascular placed tubes and thrombosis occurs in vessels with a diameter < 3mm [49].

However, the Bureau of Mines of the Department of the Interior [50] suggested more ductile wires could be produced by distillation in a vacuum or by alloying with less reactive elements such as Au or Ag. In 1910, a technique was introduced where metallic ring plates with punched holes were used to fix the vessel ends and connect rings with a pressure less than 2.3 kg/in^2 [51]. The Mg rings held their original shape for around 1 month before beginning to break down and were completely absorbed within 80-100 days [51]. Alongside this, Lespinasse also introduced a Mg plate with holes for repairing lateral slits in vessels as the ring plates prevented the entry of foreign material into the lumen of reconnected vessels, thus the vessels were free from clots [51].

It was not until 1935 that a patent was filed for a “Mg rope” consisting of a mesh of thin wires surrounding a stronger, guiding wire bundle [52] as a suture, which benefitted from the superior processing of Mg having overcome the issues of low tensile strength and stiffness obtained from cold work hardening [52]. Stone and Lord used pure Mg and Mg-Al wires to favour clotting in aortic aneurisms in dogs in 1951 and were found to be twice and three times as thrombogenic as SS wires, respectively [53]. The alloying with Al allowed the required bending for clinical application and improved the thrombogenic capacity of the wire. However, the alloyed wires had undergone almost complete dissolution by 21 days post-implantation [53]. This rapid dissolution rate was given as a limitation for many clinical applications as ligatures. However, Jorgensen patented a modified haemostatic clip design in 1986 [54], which had been inspired by absorbable metal clip Andrews had published in 1917 as a substitute for ligatures and deep sutures [48]. This was due to the benefits that the absorbable metals were not acting as permanent foreign bodies and alloying had been seen to improve mechanical properties such as ductility, flexibility and toughness [48].

2.2.5 Musculoskeletal Applications

In 1900, Payr proposed a variety of potential implants to perform different functions such as regaining joint functions and other osteosynthetic applications. The use of Mg plates and sheets was proposed to prevent reunion of dissected bone tissues by a dense, fibrous layer after full resorption [46, 55] with poor *in vivo* results [47]. It took further work by Chlumsky, who interposed thin sheets between freshly separated bone surfaces in knee joints, to prevent joint stiffness in dogs and rabbits [56]. This work also accomplished restoration of joint motion in animals and humans although there was concern that these joints would stiffen again over time [57].

Other uses for Mg sheets and plates, alongside pins, nails, wires, pegs and cramps, include stabilisation and fracture fixation. An early clinical trial in a 17-year old patient found that, one day after implantation in the leg, extensive subcutaneous gas cavities had formed causing local swelling and pain, resulting in removal [58]. Lambotte continued clinical investigations treating supracondylar fractures in children due to the rapid healing process and small implant volume required, finding that total joint restoration and function could be achieved with the only complication being the formation of gas cavities [59]. However, these cavities were not a major concern in any case and disappeared after several weeks [58]. Throughout clinical trials, Lambotte learned that Mg cannot be implanted with other metallic implants due to preferential electrolytic corrosion, and subsequent failure of Mg. However, implants made strictly of Mg would be suitable for use fixing many types of fractures varying in location from the humerus head fractures to diaphyseal and epiphyseal fractures in the limbs [58]. Despite critical reports of Mg from Groves [60] and Zierold [61], Verbrugge *et al.* [62] investigated the effects of a solid Mg cylinder implanted in the femura of dogs and rabbits, which maintained mechanical properties for between 4 – 6 months before reaching the point of degradation where described as hollow and brittle. Due to the normal bodily reactions maintaining a pH equilibrium and the

absence of toxic effects to the corroding magnesium, such as cell necrosis, Verbrugge stated that implanted Mg is not toxic or an irritant. But requires a slow corrosion rate to allow callous formation which holds the bone together as it hardens over time, allowing the healing of the bone and gradual restrengthening [63].

Conversely, McBride stated that Mg metal plates and medullar pegs were not suitable due to the rapid absorption when plates are placed on the bone and that volatile gas formation from pegs requires an exit into the surrounding soft tissue [64, 65]. Despite this, screws tended to be more corrosion resistant than plates by observation, especially when they were fitted tightly into cortical bone. Safer fixation could be achieved by using a higher quantity of Mg than was required for the expected period of implantation allowing for a longer degradation period before loss of structural integrity [64]. The Mg alloys employed remained stable for 3 – 7 weeks and accomplished fixation if the drill holes were sufficiently small so to be integrated with the threads, and if they were applied with a good mechanical advantage when rejoining the separated bone fragments [64]. Another benefit was that the Mg stimulated early cell proliferation within a matter of hours, however, it must be noted that the callus produced should not be trusted too early for firmness as a good implant site.

The alloying of Mg with Cd was explored in the form of a plate and screw combination [66] and was successfully used to treat 34 pseudoarthritis cases with complete resorption of the osteosynthesis material and stimulation to form callous bone. It was hypothesised that this stimulation was caused by the Mg implant neutralising the inflammatory tissue's acidic environment and so a specially designed intramedullary rod or plate could be utilised for the rapid consolidation of bone fractures [66].

2.2.6 General surgery

Since 1900 Mg has been used in general surgery for many functions. Payr recommended Mg sheets and plates for suturing well-vascularised organs like the liver and spleen and has been successfully applied in animals and humans [47, 67]. Plates were used to close the wound by adjusting the liver resection surfaces and plates were connected using iodine-catgut sutures and 50% resorption was seen for large plates between 3 and 5 weeks [67]. Evolved hydrogen gas proved to be beneficial as it impregnated the fibrous tissue during formation, stopping local bleeding by the tamponade effect – a decrease in cardiac output and shock, which was in turn enhanced by adhesion of the omentum majus fold of the stomach, intestine and the abdominal wall to the resection area [67].

Cavernous haemangioma, the mass formed from swelling of capillaries, and large-vessel aneurysms were also treated using Mg arrows in a 14-year old patient, where the arrows were implanted at the chin [68] causing the tumour to become denser within the first days of treatment. This treatment is based on the principle that enhanced blood clotting caused by the hydrogen evolution from degrading Mg, will mechanically destroy the endothelium and septa of the tumour [69] without causing gas embolization. This technique was trialled again in 1981 in 27 haemangioma patients, including a 3-month old, with a 50% success rate although no adverse effects were observed in a 5-year follow up [70]. This is likely due to a theory presented by Hoffheinz and Dimitroff, whereby the rapid corrosion of Mg in haemangioma is enhanced when located in organs with a higher blood-flow, leading to earlier transformation of tumour tissue into fibrous granulation tissue [71].

A further surgical application for Mg tubes is as connectors for intestinal anastomosis/neurorrhaphy (connection between two structures). Due to the tube design consisting of a “male spring” and a female part to secure the connection after joining [72], the

number of catgut sutures were able to be reduced and connection made between two nerve ends or damaged intestine tissues.

Fontenier *et al.* investigated *in vitro* and *in vivo* use of various Mg metals and alloys as dissolvable anodes for bioelectric batteries for pacemakers. In this case industrial-grade-purity Mg outstripped the performance of the Mg-Mn alloy in terms of biocompatibility [73] due to possible toxicity of manganese (Mn) in the body, despite neither metal showing subcutaneous necrosis and corroding uniformly [72] as high-purity Mg is known to do.

2.2.7 Tissue Response to Corroding Mg

Since the inception of Mg implants, the histological results of the tissues surrounding the implants have been of great interest as authors have reported the severe influence of corroding Mg on the peri-implant tissue [45, 46, 55, 67, 56]. Around the implants, the number of round cells and granulation tissue were seen to increase, with the granulation tissue containing small, black, metallic particles as foreign body inclusions [56, 47]. These both indicate the enhanced bioactivity and proliferation which leads to greater healing effects. Payr observed enhanced activation of blood clotting from corroding implants, exacerbated by the hydrogen gas evolution [67], leading to the high vascularity of the tissue. However, if no clotting occurs, then only a partly corroded, black surface of the implant is seen [74]. This high vascularity has been replicated through *in vivo* studies in rabbits where Dow metal pins were inserted and observations of highly thickened and vascularised periosteum in new bone formation were seen [63]. Interestingly, the new bone formed without the appearance of osteoclasts but with cystic cavities [63], likely due to the gas evolution, which indirectly causes slight bone damage, lowering the tensile strength, that repairs after full metal corrosion [75].

Depending on the composition of implants, certain pathophysiological responses can be seen. In 1980, Wexler investigated the responses of spontaneously hypertensive rats to Mg-Al wire

implants inserted into the abdominal aorta, carotid and renal arteries [76]. The small addition of Al to the wires had the effect of lowering blood pressure, increasing adrenal glandular weight and changing the enzyme and hormone levels of the rats when compared to a control group [76]. However, fibrocellular lesions were observed around the wire alongside cholesterol-positive clefts in the arteries [76] which is due to the addition of Al as this phenomenon had not been observed with pure Mg implants.

2.2.8 21st century developments

In the recent few decades, interest in Mg as a biomaterial has been reignited due to greater understanding of factors such as composition, microstructure, grain size, texture [77] and their influence on the corrosion rate and biocompatibility of Mg and its alloys. As stated above, pure Mg degrades too quickly for most potential orthopaedic applications [36] and so alloying with other materials has come to the forefront of research to reduce corrosion rate and improve mechanical properties of the implant [43]. This may be achieved through grain refinement, solid solution strengthening and precipitation hardening.

Research on Mg-alloys originally focussed on the potential of commercial alloys such as AZ31 [78], AZ91D [77] and WE43 [79], Table 2.3, but the suitability of some alloys was questioned upon the discovery that some of the alloying components are toxic to the body. For example, Al primarily accumulates in the nervous system and implicates the pathogenesis of Alzheimer's due to its influence on AβP cross-linkers [80]. Also lithium (Li), when exceeding 2 mmol/L in plasma reduces kidney function and neurotoxic effects are observed [80]. As a result, efforts have moved towards designing new, biocompatible or low toxicity alloying element systems.

Mg-Ca alloys are intriguing as Ca is the most abundant mineral in the body and acts as a grain refiner for Mg alloys, improving the material strength according to the Hall-Petch law [81] which states the smaller the grain size of a material, the higher the elasticity limit. Their good

combination of mechanical and corrosion properties in multiple studies [82, 83, 84], with even a 0.6 wt% addition, improving bending strength, compressive strength and corrosion resistance of pure Mg, are of interest [83]. However, as the Ca content is increased above 5 wt%, alloys tend to become too brittle due to the increased precipitation of Mg_2Ca which serves as a source for cracking and reduces ductility [82]. Even with the improvement of corrosion resistance, the restrictions on Ca addition due to machinability, coupled with fast degradation within bone [82], Mg-Ca alloys struggle to satisfy the mechanical and corrosion requirements for bone implants.

Bornapour *et al.* [85] investigated biocompatibility and corrosion of Mg-Sr alloys since strontium (Sr) is chemically and physically similar to Ca, acting as a grain refiner to Mg-alloys. It was found that Mg-Sr alloys containing <1 wt% Sr had a slower corrosion rate than pure Mg but additions of >1 wt% accelerated the corrosion rate [85]. Sr accumulates in the skeleton, mostly in trabecular bone and has shown the ability to substitute for Ca in the formation of hydroxyapatite (HA) [86], which presents at the interface between the alloy and corrosion products, slowing the corrosion rate of the alloy.

Zn is another commonly used alloying element for Mg due to its solid solution and precipitation strengthening properties [87] along with being an essential component to a range of structural, catalytic and regulatory functions in mammals [88]. Due to the galvanic effect of Mg_2Zn precipitates, other alloying elements are generally needed to counteract the effect on corrosion rate but these additions of elements such as Ca, lead to increased size and number of precipitates thus reducing corrosion resistance of these alloys [89]. Alloying with rare earth elements such as Yttrium (Y), allows the formation of an icosahedral quasicrystalline MgZnY phase in situ during solidification, which is isotropic and has properties of high hardness, corrosion resistance and low interface energy and friction coefficient [90]. Most of the successful *in vivo* reports on Mg implants are alloys containing rare earth elements, which

benefit from similar ionic radii to Ca and have the possibility to be an isomorphous replacement to Ca [91]. Rare earth elements exist in the body in minute levels suggesting biocompatibility and research has demonstrated that many rare earth elements exhibit anti-carcinogenic properties [92], as well as their strength at high pressure around 160 MPa and creep resistance [93]. When selecting which rare earth elements to incorporate in Mg-alloys, it is best to select elements with high solubility in magnesium to avoid the formation of intermetallics during processing. This is to avoid inducing galvanic corrosion [94] and due to this high solubility, it is possible to tailor mechanical and degradation properties over a wide range by adjusting alloy composition and utilising heat treatments. Also to be taken into consideration are the cost of rare earth elements and the difficulties with production due to their chemical similarity making them complex to extract from one another [94]. The Mg WE43 alloy is beneficial for biodegradable applications due to the rare earth element additions and has been brought to market in the form of the MAGNEZIX® compression screw, which was approved in Germany as the first Mg-based implant for use in humans worldwide in 2013 [95]. However, more research is needed to find a solution for larger implant applications as a larger surface-area of an implant will have a different degradation profile to that of the MAGNEZIX® compression screw.

One of the reasons for Mg's poor corrosion resistance is the internal galvanic corrosion caused by secondary phases and impurities [96]. A way to combat this is to fast-cool the molten alloy below its glass-transition temperature to avoid crystallisation and form a bulk metallic glass, with alloy contents able to extend beyond the original equilibrium solubility [97]. Mg-Zn-Ca glasses have been developed such that the high Zn content in solid solution allows the formation of a partial passivation surface layer, reducing hydrogen evolution levels and exhibiting a more uniform corrosion morphology during testing [98]. However, a primary concern is intrinsic brittleness due to structural relaxation [97] which may cause issues for *in*

vivo testing, where the alloy will be placed under stresses and therefore other solutions may be more suitable for implant applications.

Surface coatings and treatments present a promising method for implants due to their improvement of properties of the underlying material. For Mg-alloys, surface modifications are primarily used to improve the corrosion resistance of the alloy [37] through means of a chemical, physical or combination treatment. Physical deposition coatings utilise various techniques such as electrodeposition [99], physical vapour deposition [100] and sol-gel deposition [101] to deposit a protective coating on the surface of the substrate, which often act as a sacrificial barrier to delay the onset of corrosion of the underlying alloy. Investigations into the application of a CaP coating have demonstrated that the corrosion resistance of Mg-based alloys can be improved [102]. CaP coatings are also highly biocompatible, are an important precursor for bone growth and have already been used in a variety of orthopaedic applications [15, 103, 104]. However, due to difficulties controlling aspects such as phase formation, cracking and poor adherence [37], a complete solution for orthopaedic applications has not yet been found. However, the potential for combining this with another technique is promising. Recently, there has been investigation into phosphate-based glasses (PBG) as a potential surface coating for biodegradable applications [105] due to their ability to be completely resorbed in a biological environment combined with their tailorability and corrosion resistant properties [106].

Both CaP and PBG coatings show promising possibilities for orthopaedic applications and will be explored in further depth in later sections of this review. The next section discusses the corrosion mechanisms of Mg and its alloys, which need to be overcome for further advancement in this field.

2.3 Introduction to Corrosion

The corrosion phenomena of metals in metal-fluid systems is defined as “an electrochemical process that destroys the bulk material, starting at the metal surface” [79]. The corrosion of metal is caused by an unalterable oxidation-reduction reaction [26] in which there are two parts: an anodic (Equation 2.1) and a cathodic (Equation 2.2) reaction. The anodic reaction, in which the metal dissolves in the medium, providing ions to the electrolyte, can be expressed as [26]:

Equation 2.1

$$M \rightarrow M^{n+} + ne^{-}$$

The electrons which have been released from the metal are consumed by other species in the electrolyte, giving rise to the cathodic (reduction) portion of the reaction, which is given by the following equation in a natural or alkaline solution:

Equation 2.2

$$O_2 + 2H_2O + 4e^{-} \rightarrow 4OH^{-}$$

An equilibrium of the corroded surface is reached as the rate of metal ions entering and leaving the solution becomes the same. This means that the flow of current is equal in opposite directions and the net current is zero. However, the metal ion dissolution leads to the surface obtaining a negative charge, which attracts ions from the solution to the surface. This causes a non-homogenous ion distribution at the surface, with an electric double layer formed causing a potential difference across the interface [107]. The open circuit potential (OCP), defined as the electrode potential of a working electrode relative to the reference electrode when no potential or current is applies, is affected by increases in either the anodic or cathodic reaction as the equilibrium state is disrupted, which then allows either passivation or corrosion processes to continue [108].

The standard electrode potential, E^0, is a thermodynamic equilibrium potential which denotes the tendency of a metal to corrode in aqueous media. E^0 is measured relative to a standard hydrogen electrode (SHE) with a potential of 0V and a more negative value represents a stronger tendency for spontaneous corrosion [26]. Table 2.4 summarises the E^0 values for various metals.

Table 2.4 Standard electrochemical series for selected metals [92]

Metal	Half-Cell Chemistry	E^0/ V
Li	$Li^+ + e^- \leftrightarrow Li(s)$	-3.05
Na	$Na^+ + e^- \leftrightarrow Na(s)$	-2.71
Mg	$Mg^{2+} + 2e^- \leftrightarrow Mg(s)$	-2.37
Zn	$Zn^{2+} + 2e^- \leftrightarrow Zn(s)$	-0.76
Fe	$Fe^{2+} + 2e^- \leftrightarrow Fe(s)$	-0.44
Ni	$Ni^{2+} + 2e^- \leftrightarrow Ni(s)$	-0.25
H	$2H^+ + 2e^- \leftrightarrow H_2(g)$	0.00
Cu	$Cu^+ + e^- \leftrightarrow Cu(s)$	0.34
Ag	$Ag^+ + e^- \leftrightarrow Ag(s)$	0.80
Pd	$Pd^{2+} + 2e^- \leftrightarrow Pd(s)$	0.95

It is useful to note that comparing the values of E^0 and OCP can relay certain information about the surface layer of a metal. For example, if a metal demonstrated values of E^0 > OCP, it would mean that the metal was not in direct contact with the solution as a passivation film has been developed [26]. The values of OCP can vary as a function of the physical and chemical condition of the metal surface and solution [26] and as such, the galvanic series, a list of corrosion potentials with respect to a reference saturated calomel (Hg_2Cl_2) electrode (SCE), allows the relative corrosion resistances of different metals to be compared. The OCP of Mg at 25ºC in NaCl is 1.63V (SCE) [109].

2.3.1 Corrosion Mechanisms of Mg and its alloys

Previous literature [36, 110, 111, 112, 113] has shown that during the anodic dissolution of Mg-alloys, Mg was still the main component dissolving into solution. This suggests that even for

Mg-alloys, the corrosion process is dominated by the same processes as for pure Mg. This section will explore the general corrosion mechanism of pure Mg. However, it must be noted that alloying elements critically effect the corrosion reactions.

The dissolution of Mg in aqueous environments generally proceeds by an electrochemical reaction with water. This produces magnesium hydroxide and hydrogen gas, such that the corrosion of magnesium is relatively insensitive to the concentration of oxygen [114, 115, 116], despite the presence of oxygen being an important factor in atmospheric corrosion [117]. The overall corrosion reaction for Mg is given by Equation 2.3 [114]:

Equation 2.3

$$Mg + 2H_2O \rightarrow Mg(OH)_2 + H_2$$

This overall reaction can be expressed as the sum of the following partial reactions:

Equation 2.4

$$Mg \rightarrow Mg^{2+} + 2e^- \ (anodic\ reaction)$$

Equation 2.5

$$2H_20 + 2e^- \rightarrow H_2 + 2OH^- \ (cathodic\ reaction)$$

Equation 2.6

$$Mg^{2+} + 2OH^- \rightarrow Mg(OH)_2 \ (product\ formation)$$

This coupled electrochemical reaction at the Mg surface is illustrated below in Figure 2.2. The electrons lost by Mg oxidation are consumed in the reduction of water to form a passive hydroxide layer and gaseous hydrogen.

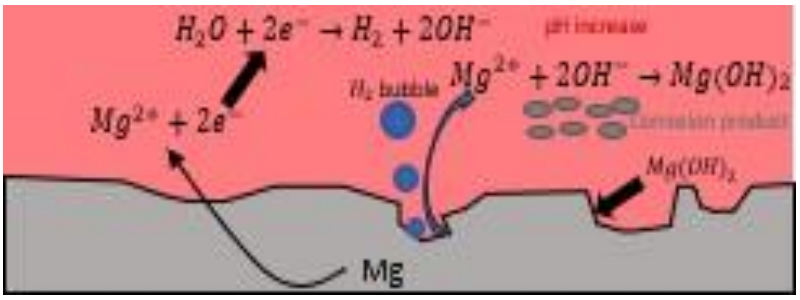

Figure 2.2 Schematic representation of Mg degradation in an aqueous solution

As shown in Figure 2.2, there is an increase in pH of the solution due to the formation of hydroxide ions. It has been shown that the formation of magnesium hydroxide raises the pH to *ca.* 11 [114]. The atomic hydrogen produced at the corroding surface can either enter the magnesium and dissolve in its lattice [118], or it evolves to form bubbles of H_2, which has been hypothesised to account for a proportion of corrosion cracking in $Mg(OH)_2$ [118].

2.3.2 Negative Difference Effect

Magnesium experiences an electrochemical phenomenon known as the negative differential effect (NDE), which should be regarded as a common process in the corrosion of magnesium [119]. For most metals and alloys like Fe, steels, Zn, etc., an increase in applied potential, E, or current density, I, will increase the anodic reaction rate alongside a decrease in the cathodic reaction rate. Similarly, an increase would be seen in the anodic dissolution rate alongside a decrease in the cathodic hydrogen evolution. However, it has been observed that the hydrogen evolution behaviour on magnesium appears to act contrary to the basics of electrochemical theory [120, 121], as illustrated in Figure 2.3.

This effect is characterised by an increase in rate of hydrogen evolution with increasing anodic overpotential relative to the open circuit, providing a local cathodic reaction for a significant portion of the anodic reaction [122]. This causes both the anodic and cathodic reactions to increase with increasing applied potential. This is shown by the reaction rate I_{Mg} straying from the expected path along I_a and the hydrogen evolution following I_H until point $I_{H,m}$ rather than the expectation of following line I_c. The difference, Δ, for applied galvanostatic current density I_{appl}, where $I_{appl} = I_{Mg,m} - I_{H,m}$ [123], is given by Equation 2.7:

Equation 2.7

$$\Delta = I_0 - I_{H,m}$$

Where I_0 is the spontaneous hydrogen evolution reaction rate on Mg in the electrolyte at the corrosion potential and $I_{H,m}$ is the measured hydrogen evolution rate for the corresponding applied current. As $I_{H,m}$ is higher than I_s, the difference value for Mg is negative.

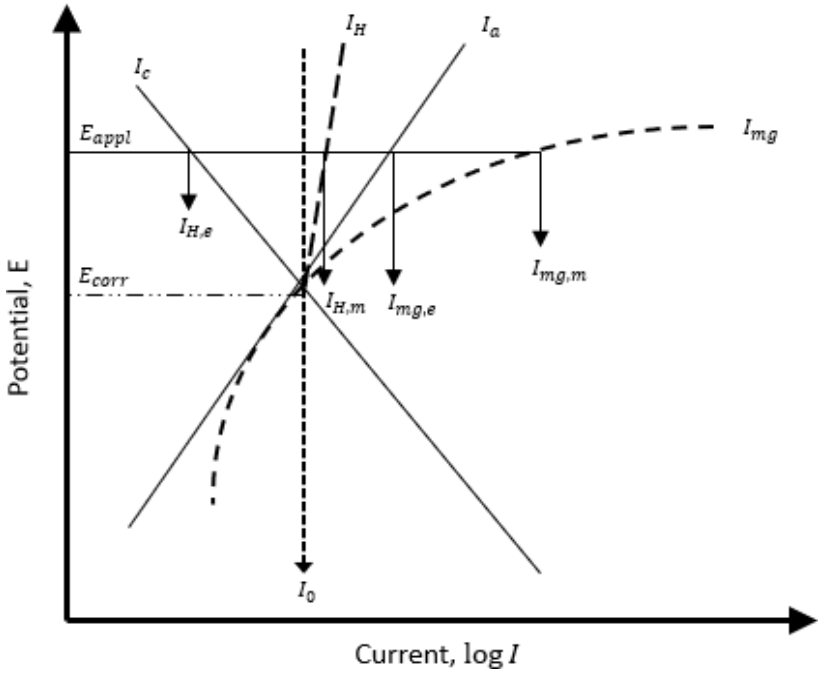

Figure 2.3 The Negative Differential Effect (NDE) exhibited during Mg corrosion showing the rate of H evolution to increase with increasing anodic polarization

There have been several theories proposed as to the origin of the NDE. Such as noble impurity element enrichment [124, 125], non-faradaic mass loss – where the overall electrode composition changes with ongoing current supply, *via* metal spalling [126, 127], formation and dissolution of hydrides and partially protective films [128, 129, 130, 131], and univalent Mg-based dissolution followed by further oxidation of $Mg^{+} \rightarrow Mg^{2+}$ in solution [132, 133], a model of which is illustrated in Figure 2.4.

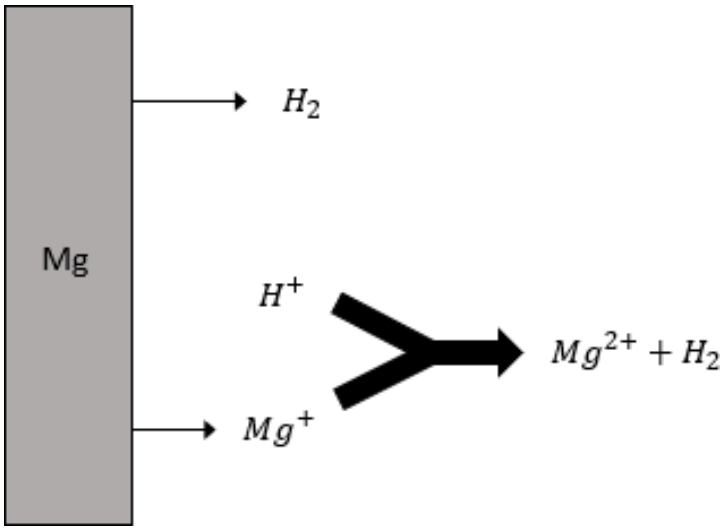

Figure 2.4 Mono-valent Mg ion model

Currently, there is no consensus on the physical origins of the NDE, however, it has been observed that during cathodic polarisation, a passivation film covers the surface of Mg when a sufficient cathodic potential ($E < E_{pitting}$) is achieved [134].

During anodic dissolution, the passivation film starts to break down as current density or applied potential increases above the pitting potential, $E_{pitting}$ and the film becomes progressively disturbed [43]. As the film is progressively disturbed, exposing the Mg surface, anodic dissolution becomes easier and involves the intermediate species of monovalent Mg^{+} ions, produced electrochemically [43]. It must be noted that these ions have not been observed in experimental work, but it is assumed that monovalent Mg^{+} is a very short-lived intermediate

that cannot be detected [128]. It is hypothesised that these monovalent ions react and produce hydrogen following the below sequence [43]:

Equation 2.8

$$2Mg^{+} + 2H^{+} \rightarrow 2Mg^{2+} + H_2$$

It has also been observed that the hydrogen produced is proportional to the film formation of $Mg(OH)_2$ [135] and involves reactions of both Mg^{+} and Mg^{2+} with water to produce hydrogen molecules. Recent modelling efforts [136, 137, 138, 139, 140] have shown that water dissociation and hydrogen evolution are more likely on surfaces containing hydroxides and also with the presence of impurities, such as transition metals and many rare earth metals. However, Taylor [140] was the first to simulate the NDE by exploring a Tafel based reaction mechanism and apply a surface kinetic model where it was assumed that sites where OH was adsorbed were most vulnerable to dissolution as Mg-OH bonds have a tendency to weaken adjacent metal-metal bonds [136].

2.3.3 Passivity and passivation layer breakdown

The natural formation of a protective film on the surface of a metal is known as passivity. This occurs due to the reaction of a metal with its environment, leading to a reduction in the chemical or electrochemical activity of the metal [141]. Mg's corrosion resistance in specific environments generally depends on the film characteristics and properties. For example, MgO is formed on the surface of Mg when exposed to the ordinary environment [37]. The protection provided by this film is limited and does not show the same protective ability and stability as oxide films that form in atmosphere on metals such as aluminium or titanium alloys [142]. Typically, the surface layer on Mg alloys is unstable and can break away easily due to the ease with which the crystal lattice is cleaved. The thickness of these layers tend to be between 20 -

50nm thick [143, 144, 145] and in air will consist of an inner layer of MgO and an outer layer of $Mg(OH)_2$, which can be seen as humidity is sufficient for the formation of a hydroxide layer [37]. In an aqueous environment, the initial layer hydrates to form a duplex layer similar to that of an air-formed film [146], consisting of inner MgO and outer $Mg(OH)_2$ layers. There is a clear correlation between the composition of the layers and the thickness of the coating in that hydration results in thickening of the film [143], where the inner MgO layer retained a constant thickness and the outer hydroxide layer increases in thickness [144].

In the case of alloys, a three-layer model has been developed for the characterisation of surface passivation films after immersion in NaCl solution [36], an example of which is illustrated in Figure 2.5. The passivation layer generally requires thickening through treatment such as thermal oxidation to provide enough protection to avoid events such as hydrogen burst during initial immersion in a chloride-containing environment like simulated body fluid (SBF) [96]. However, over-thickening of these films must also be avoided to prevent issues regarding film stresses. These films follow a square-root law of oxide growth over oxidation time with a thickness of a few µm being developed commonly [96]. This general square-root law is given by Equation 2.9:

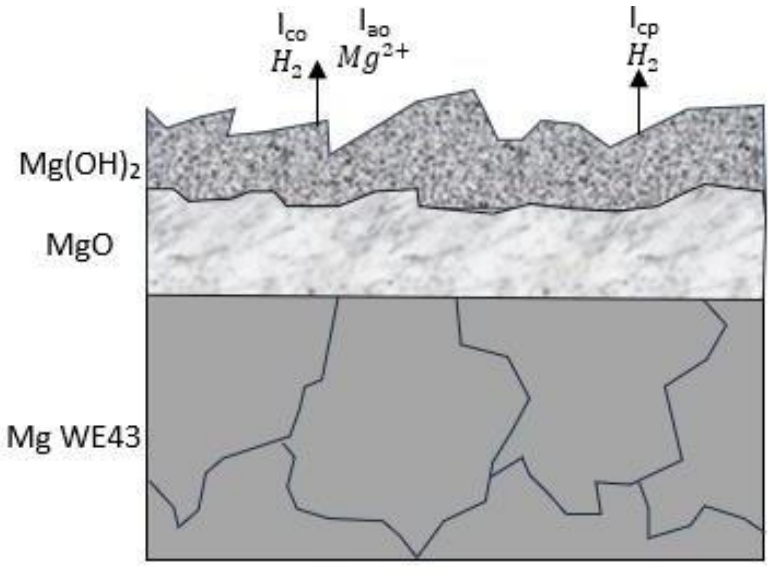

Figure 2.5 Schematic of the corrosion interface of Mg WE43 alloy in NaCl

Equation 2.9

$$d_{ox} \propto L = (Dt)^{1/2}$$

Where d_{ox} is the thickness of the growing oxide, L is the diffusion length, D is the diffusion coefficient of the oxygen carrying species and t is time.

The combined oxide and hydroxide films act as protective layers [114, 134], by inhibiting the release of metal ions into the solution, the migration of solution anions into the metal and the migration of electrons across the interface. However, in a chloride-containing environment, the hydroxide layer tends to become extensively nanoporous and results in rapid non-protective corrosion [147], due to the large surface area of the porous film. The corrosion mechanism is supported by the formation of $MgCl_2$ [114] through the form of pit nucleation in Equation 2.10 [148]. This reaction is expressed as Equation 2.11 [149]:

Equation 2.10

$$Mg + 2Cl^- \rightarrow MgCl_2 + 2e^-$$

Equation 2.11

$$Mg(OH)_2 + 2Cl^- \leftrightharpoons MgCl_2 + 2OH^-$$

The dissolution of Mg^{2+} ions in media and the hydrogen evolution during corrosion depends on the conditions at the surface and into the bulk metal. The different types of corrosion observed on Mg surfaces are reviewed below, prior to a description of methods used to measure corrosion rate.

2.3.4 Types of corrosion

Magnesium alloys are readily active in terms of tendency to corrode and are weakened by issues such as impurities and the nature of the hydroxide layer [109, 114]. They are also affected by the environment in which they reside [121] and this can cause them to corrode in different mechanisms of which the main types for Mg alloys are described below:

2.3.4.1 Galvanic Corrosion

Galvanic corrosion occurs when two metals with different electrochemical potentials are in contact, in the presence of an electrolyte [150]. Magnesium is the most active metal in the galvanic series [151] and as such acts as an anode, which corrodes and produces corrosion products on the contact site with the cathode [152]. An example of this is illustrated below in Figure 2.6. Magnesium alloys are also highly susceptible to microgalvanic corrosion, because of impurities such as Nickel (Ni), Iron (Fe) and Copper (Cu), which feature low hydrogen overvoltages, are known to form efficient cathodes for the galvanic corrosion of magnesium [114, 121, 150].

Besides impurities, intermetallic compounds in the Mg matrix can be of importance for microgalvanic corrosion behaviour, as each secondary phase results from an interaction of Mg and a nobler alloying element present, see Figure 2.7.

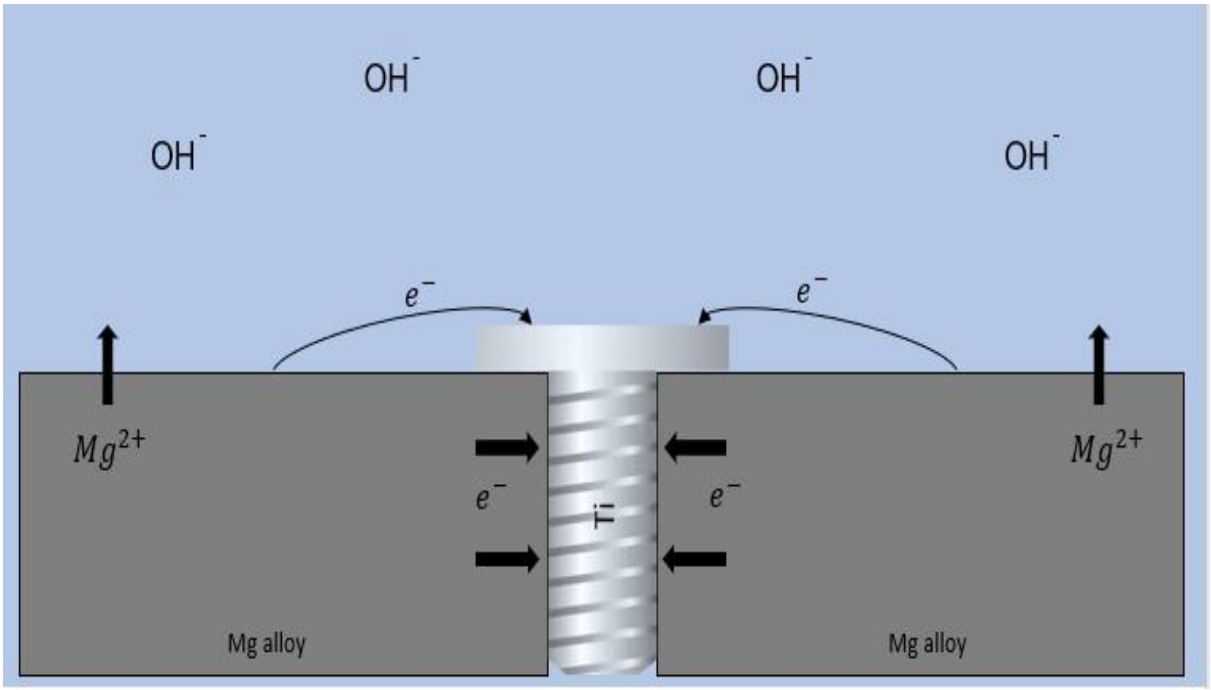

Figure 2.6 Schematic of galvanic corrosion between Mg alloy and a Ti screw

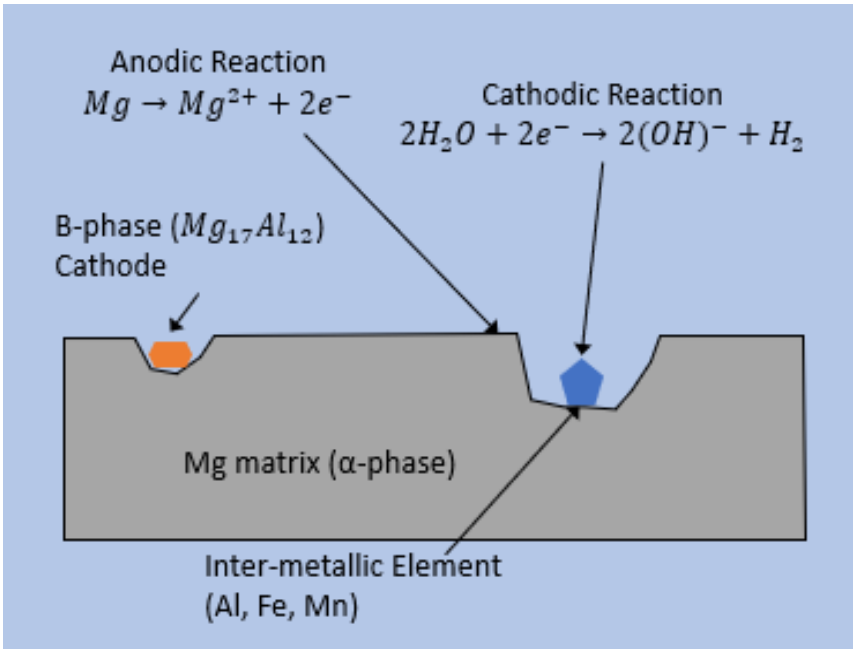

Figure 2.7 Galvanic corrosion resulting from inter-metallic elements

2.3.4.2 Pitting Corrosion

Pitting corrosion of Mg results from the rapid corrosion of small-localized areas, which damage the protective surface oxide layer [152], as illustrated in Figure 2.8. This form of corrosion can be more problematic than other forms of corrosion as surface pits are difficult to see due to the presence of corrosion products often obscuring the areas where pits form [152]. The environment within the pits is aggressive due to the high corrosion potential causing a high localised pH change and subsequently causes the pit to enlarge and grow downwards after initial nucleation, perforating the metal matrix [153]. The mouth of the pit is small and thus prevents the dilution of pit contents, adding to the acceleration of corrosion, increasing stress produced by the pit and increasing the potential of crack formation [150].

Pitting corrosion develops further due to the presence of impurities caused by the galvanic effect. The galvanic differences in the Mg alloy microstructure can also assist in further pit nucleation [154, 155]. The parameters used to indicate resistance to pitting corrosion are as follows: 1) The passive current density i_p that measures the protective quality of the passivation layer, and 2) The breakdown potential E_b, denoting the passivation layer's resistance to breakdown and pitting attacks [114].

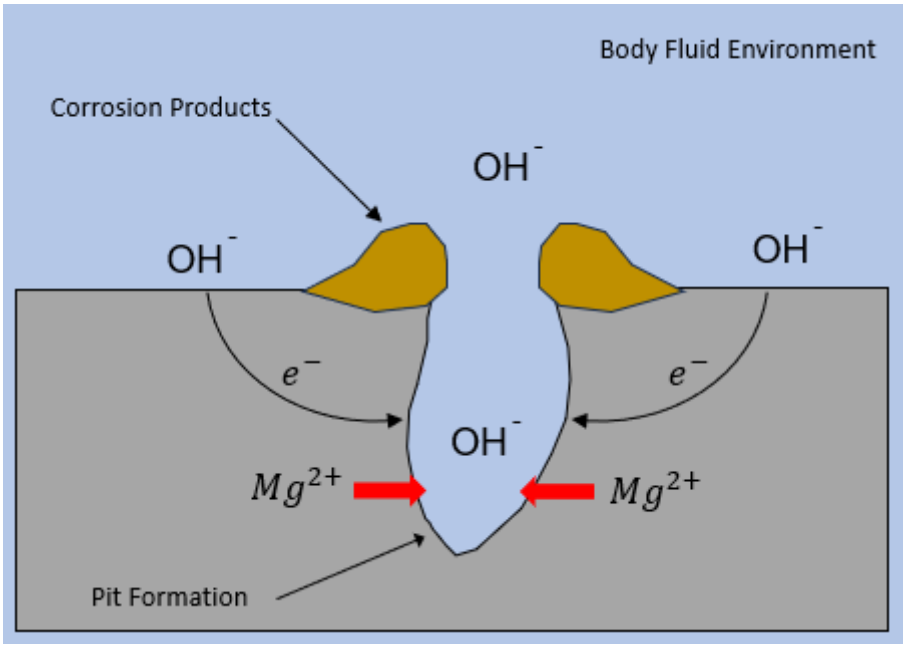

Figure 2.8 Schematic of a site of pitting corrosion at the surface of a Mg component

2.3.4.3 Stress Corrosion Cracking (SCC)

When an electrochemical potential is formed between stressed and unstressed regions of a metal under load, the chemical activity of that metal increases [152]. The corrosion rate increases roughly 2-3 times above that of the normal uniform rate [152] and results in small cracks concentrating stress (see Figure 2.9). In Mg, SCC is mainly transgranular, as a result of

precipitates forming along grain boundaries in Mg-alloys [42, 114] and MgH_2 formation may be involved in hydrogen embrittlement [114].

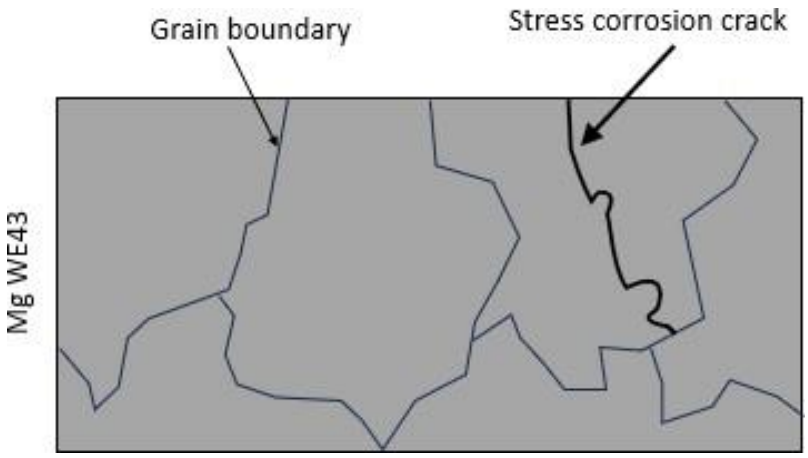

Figure 2.9 Stress Corrosion Cracking of a Mg alloy

2.3.4.4 Crevice Corrosion

Crevice corrosion is a local contact corrosion, which occurs between a metal and a metal/non-metal component where there is not a large enough gap between components to allow for the flow of media [152]. The stagnation that occurs results in the build-up of Mg ions, causing a concentration gradient to form between the entrance and the dead end of the gap. This corrosion cell formed starts to attack the metal components [156], as illustrated in Figure 2.10. However,

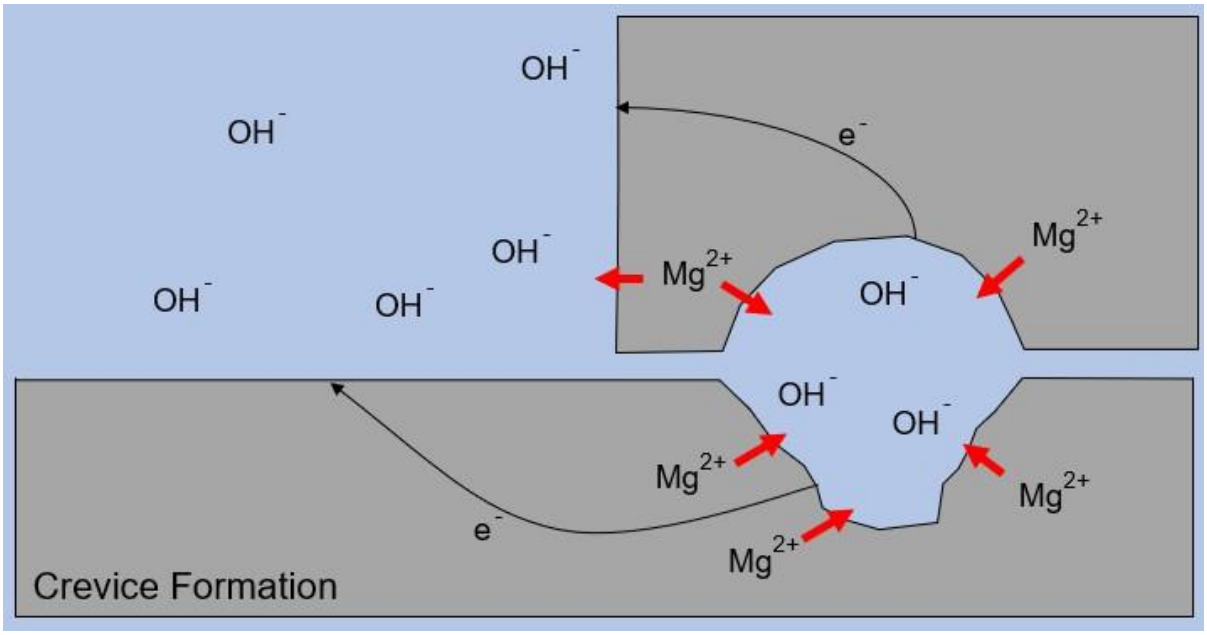

Figure 2.10 Schematic of crevice corrosion between Mg components in a body fluid environment

Mg-alloys are usually unaffected by crevice corrosion due to their insensitivity to oxygen concentration differences [114].

2.3.4.5 Filiform Corrosion

Filiform corrosion is caused by an active corrosion cell moving across a metal surface. Thread-like filiforms are initiated on the surface, having a protective coating in which pitting starts followed by the formation of narrow, semi-cylindrical filaments develop from the pit [26]. The head acts as the anode and the tail as the cathode [109]. Filiform corrosion occurs under protective coatings and anodized layers [157] and is driven by hydrogen evolution occurring on the head and outside each filament [158, 159].

2.3.4.6 Intergranular Corrosion

Intergranular corrosion is a deep and narrow pathway and can develop at a Mg-alloy surface due to grain boundary corrosion [109]. However, Mg and its alloys are generally immune to intercrystalline attack [114] because corrosion cannot penetrate inwards along grain boundaries [42] due to the boundary phases being cathodic to the grain interior [160, 114]. Instead, granular attack leads to undercutting and removal of grains [161], delineated by their boundaries with the Mg matrix.

The most common types of corrosion experienced by Mg and its alloys are filiform and pitting corrosion [162] and overall, Mg corrosion occurs through Mg ion dissolution and corrosion product formation of magnesium hydroxide and hydrogen gas. Corrosion measurement methods are discussed in the following section.

2.4 Measurement of Corrosion – *in vitro* and *in vivo*

Measuring the corrosion of Mg in a biological or simulated environment is important in the effort to better understand the suitability of Mg for *in vivo* applications. *In vitro* tests act as a qualifying step to determine whether a model would be suitable for an *in vivo* study. However, due to the different techniques used and difficulty of accurately imitating body responses, there has not been a strong correlation between *in vitro* and *in vivo* tests to date, which could potentially lead to misinterpretation of data.

2.4.1 In vitro testing

Most *in vitro* corrosion measurement methods can be categorised as either steady-state or dynamic, depending on the test parameters [163], with static corrosion tests being further categorised into polarised and un-polarised. This further categorisation is related to the presence of a driving force such as electrochemical polarisation, which is either applied or measured during the test [163]. *In vitro* studies should be carried out in an environment that mimics the body environment conditions, such as physiological temperature, pH and composition (see *Section 2.5*).

2.4.2 Steady-state testing

2.4.2.1 Unpolarised experiments

Mass loss

Mass loss experiments are generally simple and, in theory, only require a sample, corrosion medium and an accurate microbalance. The samples are cleaned in solutions such as acetone or ims, dried and placed in the corrosion medium, such as NaCl or Dulbecco's Modified Eagle Medium (DMEM), for varying periods of time depending on desired application (short term 12 – 24 h, medium term 7 – 10 d, long term 21 – 30 d), after which the sample is removed and

weighed to find the change in mass [158]. Prior to measuring final mass, a cleaning solution, such as dilute chromic acid, is used to remove corrosion products from the surface of the sample to obtain an accurate measurement using the microbalance [149]. The corrosion rate *in vitro* can be measured under these conditions and calculated using the ASTM-G31-12a protocol given by Equation 2.12:

Equation 2.12

$$CR = \frac{K\Delta W}{At\rho}$$

where CR is corrosion rate (mm/year); K is a constant (8.76×10^4); ΔW is weight loss (g); A is original exposed surface area (cm^2); t is exposure time (h); and ρ is standard density (g/cm^3) [164].

Results obtained from mass loss experiments are typically accurate, assuming minimised issues with removing the corrosion layer. Although a substantial degree of corrosion, usually a few wt%, is necessary for precise measurement of mass change, requiring multiple replicates for confidence. A benefit of mass loss testing is that it can be incorporated simultaneously with other *in vitro* tests, such as pH monitoring or electrochemical experiments [165]. However, one cannot characterise the corrosion mechanisms involved in the corrosion process, only observe that one alloy corrodes faster than another through this method. Therefore, other techniques are needed to provide more appropriate information [165] such as potentiodynamic polarisation, showing that alloys have different corrosion potentials and relative anodic and cathodic reaction kinetics [163].

The corrosion of Mg results in the release of hydrogen gas, Mg^{2+} and hydroxide (OH^-) ions into the medium, causing the pH to have a localised basic shift. This pH shift is known to promote the formation of $Mg(OH)_2$ passivation layers [166, 167], protecting the underlying

substrate from the corrosion media, leading to a steady state in the corrosion rate and a potential weight gain [163, 158]. Additionally, this pH change may affect the ratio of media volume to sample surface area of which the ASTM recommended solution volumes (0.2-0.4 mL/mm^2) are considered too small to accommodate rapid pH changes. As such, best practice suggest maintaining as large a volume of media as practicably possibly [163].

Hydrogen Evolution Measurement

For Mg, the overall corrosion reaction at its corrosion potential is represented by Equation 2.13, where one atom of Mg generates one hydrogen gas molecule in water [168]:

Equation 2.13

$$Mg + 2H_2O = Mg^{2+} + 2(OH)^- + H_2$$

Thus, 1 mol of hydrogen gas (22.4 L) will directly correspond to the dissolution of 1 mol Mg (24.31 g) [123].

In the hydrogen evolution experiment, a sample is submerged in corrosion media and a collector is placed directly above the sample, also submerged in the media, to capture the hydrogen gas as it is liberated [163]. A typical setup consists of an inverted funnel and a burette, as illustrated in Figure 2.11, both filled with corrosion medium that is displaced as the hydrogen gas evolves [169, 167, 170].

The benefits of the hydrogen evolution test are that it is unaffected by the formation of corrosion products and that measurements can be taken throughout the experiment at different time points so a more accurate degradation profile can be obtained [163]. However, similar to the mass loss testing, this technique does not provide any information on the corrosion mechanisms taking place. Furthermore, during the initial stages of corrosion, there is an insufficient amount of hydrogen produced that negates accurate and reproducible measurements as the 0.26 mL of H_2 dissolved in 250 mL H_2O often used in these experiments

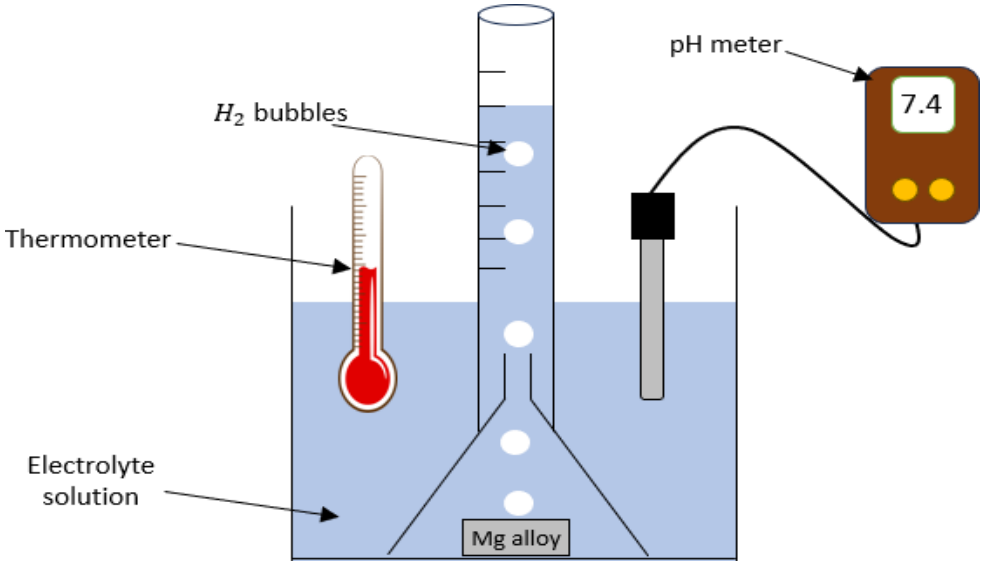

Figure 2.11 Schematic of a typical experimental arrangement for hydrogen gas evolution experiments

can provide a large error source [163]. The solubility of H_2 is another factor that must be considered, as it varies depending on the temperature and media volume to sample surface area ratio. Altogether, the test is unsuitable for the study of early-stage corrosion or highly corrosion-resistant materials, which only liberate low levels of H_2 [163].

pH monitoring

During the corrosion of Mg, OH^- ions are released into the media and result initially in an intense increase of local surface pH, which ultimately increases the pH of the bulk solution [9]. The relative pH increase can be used as an estimate to the corrosion rate. This technique has been used widely to provide qualitative results [171, 172] by measuring pH levels close to, and away from, the surface of the sample [173]. It is not recommended to use pH monitoring for Mg alloys in SBF as the pH will increase to a level where it exceeds the physiological range (7.4-7.6) before any significant information is provided and this increase will also have a significant impact on the corrosion rate [174]. Therefore, pH monitoring is mainly used to maintain a controlled pH range in the solution for another test rather than being an effective test itself [163].

2.4.2.2 Polarised experiments

Potentiodynamic polarisation (PDP)

PDP is the most commonly used electrochemical technique for studying the corrosion of Mg alloys. It is typically preceded by a set exposure time where the open circuit potential (OCP) is recorded by finding the electrode potential relative to a reference electrode when no current is applied to the cell [163]. Then voltage is then swept at a controlled rate through pre-set potentials between the Mg and an inert metal electrode (eg. platinum, Pt), starting at values more negative than the OCP and increasing to values more positive than the OCP [163] producing a curve of potential versus current density as illustrated in Figure 2.12, also known as a Tafel plot. An example of the setup for this technique can be seen later in Figure 2.18 as the setup is similar with the exchange of electrolyte for corrosion media.

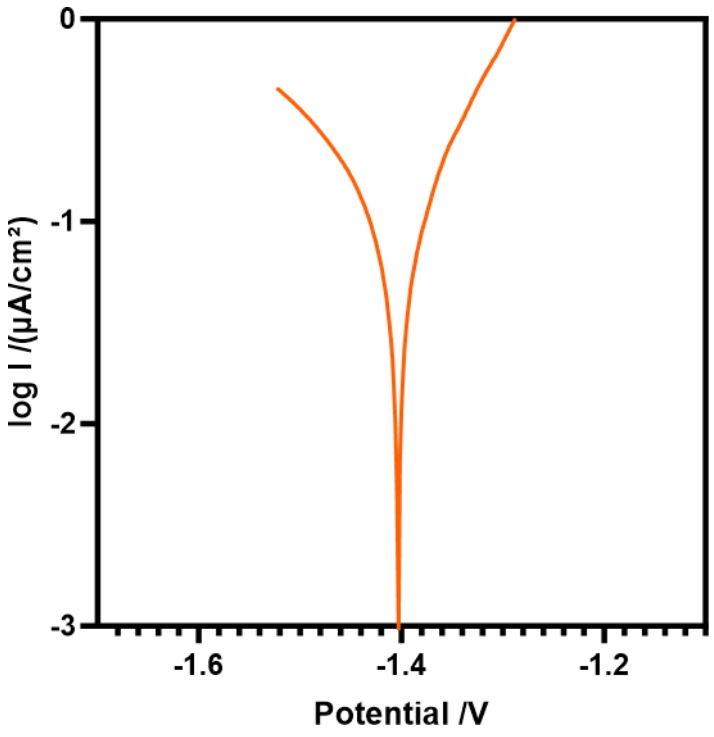

Figure 2.12 Polarisation curve of Mg WE43 alloy in DMEM scanned over a potential range of -2V to +1.5V of OCP

The point of intersect between the anodic and cathodic regions is the corrosion potential, E_{corr} and corresponds to the corrosion current density, i_{corr}. The corrosion rate can be measured by Tafel extrapolation of the anodic and cathodic branches based on Equation 2.14 [175]:

Equation 2.14

$$CR_i = K\frac{i_{corr}}{\rho}EW$$

where CR_i is corrosion rate (mm/year); K is a constant (3.27×10^{-3} mm.g/μA cm year); i_{corr} is corrosion current density (μA/cm^2); ρ is the standard density (g/cm^3); and EW is the equivalent weight (atomic weight/no. electrons to oxidise an atom of the element in corrosion process eg. Mg EW = 12.15).

Due to the nature of PDP tests being destructive (excessive currents in a short time), a sample can only be scanned once which limits the utility of surface analysis such as SEM as the surface reactions are artificially accelerated during testing [163]. Conversely, PDP can be used to determine the effects of organic components, such as proteins and amino acids, on individual phases to allow optimisation of microstructure [176].

2.4.3 Dynamic testing

The above static testing methods are useful indicators when assessing the potential of a material during corrosion [79]. But they are not a true reflection of the dynamic physiological environments that a material will experience in practice, especially as body fluid is in a continuous exchange process as the blood circulates [149]. Therefore, it is important to design and utilise tests which mimic physiological systems, *via* media refreshment and circulation, to improve understanding and develop third generation biomaterials – which combine the concepts of biodegradability and bioactivity. This could potentially be achieved by applying test parameters to simulate changing physiological conditions, such as temperature, pH, blood

flow rate and shear stress [177]. Consideration should also be given to the specific application and intended implantation areas as parameters like blood flow rate will change significantly from smaller areas, such as fingers, to larger areas, like thighs, with blood flows rates around 9.1mL/min [178] and 3.5L/min [179], respectively.

2.4.4 In vivo testing

Before an implant product can be marketed and clinically used, it must go through rigorous testing for safety reasons. Firstly in animal models and then eventually on humans to test for properties, such as cytotoxicity and biocompatibility. It is known that *in vitro* tests do not accurately represent the degradation profile of a metal *in vivo* due to the environmental differences (as mentioned in dynamic testing section) [149], and as such, clinical trials in real-life situations are needed. Furthermore, it must be noted that despite extensive selection processes, animal trials still have the potential to generate results which may not translate to humans. Thorough care is therefore needed.

As such, there are many factors which need to be considered before performing *in vivo* experiments, for instance time, costs, as well as harm and discomfort caused to test subjects [163]. Most commonly selected for animal trials are rats and rabbits [180] with a preference for testing fracture healing in femoral fractures [181, 182, 183]. *In vivo* measurement of corrosion in animals is generally performed by implanting the material, observing the healing processes followed by the euthanizing of the test subject for harvesting of the implant for characterisation [184, 185] through computed tomography and weight loss methods. Other measurements taken tend to be focussed on bone adhesion through tensile testing and bone histomorphometry measurements to help understand cell function, metabolism and distribution of bone tissue.

The corrosion of Mg-alloys *in vivo* is much more complex than *in vitro* and is nonlinear [186, 187, 188], therefore, calculated corrosion rates may be different due to follow-up times postoperatively. It has also been found that when comparing *in vitro* to *in vivo* tests, the corrosion rates tend to be lower *in vivo* [189] with large variations due to the placement of implants within the body [190]. Due to complexities of the degradation process *in vivo*, the corrosion mechanism remains uncertain [191] and more studies would be beneficial to quantify the *in vivo* degradation mechanisms.

Currently, it remains that *in vitro* tests are much simpler and easier to perform with many different types of assays, cells and media to choose from to show a multitude of biological responses to a potential implant material. The following section will address the common biological *in vitro* tests and different media used to perform these tests.

2.5 Introduction to cell testing

The *in vitro* biocompatibility analysis of a potential biomaterial is an important initial step in the determination of material safety for use *in vivo*. Regarding Mg testing, there are primarily two different techniques used to assess biocompatibility in cardiovascular applications. These are haemolytic assays [192, 193], used to assess the biocompatibility of the materials with blood, and investigation of coagulation and platelet aggregation [194, 195]. Whereas for orthopaedic applications, *in vitro* analysis is generally carried out using cell culture tests derived from international standards ISO 10993-5 and ISO 10993-12 with the utilisation of the Neutral Red Uptake (NRU), 2,3-bis-(2-methoxy-4-nitro-5-sulfophenyl)-2H-tetrazolium-5-carboxanilide (XTT), 3-(4,5-dimethylthiazol-2-yl)-2,5-diphenyltetrazolium bromide (MTT) and colony formation cytotoxicity tests. However, *in vitro* testing is not limited to these endpoint assays with various methods such as electron microscopy being able to aid

quantification of the test results. These cell culture tests can be split into three categories: Extraction, indirect contact and direct contact.

2.5.1 Cell culture testing

2.5.1.1 Elution Testing

During an extraction test, cultured cells are exposed to samples for variable lengths of time in a chosen culture media, with the intent to use that media to examine the cytotoxic or proliferative effects of the material on the cells. These end point assays of these tests are commonly colorimetric assays in which cellular metabolic activity reduces a tetrazolium salt to a coloured formazan product [194, 196, 195, 197], allowing quantification of the number of living cells or cytotoxic/proliferative potential of the material. Other common endpoint assays can be used to measure cell damage and specific aspects of cellular metabolism. However, it must be noted that research has indicated that Mg ions promote the conversion to formazan [198] and so may report a higher cell viability than is truly occurring. Despite this, tetrazolium assays have remained popular as thorough washing of the cells before testing has shown to mediate this effect [197].

2.5.1.2 Indirect and Direct Contact

Indirect contact testing is typically assessed by agar or filter diffusion methods to assess cytotoxicity using approaches similar to those discussed above in *Section 2.5.1.1.* A buffer layer is used to prevent direct contact between the material being assessed and the cellular suspension. Staining methods are generally used in combination with an endpoint assay to quantitatively determine the cytotoxicity effects of the material of interest.

Direct contact tests involve the growth of cells directly on the material of interest. In general, most direct contact tests utilise fluorescent dyes in association with fluorescent microscopy [199, 200] to allow visualisation of the seeded cells on the samples. Another way of visualising

these cells involves fixing them to the surface and drying them with ethanol before sputter coating with a layer of gold or platinum for visualisation with scanning electron microscopy [201, 104]. The number of cells adhered can then be quantified and the morphology assessed to give an indication of material biocompatibility. A summary of these methods is presented below in Table 2.5.

The three methods (extraction, indirect and direct contact) quantify cell viability and can be used with a variety of cell types including adherent primary cells and adherent cell lines from either human or animal origin. Primary endothelial cells (cultured directly from living tissue) are often utilised for Mg-based materials intended for use in cardiovascular applications [202], whereas osteoblastic cells or primary bone marrow stromal cells are more suitable for orthopaedic investigations [203]. This is due to their ability to investigate specific cellular responses that could indicate the material effects on bone tissue.

The most common indicator of osteoblastic differentiation is alkaline phosphatase (ALP) activity [203]. However, the reverse transcription-polymerase chain reaction can also be used to identify osteoblastic differentiation markers such as osteopontin, bone sialoprotein, osteocalcin and pre-collagen type I [203]. As such, the fibroblastic cell lines associated with these reactions can be used as a general tool for assessing the cytocompatibility of Mg materials for any biomedical application [104].

An issue with *in vitro* assays is the lack of comparability from study to study as a number of variables can affect the results gathered. These variables can include cell-type, choice of technique and time points investigated. Another potential error source is the cytotoxicity, which is likely associated with increased osmolality and pH change associated with Mg corrosion, adding further variables to the biocompatibility analysis of solution volume, concentration and whether the pH is adjusted. These error sources are minimised by using guidelines standardised

in the ISO standards but as they are not completely eradicated, these *in vitro* tests should only be used as an indicator of material behaviour and cytocompatibility rather than extrapolating to an *in vivo* environment.

Table 2.5 Common in vitro assays used for cell culture testing

Assay	Assessed Variable	Summary	Ref
Alamar Blue	Mitochondrial Activity	Based on enzymes reducing nonfluorescent dye to a pink, fluorescent compound. Fluorescence measured.	[204]
Methyl Tetrazolium MTT		MTT salt converted to purple formazan by succinate dehydrogenase within mitochondria. Formazan accumulates in healthy cells and absorbance measured.	[205]
XTT		Reduced salt to formazan product. Intracellular reactions allow enhanced sensitivity. Formazan accumulates in healthy cells and absorbance measured.	[205]
Alkaline Phosphatase ALP	ALP activity	ALP is a hydrolase enzyme which catalyses dephosphorylation of substrates and regulates intracellular processes. Fluorescence measured.	[206]
ATPlite	Determination of cellular ATP	Reagents added lysing cells and stabilizing ATP. Well plate is dark-adapted before luminescence is measured.	[204]
Caspase-3 Fluorometric	Determination of caspase-3 activity	Based on hydrolysis of a peptide substrate, resulting in release of a fluorescent compound. Intensity of signal measured and is proportional to amount of cleaved substrate.	[204]
Coomassie Blue Protein	Alteration of total cellular protein	Investigates cell growth by protein alteration with Coomassie Blue dye and absorbance measured. Cell viability expressed as fraction of negative control.	[207]
Lactate Dehydrogenase LDH	Membrane Activity	Based on measurement of LDH activity in extracellular medium. Loss of LDH and release into culture medium indicates irreversible cell death.	[205]
Neutral Red	Cell growth	Measure's inhibition of cell growth based on the uptake of neutral red dye by living cell. Absorbance measured.	[207]
ELISA Osteocalcin	Osteocalcin level	Assay kit detects intact osteocalcin for quantitative measurement in human serum, plasma and cell culture supernatants. Absorbance measured.	[208]
Pico Green	DNase activity	PicoGreen dye binds to dsDNA and fluorescence increases. λExo added and begins digestion of free deoxyribonucleic monophosphates, displacing PicoGreen. Fluorescence measured	[209]
ToxiLight	Cellular necrosis	Cells exposed to toxic agents for 24h before addition of assay solution. Luminescence measured.	[204]

2.5.2 Test media

The choice of test media for cell culture is critically important as the variables associated with this choice can dramatically affect the results pertaining to corrosion rate and corrosion mechanisms undergone by the Mg sample extract. The factors affected include pH control, temperature, composition, investigated time points and solution volume etc. [163, 217].

Table 2.6 Common culture media and their application in cell culture testing

Media	Description	Applications	Ref
Dulbecco's Modified Eagle's Medium DMEM	A basal medium based on MEM but modified to have a higher concentration of amino acids and vitamins.	Widely used for mammalian cell culture and also used in electrochemical measurements and bioactivity assessment of metals.	[210, 211]
Endothelial Growth Medium EGM	A low serum medium with defined growth supplements to allow metabolic and growth factor studies.	Optimized for cultivation of endothelial cells from large blood vessels but also used for pluripotent cells. Used for angiogenesis.	[212]
Ham's nutrient mixture – F12	A mix of amino acids, vitamins, inorganic salts and other components. Contains wider variety of components that other media although still requires supplements of FBS and a pH buffer.	Designed primarily for single cell plating. Not well suited to populations over 10^5 cells/ml.	[213]
Modified Eagle's Medium MEM	A mixture of salts, vitamins and amino acids designed to allow cell cultures to be kept for longer without refeeding.	Cultivation of mammalian cells in either monolayer or suspension	[214]
Medium 199	A basal media containing no proteins, lipids or growth factors. Can be combined with Earle's salts for CO_2 incubation or Hanks' salts for non-CO_2.	A medium associated with culture of pluripotent stem cells. Widely used in virology and vaccine production.	[212, 215]
Ringer's solution	A solution of salts dissolved in distilled water in concentrations designed to match those of plasma.	A medium used to restore and maintain volume of blood during surgery. Used with mammalian blood cells.	[216]

Due to this potential to obtain a variety of results, there has been a movement towards using solutions which are physiologically relevant to the expected *in vivo* environment and therefore the cell lines can be selected for testing based on the selected media. This is generally achieved by the addition of serums containing a variety of hormones and other supplements [218]. A summary of common culture media is listed in Table 2.6.

2.6 Introduction to Phosphate-based Glasses (PBG)

Bioresorbable PBGs have the ability to be tailored to deliver ions during dissolution [219, 220, 221], and this advantage could be extended to the production of thin-film coatings for biomedical applications [222, 223, 224]. The degradation time of these glasses can vary from hours to several months by altering the composition of the glass [225] making PBGs a promising material in delaying the onset of Mg degradation in orthopaedic applications.

2.6.1 Glass Formation and Structures via Conventional Melt Quenching

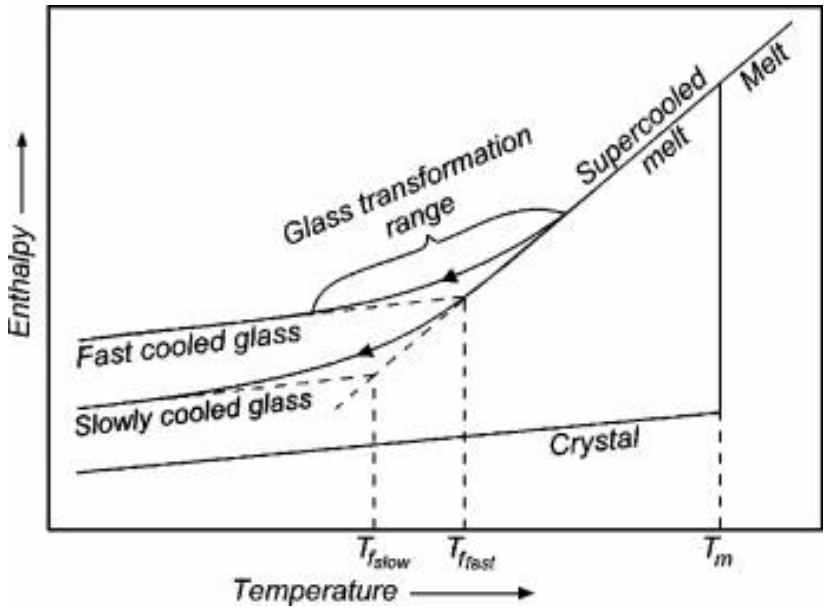

Figure 2.13 The effect of temperature on the enthalpy of a glass forming material [337]

Glasses have a near random molecular alignment termed “amorphous”, created through the rapid cooling of a liquid network to below or near the glass transition temperature T_g [226]. This occurs due to the glass structure having insufficient time to align upon cooling, leading to high entropy and enthalpy states as illustrated in Figure 2.13.

Network forming elements include Silicon (Si), phosphorous (P), boron (B) and less commonly germanium (Ge) and Arsenic (As) [221]. PBGs are also less common outside of biomaterials due to their resorbable nature. Phosphate glasses which are entirely composed of network forming backbone (e.g. Vitreous P_2O_5), are hygroscopic and readily resorb in the atmosphere. Coupled with their difficulty to manufacture, this means that network modifier ions such as Ca, Mg and Na are added to the structure by ionic bonding with oxygen to modify the thermal properties and dissolution rates [221, 227]. These compositional changes can also be used to provide preferable ion leaching into the environment.

PBGs generally have melting points in the range of 900-1200ºC [226]. But due to their poor thermal conductivity causing uneven cooling [225], there is a volume variation during glass forming which produces large residual stresses within the glass. These stresses can be released through annealing [226], where the glass is brought above the glass transition temperature T_g to allow for molecular mobility.

PBGs are less durable than their silicate counterparts, which is attributed to their structural arrangement and hydration ability [228]. P has a charge of 5^+ compared to a 4^+ charge for Si and both form a tetrahedral structure, leading to the formation of 4 single oxygen bonds for Si or 3 single and 1 double bond for P, which forms a terminal end unit (see Figure 2.14). The network is composed of bridging oxygens (BO) that connect tetrahedral units through the backbone P—O—P structure. In more complex phosphate structures, the tetrahedra are classified using Q^n terminology, where “n” represents the number of BO per tetrahedron. The

network of a PBG can be classified by the oxygen to phosphorous ratio, which indicates the number of tetrahedral links between neighbouring tetrahedra. PBGs can be made with a range of structures, from a cross-linked network of ultraphosphate (Q^3) tetrahedra to polymer-like metaphosphate chains (Q^2 tetrahedra) to small Pyro- and Orthophosphate anions (Q^1 and Q^0 respectively) [229]. These pyro- and orthophosphate glasses are also known as "invert" glasses. The tetrahedral units of the Q^n structures are illustrated in Figure 2.14.

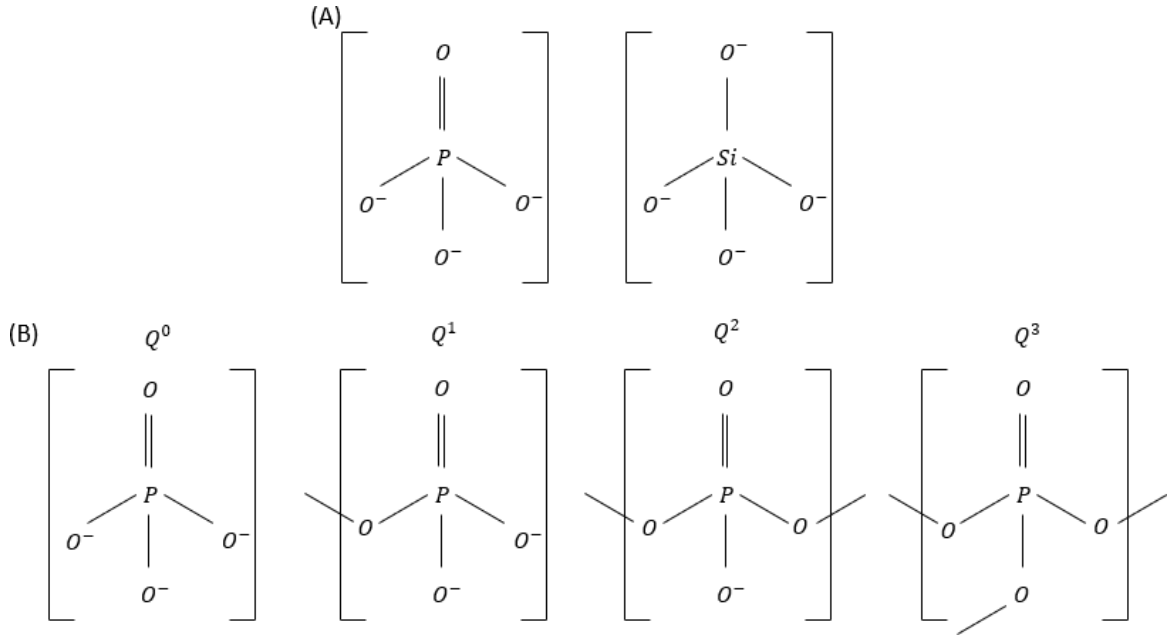

Figure 2.14 (A) Phosphate and Silicate tetrahedra (B) Structural units regarding the number of binding oxygens per tetrahedra. Q0 orthophosphate, Q1 pyrophosphate, Q2 metaphosphate and Q3 ultraphosphate

Non-bridging oxygens (NBO) are locations where oxygens are terminated by an ionically bound network modifier. These modifiers will be bound to a P=O or P—O^- in the structure of the tetrahedra. PBGs are also classified depending on the number of modifiers used within the network [230]. The classifications are binary (1 modifier), ternary (2 modifiers), quaternary (3 modifiers) or more complex (4 or more modifiers), which can be useful for tailoring glasses to have greater durability and biocompatibility. Modifier ions affect the glass properties due to their valence and atomic properties [228] and can function in the network as cross-linkers and depolymerisers. Monovalent ions such as Na^+ depolymerise the network, whereas ions of Ca^{2+},

Mg^{2+} and Ti^{4+} are examples of cross linkers, linking 2 or more tetrahedra through ionic linkages [231] whose bonding strength is increased with charge/size ratio [226]. Another group of elements exist in glasses as intermediate oxides which can fit into the network as either network formers or network modifier ions. These include Al, Fe and Ti [221, 226].

2.6.2 Influencing PBG behaviour

Work on binary, ternary and quaternary PBGs have shown that changing the molar concentration of different modifiers induces a change in the durability of the glass, increasing the resistance to chemical decomposition [232, 224, 233, 234, 235]. Durability is just one of the properties that can be modified through the addition of different modifier ions in the form of oxides. Ions such as Fe [236, 237] and Ti [238, 239, 240] have both been shown to improve the durability, whereas ions such as Cu [241] and Ag [242, 220] have been shown to be beneficial for their antibacterial properties. Another important factor in modifying PBGs is to improve the bone tissue generation and proliferation, and Mg [243, 244], Ca [227, 245, 238], Sr [246, 247] and fluorine (F) [248] have all been found to have this effect.

Over recent years, the desire for PBGs to be used as degradable implant materials has increased. Several studies have been carried out [224, 234, 235, 249, 250] with the general focus being on glasses comprised of 40-50 mol% P or above. As such, it is important for these glasses to have good cytocompatibility with osteoblasts and osteoblast-like cells. In ternary PBGs it was found that increasing the CaO content would in turn increase the cytocompatibility and this increase was attributed to the improved durability of the glass. Studies have also shown that elements such as Fe, Mg and Ti are effective when trying to increase cell adhesion and proliferation [224, 235, 250, 251] although it was not proven whether this occurred due to enhanced durability or to changes in the glass chemistry.

Calcium is widely known as the main mineral component of bone and has been shown to be essential for the formation and *in vivo* precipitation of hydroxyapatite [252]. It is often included in PBG structures for its ability to function as a divalent cation reducing the solubility as compared to the sodium monovalent ion [253, 20]. Sr has been considered as a substitution for Ca due to their structural similarities and a relative improvement of bioactivity [253, 254], resulting from promotion of osteoblast precursor attachment [255]. Due to its ionic radius, Sr increases the network size, maintains charge and increases glass solubility.

MgO can fit into the PBG glass structure as Mg^{2+} improving the relative durability of the structure compared to Ca and Sr, which subsequently results in an improved biocompatible performance [244]. However, Mg^{+} ions hav been shown to inhibit apatite crystallisation, leading to the stabilisation of an amorphous HA layer [256, 257].

In attempts to extend the dissolution rate, Fe and Ti have been incorporated into PBG structures. Addition of Fe_2O_3 up to 5 mol% has shown to increase the durability of the glass by increasing cross linking between phosphate tetrahedra, forming P—O—Fe bonds in the glass network [224]. Substituting CaO for up to 5 mol% Fe_2O_3 was beneficial for cell attachment and differentiation and increased chemical durability of the glass [224] and a similar trend was noticed when Fe_2O_3 replaces Na_2O [258, 259]. The inclusion of Ti within the glass structure leads to the formation of Ti^{4+} cross-linkers within the backbone as P—O—Ti and similarly to Fe, improves the durability of the glass [239].

Eisenberg *et al.* [260] discovered that by substituting one cation for another of either higher valence or smaller atomic radius, giving a higher charge density, increases the transition temperature T_g. The order was confirmed to be $Ba^{2+} < Sr^{2+} < Ca^{2+} < Mg^{2+}$ for the alkali earth elements and $Cs^{+} < Rb^{+} < K^{+} < Na^{+} < Li^{+}$ for alkali elements [261].

In the last several years, a push to increase the cytocompatibility of these degradable PBGs has expanded research into lowering the P content of the glasses, thus shifting the glass structures to a classification of “invert” glasses. De Melo *et al.* [262] observed that transitioning the Q species of the PBGs to invert structures by replacing the P with Ca, supported a 4.3 times increase in the number of adhered cells as compared to metaphosphate glasses. This would allow for the control of cell adhesion profiles and increasing the level of adhesion expands the applications of these glasses where cellular support and recruitment are of increased value for many orthopaedic applications.

2.6.3 Dissolution of Phosphate Based Glasses

Studies on the dissolution of PBGs have frequently been conducted in either deionised or distilled water [228, 222, 20, 236, 263]. However, in attempt to better simulate *in vivo* environments, a suitable *in vitro* media is used to mimic body conditions, with the solution being chosen to be closely related to the point of use. Some of the most commonly used media include simulated body fluid (SBF), simulated urine (SU), Dulbecco’s modified eagle medium (DMEM) and phosphate buffered saline (PBS) [242, 264, 265].

The dissolution of PBGs is dependent on several factors including glass composition, solution pH, temperature, thermal history of the glass and the glass surface area to solution volume ratio [266, 263]. It has been reported that three types of reaction can take place during the process of dissolution of PBG in aqueous media, namely acid/base, hydrolysis and hydration reactions [263, 267]. The acid/base reaction is responsible for disrupting the ionic interactions between the glass chains and is highly dependent on pH [228]. During this reaction, the glass surface becomes saturated with acidic hydrogen ions or basic hydroxide ions, increasing linearly with

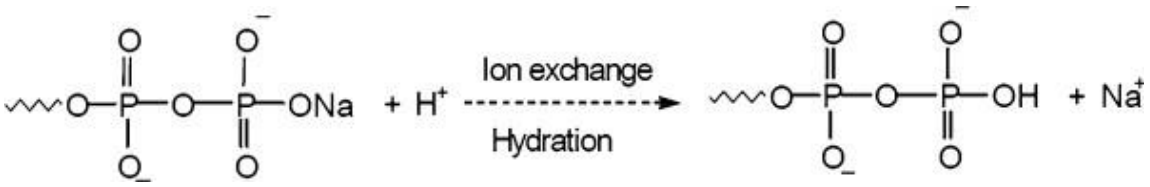

Figure 2.15 Hydration of a PBG chain by ion exchange

time until uptake is no longer possible [228]. The next step is hydration and an ion exchange reaction takes place where the high mobility cations of the glass, such as Na^+, are exchanged with hydrated hydrogen ions (H_3O^+), (illustrated in Figure 2.15) and as a result, a hydrated layer forms on the glass surface. The network is then broken down by a hydrolysis reaction, resulting in the cleavage of P—O—P bonds and phosphate chains of different lengths are released into the solution. This reaction is heavily dependent on pH as an acidic medium enhances bond dissociation with respect to neutral solutions, resulting in a higher rate of hydration and dissolution [267].

Bunker *et al.* [228] divided the dissolution process into two kinetic periods according to mass loss profiles, where the first stage follows the relationship $t^{1/2}$ and the second stage is linear with time. The higher dissolution rate in the first half can be explained by the disentanglement of phosphate chains from partially hydrated chains when surrounded by water. This occurs until a steady state is reached by the hydrated layer and, assuming the ionic strength of the solution is not allowed to increase [267], by changing media on a regular basis, then the kinetics should obey a linear t^1 law.

The dissolution rate can range between 10^{-4} and $10^{-9} gcm^{-2}min^{-1}$ [228] and the rate is largely sensitive to the glass composition. When investigating the effect of increasing K content at the expense of Na, Knowles *et al.* [268] found that the solubility decreased with increasing K_2O. They hypothesized that a larger ionic radius would have a larger disrupting effect on the structure as compared to Na and would tend to weaken the network.

Generally, a higher valence cation oxide will have a greater influence on the solubility of phosphate glasses. For example, trivalent cation oxides such as Fe^{3+}, titanium (Ti^{3+}) and B^{3+} have been found to have a larger effect on solubility than monovalent or divalent oxides [269, 224, 236, 270], due to the strengthening effect via cross-linking of the phosphate network.

Iron can exist as both Fe^{2+} and Fe^{3+}, with both network modifier or network former properties [271]. Fe^{3+} ions exist in either tetrahedral or octahedral coordination [272, 273], whereas the larger Fe^{2+} ions locate themselves in octahedral sites. It has also been found that the concentration of Fe^{2+} decreases with the increasing Fe_2O_3 content [224, 271]. The coordination of network modifiers has been shown to have preferable orientations for improving the durability of the glass. An example of this is boron, which can form BO_3 trigons and BO_4 tetrahedrons [274, 275], where the triangles cause a decrease in chemical durability and the tetrahedrons cause an increase in durability [276] as the triangular units are not as resistant to the action of leaching solutions.

It has been reported that the hydration energy for phosphates decreases in the order of $Q^2>Q^1>Q^0$ [269] and that the P_2O_5 content can be tailored to reduce the dissolution rate. A reduction from 50 to 45 mol% P_2O_5 shortens the network chains, making it less susceptible to hydration [277]. Dohler et al [278]. Reported that decreasing phosphate content from 55 to 35 mol% significantly reduced the dissolution rate from 90 to 15% after 24h immersion in tris buffer.

The dissolution rate largely increases when exposed to extremes of pH [228]. The rate increases dramatically when exposed to acidic solution with a pH <5 as network breakage is highly sensitive to hydrated H^+ ion attack. The dissolution rate also accelerates in basic solutions but to a lesser extent. In aqueous media, long phosphate chain structures lower the pH of the solution due to the hydrolysis of P—O—P bonds [278]. However, this effect is not seen with

short-chain structured glasses as they dissolve by a combination of hydration and hydrolysis and do not have a large effect on solution pH.

As stated previously, during the melt quenching of PBGs, there are internal stresses developed due to the uneven cooling. Annealing has been used to reduce these stresses, changing the mode of solution degradation and making the heat-treated glass more durable [279]. It was suggested by Otto [280] that during the annealing process, the structure rearranged itself to attain a more stable configuration by reforming broken bonds and allowing some bonds to reach a more stable state [280].

2.7 Radio Frequency Magnetron Sputtering (RFMS) of metallic glasses

The RFMS of phosphate-based glasses is a relatively new concept and as such, has little available literature on the potential of PBGs. Therefore, this section reviews the literature relating to the sputtering of bulk metallic glasses followed by the sputtering of phosphate-based glasses.

RFMS thin film coatings have been shown to deposit dense, uniform coats with nanometre precision of applied thicknesses which conform to the underlying substrate [281]. This is due to the atom-by-atom condensation on the surface of the substrate allowing uniform thin coats a few micrometre thick with superior adhesion strengths upwards of 60 MPa [282, 283, 284].

Bioactive Si-based glasses were first deposited as a coating by RFMS in 2003 [285]. It was suggested that the coatings were bioactive in SBF due to the precipitation of what appeared to be an apatite layer. Since then, research has been conducted with the focus of optimising the deposition system to achieve superior bioactive and adherence properties [286, 287] through the adjustment of various sputtering parameters [288, 289, 290, 291].

Study of bioactive glass with composition SiO_2 – 40.08, CaO – 29.1, MgO – 8.96, P_2O_5 – 6.32, CaF_2 – 5.79, B_2O_3 – 5.16 and Na_2O – 4.59 wt% was used to evaluate the influence of deposition pressure on the structure, composition and biomineralisation capability of a Bioglass film after 30 days immersion in SBF [289]. It was noticed that the target composition was not stoichiometrically transferred to the films, which may be explained by network rearrangement occurring during film growth and the sputtering of a complex target structure. However, immersion showed successful formation of a Ca-deficient apatite precipitate on the surface of the glass coating, as shown in Figure 2.16.

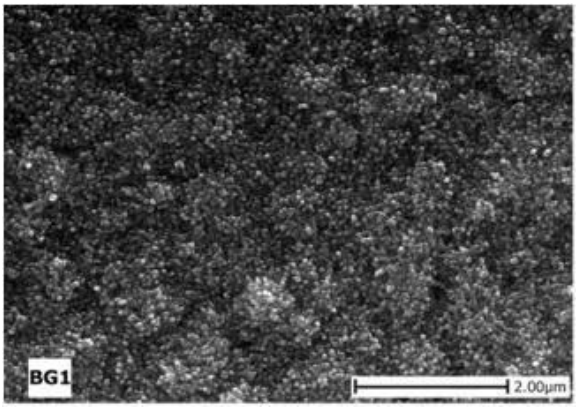

Figure 2.16 SEM of apatite layer formed after immersion in SBF for 30 days [272]

This appeared to follow the first steps of Hench's chemical growth mechanism [292, 293] as Si—O—Si linkages were perturbed by continuous formation of non-bridging oxygen type linkages, showing a favouring of processes by a higher biomineralisation rate [294, 295]. A partially crystallised carbonated HA (CHA) layer grew on all bioglass samples during the 30 days immersion and indicated continuous precipitation of Ca through the recorded growth of the HA layer between 15 and 30 days [286]. Precipitation occurs gradually granule by granule, until they start coalescing to form a dense layer. The thickness of these HA layers grown in SBF correlates with the biomineralisation of the coatings and was found to be more efficient within the thicker layers [287]. The structure of these HA layers continuously changes throughout the growth process and depending on the working pressure, longer growth

saturation time intervals can be expected whilst in higher pressure environments [296]. Hench's law can provide an explanation for higher biomineralisation rates as the first stage of SBF immersion is said to involve the rapid exchange of Na^+ ions from the glass for H^+ and H_3O^+ ions from the solution. This initialises formation of a silica-rich layer known to favour nucleation of Ca-P type layers, catalysing the CHA chemical growth mechanism [296]. With increasing CHA thickness, the Ca:P ratio also increases [289] due to the preferential ion leaching of Si, Mg and Na from the coating [291].

Silica glasses have shown that with increased crystallisation, their degradation rate is reduced [286]. 45S5 Bioglass® was found to have a peak crystallisation temperature of 715 ºC with nucleation occurring from 566 ºC [297]. Annealing as a post-treatment has resulted in partially crystallised bioactive glass coatings which may improve coating durability and has the benefit of reducing micropores in the coating due to the deposition process [288].

In a more recent study, a coating of composition - 40Fe, 23Cr, 7Co, 6P, 5B, 5Si (at%) was deposited onto steel [298]. This research demonstrated the benefit of including P in the glass matrix as the film thickness increased from 551.7 to 716.3 nm in the presence of P. The structure formed from deposition of this glass was fully amorphous, indicated by the presence of a white halo illustrated in Figure 2.17(b). The presence of P altered the growth structure in the cross-section and formed columnar microstructures, consistent with sputtered films, as compared to the featureless and dense P-free structure.

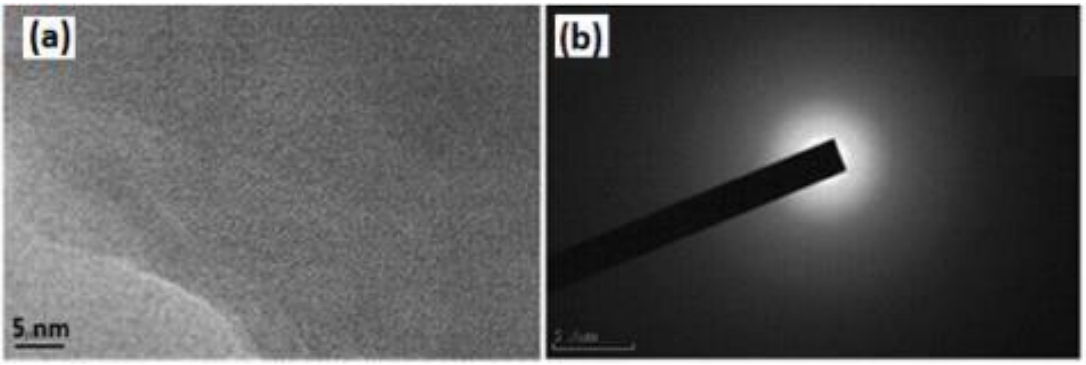

Figure 2.17 (a) TEM image (b) SAED pattern of Fe40Cr23Mo14Co7P6B5Si5 thin-film metallic glass deposited onto Si wafer substrate [281]

The compositions of these coatings were found to have 4 %at oxygen as a result of residual oxygen in the sputtering chamber. As seen by Stan *et al.* [287], coatings created with low percentages of oxygen of *ca.* 7 at% favour dissolution, silica hydration and enhanced bioactivity. Mapping analysis of the film surface showed that constituent elements were distributed evenly throughout the film, and it was suggested that the metallic glass alloys may have a uniform chemical composition due to their irregular structure, random distribution, lack of dislocations and grain boundaries [298]. This uniformity can in turn lead to uniformity of mechanical, chemical, and physical properties of the film.

The first instance of sputtering phosphate glasses was in 2015 when Stuart *et al.* [100] explored the relationship between target glass compositions and the subsequent substrate composition. During the deposition process it was observed that there was a change in composition between the target and coating deposited. The phenomena of preferential sputtering occurred showing an increase in the amount of network-modifying alkali metal oxides and a decrease in the composition of P_2O_5 and Fe_2O_3 relative to the target composition [100]. This occurs due to the various sputtering rates of the different constituent elements, which vary with atomic properties, such as mass, density, size and relative bonding strengths [281]. Similarly to the findings of Stan *et al.* [288], varying the sputtering pressure will affect the stoichiometry of the

deposited coating of the PBG with increasing the Ar pressure up to 0.45 Pa, showing the closest coating stoichiometry relative to the target glass [100]. This result was reproduced by Tite *et al.* [299], who observed a progressive augmentation of the P_2O_5 content at the expense of CaO concentration as sputtering pressure was increased from 0.2 to 1 Pa. A linear relationship was also seen with the sputtering pressure increase giving a deposition rate increase as is common for magnetron sputtering. However, as the working gas pressure increases, the film density decreases [300], due to the reduction in mean free path (average distance a sputtered atom can travel prior to collisions), such that the probability of collisions increases and makes it more difficult for atoms to diffuse inside the structure of the coating. This shows that there will be an optimum pressure for balancing the deposition rate and stoichiometry and maintaining a compact, dense structure to reduce the dissolution rate [301].

In another study, Stuart *et al.* [302] demonstrated the ability to obtain a continuous and adherent coating alongside phase purity in comparison to thermal splat methods [303, 284]. The coatings were seen to adhere to the macro-topological features on their substrates, also described as good step coverage, which has been previously seen from the process of magnetron sputtering of PBGs [105]. Pits in the deposited coating were seen to grow in size with increasing deposition power and deposition rate, increasing the relative roughness. Optimisation of substrate temperature suggests that lower working temperatures produce smoother films, whilst increasing parameters such as power, deposition rate and pressure contribute to a roughened surface [304]. Therefore, parameters must be varied to match the application as the diffusion of the adatom must be greater than or equal to the rate of void formation for surface roughening to be prevented [281]. This diffusion may be controlled by exceeding a critical temperature; in order to maintain an amorphous film, the diffusion should be kept low [281] by keeping the temperature low, since increasing temperature may improve atomic diffusion until nucleation and crystallisation occur [100].

During a study on the effect of a post-deposition annealing stages on mechanical and solubility behaviour of PBG coatings and improving mechanical properties through molecular relaxation [305], the Ca:P ratio was reported to increase [106], potentially due to surface phosphorous deficiency [306]. Similarly, to SBGs, a partially amorphous and crystalline structure develops as Fe ions are promoted into vacancy sites [307], with the effect of increasing the brittleness and hardness with a prolonged dwell time. The annealing process was also seen to reduce the interfacial failure load to 45.7 MPa, a considerably lower value than the expected tensile strength of 72.6 MPa, suggesting that the annealing was not beneficial to the coating structure and mechanical properties.

2.8 Electrochemical deposition of CaP/HA

In addition to sputter deposition routes to deposit thin films, electrodeposition has also been considered due to the ability to rapidly deposit coatings of compounds such as CaP with a significant thickness around 10 – 20 μm [308], providing a thick layer of protection between the environment and underlying substrate.

2.8.1 CaP electrodeposition process

Electrodeposition is a widely used surface engineering technique in which the anode material dissolves by applying an electrical current to reduce ions at the cathode/electrolyte interface, to deposit a coating on the cathode surface [309]. The electrolyte provides an electrical circuit between electrodes in the cell [310] and offers an alternative to dry coating methods. During the electrodeposition of HA, calcium- and phosphorous-containing salts are dissolved in water to prepare the electrolyte, taking advantage of pH-dependent solubility of calcium phosphate salts [311]. This benefits of utilising this coating technique include the room temperature working temperature, rapid deposition of uniform coatings in a matter of minutes and the possibility to incorporate reinforcing agents [312, 313]. However, the adhesion strength is poor

around 15 – 30 MPa, compared to the required 50.8 MPa, and there is difficulty controlling the electrolyte parameters which can leave residual stress in deposited coats [312, 313].

During the electrodeposition of HA, the following reactions occur at the cathode surface [314, 315]:

Equation 2.15

$$O_2 + 2H_2O + 4e^- \rightarrow 4OH^-$$

Equation 2.16

$$2H_2O + 2e^- \rightarrow H_2 + 2OH^-$$

Equation 2.17

$$2H^+ + 2e^- \rightarrow H_2$$

Equation 2.18

$$H_2PO_4^- + OH^- \rightarrow HPO_4^{2-} + H_2$$

Equation 2.19

$$HPO_4^- + OH^- \rightarrow PO_4^{3-} + H_2$$

The gaseous hydrogen formed in Equation 2.16 and Equation 2.17, causes a pH increase to *ca.* pH 10 due to the increase in concentration of OH^- ions which can further increase the number of hydrogen phosphate and phosphate ions through Equation 2.18 and Equation 2.19. The nucleation and growth of CaP phases is often attributed to this pH increase as the hydroxide diffusion from the cathode surface results in an electron transfer which attracts solution ions to the cathode surface. This process is illustrated below in Figure 2.18.

The main CaP phases formed were dicalcium dihydrogen phosphate (DCPD), octacalcium phosphate (OCCP), tricalcium phosphate (TCP) and HA [316, 317]. TCP exists in the form of an inclusion, whereas the other phases contribute to the structure of the deposited film with

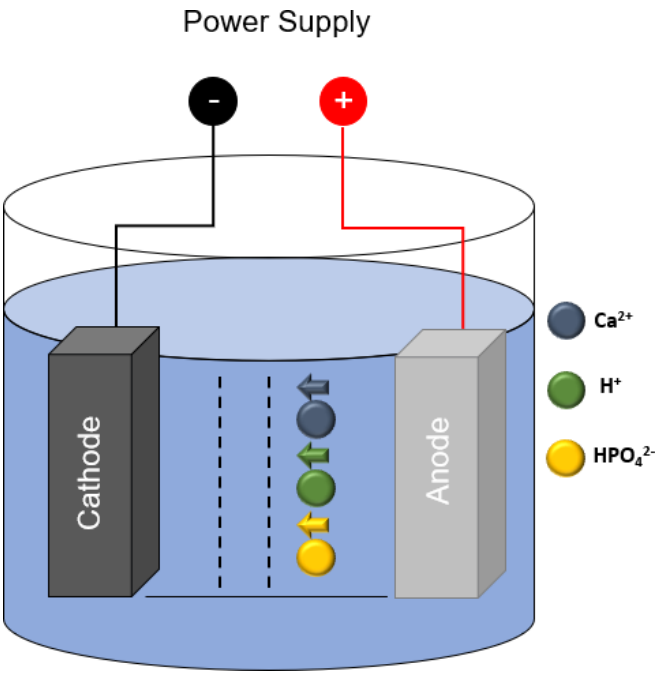

Figure 2.18 Schematic illustration of ion deposition during the electrodeposition process

DCPD being the dominant phase over HA in the absence of sufficient hydroxide ions [318]. This occurs as DCPD is stable at pH <5 and precipitation of DCPD is promoted in acidic conditions where there is a low amount of OH^- ions in the electrolyte solution [319]. HA is the preferred phase for CaP coatings due to it having the highest stability, bioactivity, lowest biodegradability [320] and its Ca/P molar ratio of 1.67 [321], which is the same ratio as in the native osseous CaPs. The process parameters can be adjusted to encourage the precipitation of HA through a variety of methods.

Dominant HA precipitation occurs when the pH of the electrolyte surrounding the cathode is above 6.2 [322] but other studies have indicated that the preferred pH range is between 9.5-12 [323]. This has been achieved through the addition of H_2O_2 as this provides an additional electrochemical source for the generation of hydroxide ions [324], which in turn increases the solution pH and allows the hydroxide ions to accumulate at the cathode surface and react with the calcium and phosphate ions in the bulk electrolyte solution. Investigations have shown that when the electrolyte solution has a high concentration of hydroxyl ions, then a higher volume fraction of the HA phase is achieved in the deposited layer [325, 326, 327]. This increase is due

to the initial crystallisation step of supersaturation generation, which initiates as the saturation index becomes positive when the pH reaches 6.2 and becomes increasingly positive as the pH increases further [327]. The following crystallisation steps of nucleation and growth are then able to occur. However, if during the electrodeposition process the conditions are too acidic to promote the formation of HA, the DCPD phase formed can be retroactively converted to HA through immersion into a NaOH containing alkaline solution [308].

Another way to adjust the electrodeposition process is to vary the type of power supply used as the deposition can be carried out under constant cell voltage, galvanostatic or potentiostatic control [328] and can also be applied using direct current, pulsed current or reverse pulsed current [328]. By varying these parameters, significant differences in the morphological, microstructural, mechanical and corrosion properties of the deposited HA coatings can be seen [319, 329, 330]. Saremi *et al.* [330] indicated that using pulsed current gives a more compact structure than that of direct current, whilst the particle morphology remained unchanged. Pulsed current also showed the potential to deposit coatings of only HA, whereas direct current coatings showed DCPD in XRD analysis [330] as the relaxation time enables existing ions in the bulk electrolyte to diffuse towards the cathode's working surface, promoting the growth of HA [16]. The mechanism is yet unclear, although it is thought that the polarisation concentration may inhibit saturation required for crystalline deposition, but both a better corrosion performance [330] and 80% increase in adhesion strength [16] were observed by using pulsed current deposition rather than direct current. The effects of changing current density can be split into two groups: changing the coating morphology and varying grain size/porosity. Aside from the contribution of current density to the full surface coverage, an increase in current density will change the morphology due to the high deposition rate restricting hydrogen bubble generation over the surface, which may separate the microstructure into islands rather than one homogenous film [331]. Even a 20 $mAcm^{-2}$ increase can result in

a change of morphology from a plate-like to a needle-like structure [332]. An optimum current density can be defined for each application, since increasing the current density is beneficial for deposition of a thick, nanostructured coating with controlled porosity up to a limit. But increasing the density further results in an increased grain size, excessive porosity and increased volume of micro-cracks due to an increase in residual stresses from a negligible stress below 0.4 mA/cm^2 to *ca.* 20 MPa at a current density of 10 mA/cm^2 [333, 334].

2.8.2 CaP deposition for orthopaedic applications

The aims of using CaP/HA coatings in orthopaedic applications are to functionalise the surface to promote cell adhesion and growth [335], to permit sufficient nutrient penetration through the coating to newly forming bone [336], whilst acting a base material with sufficient biocompatibility [337]. Many studies have been conducted on the application of a CaP coating to biodegradable polymers, such as polylactic acid (PLLA), poly(lactic-co-glycolic) acid (PLGA), polycaprolactone (PCL) and nondegradable metals like Ti, stainless steel (SS) and cobalt (Co) alloys but the elastic moduli of the polymeric materials are generally much lower than that of cancellous bone in the range of 10 – 100 MPa compared to the range of 120 – 910 MPa for various locations of cancellous bone [338].

The research into coating Ti implants with CaP has progressed to commercial clinical use after *in vivo* investigations in animals giving indications of stronger and faster fixation along with more bone ingrowth at the interface [339, 340, 341]. Hayakawa *et al.* [339] studied the influence of surface roughness on bone bonding and formation by inserting CaP-coated Ti beads into trabecular bone in rabbits. In early bone formation, no major difference in bone contact was seen, however, after 12 weeks bone was seen across the surface and inside Ti bead implants, leading the authors to conclude that appropriate geometry and chemical compatibility at the surface can enhance bone regeneration and bone bonding to the implant. A separate study

of implants in canine mandibular molars, which perform the major portion of work in lower jaw mastication, confirmed a statistically significant increase in bone contact percentage around the alloy implant after 12 weeks with $p < 0.05$ compared to implants at 4 weeks [340]. This can be attributed to the phosphates on the surface reacting directly with surrounding osteoblastic cells, which influences cell differentiation and promotes tissue replacement. These CaP coatings were seen to increase the mean ultimate interfacial shear strength, achieving 2.29 MPa for the as-deposited coating and promotes rapid bone ingrowth in direct contact with implant surfaces [341].

In vitro studies investigating the effect of a CaP deposition onto degradable Mg-alloys have been performed with promising results. It was found that coatings on AZ31 substrate improved the corrosion protection, reducing the i_{corr} by three orders of magnitude, bioactivity, by inducing a bioactive apatite layer, [342] and mechanical strength by 20 % [343] as compared to uncoated samples. As discussed in the previous section, attaining a more closely packed coating morphology can have beneficial effects and has in multiple studies shown to decrease the anodic dissolution of Mg and its alloys [344, 345, 346, 347] through the adjustment of solution composition and coating parameters. Generally, the electrodeposition onto Mg-alloys is performed in aqueous solution, however, addition of organic solvents, such as alcohol [348, 349] can decrease the hydrogen bubble bursting during deposition, which in turn will result in the denser packing of the CaP precipitates, as shown when deposited onto Mg AZ91 [349]. These deposited films improve the corrosion resistance of Mg implants but have not yet reached a point where they alone would be enough to delay corrosion for the 180 day target period [350] to allow the complete healing process to take place.

2.9 Summary

In this chapter, the research into the use of Mg and its alloys have been discussed, with an outline of the advancements from the discovery of magnesium, to its present use as an implant material, with commentary on current and future research. With this in mind, Mg-alloys are considered to be biocompatible and resorbable with the potential to be adapted using protective coating techniques to maintain structural integrity within the body long term for orthopaedic applications. The coating techniques of physical vapour deposition and electrodeposition have been explored for phosphate-based glasses and calcium phosphate, respectively, and both have shown promise regarding delaying the onset of corrosion and enhancing the biological behaviours of a base substrate Mg-alloy. Accordingly, this thesis seeks to combine and improve the understanding of different disciplines to present an applicable solution for a bioresorbable implant for orthopaedic applications, such as fracture fixation. A feasibility study on the combination of these deposition techniques with the aim of improving biocompatibility and corrosion resistance, will be described. A calcium phosphate layer will be deposited onto Mg WE43 alloy by wet electrochemical deposition followed by the forming of a PBG into a target and RFMS of the PBG to deposit a top complimentary top layer of PBG. Further, an in-depth discussion on the morphology and microstructure of Mg WE43 and the applied thin films will be presented. The biological effects of the alloy on cells and *in vitro* testing will also be discussed. The justification for the investigation of the bilayered coating is that by nature, the electrodeposited CaP layer has voids in the surface of the coating due to the competing rates of nucleation and crystal growth during the deposition process. Despite this morphology, the ability to deposit relatively thick coatings as compared to other methods such as plasma spraying in a relatively short deposition time was taken into consideration when selecting the deposition method. RFMS of PBG was selected as the complimentary coating layer as the method will deposit an amorphous layer on top of the CaP which will provide a base coverage

over all of the Mg WE43 alloy and the heating effects observed during the RFMS process may also see the benefit of an annealing effect on the CaP layer. As there has been a relatively small amount of research into “invert” PBGs but promise shown for the cytocompatibility effects, these type of PBG were chosen to be investigated.

The following section details the experimental methodology used to create targets and subsequently deposit materials onto substrates as thin films. Furthermore, the processes for compositional, structural, and morphological characterisation will be presented in advance of assessment of *in vitro* dissolution and biocompatibility.

Chapter 3 - Materials & Methodology

3.1 Introduction

The experimental procedures utilised for the production and characterisation of thin-film CaP/PBG coatings deposited on Mg-alloy samples investigated in this thesis are detailed in this Chapter. Table 3.1 summarises all source materials used. Table 3.2 gives an overview of the various coating types investigated, summarising the processes, samples and the principles of each process development investigation. *Section 3.2* describes the samples of materials investigated for benchmarking purposes along with the conditions used to deposit the CaP and PBG coatings through the methods of edp and RFMS and the post edp thermal annealing treatment application. *Sections 3.3, 3.4* and *3.5* describe the basis of characterisation methods, cytocompatibility and corrosion tests applied respectively.

Table 3.1 Materials, suppliers and purity

Material	Supplier Name	Form	Purity %
Mg WE43	Magnesium Elektron, UK	Ingot	-
$Ca(NO_3)_2$	ThermoFisher Scientific, UK	Solid crystalline	-
$NH_4H_2PO_4$	ThermoFisher Scientific, UK	Granules	-
H_2O_2	ThermoFisher Scientific, UK	Liquid	10/cc
HNO_3	ThermoFisher Scientific, UK	Liquid	99.9
NH_4OH	ThermoFisher Scientific, UK	Liquid	99.9
NaH_2PO_4	Sigma Aldrich, UK	Powder	>99
Na_2CO_3	Sigma Aldrich, UK	Powder	>99.5
$CaHPO_4$	Sigma Aldrich, UK	Powder	>98
$CaCO_3$	Sigma Aldrich, UK	Powder	>99
$MgHPO_4.3H_2O$	Sigma Aldrich, UK	Powder	>98
Ar	BOC Pure shield, UK	Gas	99.998
Dulbecco's Modified Eagle Medium	ThermoFisher Scientific, UK	Liquid	-

3.2 Substrate Preparation

3.2.1 Magnesium WE43 alloy discs preparation

A Mg WE43 ingot was cut into 1 mm thick sheets by wire erosion (Electric Discharge Machining (EDM)). A fly press was used to punch Mg WE43 discs (10mm diam. x 1mm thick) from the wire cut sheets. Discs were then sonicated for 15mins each in acetone and subsequently Industrial Methylated Spirit (IMS) before being dried in a stream of compressed air.

3.2.2 Grinding and Polishing of Magnesium WE43 discs

Initial optical profilometry examination determined that the roughness of the Mg WE43 alloy substrate was of a similar scale to the thickness of the deposited CaP coatings. Therefore, to allow the determination of deposition rates of the CaP and PBG layers, samples of the Mg alloy were ground and polished to provide a flat surface for comparison via a physical contact measurement method detailed in Section 3.3.1 as the polished surface was reflective and prevented accurate measurement and detection by optical methods.

The Mg-alloy discs were mounted flat on a brass block covered with a thin layer of hot wax and then left to cool to room temperature. The samples were then ground on one surface using Silicon Carbide paper, sequentially decreasing in grit size from P240 > P400 > P800 > P1200 using IMS as a lubricant for grinding papers and to aid removal of embedded grit. The samples were then polished using Silicon Carbide polishing wheels for soft materials with a 6 µm grit and then 1 µm also using IMS as a lubricant. Samples were cleaned after each grinding and polishing stage, using cotton wetted in IMS, followed by drying under a flow of cold air. No water was used in any of the grinding, polishing and cleaning stages.

3.2.3 Calcium Phosphate electrodeposition

The CaP electrodeposition method is an application of the wet chemical electrodeposition process. The wet chemical electrodeposition process is a technique used to deposit a thin layer of a substance from a solution onto a substrate surface through an electrochemical reaction. The process requires an electrochemical cell setup, typically consisting of a power supply, a reference electrode, an inert anode and a cathode of the substrate material to deposit onto. This electrochemical cell is immersed in an electrolyte solution containing the ions to be deposited onto the cathode surface which in this case would contain Ca^{2+} and $(PO_4)^-$ ions. When a voltage is applied across the electrodes, an electrical field is created within the solution. This electric field drives the charged ions in the solution towards the cathode surface, where they gain electrons and undergo a reduction reaction, forming a solid layer on the substrate. These deposits nucleate and act as templates for crystal growth when the concentration of the growing species is significantly higher that the species solubility to reach a supersaturated state. After this deposition process has concluded, there is the opportunity to apply a post-treatment such as rinsing, drying, annealing or surface finishing to enhance the coating properties, improve adhesion to the substrate or to remove any residual impurities.

An electrolyte solution was prepared by adding 0.042mol/L $Ca(NO_3)_2$, 0.025mol/L $NH_4H_2PO_4$ and 10cc/L H_2O_2 to deionized water. The pH was corrected to each desired pH level using HNO_3 and NH_4OH. The solution was stirred continuously using a magnetic stirrer of 40 mm length by 10 mm diameter at a constant 400rpm.

Tests were carried out at room temperature. Depositions were performed in a cell using a regular three electrode configuration in which Mg WE43 alloy served as the cathode, a Pt electrode acted as the anode and a saturated calomel electrode was used as the reference

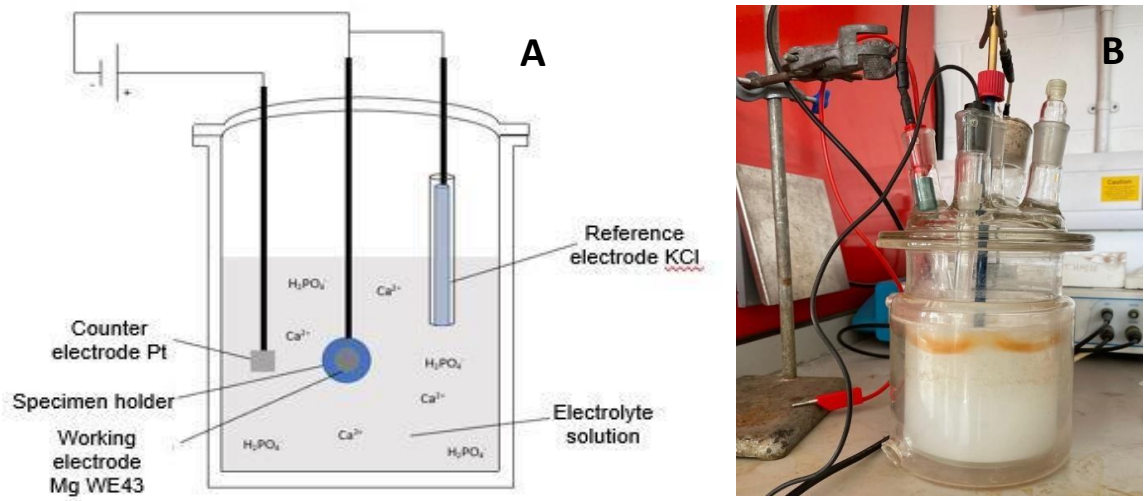

Figure 3.1 (A) Schematic of electrodeposition equipment setup (B) Real equipment used for electrodeposition

electrode (Figure 3.1). The applied potential for these tests was -3000mV. The potential was applied using a Voltalab PGZ 100 (Radiometer analytical, UK). Table 3.2 shows the variation of electrodeposition parameters investigated in this work.

Table 3.2 Electrodeposition conditions applied to produce CaP coatings

Varied Parameter	Duty cycle	pH	Deposition time /min
Duty cycle	0.2	4.5	20
	0.3		
	0.4		
	0.5		
	0.6		
	0.7		
	0.8		
	0.9		
	1		
pH	0.6	4.5	20
		6	
		7.5	
		9	
Deposition time	0.6	4.5	20
			40
			60
			120

The duty cycle is described as $t_{on}/(t_{on}+t_{off})$ in which t_{on} is the time (s) of the applied potential and t_{off} is the time (s) of no potential.

3.2.4 PBG target preparation

Phosphate Glass targets were prepared using the following precursors: NaH_2PO_4, Na_2CO_3, $CaHPO_4$, $CaCO_3$, $MgHPO_4.3H_2O$ and P_2O_5. The precursors were weighed and mixed in the relevant proportions into a Pt/5% Rd crucible (Birmingham Metal Company, UK). The crucible was placed in a furnace for drying at 350ºC for 30 min to remove moisture from the hygroscopic components, before the furnace temperature was ramped up at a rate of 10 ºC/min until reaching 1100ºC where the temperature was held for 90 min. The molten glass was poured onto a steel plate, which had been left to pre-cool in a freezer for 3 h and a similarly treated steel plate was pressed onto the molten glass to induce rapid cooling, referred to as "splat quenching". The glass was then left to cool to room temperature. The glass shards were then remelted at 5ºC above the glass transition temperature (T_g) [351], poured into a graphite target mould and left to anneal for 60 mins. The furnace was then switched off and allowed to slowly cool to room temperature. The number of targets of each type were n=1 as targets are reusable as long as stresses during the coating process do not cause them to shatter.

3.2.5 Radio Frequency Magnetron Sputtering of PBG thin films

RFMS is a Physical Vapour Deposition method used to deposit thin films onto the surface of a substrate by bombarding a "target material" with energetic ions. This in turn causes atoms or molecules to be ejected from the target surface, forming a vapour. The process is performed within a vacuum chamber to minimise the contamination of the deposit and ensure a uniform deposition on the substrate surface. The vacuum environment prevents chemical reactions of the "target material" vapour and atmospheric gases and facilitates movement of the vapour to the substrate surface without interference. The vapour contacts the substrate surface and

condenses to form a thin film which occurs through various mechanisms including nucleation, surface diffusion and aggregation of the atoms or molecules on the substrate surface. Desired coating properties such as thickness, composition, microstructure and morphology can be achieved through the variation of process parameters. The parameters typically varied are the temperature, power density, chamber pressure, target-substrate distance and gas flow rate of the bombardment gaseous ions which all affect the deposition rate of the target material. To improve performance of the deposited film, techniques such as substrate rotation and substrate biasing may be employed to improve film uniformity and adhesion.

PBG coatings were deposited using a TEER UDP-650 Type 2 closed-field, unbalanced, magnetron Physical Vapour Deposition (PVD) rig. The rig (Figure 3.2) was equipped with two radio frequency (RF) power supplies plus pulsed DC bias power supplies. The rig consists of a dual-layered wall to allow the flow of cooled water in the external wall with the inner wall leaving the chamber *ca.* 450 mm in height and 450 mm in diameter. The RF power supplies are connected to two opposing circular magnetrons, which hold 57 mm diameter targets for sputtering. In this study, only one circular magnetron was used to deposit PBG coatings, whilst the other system targets were covered in Al foil to prevent target contamination.

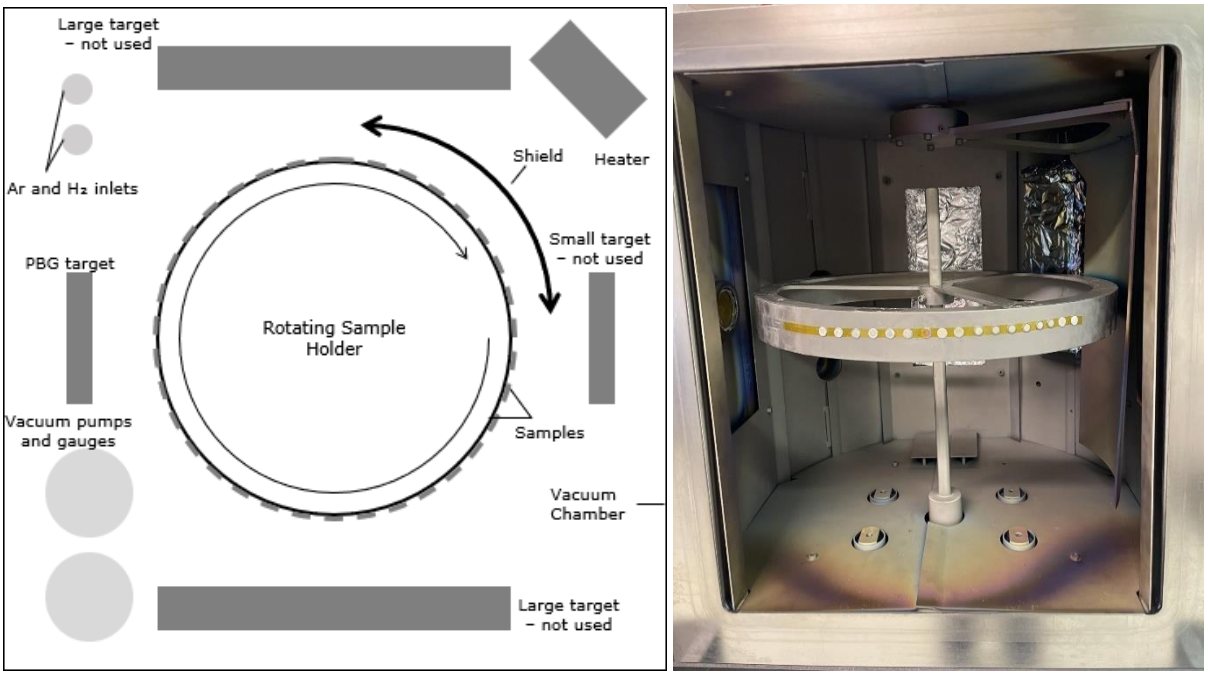

Figure 3.2 (A) Schematic of bespoke TEER magnetron sputtering rig (B) Inside view of the Bespoke sputtering rig

Samples to be coated were mounted onto a circular sample stage using double-sided polyimide Kapton tape. The samples were positioned at a working distance of 55 ± 1 mm from the target with a sample holder rotation of 5 rpm to ensure equal deposition across the substrates. Prior to deposition, the chamber pressure was reduced to achieve a base pressure of $< 1 \times 10^{-5}$ Torr, using successive rotary and diffusion pumps. Once this base pressure was achieved, Ar gas (purity 99.999%; Pureshield BOC) was introduced at a rate of 20 sccm to achieve a working pressure of $< 1 \times 10^{-3}$ Torr. A shield was positioned in between the PBG target and the substrates. The sputter target was pre-sputtered for 20 mins to clean the surface of the target using an RF power of 60 W. The sample itself was cleaned using pulsed DC (pulse width 250 kHz, step time 500 ns), with a bias voltage of -100 V at the same time. The pulsed DC bias was then removed prior to coating, the shield moved from between the target and substrates allowing deposition to commence at an RF power of 60 W for a 48 h time period.

3.3 Material Characterisation

3.3.1 CaP edp thickness measurement

Stylus-based instruments are commonly used for measuring surface texture of a material by tracing the material's surface with a stylus and recording the Z-coordinate of the tip at sequential points along the sample surface. The stylus instrument contains an electromechanical transducer to convert the stylus Z-coordinate into a voltage, which is amplified and passed through an analogue-to-digital converter to record on a computer.

The most frequently used form of stylus has a conical shape with a rounded contact edge as shown schematically in Figure 3.3. Due to the tested surfaces often being "hard" in nature such as metals, alloys and ceramics, the stylus must be composed of a robust, indestructible material such as diamond, ruby or sapphire. A 2D representation of profilometry can be obtained using the following assumptions [352]:

(1) The stylus tip has a spherical shape with radius r

(2) The lower hemisphere of the stylus tip is contacting the material surface

(3) The traced surface is drawn by the lowest point of the stylus tip

(4) There are no plastic or elastic deformations of the stylus tip or the rough surface

To measure the thickness of a coating by stylus profilometry, an enveloping curve is obtained by measuring the Z-coordinate of a circular stylus tip in contact with the sample surface and displacing the stylus along a tracing line, which includes a step from the coated surface to the uncoated surface of the sample.

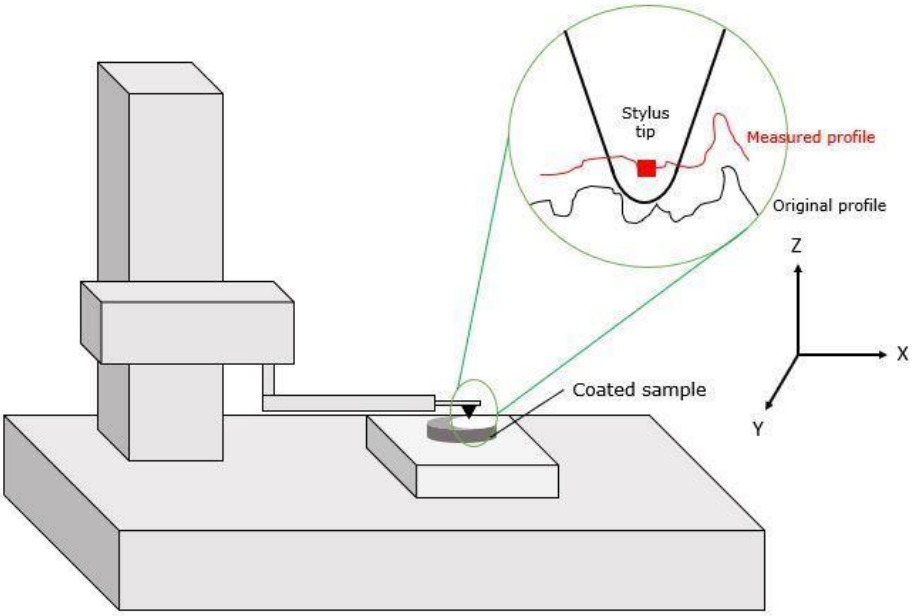

Figure 3.3 Schematic of stylus profilometer for coating thickness measurements

Mg WE43 discs were ground and polished as detailed in *Section 3.1.1* and *3.1.2*. Half of the sample was masked using double-sided polyimide Kapton tape before undergoing the coating process outlined in *Section 3.1.3*. The Kapton tape was then removed and profilometry performed using a KLA-Tencor Alpha-Step D-120 stylus profiler. Measurements of step height were taken at 3 points along the coating border at the centre point, and half way between the centre point and the edge in both directions along the coating border. The stylus was lowered to contact the coating surface near the border and moved horizontally in the x-plane over a distance of 1 mm across the coating-substrate border with measurements taken in steps of *ca.* 0.3 µm. The number of samples used for measuring each coating thickness for varying parameters was n=1 as technician time constraints were limited and multiple measurement points were taken on each coating type.

3.3.2 Scanning electron microscopy (SEM) and energy dispersive X-ray spectroscopy (EDX)

A Scanning electron microscope focuses an electron beam onto a sample area where the interaction of the high energy electrons causes the emission of secondary electrons (morphology information), backscattered electrons (relative elemental differences) and

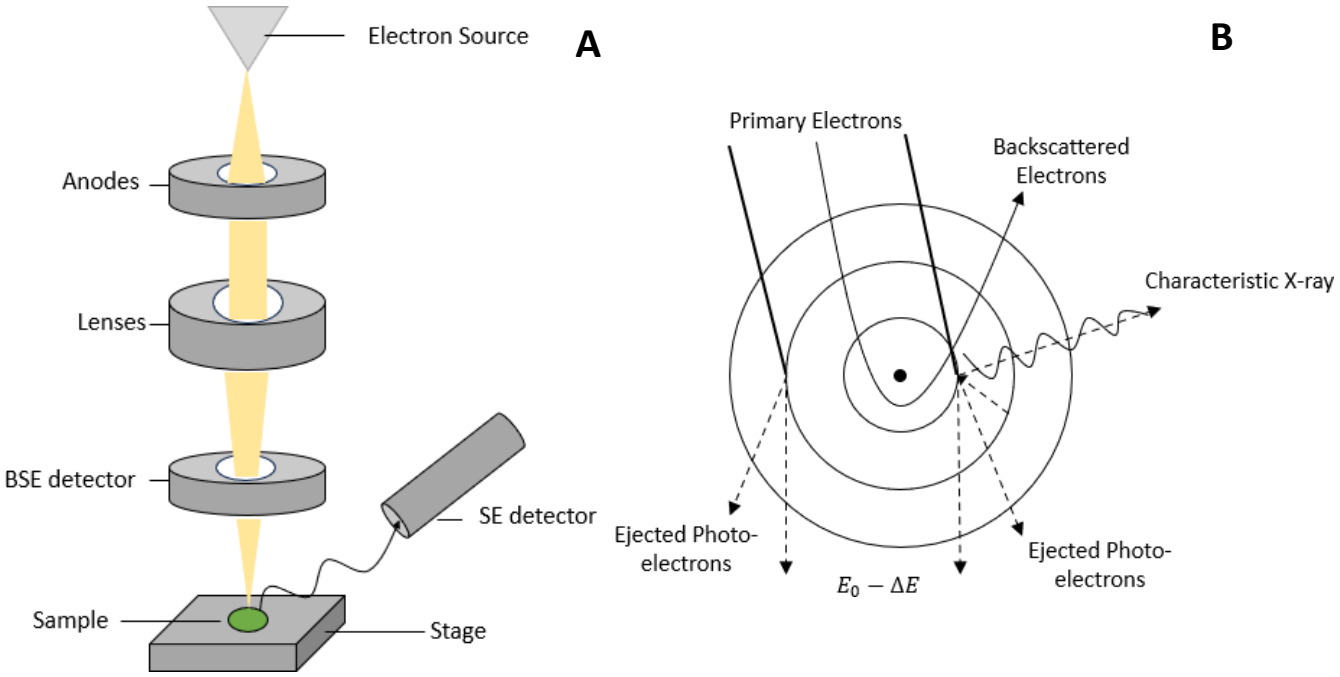

Figure 3.4 (A) Schematic of the principles of electron microscopy (B) Diagram of the origin of backscattered electrons and characteristic X-rays where E0 is the ground energy state and ΔE is the perturbed energy of the system

characteristic X-rays (quantitative elemental analysis) (Figure 3.4). The dislodged electrons can be captured by nearby atoms or may escape from the near material surface as secondary electrons if the kinetic energy is large enough, allowing for information to be gathered about the material surface topography. Elastic interactions between the incident electron beam and atomic nuclei of the sample material where the beam is scattered at roughly 180º to the incident beam angle result in backscattered electrons. Materials with larger atomic number will reflect larger amounts of incident electrons, resulting in higher brightness levels for heavier elements in the image. Due to this, backscattered electrons are useful in providing information about the sample composition. Characteristic X-rays are emitted when high energy incident electrons cause emission of a core shell electron, exciting the atom. This excitation state can be relaxed with an electron from an outer shell orbital filling the vacancy with the subsequent release of energy in the form of an X-ray, defined as the energy difference between the two electron states, allowing atomic number to be discovered. As a result of this, Electron Dispersive X-rays (EDX) can be used to quantify the sample composition.

The image resolution of SEM micrographs is dictated by the following equations:

Equation 3.1

$$d = \frac{0.612\lambda}{nsin(\alpha)}$$

Equation 3.2

$$\lambda = \frac{h}{mv}$$

Where d is the resolution power, λ is the electron wavelength, n is the refraction index and α is the incident electron angle.

The potential energy accelerates electrons and is converted from potential to kinetic energy. The associated velocity of the electron is input into the de Broglie equation (Equation 3.2) which states that the associated electron wavelength is inversely proportional to the electron's velocity. Subsequently it can be stated as accelerating voltage and thus velocity increases, there is a decrease in source wavelength leading to higher image resolution.

Samples were sputter coated with a 10nm layer of carbon to aid imaging. Imaging of substrate surfaces was performed using a JEOL 6490LV electron microscope with an accelerating voltage of 15 kV and a working distance of 10 mm. The JEOL 6490LV is calibrated to factory settings by a maintenance engineer annually. EDX mapping was conducted over *ca.* 1.7 mm^2 for coating analysis and visualisation of deposited layer crystallinity. SEM and EDX were performed on n=1 samples per coating type due to the large number of coating variants and multiple points of imaging taken per sample. The Oxford Aztec EDX system is also calibrated annually to the factory standards supplied with the system.

3.3.3 X-ray diffraction (XRD)

Spectra detailing diffraction angles and intensities, unique to crystalline phases and crystal size can be obtained by observing the scattering of incident X-rays following interaction with the

atomic outer shell of a sample. Incident X-rays are generated by a source (eg. Cu Kα X-ray gun), which bombards the Cu source with electrons generated from thermionic emission of a tungsten filament, which dislodge inner shell electrons, forming X-rays, which are then directed towards the sample. These X-rays diffract based on the structure of the material and are observed by a detector to determine angle and scattering of diffraction for constructive interference (Figure 3.5). The relationship of crystal structure and size is governed by Braggs Law:

Equation 3.3

$$n\lambda = 2dsin\theta$$

Where n denotes an integer; λ denotes the X-ray wavelength; θ denotes diffraction angle; d

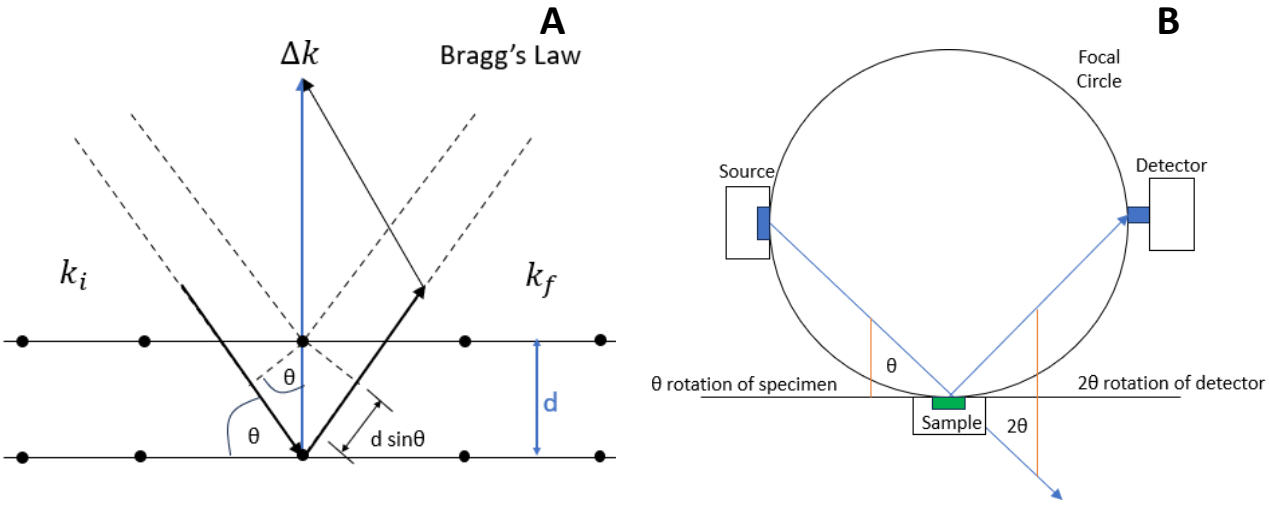

Figure 3.5 (A) Schematic of Bragg's Law regarding constructive interference of scattered waves, ki is the initial k coordinate and kf is the final k coordinate during the scan (B) Schematic of XRD diffractometer setup for Parallel Beam Scanning

denotes lattice spacing defined by a three-dimensional matrix (h, k, l) from which multiple diffraction angles may be generated.

Sample crystallinity was assessed using a Bruker D8 advanced XRD spectrometer (Cu Kα source, λ = 1.5406 Å, 40 kV, 35 mA), calibrated monthly to the Corrundum Al2O3 standard. Measurements were taken over a 2θ range from 20 to 68°; with a step size of 0.01° (2θ); a glancing angle of 1.2°; and a dwell time of 16 s. Spectra were then analysed using

DIFFRAC.EVA (Bruker) software, using the ICDD PDF-2 database for phase identification. Samples tested per coating type were n=1 due to the large number of coating types and the large time required to generate many samples.

3.3.4 *X-ray photoelectron spectroscopy (XPS)*

XPS allows for the chemical, compositional and electronic state quantification of thin-film coatings in the region of <15 nm thickness [353], as photoelectrons cannot escape the solid beyond this depth and artefacts like preferential etching, oxidation state modification and atom mixing during ion beam sputtering lead to peak shift and asymmetry beyond this depth [354]. As the sample is bombarded in an ultra-high vacuum with monochromatic X-rays, photoelectrons are emitted with kinetic energy (KE) from electron shells (Figure 3.6), which is measured by a photodetector and used to calculate the binding energy of the electron to its nucleus using:

Equation 3.4

$$E_k = h\nu - E_b - \Phi_f$$

Where E_k denotes KE of the emitted photoelectron, E_b denotes electron binding energy, Φ_f denotes work function and $h\nu$ is the incident X-ray energy defined by Planks constant and radiation frequency respectively.

High resolution scans may be used to determine the chemical and valence states of elements by measuring the shifts in binding energies caused by bonding interaction changing electrostatic attraction.

All samples were mounted onto stainless steel stubs using carbon sticky tabs. X-ray Photoelectron Spectroscopy (XPS) was conducted using a VG ESCALab Mark II X-ray photoelectron spectrometer with a monochromatic Al Kα X-ray source incident to the sample surface at *ca.* 30°. The Escalab Mark II is calibrated monthly to a Corrundum standard using

an Ag standard sample, monitoring peak position, full width half maximum and area of the Ag 3d peak. Survey and high-resolution scans were conducted in addition to the measurement of adventitious C 1s for calibration: charge corrected to 284.8 eV. Parameters for acquisition were as follows: step size of 0.1 eV; number of scans set at 5; dwell time 0.2 s for survey scans, and 0.4 s for high-resolution scans. Binding energies were measured over a range of 0–1200 eV. All spectra were analysed in Casa XPS constraining the Full Width at Half Maximum (FWHM) to the same value for all deconvoluted spectral peaks for the same element, to obtain good fits of data, as the ideal peak shapes are unknown [355]. Compositional data and chemical bond states were obtained by subtracting the background, fitting peak components and comparing to

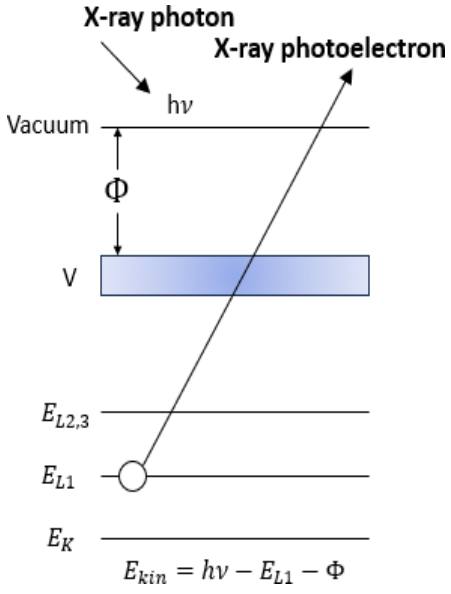

Figure 3.6 Schematic of photoelectron emission, where hv is the X-ray photon energy and E_L is the binding energy of the photoelectron to an inner core shell

known references in the literature. Shirley background was employed as it falls in between linear and Tougaard backgrounds for accuracy but is easier to use and analyse than the most accurate Tougaard background [356]. Due to the length of time required for setup and analysis of XPS, the number of samples measured per coating type was n=1.

3.4 Preliminary Cellular Assessment

Table 3.3 Equipment list used for Cell Culture Assessments

Material/Equipment	Make	Model
Benchtop Centrifuge	ThermoFisher	SL16
Microplate Shaker	Heidolph	Titramix 100
Microplate Reader (absorbance)	BioTek	ELx800
pH Meter	Jenway	3510
Fridge	Biocold	Spark-free
Freezer	Creda	Coldstore
Fume Hood	Nuaire	NU-437-400C
Incubator	Nuaire	NU-5800E
Water Bath	Clifton	Unstirred
Microscope	Nikon	Eclipse TS100
Pipetboy	Integra	2
Transfer Pipette	Samco	1 mL
Glass Plugged Pipette	Sterilin	5 mL
Glass Plugged Pipette	Sterilin	10 mL
Polypropylene Universal Container	Sterilin	7 mL plain
Polypropylene Universal Container	Sterilin	30 mL plain

3.4.1 Preparation of supplemented Dulbecco's Modified Eagle Medium (DMEM)

A 500 mL bottle of DMEM was removed from refrigeration whilst 50 mL of Foetal Bovine Serum, 5 mL of L-Glutamine, 10 mL of antibiotics-antimycotics (AA/AM), 10 mL of HEPES Buffer, and 5 mL of non-essential amino acids (NEAA) were defrosted from frozen at room temperature. 50 mL of DMEM was removed from the bottle and was subsequently discarded. 75 mg of ascorbic acid was weighed and placed into a sterile 30 mL universal tube with the L-Glutamine and *ca.* 15 mL DMEM with the contents being gently mixed by swirling the tube. The mixture was filtered through a 0.2 µm filter into a new sterile tube and poured into the DMEM bottle. The remaining components were decanted into the DMEM bottle and the contents mixed by gentle inversion. 40 mL of the supplemented DMEM was then decanted into 50 mL sterile universal tubes (allowing for media expansion during freezing) and the tubes placed into a freezer at -10 ºC for storage until required.

3.4.2 Cell Culture of MG-63 Human Osteosarcoma Cells

Supplemented DMEM was pre-warmed in a water bath at 37 ºC for 30 min. An ampoule of MG-63 cells (Public Health England Catalogue No: 86051601) were removed from liquid nitrogen storage and left at room temperature for 1 min. The ampoule was then transferred to the water bath and allowed to thaw until *ca.* 90% of the contents were defrosted before being wiped with 70% IMS and transferred to the sterile fume hood. Using a sterile Pasteur pipette, the ampoule contents were transferred to a sterile 30 mL universal taking care not to create bubbles and 9 mL of pre-warmed, supplemented DMEM was added dropwise to avoid inducing osmotic shock. The cells were gently mixed by pipetting the suspension twice. The universal was then transferred to a centrifuge and cells pelleted by centrifuging at 1200 rpm for 4 min. The resulting supernatant was decanted to reduce the concentration of Dimethyl Sulfoxide and the cell pellet re-suspended in 10 mL of supplemented DMEM media before being transferred to a labelled cell culture flask and stored in an incubator at 37 ºC and 5%CO_2. The media was replaced after 24 h to remove any dead cells.

Upon reaching 80 % confluency, the flask of cells was passaged and split into two new flasks. To achieve this, supplemented DMEM was warmed in a water bath at 37 ºC for 30 min and placed into a fume hood. The old media was aspirated from the flask using a sterile 10 mL pipette and placed into a waste container. 5 mL of Phosphate-buffered Saline was added to the flask and swirled to wash the cells before being aspirated from the cells and replaced with 1 mL Trypsin solution and incubated for 4 min at 37 ºC and 5%CO_2. The sides of the flask were then gently tapped to loosen the cells from the bottom of the flask. Using a sterile pipette, 6 mL of warm supplemented DMEM was added to the flask and swirled before aspiration and being placed in a 30 mL universal tube. This was repeated with a further 3 mL of DMEM media before the universal was centrifuged at 1200 rpm for 4 min to pellet the cells. The supernatant was removed and the cell pellet re-suspended in 2 mL of warmed DMEM, with 1 mL being

transferred to each new sterile flask, 9 mL of DMEM being added to each flask and flasks being stored in an incubator at 37 ºC and 5% CO_2 until the cells reached 80% confluency again.

3.4.3 Elution Test with Neutral Red Uptake Assay (NRU)

Indirect contact testing was performed with NRU by viable cells with parameters being adapted from ISO standard 10993-5 2009 [357]. MG63 osteoblast-like cells were seeded at a density of 40,000 cells/cm^2 in a Falcon® 96-well clear flat bottom TC-treated culture microplate to form a sub-confluent monolayer. Samples were placed into 7 mL bijou tubes with a surface area to volume ratio DMEM of 1 cm^2/3 mL and left for 1 h. The media was then removed and split for half of the exposed media to be pH-corrected to a pH of 7.4. The MG-63 cells, seeded in the 96-well plate, were then exposed to the treated media for a 24 h period and incubated at 37 ºC and 5%CO_2. After this incubation period, treated media was removed and replaced with 150 µL of Neutral Red (NR) media. After a further 2 h incubation, the NR media was removed, and cells washed with 150 µL of Phosphate-buffered Saline (PBS) solution per well. PBS was removed and 150 µL of NR destain solution (50% absolute ethanol, 49% deionised H_2O, 1% glacial acetic acid) added to each well. Subsequently, plates were shaken for 10 min at 150 rpm on a microplate shaker before being transferred to an ELx800 Microplate Colorimeter (BioTek Instruments Inc, UK) to measure NR absorption at optical density (OD) 540 ± 10 nm.

3.5 Corrosion Testing – Potentiodynamic polarisation testing

The corrosion behaviour of samples was investigated studying their cathodic and anodic electrochemical activity. All tests were performed in a cell with three electrodes; a working electrode of the sample surface seated in a purpose-made flat specimen holder (Figure 3.7), an Aldrich Ag/AgCl glass reference electrode and a Metrohm auxiliary electrode of 1 cm^2 Pt sheet. The test solution was 1 L supplemented DMEM media which was held at 37 ºC throughout the duration of testing.

The corrosion behaviour of as-deposited CaP and PBG coatings was investigated using a potentiostat (VoltaLab PGZ100, UK). Open circuit potential (OCP) scans were collected for 1 min after a 20 s settlement time, followed by potentiodynamic polarisation tests, due to the rapid degradation rate of Mg WE43 alloy. Anodic and Cathodic scans were conducted varying the potential from -2 V to + 1.5 V, with respect to the OCP, with a scan rate of 1.5 mV/s. The Voltamaster software used with the potentiostat determines the E_{corr}, i_{corr} and R_p values for the samples and allows for Tafel analysis to be performed. Sample types were tested in triplicate for repeatability and Faradays rate equation (Equation 3.5) incorporated to calculate the corrosion rate, v_{corr}, in mm/Y.

Equation 3.5

$$CR = K_1 \frac{i_{corr}}{\rho} EW$$

Where CR is corrosion rate in mm/Y, i_{corr} is the corrosion current density in µA/cm^2, K_1 represents a constant 3.27x10^{-3} (mm.g/µA.cm.Y), ρ is the density of the material (g/cm^3) and EW is the effective weight, also described as the atomic weight divided by the number of electrons needed to oxidise an atom during corrosion. In this case Mg was used and the EW = 12.15 [358]. NB: the non-SI unit Y for year is used here.

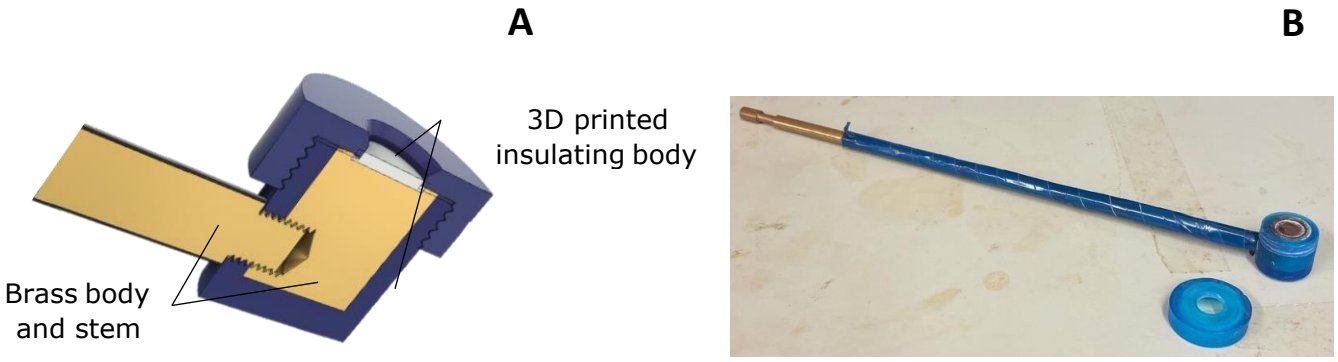

Figure 3.7 (A) Cross-sectional 3D model of purpose designed flat specimen holder (B) Physical flat specimen holder used in testing

3.6 Summary

The experimental methods and procedures used for the production of Mg alloy discs, CaP electrodeposition, PBG deposition and characterisation have been presented in this chapter. A potentiostat system was used to electrodeposit CaP layers onto Mg alloy discs whilst varying the deposition parameters. A close-field, unbalanced radio frequency magnetron sputtering system was used to fabricate novel bi-layered coatings of CaP and PBG on the Mg alloy.

A range of complementary characterisation techniques examining the chemical, structural and topographical properties were used to quantify the coatings. Profilometry was utilised to give information on the coating thicknesses, surface morphology and deposition rates, whilst XPS and EDX provided detail on the composition of the Mg WE43 samples and their deposited coatings. XRD analysed the bulk and surface structure of the coated alloy while SEM characterised the surface topography of the coatings deposited on the alloy discs.

The cyctocompatibility of the coatings was assessed using an indirect contact test with cell viability assessed using a Neutral Red Uptake assay. Corrosion performance of the coatings was investigated in DMEM at 37 ºC, using potentiodynamic polarisation for all samples.

Chapter 4 – Results

The results presented in this chapter represent the novel application and investigation of combining the electrodeposition of CaP and RFMS of thin-film PBG with a low P content, deposited onto Mg WE43 alloy to produce a composite bi-layered coating to delay the onset of corrosion and provide a protective layer to the underlying alloy substrate. To this point, there has been some research into the deposition of thin-film PBG [100, 105, 231, 302, 106, 359] but none into the effects of sputtering with low P content glasses and the manufacturing of low P targets.

Sections 4.1 – 4.3 will look at the electrodeposition process of CaP onto an Mg WE43 substrate, with the variation of duty cycle (time charge was applied for per second) being assessed in *Section 4.1*, the effects of increasing the overall deposition time from 20 min up to 120 min being assessed in *Section 4.2* and the effects in increasing the electrolyte pH from pH 4.5 – 9 is detailed in *Section 4.3*. A description of the manufacturing challenges and process for the development of PBG targets for radio-frequency magnetron sputtering will take place subsequently in *Section 4.4* with the investigations of the thin-film PBG coatings when deposited onto Mg WE43 alloy and the bi-layered coating of CaP and PBG, taking place in *Section 4.5* and *Section 4.6* respectively. A summary of the results presented in this chapter is found in *Section 4.6*.

The parameters of the edp CaP depositions performed in this chapter are listed below in Table 4.1.

Table 4.1: CaP edp deposition parameter summary

Section	Applied Potential /V	Duty Cycle	Deposition Time / min	Electrolyte pH
4.1	-3	0.2	20	4.5
		0.3		
		0.4		
		0.5		
		0.6		
		0.7		
		0.8		
		0.9		
		1		
4.2		0.6	20	4.5
			40	
			60	
			120	
4.3		0.6	20	4.5
				6.0
				7.5
				9.0

4.1 CaP coatings deposited on Mg WE43 with Duty cycle Variation

CaP coatings were deposited onto Mg WE43 disc substrates, as described in *Section 3.1.3* with the duty cycle parameter being varied. The as-deposited coatings were characterised using the combined techniques of SEM/EDX, XRD and XPS to obtain information on the morphology of deposited coatings, the phases of depositions and the surface chemistry of the coated samples. Profilometry was utilised at duty cycles 0.2, 0.6 and 1 to obtain coating thicknesses under applied deposition parameters. Further testing of 0.2, 0.6 and 1 duty cycle coatings were carried out to investigate the cytocompatibility of the coatings and cell viability when exposed to substrate-treated DMEM media in an elution test with MG-63 osteoblast-like cells.

4.1.1 SEM/EDX of varied duty cycle coatings

The electrodeposition method was utilised with the aim of depositing a layer of CaP onto a Mg WE43 alloy disc. Successful deposition of CaP was achieved with variations in the coating topography as the duty cycle of the electrodeposition process was varied as shown below in Figure 4.1.

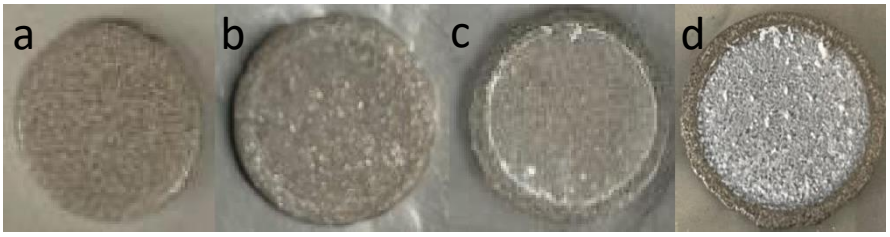

Figure 4.1 Macroscopic images of the a) Uncoated Mg WE43 alloy b) 0.2 duty cycle coating c) 0.6 duty cycle coating d) 1 duty cycle coating. Sample diameter is 10 mm.

4.1.1.1 Uncoated Mg WE43

Figure 4.2 shows the uncoated base alloy topography used for depositions as a control to compare against for the later deposited coatings, with Figure 4.2(a) showing the macroscopic view of the alloy disc. The surface topography was relatively rough, in comparison to the expected CaP deposition thickness, with height variation across the surface of the disc in the

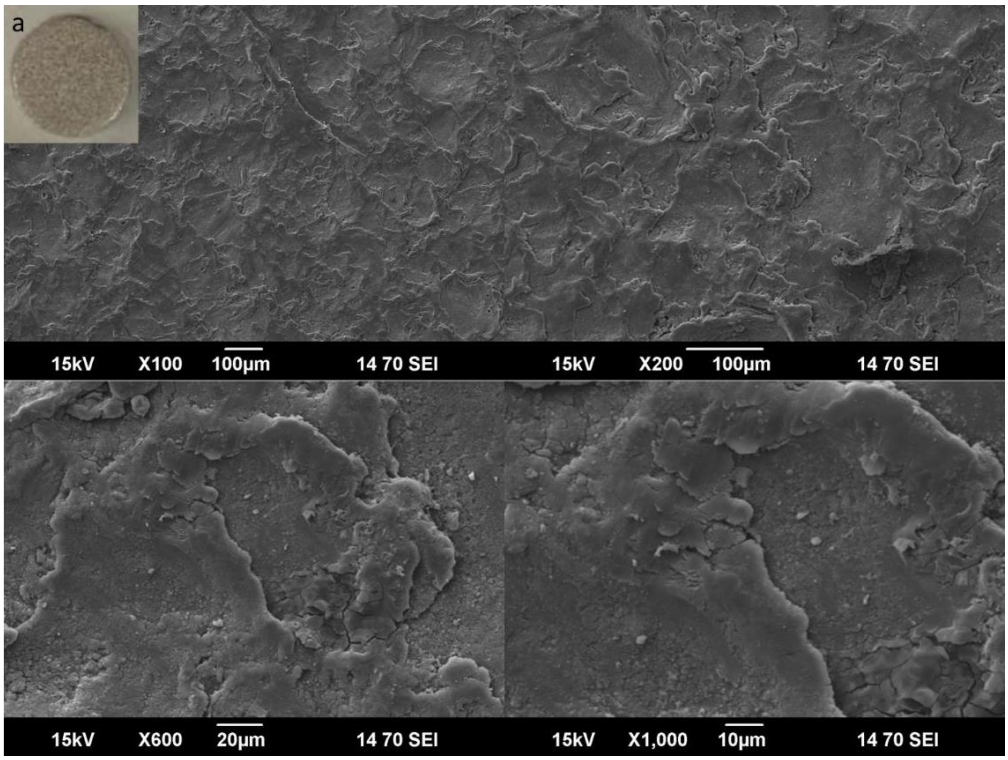

Figure 4.2: SEM images of the unpolished and uncoated Mg WE43 alloy disc (a) picture of the disc as punched from sheet Mg WE43, showing the control surface for electrodeposition

range of 5-30 µm by optical profilometry (not shown). This relative roughness required the discs to be ground and polished for later profilometry measurement (see *Section 4.1.4*). However, the discs were not polished as standard practice for the rest of the depositions.

4.1.1.2 The 0.2 Duty Cycle CaP coatings on Mg WE43

Figure 4.3 presents electron microscope images showing the generalised topography of the electrodeposited CaP coating at a duty cycle of 0.2, with a macroscopic image depicting the coating in Figure 4.3(a). The coating process deposited a crystalline structure, as confirmed by XRD analysis in *Section 4.1.2*, over the surface of the disc, leaving gaps in the coating (circled in Figure 4.3), ranging from *ca.* 30µm to 100µm in diameter. The majority of deposited crystals range in size from *ca.* 10µm to 50µm in length, with smaller crystals taking on a needle-like appearance and larger crystals taking on a plate-like structure.

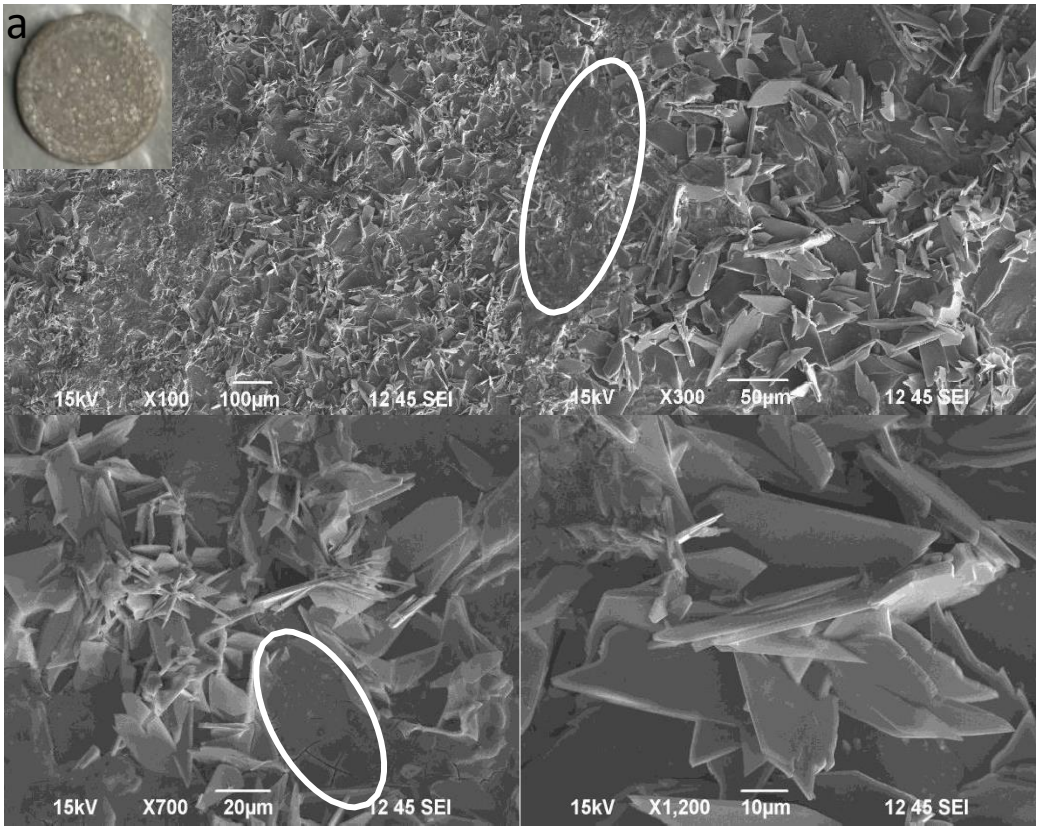

Figure 4.3: SEM images of electrodeposited CaP coating at duty cycle 0.2 showing a widespread coverage of CaP with voids in the coating topography a) a macroscopic image of the 0.2 duty cycle coating on Mg WE43 disc

4.1.1.3 The 0.3 Duty Cycle CaP coatings on Mg WE43

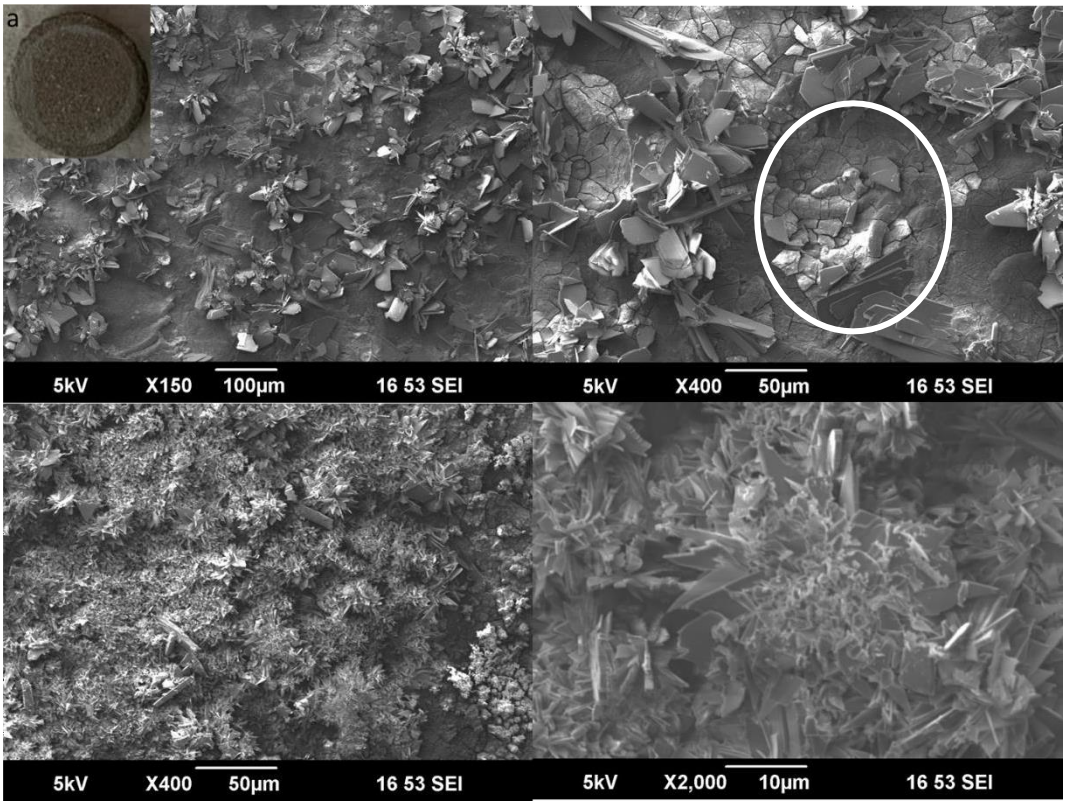

Figure 4.4: SEM images of electrodeposited CaP coating at duty cycle 0.3 showing a widespread variation in coating coverage of CaP with areas of high coating density and areas of low density a) a macroscopic image of the 0.3 duty cycle coating on Mg WE43 disc. Flaking of the surface exhibited in white circle.

For the duty cycle 0.3, there was large variation in the deposition coverage across the surface of the alloy. Higher areas of CaP deposition density giving a whiter hue on the disc, as observed macroscopically. Areas of lower CaP density showed more similarity to the uncoated alloy, as seen in Figure 4.4(a). The surface of the alloy, seen in the voids in the coating, was seen to contain small cracks in the surface with flakes (centre of circle in Figure 4.4) *ca.* 20µm in diameter to lift slightly from the surface of the disc. There were singular, plate-like deposits observed on these flaked areas. In the areas of high CaP density, there were minimal voids in the coating and crystals deposited tended to be smaller and more needle-like as opposed to larger plate-like crystals.

4.1.1.4 The 0.4 Duty Cycle CaP coatings on Mg WE43

Figure 4.5: SEM images of electrodeposited CaP coating at duty cycle 0.4 with both crystalline and amorphous deposits of CaP, with globular deposits circled and a) a macroscopic image of the 0.4 duty cycle coating on Mg WE43 disc

The deposited coating at 0.4 duty cycle showed similarities in the shape of the crystalline depositions of the previous duty cycles. However there was also an amorphous component to the coating where globules or a sheet of CaP were deposited (circled in Figure 4.5). This content was assumed to be amorphous due to similarities observed to the deposition at 1 duty cycle (*Section 4.1.1.10*), which was confirmed to be amorphous by XRD. These globules ranged from 15 - 40µm in length whilst the sheet-like regions extended up to *ca.* 300 µm in length. Voids were present in the surface of the coating but these did not completely expose the underlying alloy as there were some crystal deposits within these voids. The areas of the CaP coating which contained the globules and sheet-like structures appeared visibly whiter, macroscopically to the visible eye, and were consistent with Figure 4.5(a) where white dots and whiter haze contained a higher density of amorphous components.

4.1.1.5 The 0.5 Duty Cycle CaP coatings on Mg WE43

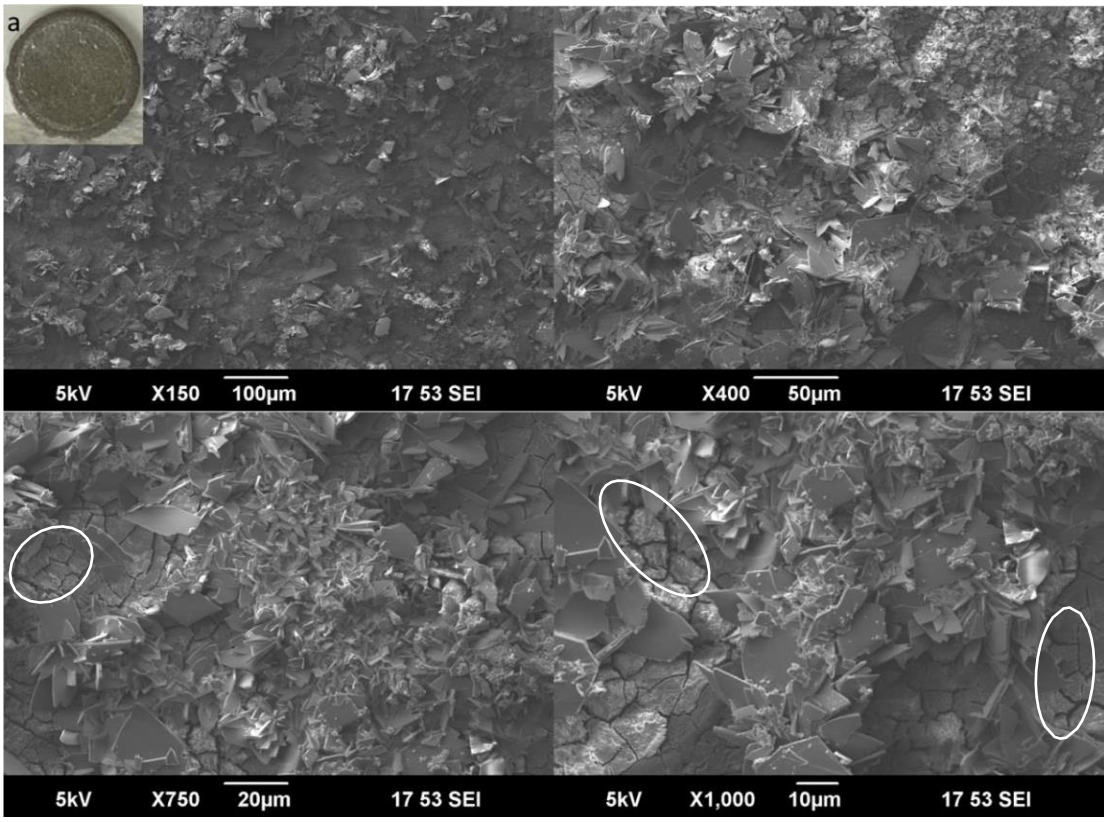

Figure 4.6: SEM images of electrodeposited CaP coating at duty cycle 0.5 with both crystalline and amorphous deposits of CaP with underlying alloy cracking in coating voids circled and a) a macroscopic image of the 0.5 duty cycle coating on Mg WE43 disc

Figure 4.6 depicts the surface topography of the CaP coating deposited at 0.5 duty cycle. At higher magnifications, significant cracking and flaking of the underlying substrate can be seen. A large surface area for these cracks was exposed due to the gaps in the electrodeposited coating (circled in white). Unlike the coating deposited at 0.4 duty cycle, there does not seem to be a CaP base layer in the voids of the coating, which correlates with the differences between Figure 4.5(a) and Figure 4.6(a) where the 0.5 duty cycle coating depicted in Figure 4.6(a) has a macroscopically visible, less strong white colouring and an overall lower proportion of the assumed amorphous CaP component. However, the coating follows the general trend of a higher duty cycle containing a higher proportion of amorphous CaP shown by presence of amorphous humps in XRD (Figure 4.13). A shift in the crystal shapes deposited was observed

with a decreased proportion of smaller needle-like crystals and an increase of the larger plate-like crystals alongside the addition of amorphous CaP structures.

4.1.1.6 The 0.6 Duty Cycle CaP coatings on Mg WE43

The CaP deposited at 0.6 duty cycle showed a combination of highly crystalline deposits, which decreased in crystal size to *ca.* 2µm - 5µm length (Figure 4.7 yellow circle), as compared to lower duty cycles of 0.4, 0.5 and were comparable to the crystals deposited at 0.2 and 0.3 duty cycles. Similarly to previous coatings, voids were observed in the coating surface (Figure 4.7 white circle) but there was not a significant degree of substrate cracking observed. A transition to a combination of crystalline CaP deposits and apparent amorphous CaP deposits occurs as the duty cycle increases (Figure 4.7). The assumed amorphous sheet structure, best seen in the micrograph of magnification x750, not only covers the base alloy but also the deposited crystal structures.

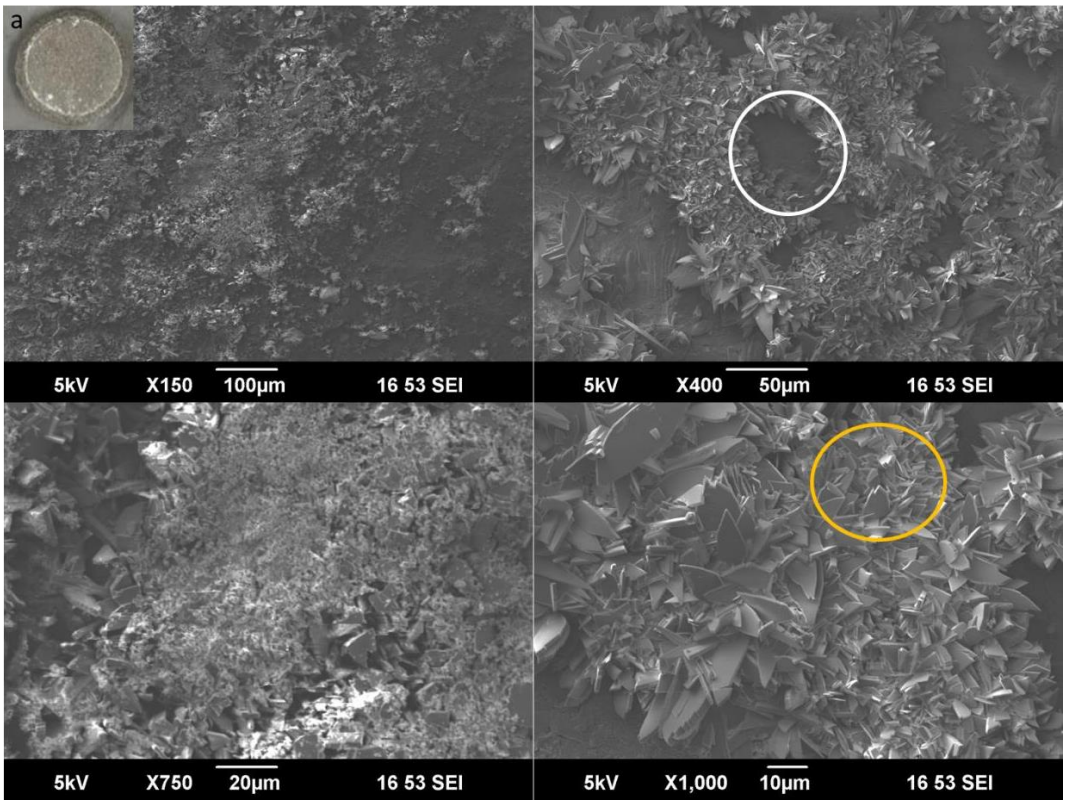

Figure 4.7: SEM images of electrodeposited CaP coating at 0.6 duty cycle showing increased coating coverage and decreased crystal size of needle-like structures (yellow circle) with typical coating voids (white circle) and a) a macroscopic image of the 0.6 duty cycle coating on Mg WE43 disc

4.1.1.7 The 0.7 Duty Cycle CaP coatings on Mg WE43

Figure 4.8(a) shows that at 0.7 duty cycle, there was a macroscopically strong, white CaP haze coverage across the surface of the alloy with the plethora of white dots depicting a large amorphous CaP content. The electron micrographs agree with this and were representative of the whole substrate surface, showing a coverage with a mixture of crystalline deposits in both the needle-like and plate-like structures. However, there was seen to be a general coverage of the "sheet-like" CaP across the majority of the crystal deposits.

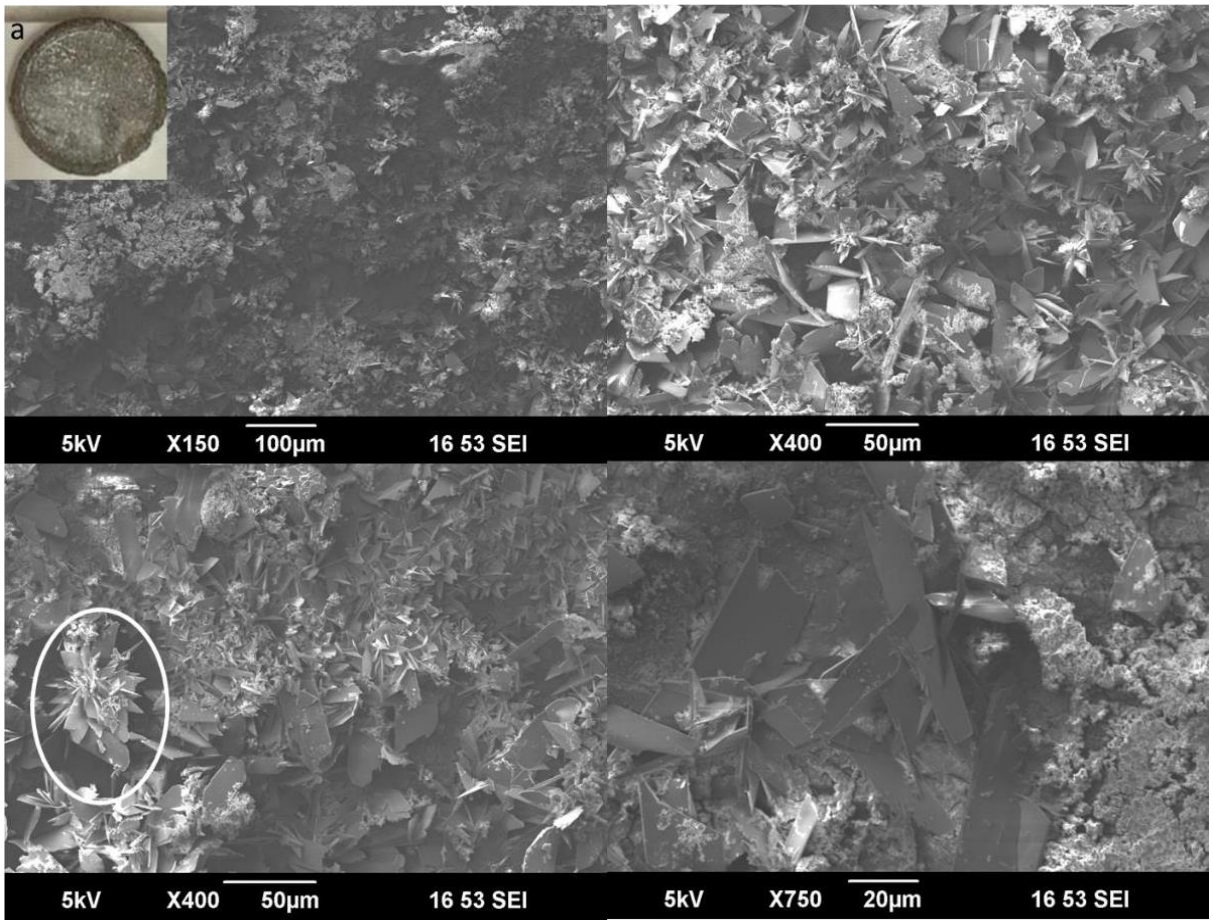

Figure 4.8: SEM images of electrodeposited CaP coating at 0.7 duty cycle showing increased coating coverage and increasing proportion of amorphous CaP. Crystal clusters typical of the coating is circled and a) a macroscopic image of the 0.7 duty cycle coating on Mg WE43 disc

4.1.1.8 The 0.8 Duty Cycle CaP coatings on Mg WE43

The CaP deposition at 0.8 duty cycle follows the previous trends mentioned above. There was a general coverage of the substrate with minimal voids and an increasing amount of CaP globules as compared to the lower duty cycles. This was in agreement with the coverage of white spots seen macroscopically in Figure 4.9(a). A reduction in CaP deposition was observed as crystalline deposits became more sparsely populated with increasing duty cycle. Deposited crystalline structures tended towards the larger plate-like deposits *ca.* 30 – 40 µm in diameter.

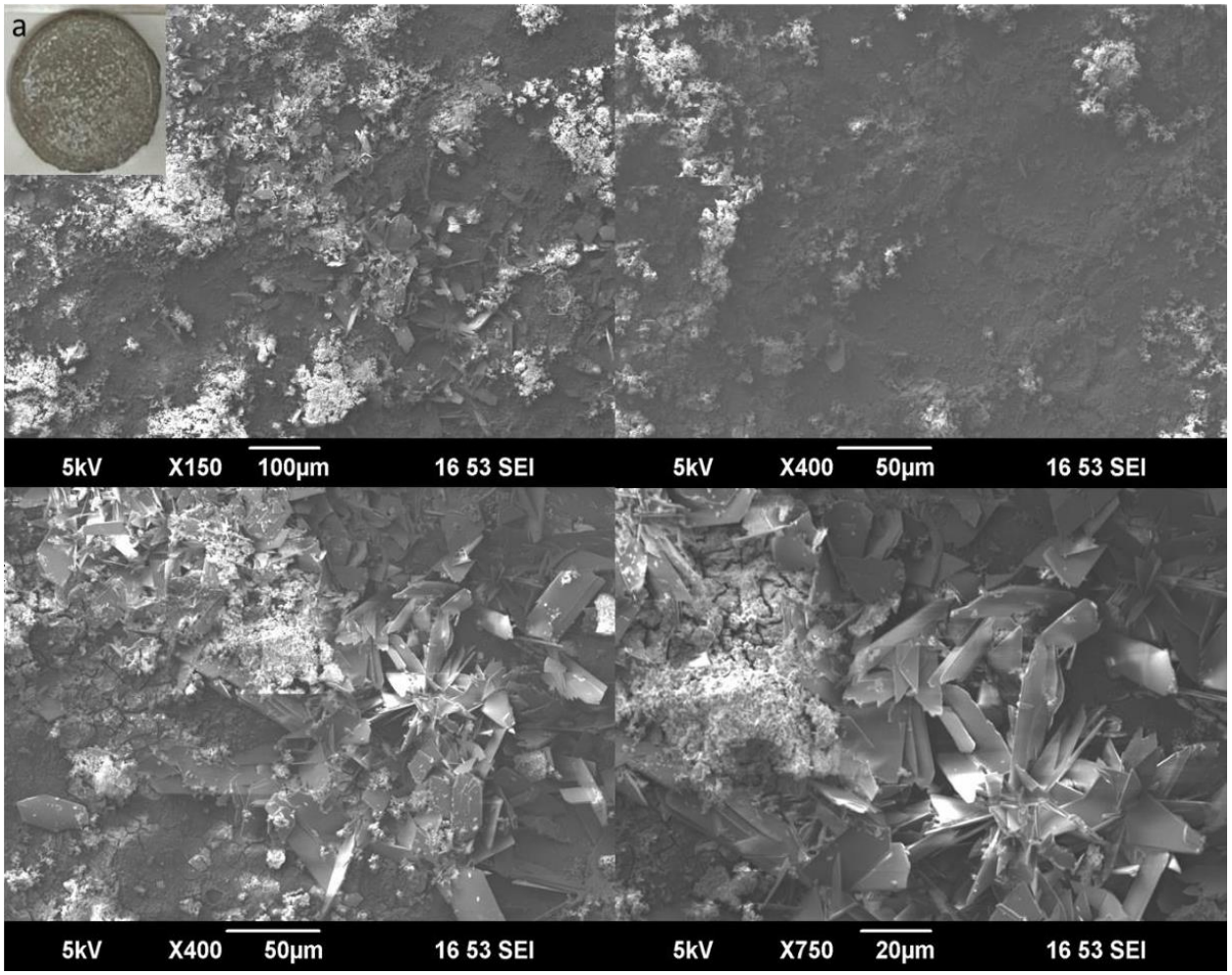

Figure 4.9: SEM images of electrodeposited CaP coating at 0.8 duty cycle depicting high coverage of amorphous CaP layer covering the alloy surface and the increasing crystal CaP size to ca. 100µm length and a) a macroscopic image of the 0.8 duty cycle coating on Mg WE43 disc

4.1.1.9 The 0.9 Duty Cycle CaP coatings on Mg WE43

Previous step-differences in coatings from varied duty cycle, had minimal variation between the 0.1 duty cycle steps. However, Figure 4.10 highlighted a large variation in the deposited coating as compared to 0.8 duty cycle. There were minimal to no crystalline deposits observed across the substrate surface and there was a new flake structure of CaP deposited, *ca.* 50 µm in length, which appears to be a midway point between the globular structure of amorphous CaP and the crystalline plate-like structures seen at lower duty cycles. Similarly, the macroscopic variations can be observed with the denser white areas of the coating depicted in Figure 4.10(a) being derived from the cumulative number of globules covering the alloy surface. Comparatively, there was a general haze observed for lower duty cycles derived from crystalline structures like that observed in Figure 4.7(a).

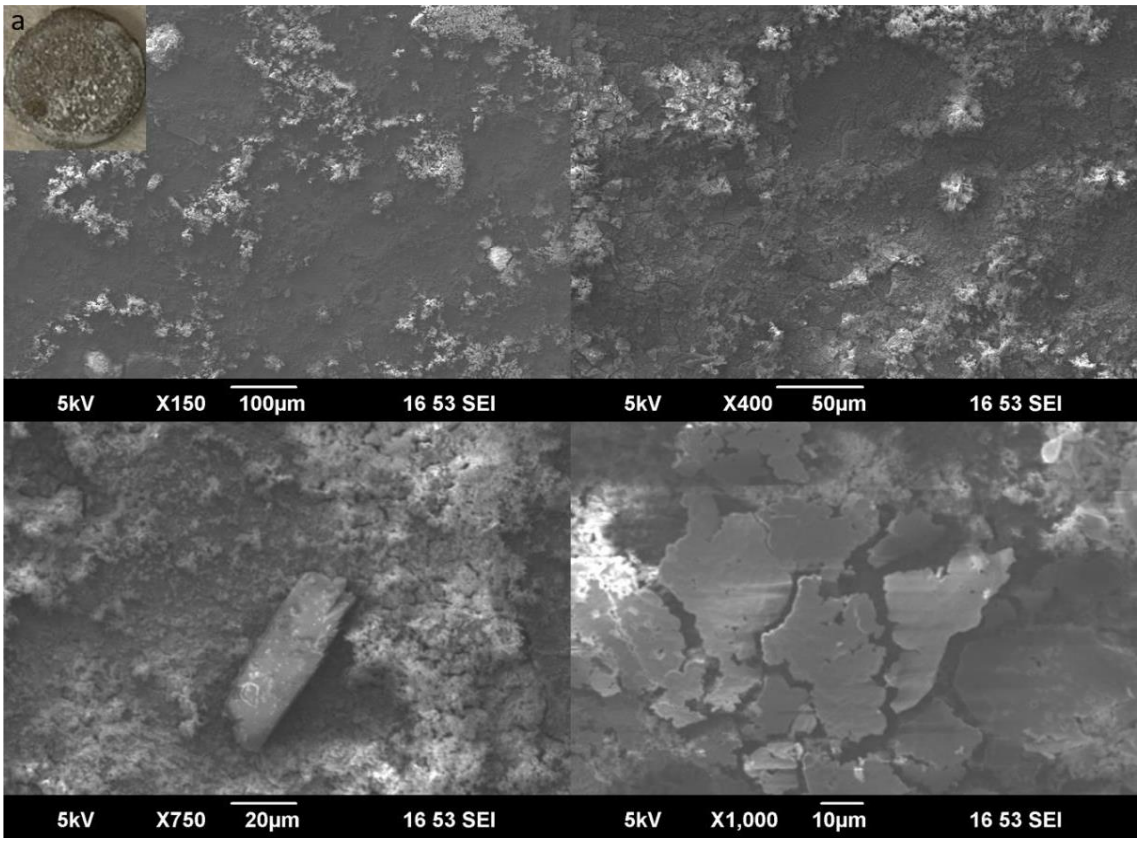

Figure 4.10: SEM images of electrodeposited CaP coating at 0.9 duty cycle depicting high coverage of amorphous CaP layer covering the alloy surface and the deposition of CaP flakes not typically seen for coating types of a lower duty cycle and a) a macroscopic image of the 0.9 duty cycle coating on Mg

4.1.1.10 The 1 Duty Cycle CaP coatings on Mg WE43

The CaP coating deposited using a duty cycle of 1 shows a complete coverage of the alloy surface with a strong white hue depicted in Figure 4.11(a). Similarly to 0.9 duty cycle, there were minimal crystal deposits with the coating predominantly being composed of globules of CaP and a sheet-like structure previously associated with amorphous CaP hump in XRD spectra (Figure 4.13), due to the lack of any crystalline CaP peaks. However, there were still height variations withing the coating itself caused by the deposited globules and crystal deposits but the underlying alloy was not visibly exposed.

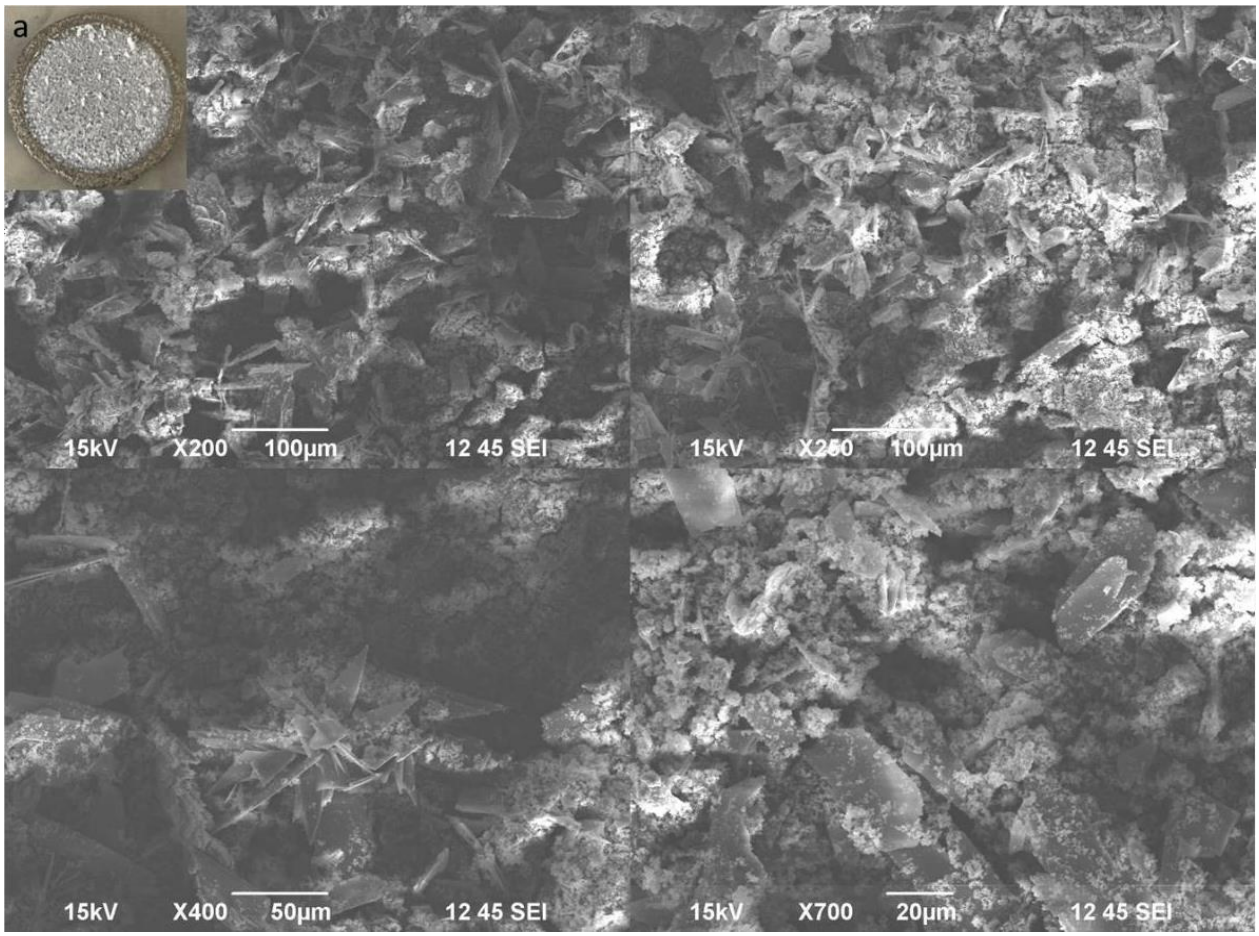

Figure 4.11: SEM images of electrodeposited CaP coating at 1 duty cycle showing full substrate coverage with large globules of amorphous CaP and a relatively small amount of crystalline deposits and a) a macroscopic image of the 1 duty cycle coating on Mg WE43 disc

4.1.1.11 Surface composition of varied duty cycle coatings by EDX

The EDX data was collected for the electrodeposited CaP coatings, in order to assess the composition of the coatings as a function of the duty cycle. Figure 4.12 shows a representative SEM micrograph from which EDX data is also gleaned. The EDX data was collated from 4 point scans within 2 micrographs of *ca.* 400 x 300 µm in Table 4.2, and shows a preferential deposition of Ca as compared to P for all deposited coatings, as well as a large oxide component featuring for all coatings. However, for the 0.6 duty cycle coating, the oxide layer contributed the lowest amount atomically to the spectra, compared to all duty cycle variants, with 50.07 at%. For reference, the next lowest oxide content was found to be 58 at% for the 0.5 duty cycle coating. Typically, with a lower O content, there was a higher contribution of Ca, with the Ca content varying from 9.62 at.% for the 0.3 duty cycle coating to 30.05 at.% for the 0.6 duty cycle coat. There was less variation across duty cycles for the P content which ranged from 5.19 at.% for 0.7 duty cycle to 19.89 at.% for 0.6 duty cycle. The Ca:P ratios suggest that various types of CaP have been deposited from brushite exhibiting a ratio around 1, Tricalcium

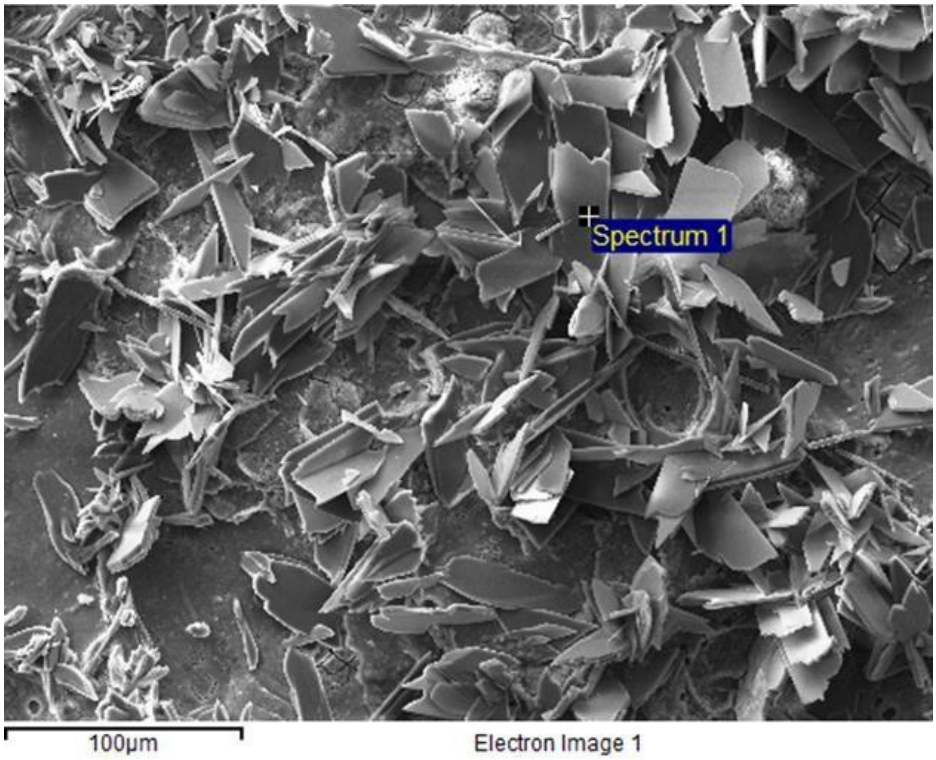

Figure 4.12: Electron microscope image used to gather EDX spectra from 0.2 duty cycle CaP coating on Mg WE43 alloy disc. Similar micrographs were used for each duty cycle variation to gather spectra.

phosphate with a ratio ca. 1.28 and other carbonated apatites typically ranging from 1.6 – 2.0 [360].

Table 4.2: Compositions of the electrodeposited CaP coatings by variation of duty cycle collected by EDX. Mean at% are shown with standard error (n=3)

Duty cycle	Element composition / at.%				Ca:P ratio
	Ca	Mg	O	P	
0.2	16.32 ± 0.88	5.92 ± 2.46	63.34 ± 0.70	15.73 ± 0.97	1.04
0.3	9.62 ± 1.56	13.91 ± 7.11	68.38 ± 4.94	8.09 ± 0.91	1.19
0.4	12.52 ± 0.29	-	77.48 ± 0.42	10.01 ± 0.13	1.25
0.5	23.95 ± 7.20	5.76 ± 1.22	58.00 ± 7.74	11.76 ± 2.03	2.04
0.6	30.05 ± 8.52	-	50.07 ± 13.63	19.89 ± 5.11	1.51
0.7	11.63 ± 0.84	2.05 ± 0.62	79.83 ± 2.86	5.19 ± 2.05	2.24
0.8	21.56 ± 3.58	4.92 ± 1.88	58.93 ± 7.05	14.16 ± 1.37	1.52
0.9	21.31 ± 3.46	5.98 ± 2.24	61.21 ± 5.55	11.51 ± 0.15	1.85
1	19.61 ± 1.10	4.73 ± 2.49	60.95 ± 0.65	14.58 ± 0.88	1.34

4.1.2 XRD spectra of varied duty cycle CaP coatings on Mg WE43 alloy disc

Figure 4.13 presents the XRD patterns of the CaP coatings deposited with varying duty cycles with an Mg WE43 control pattern for comparison. In all patterns, there was the presence of Mg peaks (ICDD database 00-004-0770) at 32.1, 34.4 36.5, 47.7, 57.4 and 63.0º 2θ which maintained a similar relative intensity across all sample types with the exceptions of 0.2 and 1 duty cycles, which recorded larger, more distinct peaks at 47.7, 57.4 and 63.0º 2θ. Indication of Mg in the samples, highlights a thin coating layer allowing the penetration of X-rays into the underlying substrate for 1 duty cycle. This may also suggest the presence of voids in the area of the coating scanned for the 0.2 duty cycle sample in agreement with the micrograph Figure 4.3 exhibiting what appeared to be voids in the coating. The Mg WE43 alloy substrate showed a phase orientation preference for the (101) plane followed by the (002) plane represented by the peaks at 36.5º and 34.4º respectively. The other Mg peaks represent the (100), (102), (110) and (103) orientations in order of increasing 2θ. The other substances determined from the XRD patterns were an amorphous hump of CaP around 10-12º 2θ and peaks matching the brushite phase of crystalline CaP at 11.6º, 21.0º, 29.3º, 30.5º and 50.2º 2θ

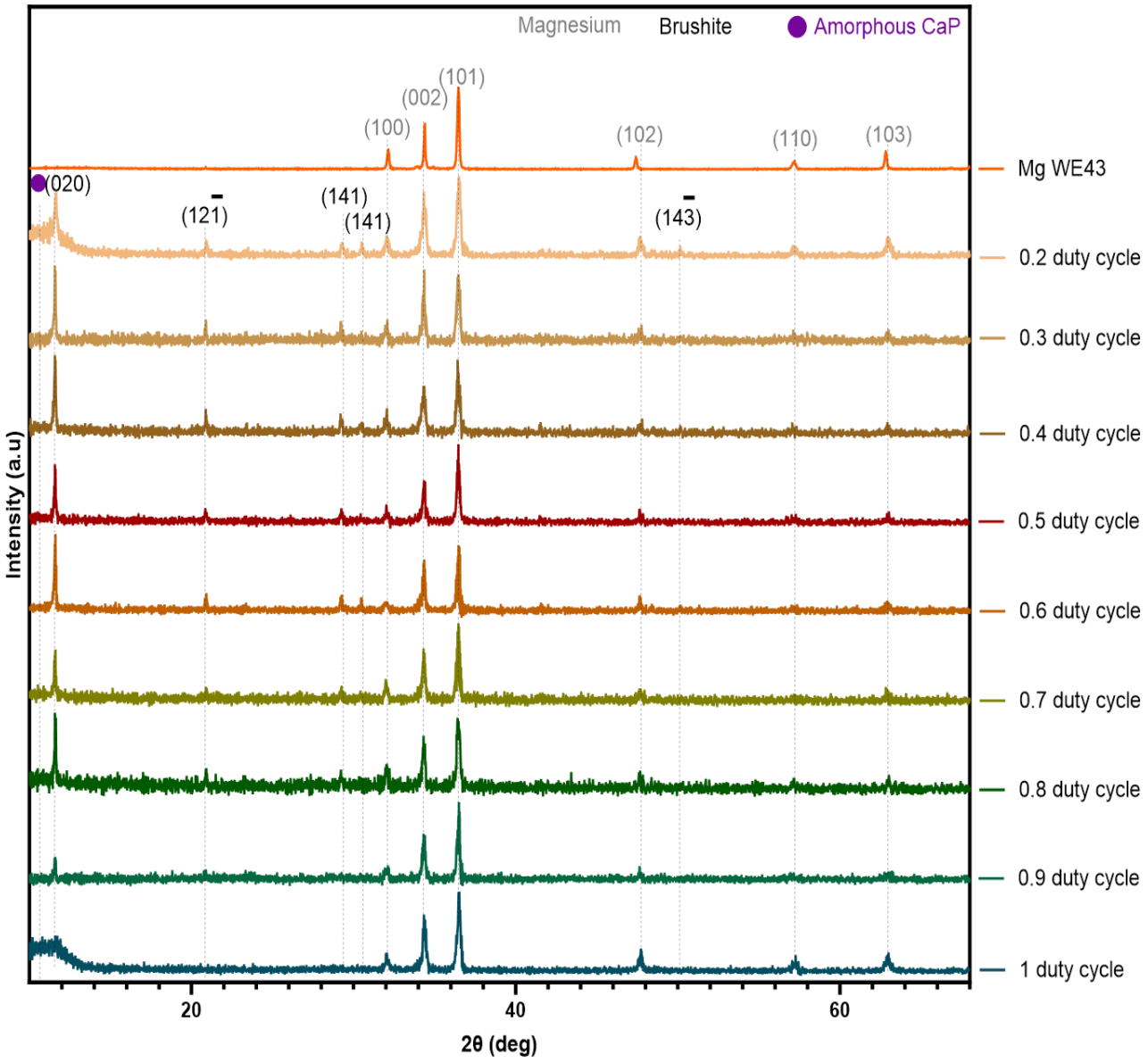

Figure 4.13: XRD patterns of as deposited CaP coatings on Mg WE43 alloy with varied duty cycle parameters. Peak deconvolutions are as follows: () – Mg:ICDD 00-004-0770, () – Brushite:ICDD 00-001-0395

(ICCD database 00-001-0395). The 1 duty cycle did not exhibit any of the brushite peaks but contained a large amorphous CaP hump. The lower duty cycles exhibited a small amorphous hump but indicated preferential crystalline growth of brushite in the (020) orientation, indicated by the peak recorded at 11.6º 2θ. The peaks recorded at 21º, 29.3º and 50.2º represent the $(12\bar{1})$, (141) and $(14\bar{3})$ orientations respectively. The highest relative intensity of brushite was observed for the 0.6 duty cycle sample, with the general trend by variation of duty cycle showing a high degree of brushite crystallinity with increasing duty cycle from 0.2 to 0.6 duty

cycle. Whereafter a transition was seen from crystalline brushite to increasing amorphous CaP with less brushite at higher duty cycles.

4.1.3 Surface compositional analysis of varied duty cycle CaP coatings on Mg WE43 by XPS

To complement the XRD observations by characterising the coatings *via* a new parameter, the surface chemistry of the coated samples was assessed using XPS. Figure 4.14(A) presents a survey scan and detailed high resolution C 1s, Ca 2s, Mg 2s, O 1s and P 2p spectra for the deposited coatings. The majority of sample types exhibited components of all of the aforementioned peaks. However the Mg WE43 alloy had no Ca or P peaks as it was uncoated. Spectra for 0.2 and 1 duty cycles exhibited no Mg 2s peak which may be due to the nature of XPS process having a decreased penetration depth into the sample as compared to XRD and as such the scan was of a relatively thick portion of the coating as they are non-homogenous. A summary of the ratio of elements composing the coating surface are listed in Table 4.3 below. Despite showing a reading for Mg from the elemental composition of the survey spectra, 0.8 and 0.9 duty cycle coatings did not contain the Mg 2s peak in the high resolution scans. There were however Mg KLL peaks observed in the survey spectra.

The high resolution spectra for the C 1s peak showed the presence of adventitious C for all coating types. CaP bonds were seen throughout the coated samples with one extra Ca component in the 0.4 duty cycle scan attributed to CaO bonding suggesting a bonding preference for O with Ca rather than O with C in the sample as there was only a C=C component of the C 1s peak for 0.4 duty cycle. Compositional analysis showed samples containing the Mg 2s peak in the XPS survey scan tended to have a lower Mg at% with no contribution greater than 10 at%. The contribution of O to the coating was largely consistent, generally contributing *ca.* 60 at% despite 0.3 duty cycle only containing one O oxidation state.

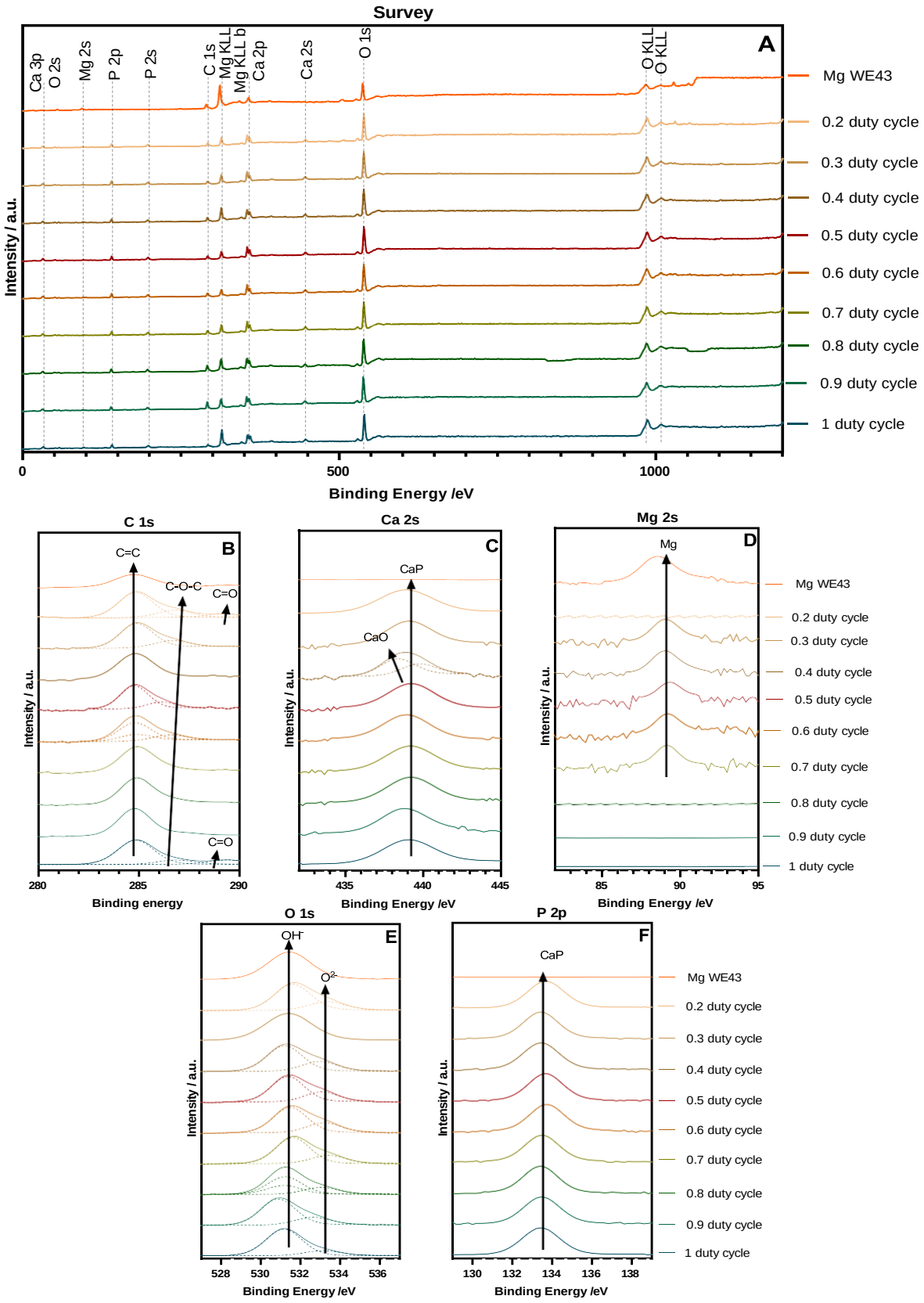

Figure 4.14 Survey and high resolution XPS of varied duty cycle CaP coatings: (A) Survey spectra (B) C 1s high resolution spectra (C) Ca 2s high resolution spectra (D) Mg 2s high resolution spectra (E) O 1s high resolution spectra (F) P 2p high resolution spectra

Table 4.3: Surface element compositional analysis for varied duty cycle coatings from XPS

Sample Type	Elemental Composition /at%					Ca:P ratio
	C	Ca	Mg	O	P	
Mg WE43	27.3	-	20.4	52.2	-	-
0.2 duty cycle	17.7	8.4	-	60.3	13.6	0.62
0.3 duty cycle	12.5	7.3	3.1	58.6	13.0	0.56
0.4 duty cycle	14.6	6.0	5.5	61.5	12.4	0.48
0.5 duty cycle	13.4	8.4	1.8	62.3	14.2	0.59
0.6 duty cycle	15.6	8.0	2.5	60.6	13.3	0.60
0.7 duty cycle	15.1	8.7	2.4	60.6	13.2	0.66
0.8 duty cycle	18.9	7.2	12.1	50.3	11.4	0.63
0.9 duty cycle	24.6	6.1	12.8	45.8	10.8	0.56
1 duty cycle	15.3	8.3	-	62.3	14.2	0.58

The previous characterisation subsections showed a relatively low coating variability between each 0.1 duty cycle step. There was a general transitional trend of a highly crystalline deposition at 0.2 duty cycle, with a lower surface coverage, transitioning to an amorphous CaP deposition at 1 duty cycle with a high surface coverage. The variability when comparing duty cycle extremes was easily observed but variability comparisons between coating types with adjacent duty cycles were difficult to make due to the similarity of coatings. Therefore, in the interest of efficiency, further investigations regarding duty cycle variation were performed using the 0.2 duty cycle, the 0.6 duty cycle and the 1 duty cycle to give an overview of the extreme points and middle of the transition of properties. The Ca:P ratios suggests that the majority of depositions were Monocalcium Phosphate (MCP) which typically exhibit a ratio of ca. 0.5 [361].

4.1.4 Profilometry of varied duty cycle CaP coatings on polished Mg WE43 for thickness measurement

As the deposition time for these samples was 20 min, profilometry of the cross-section of electrodeposited CaP coatings on polished Mg WE43 was conducted to quantify the deposition rate utilising the electrodeposition process, giving insight into the topography of the coatings.

4.1.4.1 The 0.2 Duty Cycle CaP coating profilometry

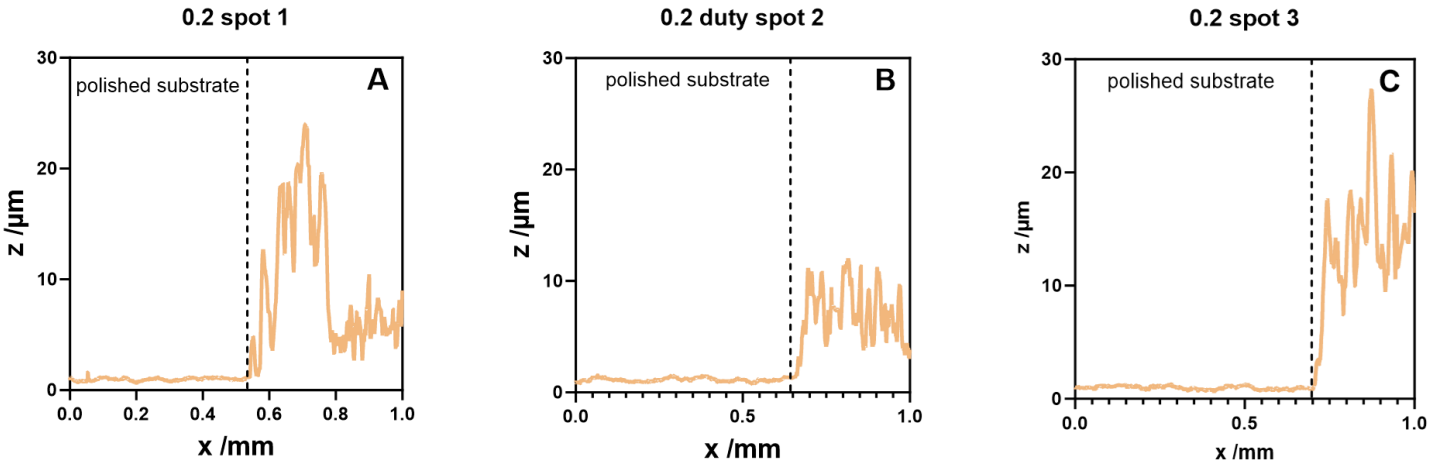

Figure 4.15: Profilometry of the 0.2 duty cycle coating measured at 3 different points along the substrate-coating border taken at A) ca. 2.5mm from left B) ca. 5mm from left C) ca. 7.5mm from left

Figure 4.15 depicts examples of the surface topography of the CaP coating deposited at 0.2 duty cycle. Measurements were performed at different spots along the step line of the coating and the uncoated, polished disc to show the level of variability along the coating surface.

The maximum height of the coating was seen to be *ca.* 26µm depicted in Figure 4.15(C). However, it must be taken into account that there was a large variability in the coating thickness as shown in SEM to be voids in the coating (*Section 4.1.1.1*). Similarly, the crystal orientation on the alloy surface will cause variation in height due to the non-uniform structure. Figure 4.15(A) combined with Figure 4.15(B) suggests there may be a base layer of CaP coating deposited across the alloy surface of *ca.* 5µm thickness with the larger crystal structures generally ranging from 10 - 20µm. Considering the variability of deposition thicknesses from 5 - 25µm, with the majority of crystal structures retaining a depth of 10 - 20µm, it can be assumed that a deposition time of 20 mins using 0.2 duty cycle gives a typical based coating thickness of 5µm with excursions of up to 25 µm.

4.1.4.2 The 0.6 Duty Cycle CaP coating profilometry

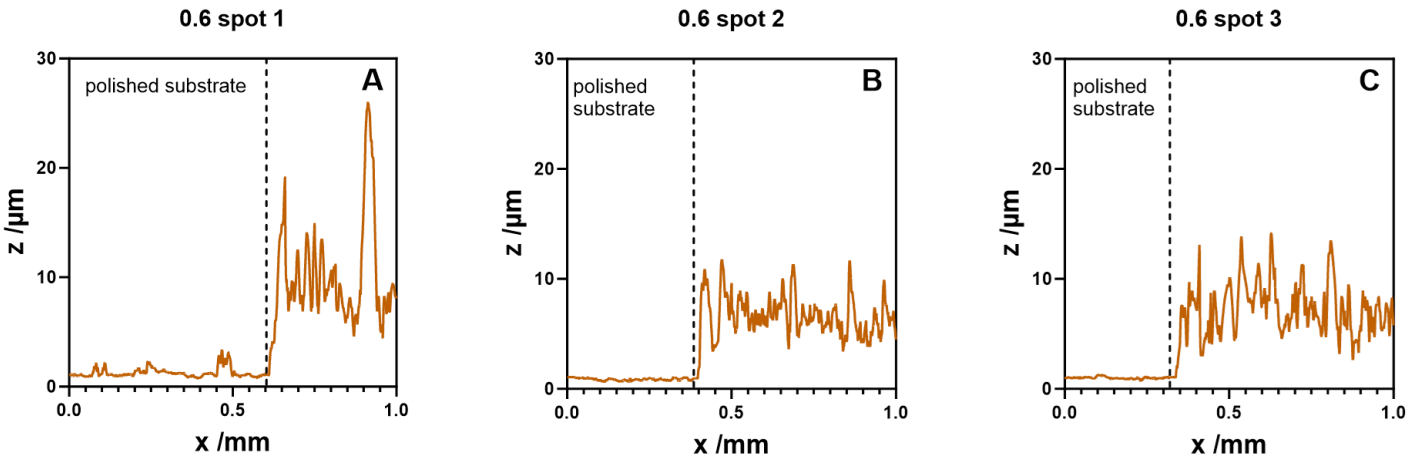

Figure 4.16: Profilometry of the 0.6 duty cycle coating measured at 3 different points along the substrate-coating border taken at A) ca. 2.5mm from left B) ca. 5mm from left C) ca. 7.5mm from left

Figure 4.16 shows the surface topography of the 0.6 duty cycle coating at 3 points along the substrate-coating border. There was a smaller height variation than that observed for the 0.2 duty cycle sample however, the coating thickness was also smaller with Figure 4.16(B, C) showing the coating thickness to be in the region of 5µm. Figure 4.16(A) shows a maximum height of *ca.* 25µm but typical excursions were around 10 - 12µm in height. The topography readings suggest that there was a base CaP coverage on the substrate *ca.* 5µm thick with crystals formed throughout the surface with a larger morphology, consistent with SEM images of crystal formation and voids to a base layer detailed in *Section 4.1.1.6.*

4.1.4.3 The 1 Duty Cycle CaP coating profilometry

Similarly to the previous profilometry measurements, Figure 4.17 suggests a base CaP coating layer of *ca.* 5µm with larger structures throughout the coating surface, with typical excursions up to 15 µm. Again the maximum height observed was *ca.* 20 µm thick, but most excursions were *ca.* 15 µm.

The average thicknesses of the electrodeposited coating profiles for the varied duty cycle depositions, were averaged across the 3 measurements and collated below in Table 4.4.

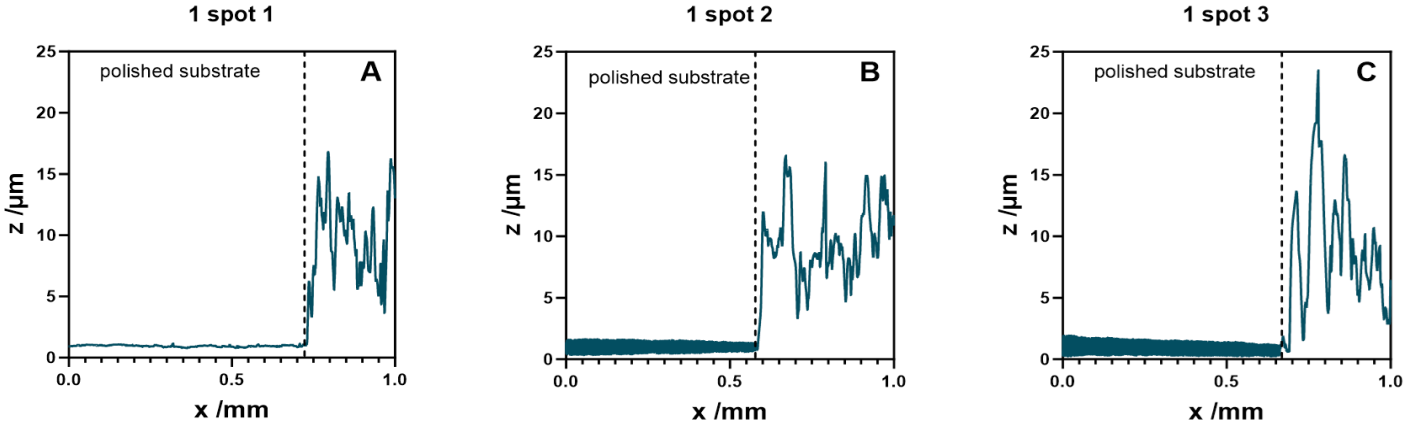

Figure 4.17: Profilometry of the 1 duty cycle coating measured at 3 different points along the substrate-coating border taken at A) ca. 2.5mm from left B) ca. 5mm from left C) ca. 7.5mm from left

Table 4.4 Average CaP coating thickness by variation of Duty cycle parameter with standard error of mean (n=3)

Duty Cycle	Average Profile Thickness /µm
0.2	9.72 ± 1.81
0.6	7.41 ± 0.84
1	8.80 ± 0.13

4.1.5 Elution Cytocompatibility Testing for varied Duty Cycle CaP coatings on Mg WE43

Figure 4.18 shows the cell viability of osteoblast-like cells after exposure to treated media in relation to a non-treated media (NTM) control. When the treated media was added to the cells, the cell viability of the MG-63 cells significantly drops for all sample types with varying degrees of significance between each coating and the NTM control. The viability of the cells for the 0.2 duty cycle treated media was the largest of the coatings. All coatings showed a higher degree of viability than the Mg WE43 alloy control, although through statistical analysis, the differences between the sample types were not seen as significant. Statistical analysis gave a p value < 0.05 between NTM and 0.2 duty cycle, $p < 0.01$ between NTM and both 0.6 and 1 duty cycle. The p value was less than 0.001 between the NTM and Mg WE43 alloy. Figure 4.18(B) details the results when the treated media was pH-corrected back to 7.4 whilst the original untreated DMEM media maintained. This can be used to suggest whether

the ions which leach out of the samples were toxic to the viability of the cells. The only sample type that showed a lower degree of viability than the NTM control was the Mg WE43 alloy with a significance of $p < 0.05$. There was a significant difference between all coated types and the Mg WE43 alloy with $p < 0.01$, $p < 0.001$ and $p < 0.05$ for 0.2 duty cycle, 0.6 duty cycle and 1 duty cycle respectively. Despite all coating types showing increased viability when compared to NTM, there was no significant statistical difference between these results. These trends were seen across 3 tests, to show repeatability, with some variation between the degree of significance between sample types. The bars depicted in Figure 4.18 were taken from an individual test which were selected as they were representative of the trends seen across the elution tests.

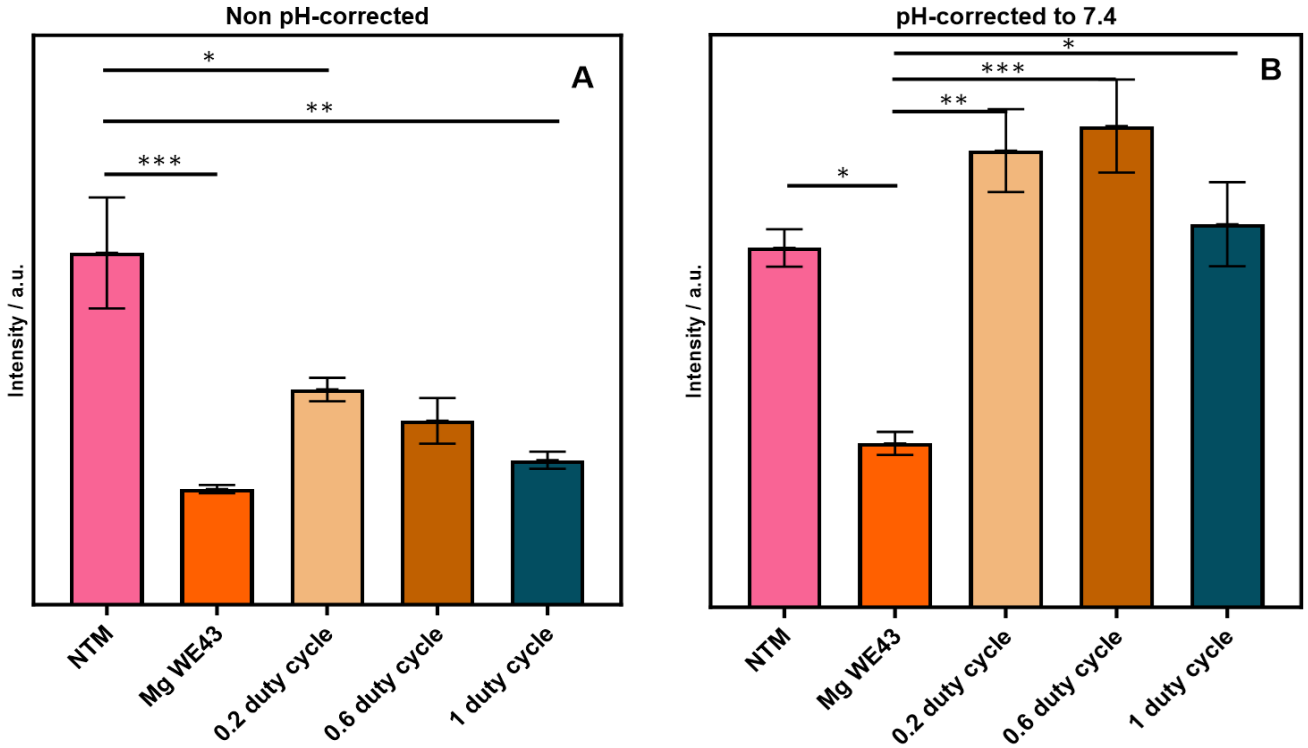

*Figure 4.18: Cell cytocompatibility test of varied duty cycle assessed using Neutral Red Assay: (A) treated DMEM media non pH-corrected (B) treated DMEM is pH-corrected to 7.4 to simulate body conditions. All values are mean values ± SEM (n=3). * - p<0.05, ** - p<0.01, *** - p<0.001*

4.1.6 Potentiodynamic Polarisation Testing for Varied Duty Cycle CaP coatings on Mg WE43

The varied duty cycles of 0.2, 0.6 and 1 all showed a more positive E_{corr} (seen in Figure 4.19) value than the Mg WE43 alloy. This more positive value tends to correlate with an improved corrosion resistance suggesting the CaP coatings improve the overall corrosion resistance of the base Mg WE43 alloy substrate. There was no trend observed for the E_{corr} values with increasing duty cycle although the most positive value was obtained by the 1 Duty Cycle sample with a value of -0.7 V. The E_{corr} values of the 0.2 and 0.6 duty cycle coatings were relatively close being -1.13 and -1.17 V respectively. However, despite these E_{corr} values suggesting higher corrosion resistance, this did not translate to a lowest corrosion rate for the investigated duty cycle samples as the i_{corr}, which is directly proportional to corrosion rate, was higher for the 0.2 duty cycle sample. The 0.6 and 1 duty cycle coatings both exhibited reduced corrosion rates (0.57 and 1.34 mm/Y respectively) compared to the Mg WE43 alloy whilst the

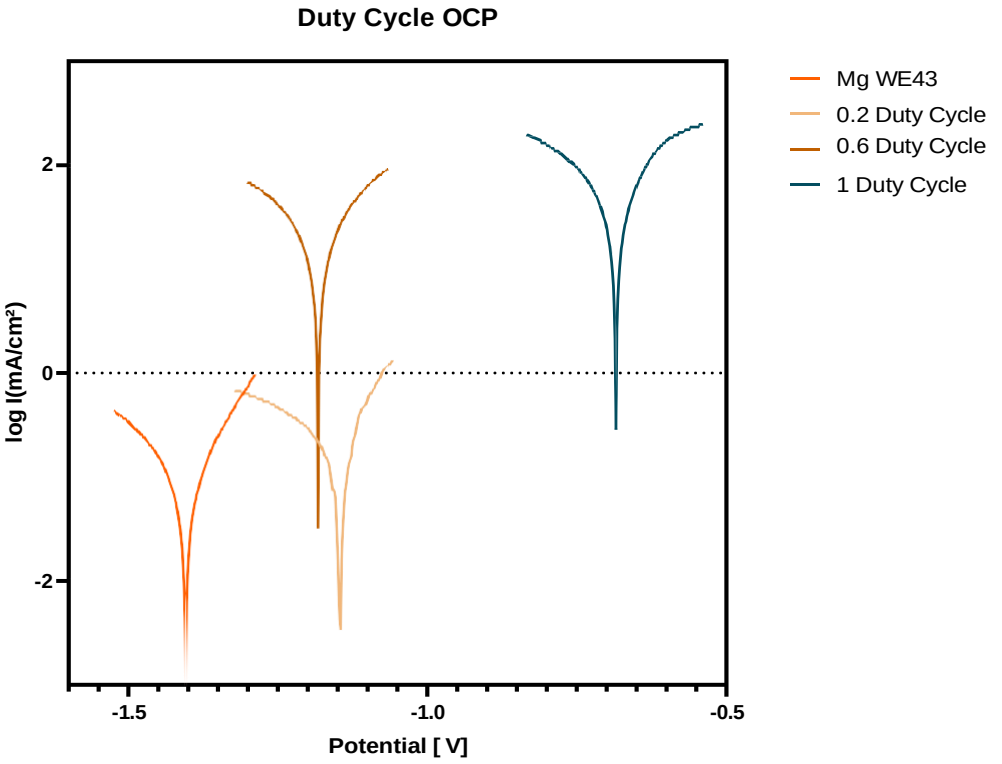

Figure 4.19 Electrochemical Corrosion Test Results for varied Duty Cycle coatings deposited on Mg WE43 discs, in DMEM at 37°C

corrosion rate increased for the 0.2 duty cycle coating to 6.44 mm/Y. The results of E_{corr}, i_{corr}, Corrosion resistance and corrosion rate are detailed below in Table 4.5.

Table 4.5 Mean Ecorr and Icorr values for each duty cycle and the resultant corrosion rate calculated with standard error (n=3)

Sample type	Corrosion Potential E_{corr} / V	Corrosion Current Density i_{corr} / (mA/cm^2)	Polarisation Resistance R_p / Ωcm^2	Corrosion Rate v_{corr} / (mm/Y)
Mg WE43	-1.42 ± 0.01	0.097 ± 0.009	264.5 ± 39.62	2.22 ± 0.030
0.2 Duty Cycle	-1.13 ± 0.23	0.282 ± 0.161	342.9 ± 254.79	6.44 ± 0.025
0.6 Duty Cycle	-1.17 ± 0.01	0.025 ± 0.011	782.5 ± 30.20	0.57 ± 0.002
1 Duty Cycle	-0.70 ± 0.01	0.059 ± 0.009	757.2 ± 91.26	1.34 ± 0.007

4.2 CaP coating deposited on Mg WE43 with Deposition Time Variation

Following the initial characterisation and viability tests, it was decided that the future samples of CaP deposition would use a duty cycle of 0.6 due to having a balance of deposition coverage and high degree of crystallinity combined with a good performance in cell viability testing and the lowest corrosion rate for varied duty cycle coatings. The CaP coatings in this section were deposited onto Mg WE43 disc substrates, as described in *Section 3.1.3* with the deposition time parameter being varied with time points of 20, 40, 60 and 120 min being used. The as-deposited coatings were characterised using the combined techniques of SEM/EDX, XRD and XPS with profilometry being utilised to obtain coating thickness. Further testing was carried out to investigate the effect of the coatings on the cytocompatibility of Mg WE43 alloy in an elution test with MG-63 osteoblast-like cells as well as potentiodynamic polarisation testing to determine if these coating types improve the corrosion resistance of the Mg WE43 alloy.

4.2.1 SEM of varied deposition time CaP coatings

4.2.1.1 20 min deposition time CaP coating on Mg WE43

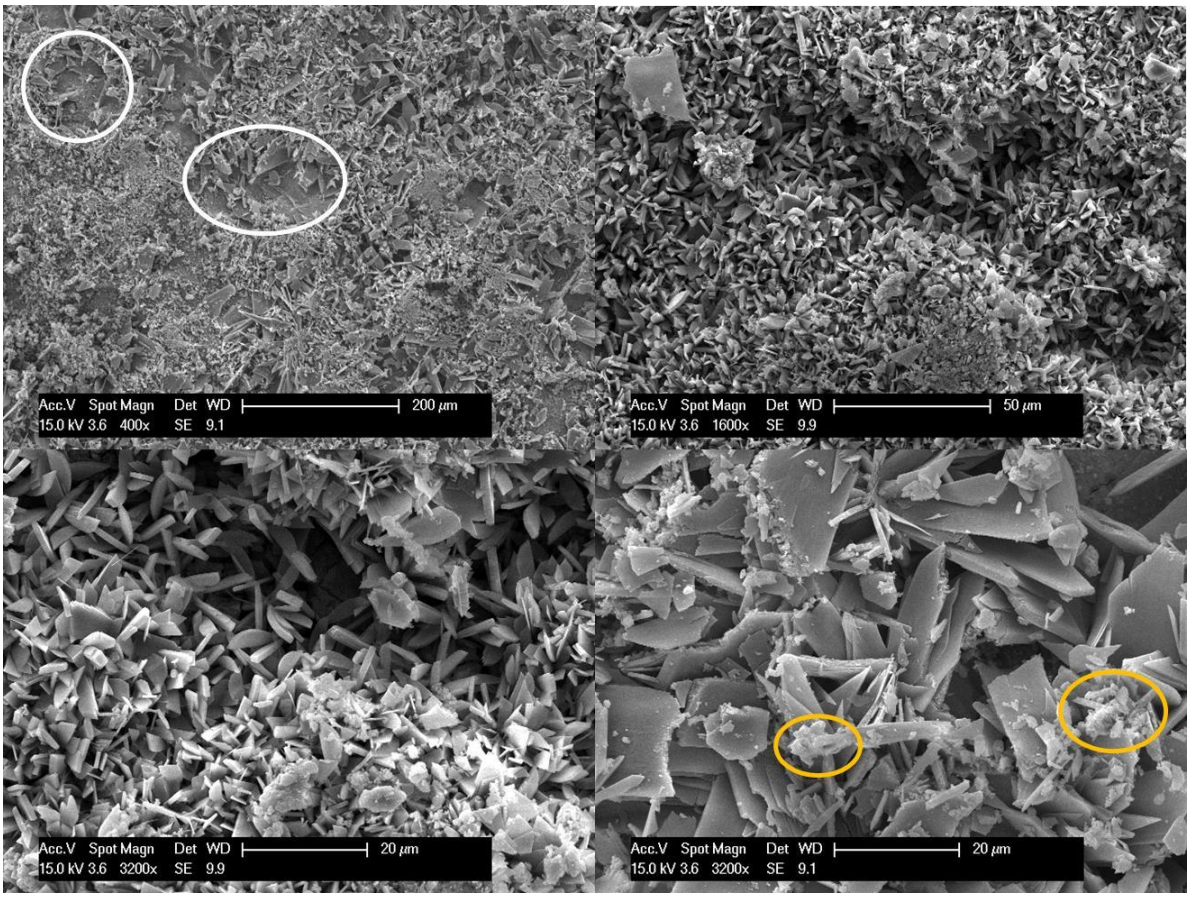

Figure 4.20: SEM images of 20 min deposition time CaP coating on Mg WE43 disc with typical coating voids circled white, examples of less common, small CaP features circled yellow

This coating type was deposited using the same parameters as the sample imaged in *Section 4.1.1.6.* Figure 4.20 shows repeatability with Figure 4.7 in that there was a crystalline deposition with some voids in the coating surface (circled in white), without substantial cracking of the alloy surface and also the presence of some other smaller CaP features (examples circled in yellow) on top of the deposited brushite crystals.

4.2.1.2 40 min deposition time CaP coating on Mg WE43

Figure 4.21 shows images taken of the CaP coating deposited with a 40min deposition time. Similarly to the previous coating type, there was a widespread coverage of crystalline deposition but this time the smaller CaP deposits were less present showing the cleaner crystal plates. However, upon closer magnification, cracks can be seen in the underlying substrate through the voids of the coatings surface. There was a variation in the size of the crystals

deposited with larger plate-like crystals *ca.* 25 - 30µm in length and smaller crystals *ca.* 2 - 5µm in length.

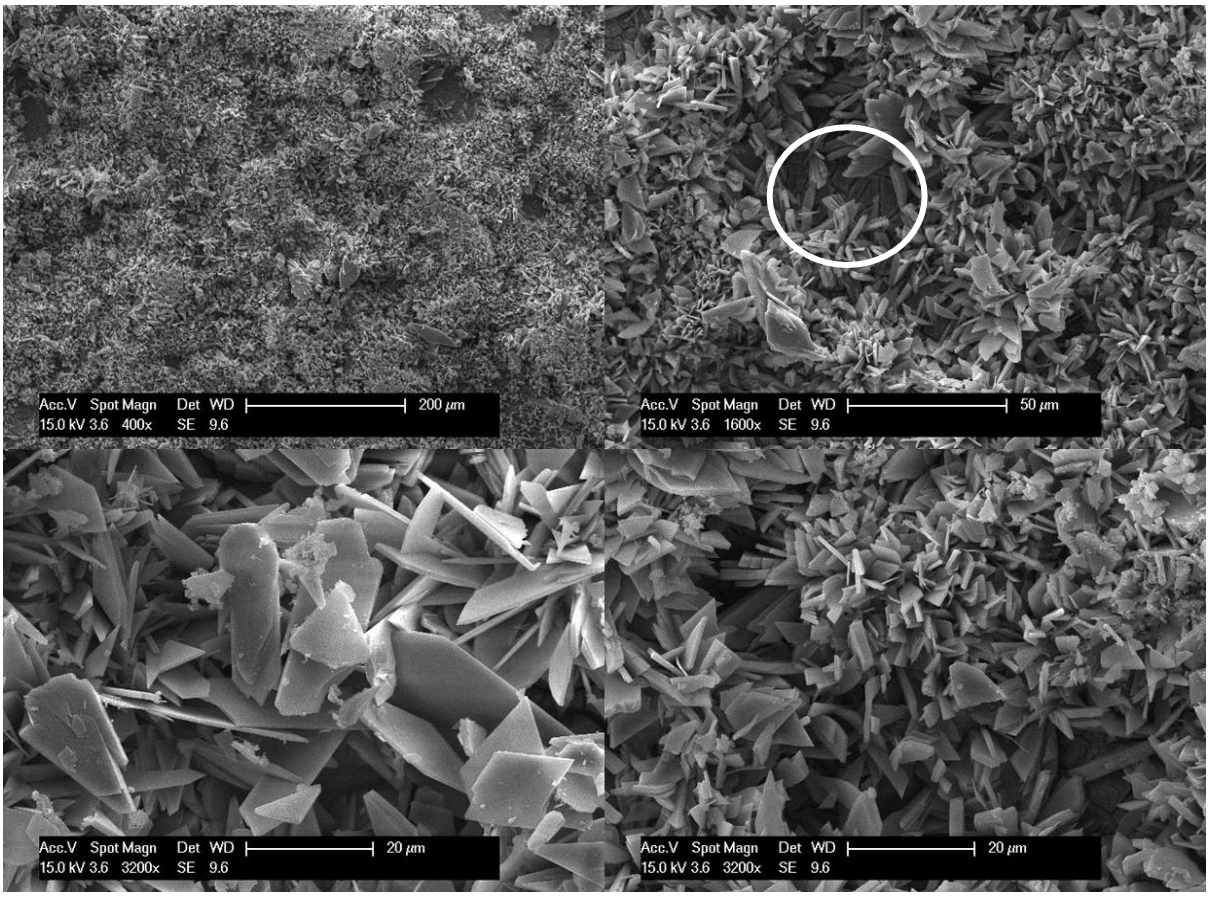

Figure 4.21: SEM images of 40 min deposition time CaP coating on Mg WE43 disc with significantly less coating voids (white circle) and a reduced crystal size of CaP deposits

4.2.1.3 60 min deposition time CaP coating on Mg WE43

The CaP coating deposited with a 60 min deposition time has similar traits with the previous coatings deposited with the shorter deposition times. Voids were clearly seen in the coating surface which seem to penetrate the whole way through the coating to reveal the underlying alloy substrate. Through these voids the underlying alloy has cracking in the top surface layer as pictured in Figure 4.22 (white circles), suggesting a reaction between the electrolyte solution used for the deposition and either the surface of the Mg WE43 alloy, or a dehydrating effect causing a cracking of the underlying deposited CaP layer. The areas without voids in the coating

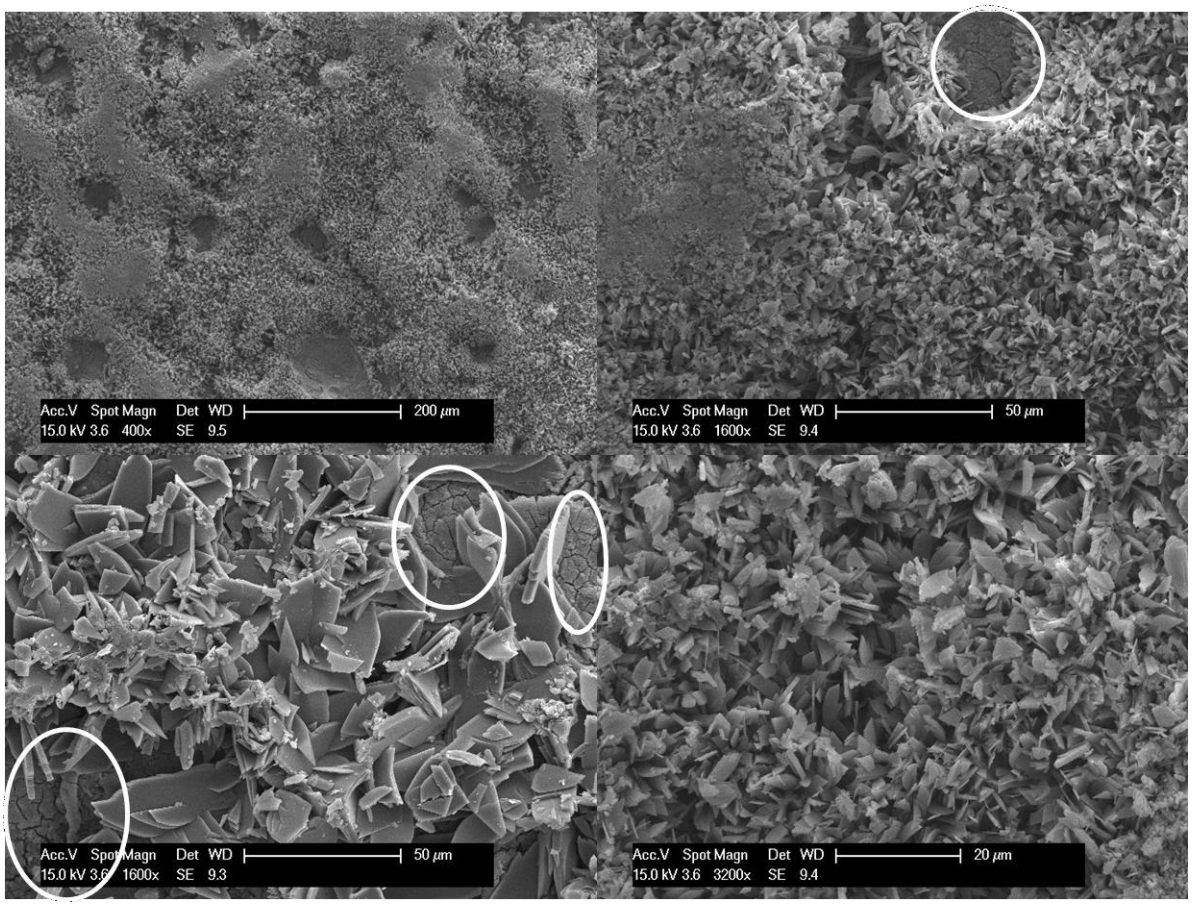

Figure 4.22: SEM images of 60 min deposition time CaP coating on Mg WE43 disc with void cracks (circled white) and a more densely packed CaP crystal coating with typical crystal size of ca.3µm length

appear to be densely packed with the small needle-like brushite crystals. There were still larger plate-like brushite crystals present, tending to grow at the void edges, but with increasing deposition time there appears to be an increasing proportion *ca.* 80 % of the deposited crystals being that of the smaller needle-like nature of *ca.* 2µm diameter. Some smaller CaP structures were also seen in a sheet-like form on top of the other deposited crystals.

4.2.1.4 120 min deposition time CaP coating on Mg WE43

Figure 4.23 depicts the CaP coating deposited with a 120 min deposition time. There were voids in the coating surface as with previous coatings but there also shows to be multi-layered crystals deposits where in some voids there was a clear crystal layer on the substrate which was not as tall as the top layer of the coating. However, there were still some voids that appear to penetrate the full thickness of the coating, exposing some cracking of the underlying substrate

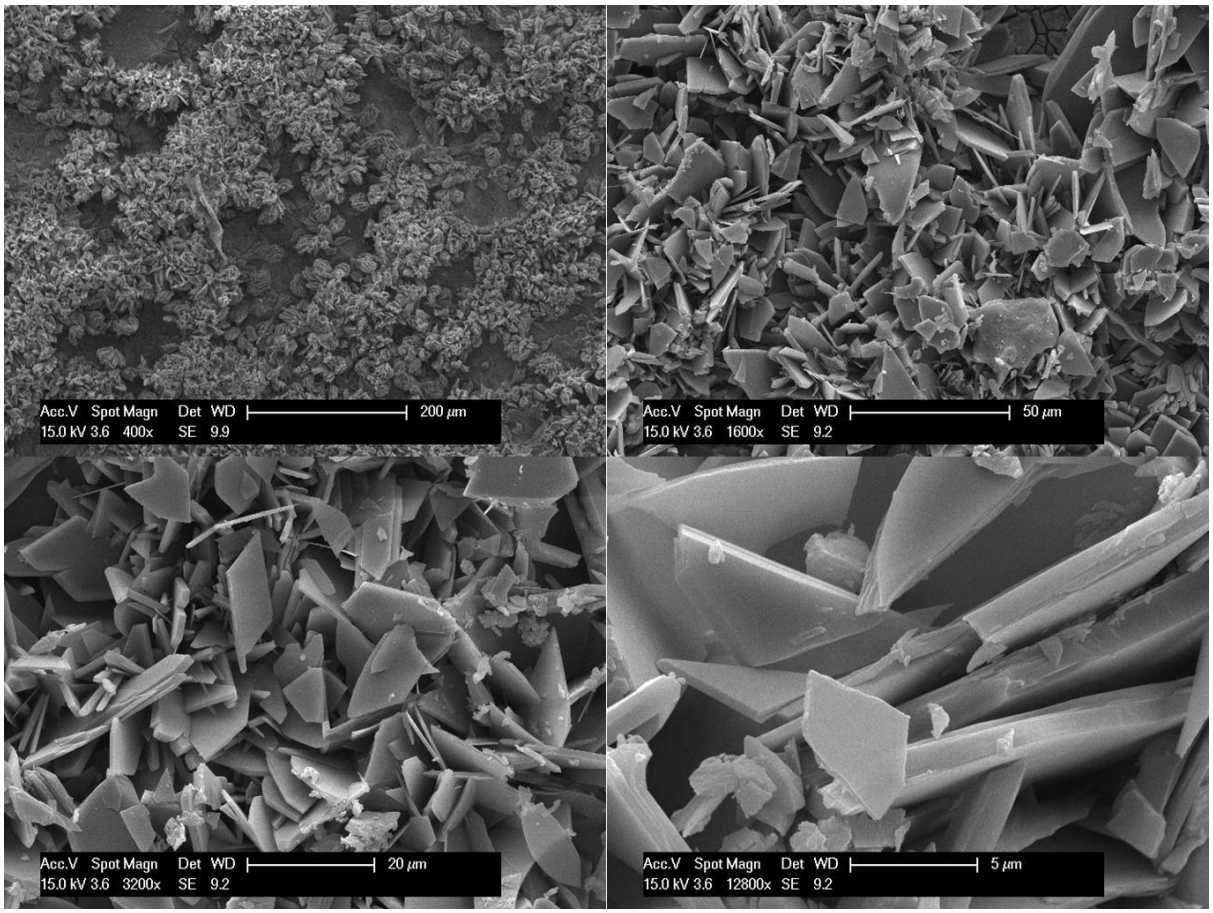

Figure 4.23: SEM images of 120 min deposition time CaP coating on Mg WE43 disc showing some voids in the coating surface and small, densely packed CaP crystals typical of coatings with deposition time over 20 mins

surface. The rest of the crystal deposits maintain the same morphology as with previous coatings with smaller crystals from 2 - 5µm in length and larger plate-like crystals around 20µm in length. Unlike the previous 60 min coating, the 120 min coating contains a larger proportion of the plate-like crystals *ca.* 50 %, as opposed to the densely packed *ca.* 2 µm needle-like crystals. As there appears to be a higher number of voids in the coating, this would suggest a larger proportion of plate-like crystals which have been seen to nucleate around the void edges.

4.2.2 XRD of varied deposition time coatings

Figure 4.24 presents the XRD patterns of the varied deposition time coatings against the uncoated Mg WE43 alloy. In all patterns, there was the presence of Mg peaks (ICDD database 00-004-0770) at 32.1, 34.4 36.5, 47.7, 57.4 and 63.0º although the relative intensity of these peaks significantly decreased to similar peak areas for the 40, 60 and 120 min samples,

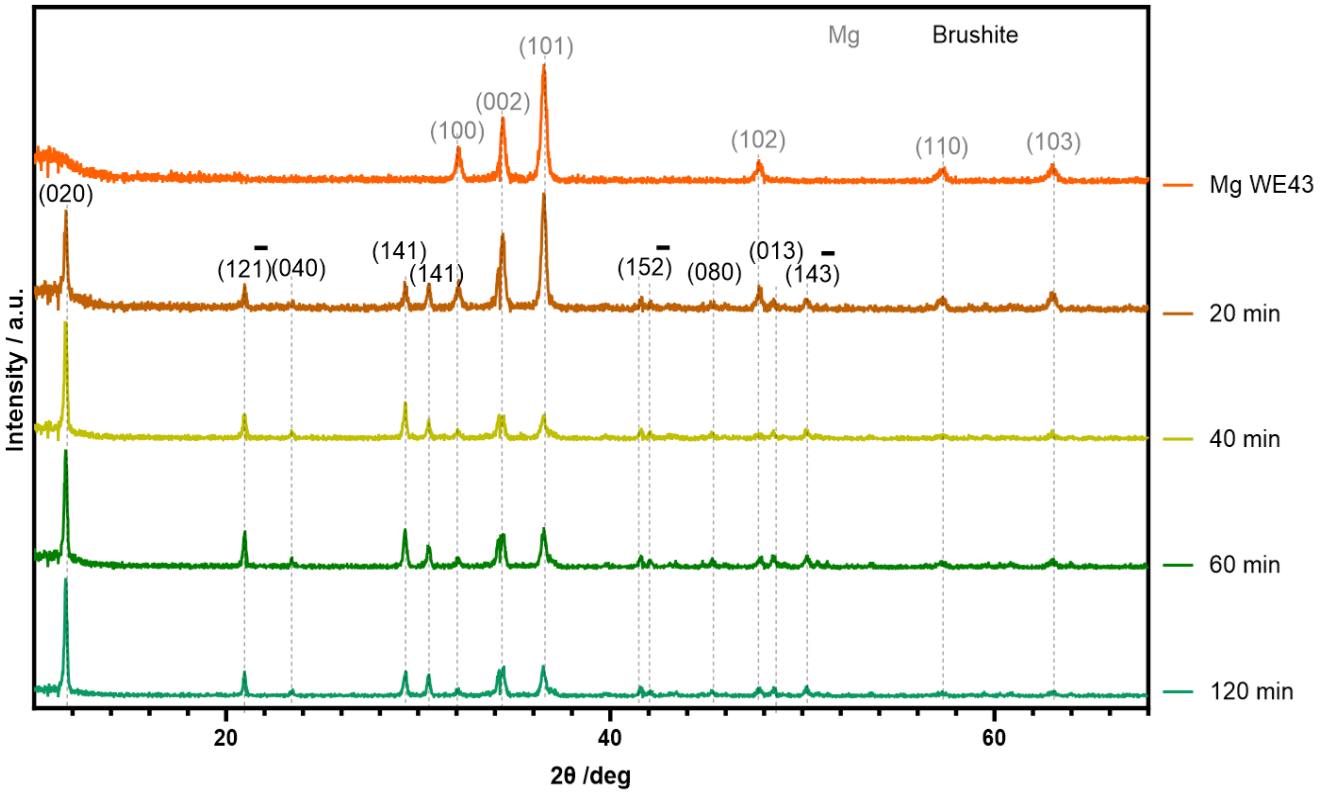

Figure 4.24: XRD patterns of as deposited CaP coatings on Mg WE43 alloy with varied deposition time parameters. Peak deconvolutions are as follows: () – Mg:ICDD 00-004-0770, () – Brushite:ICDD 00-001-0395

indicative that the coating thickness had not changed for these latter deposition times. The 20 min deposition showed a similar intensity of the Mg peaks as the Mg WE43 alloy control. Details as to the phase orientation of Mg peaks are presented previously in *Section 4.1.2*. The relative intensity of Mg peaks decreased due to the increase of CaP content in the coatings. Peaks at 11.6, 21.0, 23.2, 29.3, 30.5, 41.6, 48.5 and 50.2º 2θ closely match ICDD database 00-001-0395 for brushite. These peaks increased in relative intensity from the 20 min deposition to the 40 min deposition but seemed to remain at a similar relative intensity for the 60 min and 120 min depositions as stated above. Preferential growth of brushite was in the (020) plane represented by the peak at 11.6º 2θ with the highest relative intensity. The peaks recorded at 21, 23.2, 29.3, 41.6 and 50.2º represent the $(12\bar{1})$, (040), (141), $(15\bar{2})$ and $(14\bar{3})$ planes respectively. As the relative intensity of CaP peaks did not increase significantly after the 40

min deposition time mark, it suggests that the coatings may be very similar in nature and the deposition of increasingly thick CaP layers may be impeded after the 40 min timepoint.

4.2.3 XPS spectra of varied deposition time coatings

Figure 4.25(A) presents a survey scan and detailed high resolution C 1s, Ca 2s, Mg 2s, O 1s and P 2p spectra for the deposited coatings. The majority of sample types exhibited components of all of the aforementioned peaks with the notable exceptions of the Mg WE43 alloy expectedly not showing Ca 2s or P 2p peaks (Figure 4.25 (C,F)) and both 60 and 120 min depositions exhibiting no Mg 2s peak (Figure 4.25 (D)). There were however Mg KLL peaks seen in the survey scan but the relative intensity of these peaks were significantly lower than for other sample types. A summary of the ratio of elements composing the coating surface are listed in Table 4.6.

Table 4.6: Surface element compositional analysis for varied deposition time coatings by XPS

Sample Type	Elemental Composition /at%					Ca:P ratio
	C	Ca	Mg	O	P	
Mg WE43	27.3	-	18.6	52.2	-	-
20 min	16.2	6.5	5.9	58.7	12.7	0.51
40 min	16.3	7.0	6.1	58.1	12.6	0.55
60min	12.2	6.6	-	65.9	15.2	0.43
120 min	13.0	8.6	-	64.0	14.5	0.59

For all sample types, the C 1s high resolution scan (Figure 4.25 (B)) exhibited a single peak at 284.8eV which was attributed to a C=C bond. For the 60 min and 120 min samples, due to the lack of a Mg 2s peak, this suggested that the other bonding present must be a contribution of bonding including the other elements present of Ca, O and P. Therefore the slight binding energy shifts were attributed to bonding from a $Ca(PO_4)$

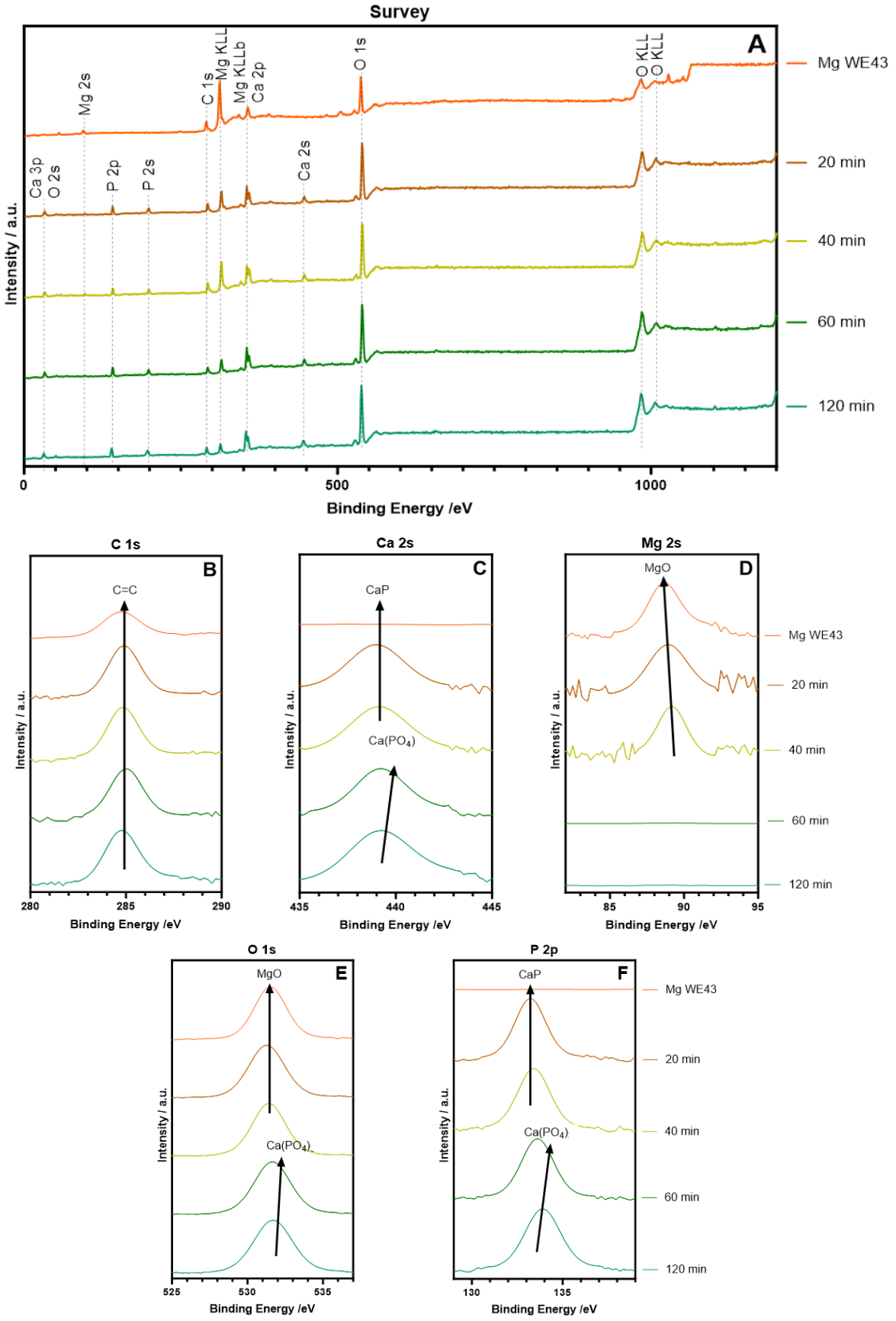

Figure 4.25 Survey and high resolution XPS of varied deposition time CaP coatings on Mg WE43 discs: (A) survey scan (B) C 1s high resolution spectra (C) Ca 2s high resolution spectra (D) Mg 2s high resolution spectra (E) O 1s high resolution spectra (F) P 2p high resolution spectra

compound with a binding energy of 133.5 eV for the P 2p peak and 438.6 eV for the Ca 2s peak, whilst bonding in the lower deposition time samples was attributed to MgO and CaP. The binding energies were slightly shifted from the expected values [362, 363], but also have a relatively large standard deviation across the literature so were considered the most likely for the peaks. Another factor contributing to the assignment of the peaks was that the existence of high resolution Mg 2s peaks for the 20 and 40 min samples attributed to MgO, would suggest that the O 1s peaks for the 20 and 40 min samples would also be from the MgO. However, the presence of an O 1s peak for the 60 and 120 min samples would therefore exist in a different compound as there were no Mg 2s peaks exhibited for these samples. Compositional analysis showed relatively similar proportions of each element across the coated sample types with the O at.% contribution increasing by roughly the same amount as the reduction of Mg contribution. There was also a shift in the Ca:P ratio as the P content increased for the 60 min and 120 min samples suggesting a different type of CaP bonding present which would be in agreement with the binding energy shifts shown in the high resolution scans of Figure 4.25. The Ca:P ratios calculated showed a similar deposition characterisation to that of the varying duty cycles with ratios of ca. 0.5 suggesting MCP deposition [361].

4.2.4 Profilometry of varied deposition time coatings for thickness measurement

4.2.4.1 20 min deposition time CaP coating profilometry

The profilometry measurements for the coating deposited using these parameters can be seen above in *Section 4.1.4.2.* However, the average value for coating thickness deposited using these parameters is also listed below in Table 4.7.

4.2.4.2 40 min deposition time CaP coating profilometry

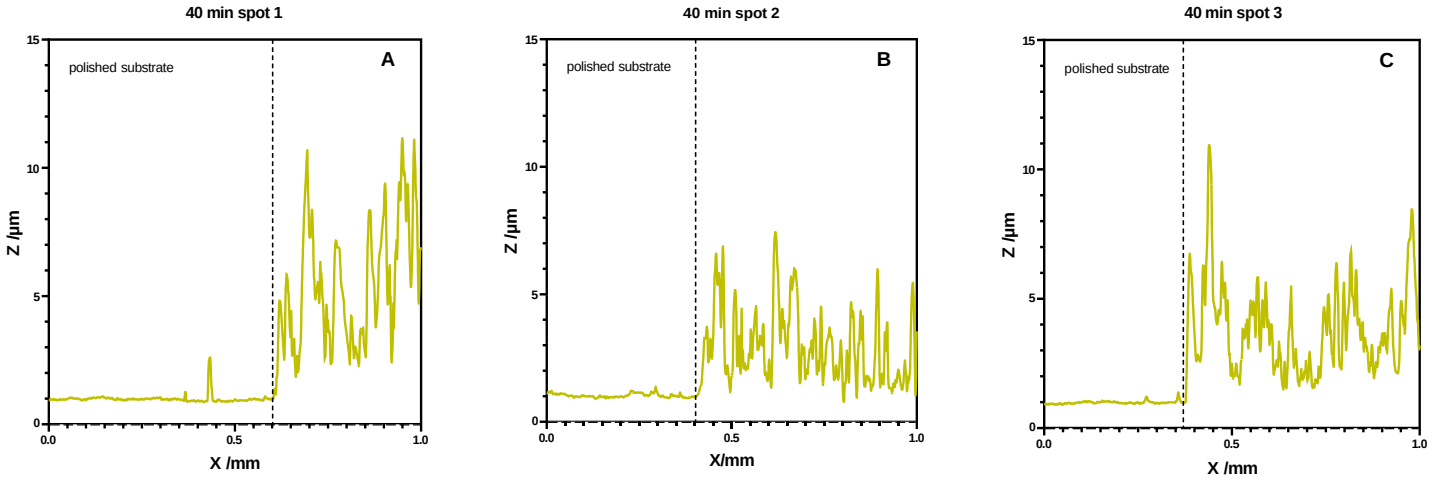

Figure 4.26: Profilometry of the 40 min coating measured at 3 different points along the substrate-coating border taken at A) ca. 2.5mm from left B) ca. 5mm from left C) ca. 7.5mm from left

Figure 4.26 depicts the profilometry of the coating thickness deposited at the 40 min time point. There appeared to be a base coating layer measured of *ca.* 2 – 3 µm although it must be considered that there could be voids present that penetrate through the coating to the alloy surface which cannot be accurately depicted due to the sensitivity of the stylus probe. The largest deposition was recorded to be in the region of 10 µm. The thickness was relatively similar to that observed for the 20 min deposition in general, although the 40 min sample lacked the larger deposit around 20 µm thick which would follow with the suggestion that deposited crystals tended to be the smaller, needle-like variety as opposed to the larger plate-like variety.

4.2.4.3 60 min deposition time CaP coating profilometry

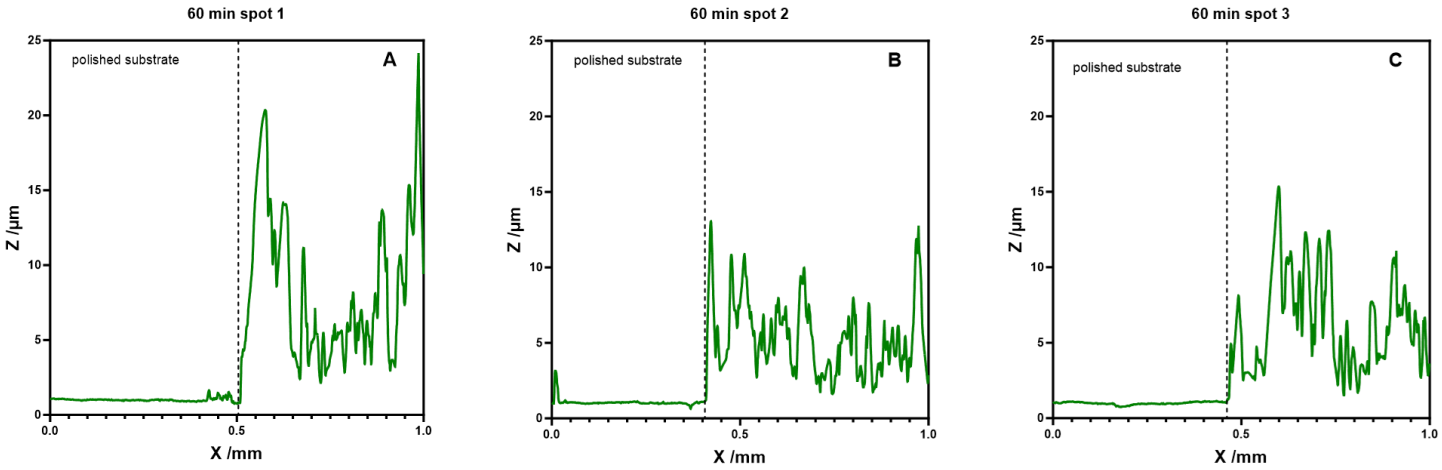

Figure 4.27: Profilometry of the 60 min coating measured at 3 different points along the substrate-coating border taken at A) ca. 2.5mm from left B) ca. 5mm from left C) ca. 7.5mm from left

The 60 min deposition time sample, depicted in Figure 4.27, shows similarities to the deposition of the 40 min sample but with areas of thicker deposition. Again, there appears to be a base layer *ca.* 2 – 3 µm thick with peaks showing either large crystals or a peak of more densely packed structures in the range of 10 – 20 µm thick. However, as seen in Figure 4.27(A), there was a large step in the heights of the coating which suggests there were gaps in the coating surface, although these do not appear to penetrate to the alloy surface.

4.2.4.4 120 min deposition time CaP coating profilometry

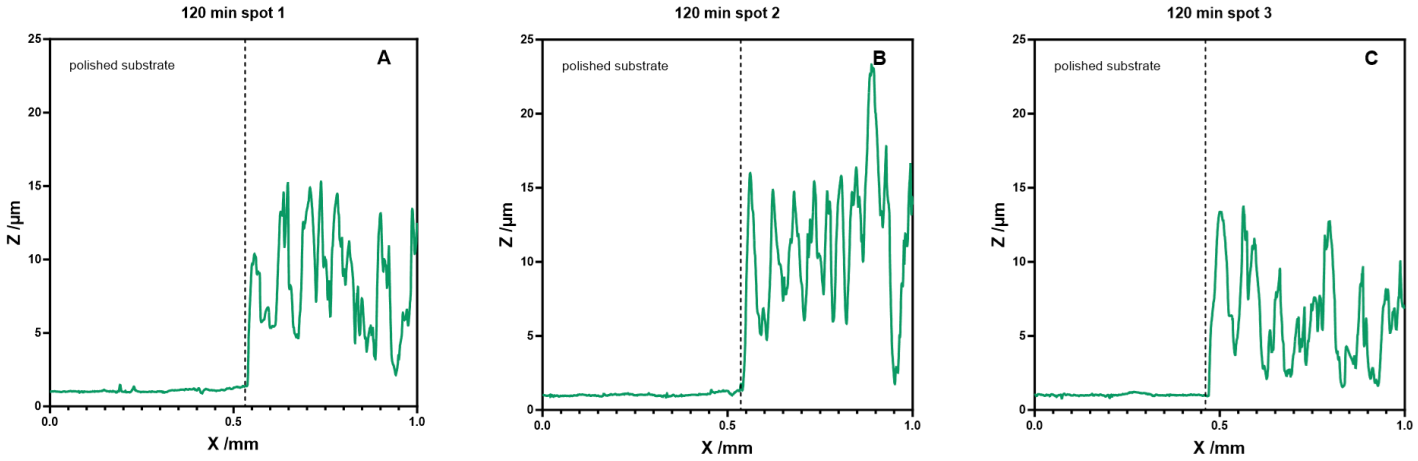

Figure 4.28: Profilometry of the 120 min coating measured at 3 different points along the substrate-coating border taken at A) ca. 2.5mm from left B) ca. 5mm from left C) ca. 7.5mm from left

Figure 4.28 depicts the coating thickness recorded at 3 points across the substrate-coating border. There were a significant number of peaks showing deposits of greater than 10 µm thickness with the largest peak showing a deposit of *ca.* 22 µm in depth. Similar to the other samples measured, there appears to be a layer deposited onto the base alloy substrate with a thickness of *ca.* 2 - 3µm.

The average thicknesses of the electrodeposited coating profiles for the varied deposition time depositions, were averaged across the 3 measurements and collated below in Table 4.7.

Table 4.7 Average thickness of CaP coatings with varied deposition time parameter calculated with SEM (n=3)

Deposition Time /min	Average Profile Thickness /µm
20	7.41 ± 0.84
40	3.65 ± 0.58
60	6.29 ± 0.74
120	7.92 ± 1.18

4.2.5 Elution Cytocompatibility Testing for varied deposition time CaP coatings on Mg WE43

Figure 4.29 shows the cell viability of MG-63 cells after 24 hours exposure to DMEM treated with each sample type both as treated (Figure 4.29(A)) and pH-corrected to 7.4 (Figure 4.29(B)). For the non pH-corrected media, there was a drop in cell viability for all samples types as compared to the NTM control. However this drop was not statistically significant between the NTM and both the 20 min and 40 min deposition, whereas the values for significance between the NTM and the other sample types were $p < 0.05$ for the Mg WE43 alloy and 60 min deposition and $p < 0.01$ for the 120 min deposition. When comparing with pH-corrected media, there was an improvement in the cell viability levels for all coating types whereas the performance of the Mg WE43 alloy remains similar to the non pH-corrected test. The largest improvement in cell viability was seen for the 120 min coating which had a higher viability than the NTM control although this difference was not statistically significant. However, there was statistical significance observed between the 120 min deposition and both

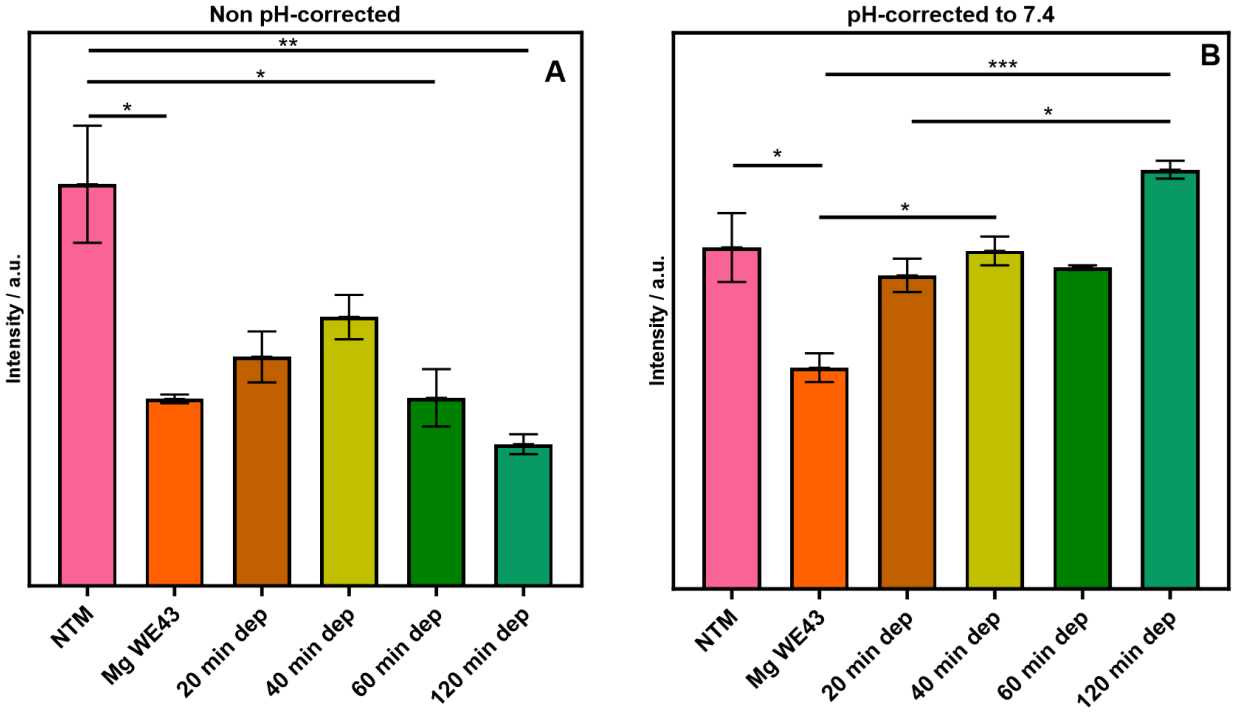

*Figure 4.29: Cell cytocompatibility test of varied deposition time assessed using Neutral Red Assay: (A) treated DMEM media non pH-corrected (B) treated DMEM is pH-corrected to 7.4 to simulate body conditions. All values are mean values ± SEM (n=3). * - p<0.05, ** - p<0.01, *** - p<0.001*

the Mg WE43 alloy and 20 min deposition giving p values of $p < 0.001$ and $p < 0.05$ respectively. The other statistical differences seen were $p < 0.05$ between NTM and Mg WE43 samples and $p < 0.05$ between the 40 min deposition and Mg WE43 samples.

4.2.6 Potentiodynamic polarisation testing for varied deposition time coatings

Figure 4.30 shows an example of the Tafel plots generated from PDP testing for each sample type of deposition time variation. Each sample type was repeated in triplicate with the results being averaged and collated below with calculated corrosion rate in Table 4.8.

In general, a more positive E_{corr} is preferable for corrosion resistance. Of all the sample types, the Mg WE43 alloy had the most negative value of -1.42 V, which suggests that every coating type improves the corrosion resistance of the alloy. No particular trend was seen for the coated samples as the values range from the most positive -1.10 V for the 40 min deposition to the most negative of coating types -1.33 V for the 60 min sample. Conversely, a lower i_{corr} is

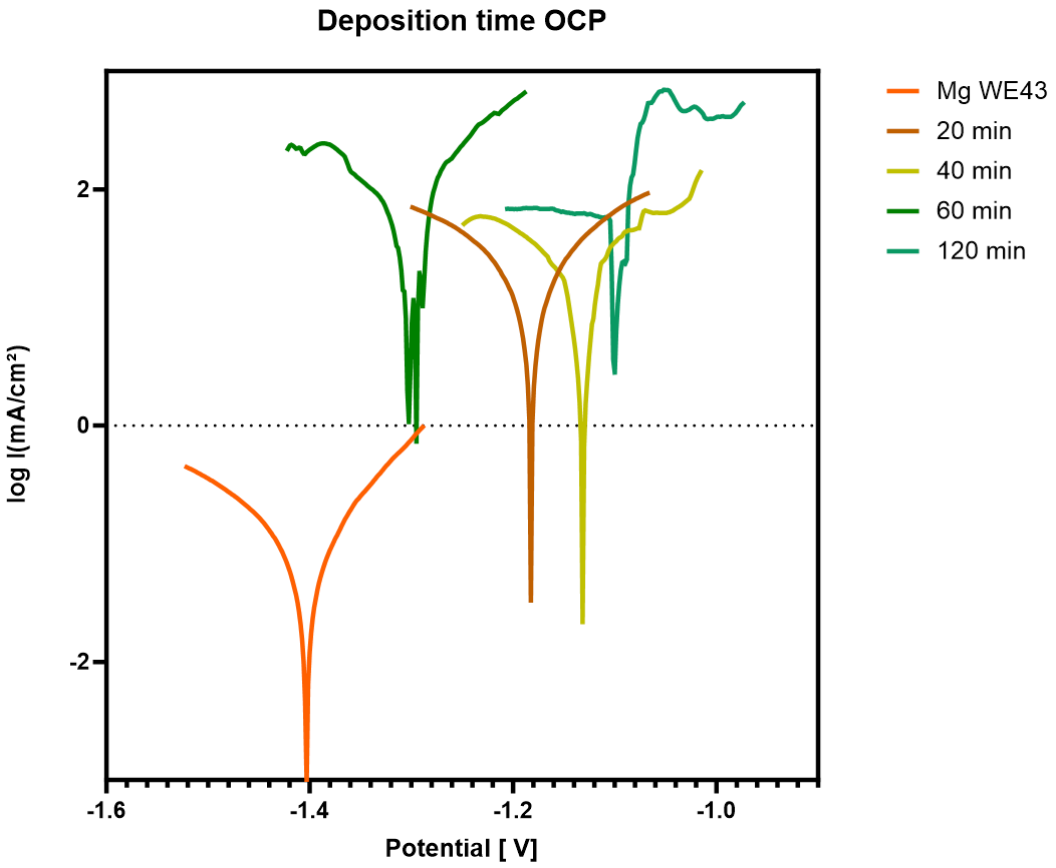

Figure 4.30: Electrochemical Corrosion Test Results for varied deposition time coatings deposited on Mg WE43 discs, in DMEM at 37°C

preferred as it is the factor used in Faraday's rate equation (Equation 3.5) to calculate the corrosion rate. The Mg WE43 alloy exhibits the highest i_{corr} value of 0.097 mA/cm^2 which demonstrates all coating types reduced the corrosion rate (Table 4.8). The lowest corrosion rate was exhibited by the 20 min deposition time coating with a v_{corr} of 0.57 mm/Y. However, the second lowest corrosion rate was seen for the 120 min deposition time sample at 0.88 mm/Y.

Table 4.8: Mean Ecorr and Icorr values for each deposition time and the resultant corrosion rate calculated with SEM (n=3)

Sample type	Corrosion Potential E_{corr} / V	Corrosion Current Density i_{corr} / (mA/cm^2)	Polarisation Resistance R_p / Ωcm^2	Corrosion Rate v_{corr} / (mm/Y)
Mg WE43	-1.42 ± 0.01	0.097 ± 0.01	264.5 ± 39.62	2.22 ± 0.030
20 min	-1.17 ± 0.01	0.025 ± 0.01	782.5 ± 30.20	0.57 ± 0.002
40 min	-1.10 ± 0.14	0.048 ± 0.04	752.4 ± 385.29	1.11 ± 0.025
60 min	-1.33 ± 0.02	0.061 ± 0.01	296.4 ± 64.21	1.40 ± 0.004
120 min	-1.16 ± 0.19	0.039 ± 0.03	423.0 ± 7.59	0.88 ± 0.022

4.3 CaP coatings deposited on Mg WE43 with Electrolyte pH variation

The third parameter of the electrodeposition process selected to be varied was the pH of the electrolyte solution. As hydroxyapatite is the preferable CaP phase to be deposited, as explained in *Section 2.8.1*, and is more stable at a higher pH than the previously used pH 4.5, the electrolyte pH was varied to investigate whether using a higher solution pH would promote the formation of hydroxyapatite crystals onto the Mg WE43 alloy as opposed to the brushite crystals previously deposited. The effect of changing electrolyte pH on the cell viability and corrosion rate will be examined in the following section.

4.3.1 SEM of varied electrolyte pH CaP coatings on Mg WE43 alloy

4.3.1.1 Electrolyte pH 4.5 CaP coating on Mg WE43

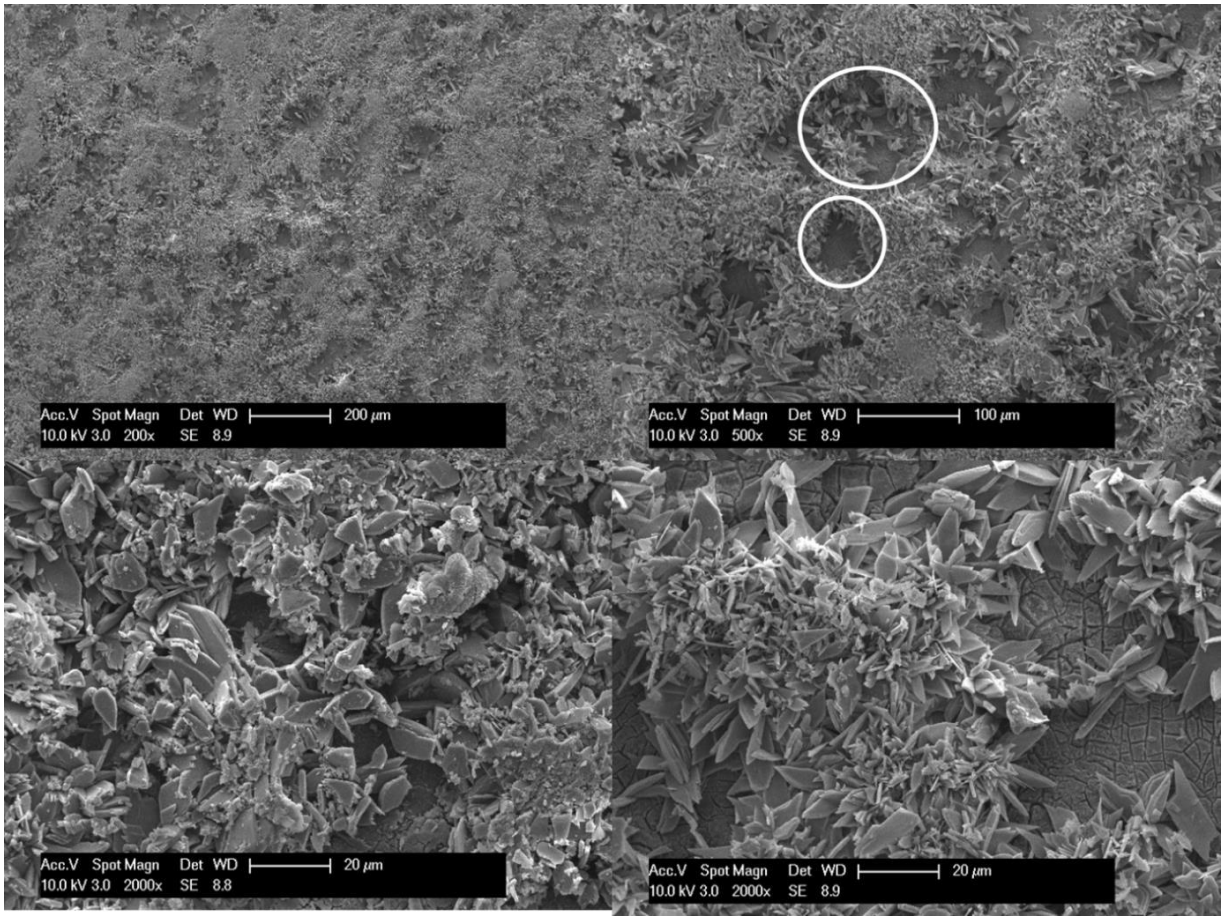

Figure 4.31: SEM images of the CaP coating deposited with electrolyte pH 4.5 showing a large coverage with some voids in the coating (circled white) and some cracking observed within the voids

Figure 4.31 depicts a CaP coating deposited using the same parameters as seen in *Sections 4.1.1.6* and *4.2.1.1*. There was a general repeatability shown for the coatings deposited at these parameters, as there was a large coverage of CaP crystals with some voids observed (circled in white). However, there was some significant cracking observed in the voids unlike previous samples suggesting a reaction of the substrate with the electrolyte solution or cracking of a base layer due to coating dehydration during deposition. Some of the smaller CaP structure was also deposited on the coating as previous samples have shown.

4.3.1.2 Electrolyte pH 6 CaP coating on Mg WE43

Figure 4.32 depicts the as-deposited CaP coating this time using an electrolyte pH of 6. Visually there appears to be a decreased deposition of both the smaller needle-like and larger plate-like

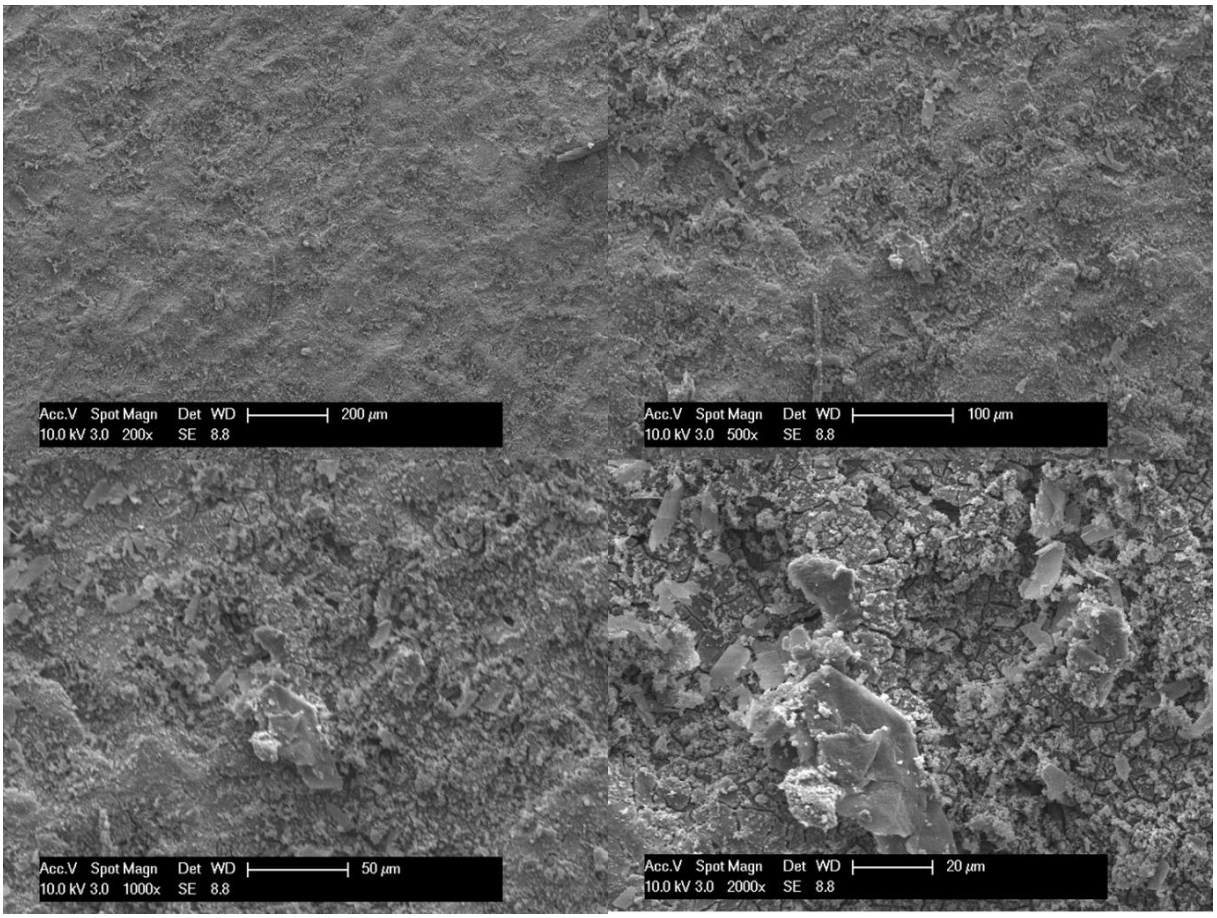

Figure 4.32: SEM images of the CaP coating deposited with electrolyte pH 6 showing the very sparse deposition of CaP and cracking of the underlying Mg WE43 alloy surface

structures at this electrolyte pH, suggesting the variation of pH may inhibit the deposition of CaP as compared to an electrolyte pH of 4.5. There were still some plate-like crystals observed on the surface of the Mg WE43 alloy substrate *ca.* 20µm in length with some larger than this. There were not any small needle-like crystals, characteristic in previous coating types investigated, observed at this electrolyte pH but there was cracking of the underlying substrate/CaP base layer. Small flake-like structures were seen to compose the majority of the deposition on the alloy surface and also rested on top of the larger plate-like crystals.

4.3.1.3 Electrolyte pH 7.5 CaP coating on Mg WE43

Figure 4.33 shows micrograph images of the CaP coating deposited with an electrolyte pH of 7.5. The deposition was visibly sparser than the deposition at pH 4.5 resulting in larger voids,

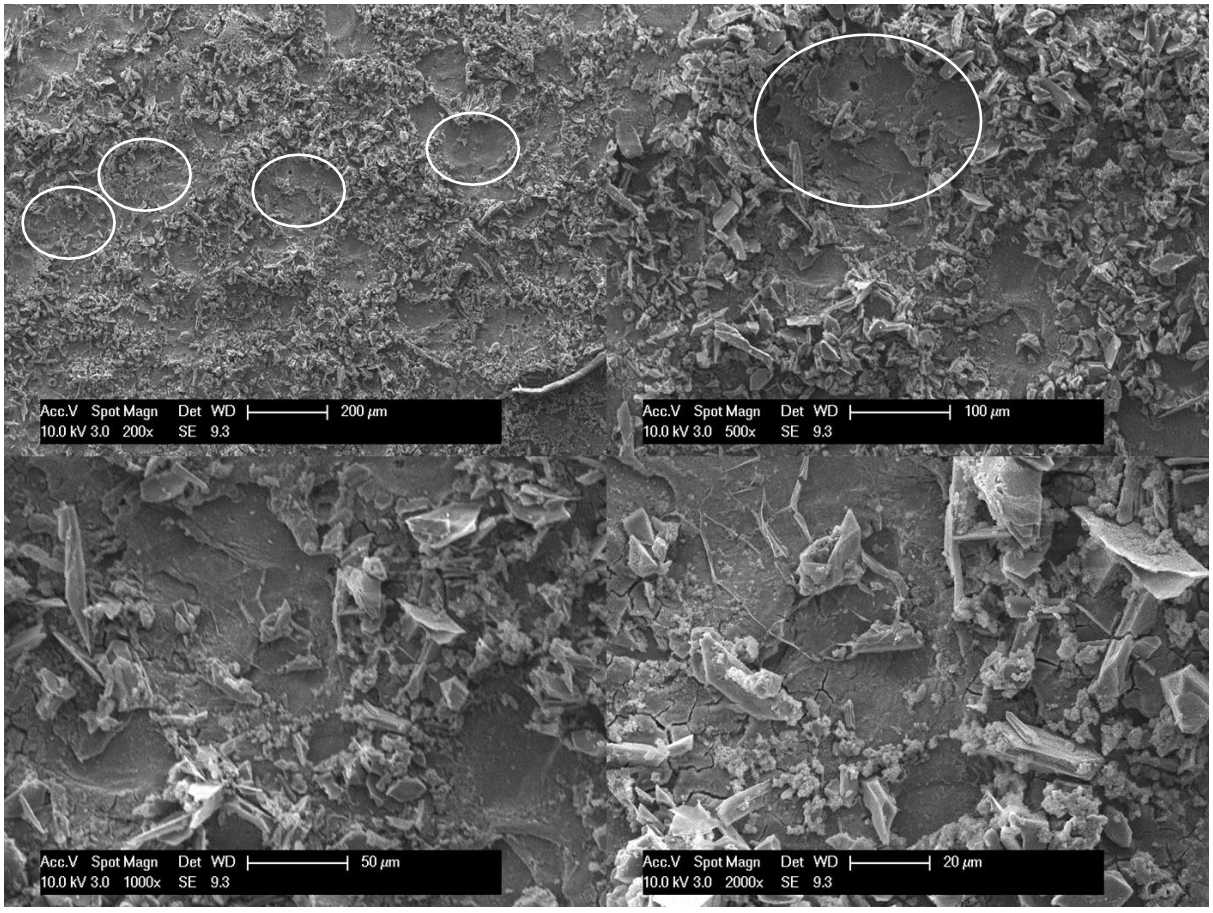

Figure 4.33: SEM images of the CaP coating deposited with electrolyte pH 7.5 with a large proportion of voids in the coating surface (white circles) and cracking of the underlying alloy. Cap crystals deposited are of the large plate-like nature

ca. 150 µm diameter compared to *ca.* 50 µm for pH 4.5 (circled white). Cracks can also be seen in the surface of the substrate. The crystals deposited tend to be large plate-like crystals *ca.* 20 µm in length, which were more isolated and less densely packed than observed for pH 4.5, as opposed to smaller needle-like morphologies, which were generally observed in areas of higher deposition density. There were also CaP deposits observed with a small globular appearance, *ca.* 2 – 4 µm similar to those observed for the previously investigated 1 duty cycle sample.

4.3.1.4 Electrolyte pH 9 CaP coating on Mg WE43

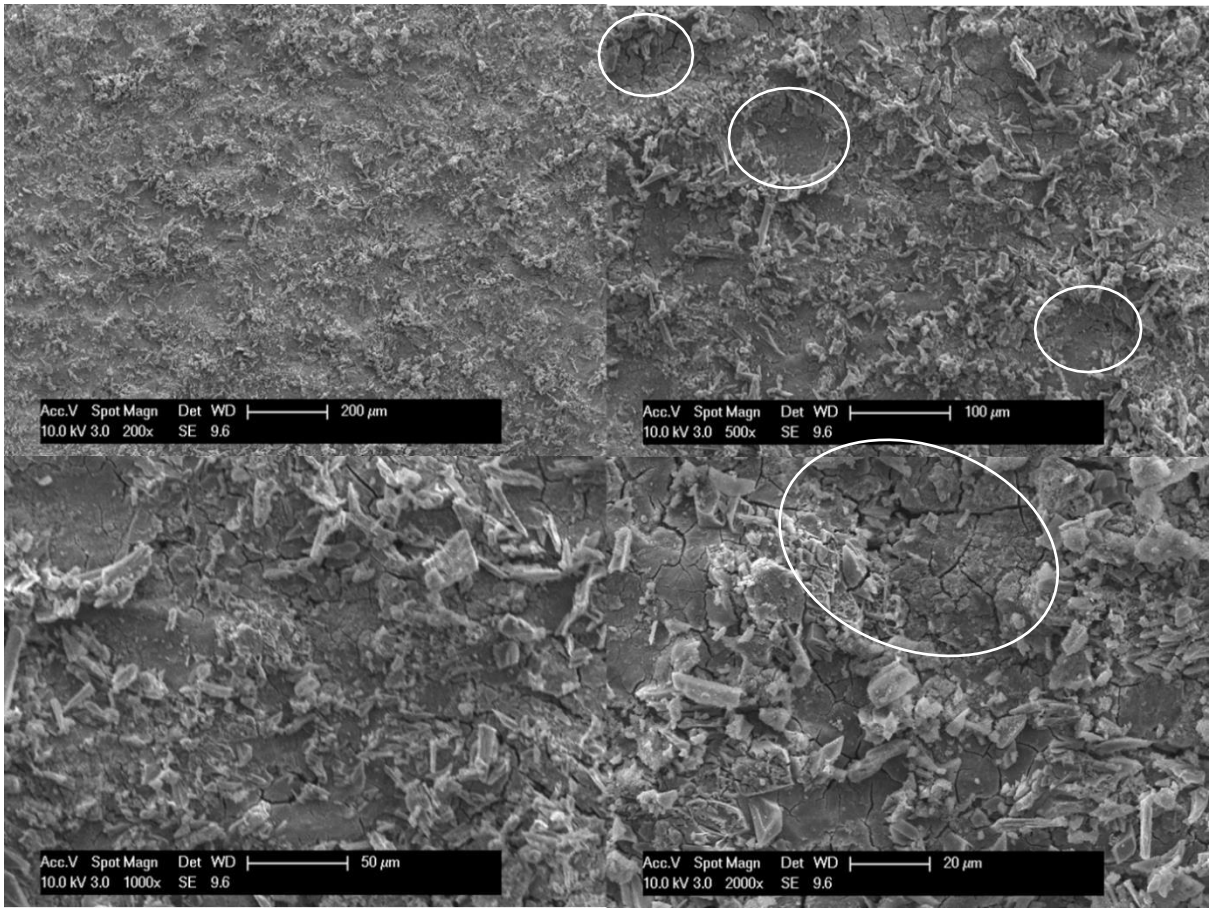

Figure 4.34: SEM images of the CaP coating deposited with electrolyte pH 9 with significant cracking of the Mg WE43 alloy surface observed and a sparse deposition of CaP with large portions of the surface not covered

The appearance of the coating deposited at electrolyte pH 9 was relatively similar to that deposited at pH 7.5. Many voids (*ca.* 100 – 150 µm in diameter (circled white in Figure 4.34)) were present leaving the underlying surface exposed. However, compared to the pH 7.5 sample,

there were an increased number of cracks observed, showing the substrate has reacted with the electrolyte solution and shown signs of early onset corrosion behaviour. The crystal morphology tends to be larger and plate-like in the region of 10 – 20 µm long with other smaller, globular depositions observed as stated above.

4.3.2 XRD of CaP coatings deposited on Mg WE43 disc with varied electrolyte pH

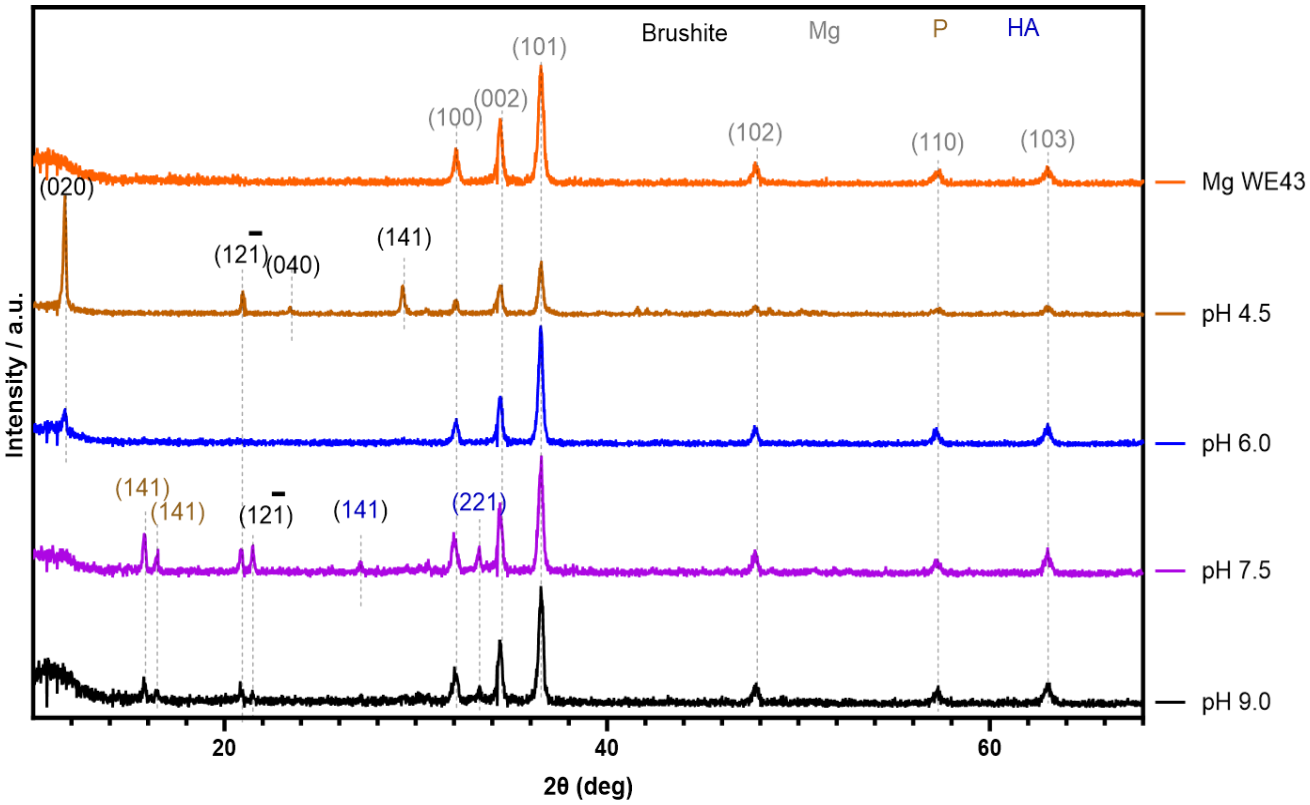

Figure 4.35: XRD patterns of as deposited coatings on Mg WE43 alloy with varied electrolyte pH. Peak deconvolutions are as follows: () – Mg:ICDD 00-004-0770, () – Brushite:ICDD 00-001-0395, () – P:ICDD 00-044-0906, () – HA:JCPS 01-089-4405

Figure 4.35 presents the XRD patterns of the varied electrolyte pH coatings against the uncoated Mg WE43 alloy. In all patterns, there was the presence of Mg peaks (ICDD database 00-004-0770) at 32.1, 34.4 36.5, 47.7, 57.4 and 63.0º although there was a decrease in the relative intensity of these peaks for the pH 4.5 sample type, indicating the pH 4.5 sample had a thicker or more continuous coating. Details as to the phase orientation of Mg peaks are presented previously in *Section 4.1.2*. Peaks at 11.6, 21.0, 23.2 and 29.3º 2θ closely match ICDD database 00-001-0395 for brushite, representing the (020), $(12\bar{1})$, (040) and (141)

planes respectively. There was a significant decrease in the relative intensity of brushite peaks as the pH was increased above pH 4.5, with the peaks at 23.2 and 29.3º becoming negligible in all other coated patterns. The peak at 11.6º was negligible in the pH 7.5 and pH 9 samples but was still seen at pH 6 despite a significant reduction in relative intensity. New peaks were observed for the pH 7.5 and pH 9 samples showing the deposition of P at 15.8 and 16.2º 2θ, which showed preference for the (141) plane in accordance with JCDD database 00-044-0906. The other newly formed peaks at 27.0 and 33.6º were representative of the (002) and (221) orientations of hydroxyapatite according to JCPDS card 01-089-4405. However the peak at 27º was only seen for the pH 7.5 sample.

4.3.3 XPS spectra of varied electrolyte pH coatings

Figure 4.36 presents a survey scan and detailed high resolution C 1s, Ca 2s, Mg 2s, O 1s and P 2p spectra for the deposited coatings varied by electrolyte pH. The majority of sample types contained all of the aforementioned peaks with the exceptions of the Mg WE43 alloy, as expected, not containing Ca 2s or P 2p peaks (Figure 4.36 (C,F)) and the pH 7.5 sample not exhibiting a Ca 2s peak (Figure 4.36 (C)). The relative intensity of Mg KLL peaks was shown to be significantly lower in the pH 4.5 and pH 6 samples as compared to the alloy control and both pH 7.5 and pH 9 samples which was also shown by the elemental analysis in Table 4.9 where a drop was seen in the at.% of Mg for the pH 4.5 and pH 6 samples, from 27.3 to 15.3 and 16.5 at% respectively. For all sample types, common peaks were observed denoting adventitious carbon. All of the other high resolution scans showed a single peak for each element which showed minimal to no shifts in binding energy. The O content of each sample remained relatively similar in the region of 50 – 60 at.%. At higher pH value, the P content was seen to drop from 14.2 at% at pH 4.5 to 5.8 and 8.0 at.% for pH's 7.5 and 9 respectively. Similarly, the at.% of Ca dropped at higher pH which suggests that a lower pH may allow faster deposition of the CaP coatings.

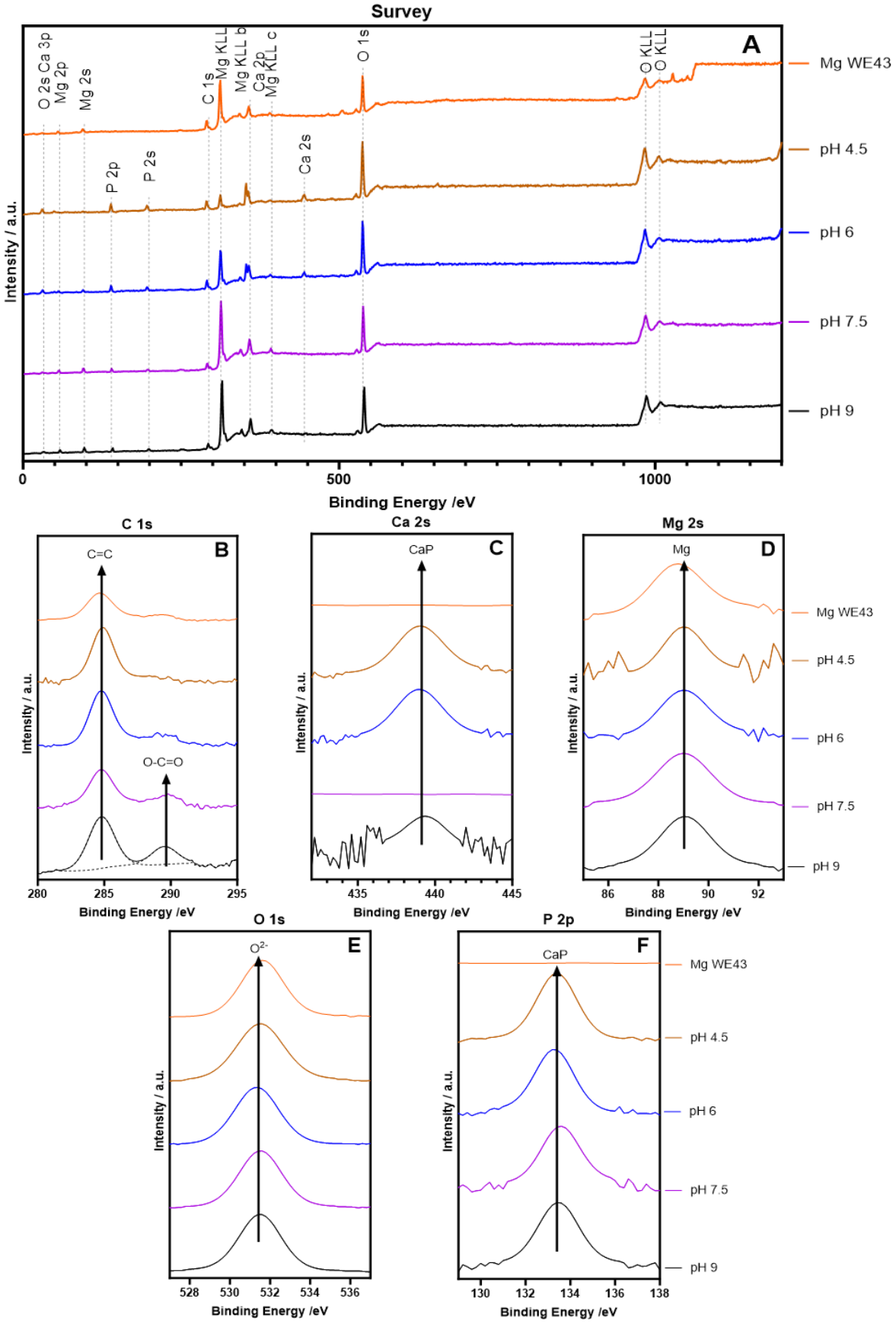

Figure 4.36 Survey and high resolution XPS of varied electrolyte pH CaP coatings: (A) survey scan (B) C 1s high resolution spectra (C) Ca 2s high resolution spectra (D) Mg 2s high resolution spectra (E) O 1s high resolution spectra (F) P 2p high resolution spectra

Table 4.9: Surface element compositional analysis for varied electrolyte pH coatings by XPS

Sample Type	Elemental Composition /at%					Ca:P ratio
	C	Ca	Mg	O	P	
Mg WE43	27.3	-	18.6	52.2	-	-
pH 4.5	15.3	8.1	2.7	59.7	14.2	0.57
pH 6.0	16.5	6.1	7.0	59.5	10.8	0.56
pH 7.5	15.5	-	18.8	59.9	5.8	-
pH 9.0	20.2	1.0	16.6	54.2	8.0	0.13

The depositions at pH 4.5 and 6 are suggested to be MCP due to their Ca:P ratio being ca. 0.5 [361] but at a pH above 6, the deposition is calcium deficient with small proportions of Ca detected.

4.3.4 Profilometry of varied electrolyte pH coatings for thickness measurements

4.3.4.1 Electrolyte pH 4.5 CaP coating on polished Mg WE43 profilometry

The profilometry measurements for the coating deposited using these parameters can be seen above in *Section 4.1.4.2.*

4.3.4.2 Electrolyte pH 6 CaP coating on polished Mg WE43 profilometry

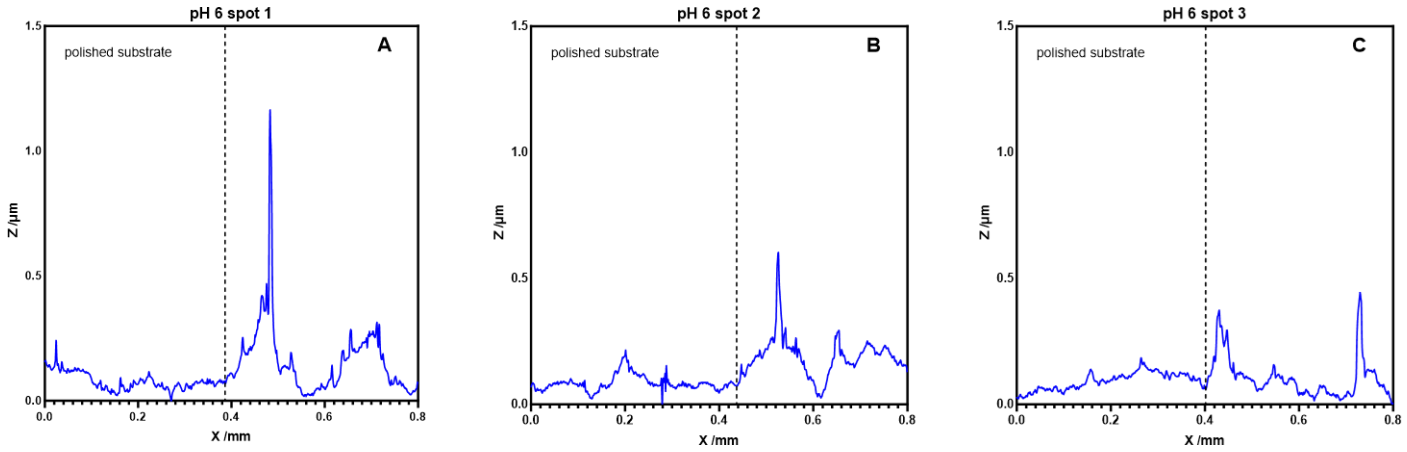

Figure 4.37 Profilometry of 3 points along the coating-substrate border of CaP coating deposited with electrolyte pH 6 taken at A) ca. 2.5mm from left B) ca. 5mm from left C) ca. 7.5mm from left

The 3 profilometry measurements taken for the CaP coating deposited at electrolyte pH 6 (Figure 4.37) show signs of a sparse deposition consistent with images shown above in *Section 4.3.1.2.* The thickness of the coating was difficult to determine as the roughness of the coating was relatively similar to that of the polished Mg WE43 alloy. However, there were some

excursions *ca.* 0.5 – 1 µm in height which were much smaller than those observed for other varied deposition parameters.

4.3.4.3 Electrolyte pH 7.5 CaP coating on polished Mg WE43 profilometry

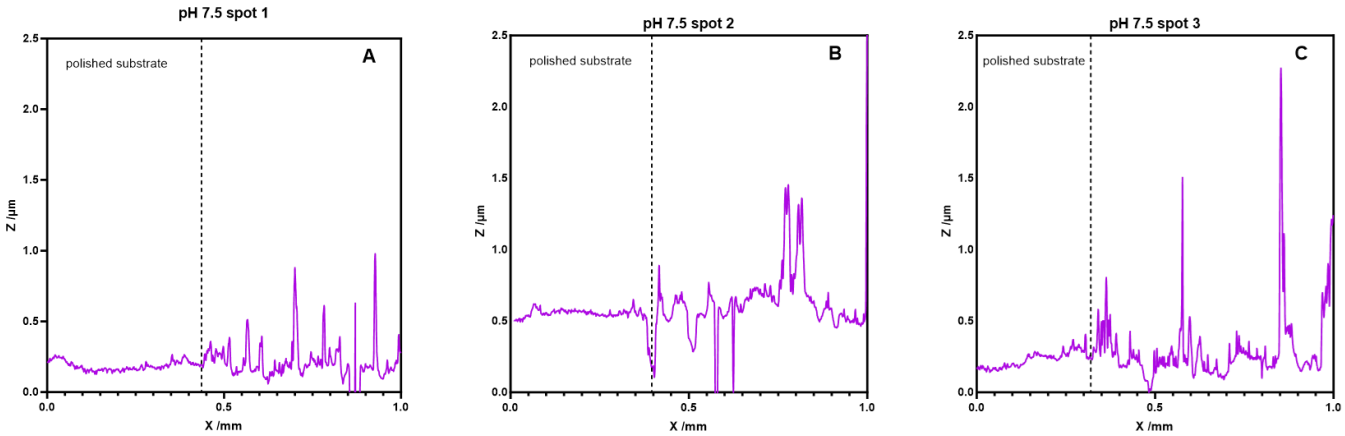

Figure 4.38 Profilometry of 3 points along the coating-substrate border of CaP coating deposited with electrolyte pH 7.5 taken at A) ca. 2.5mm from left B) ca. 5mm from left C) ca. 7.5mm from left

Similarly to the pH 6 deposition sample above, the excursions recorded for the pH 7.5 sample, were smaller than other varied parameters, typically ranging from *ca.* 0.5 – 2 µm in height. However, there were a higher number of distinct excursions suggesting a greater degree of CaP deposition achieved when compared to the electrolyte pH 6 sample.

4.3.4.4 Electrolyte pH 9 CaP coating on polished Mg WE43profilometry

The profilometry readings for the CaP coating deposited at pH 9, pictured in Figure 4.39, showed similar traits to both the pH 6 and 7.5 samples in terms of sparse deposition with excursions in the region of *ca.* 0.5 – 1.5 µm height. A slight curvature of the disc caused some regions of a large negative Z reading compared to the rest of the profile. These were removed for the calculations of coating thickness following.

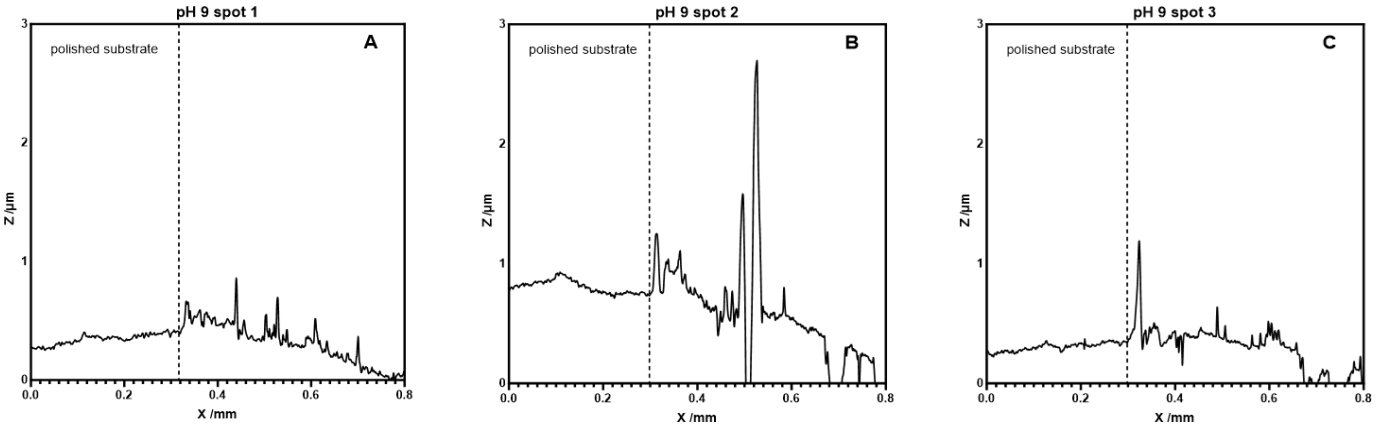

Figure 4.39 Profilometry of 3 points along the coating-substrate border of CaP coating deposited with electrolyte pH 9 taken at A) ca. 2.5mm from left B) ca. 5mm from left C) ca. 7.5mm from left

The average thicknesses of the electrodeposited coating profiles for the varied electrolyte pH depositions, were averaged across the 3 measurements and collated below in Table 4.10.

Table 4.10 Average thickness of CaP coatings with varied Electrolyte pH with SEM (n=3)

Electrolyte pH	Average Profile Thickness /µm
4.5	7.41 ± 0.84
6	0.12 ± 0.02
7.5	0.20 ± 0.03
9	0.11 ± 0.03

4.3.5 Elution Cytocompatibility Testing for CaP coatings on Mg WE43 with varied electrolyte pH

Figure 4.40 depicts a single test representative of the general trends seen across 2 repeat tests as to the cell viability of MG-63 osteoblast-like cells after 24 h immersion in treated media. When the treated media was applied to the cells, there was a significant drop in cell viability of all sample types when compared to the NTM control with a statistical significance of $p < 0.05$ for the pH 6, 7.5 and 9 samples and a significance of $p < 0.01$ between the NTM and both the Mg WE43 alloy and pH 4.5 samples. However, there was no significant difference in the performances of the coated samples when compared against each other. When the treated media

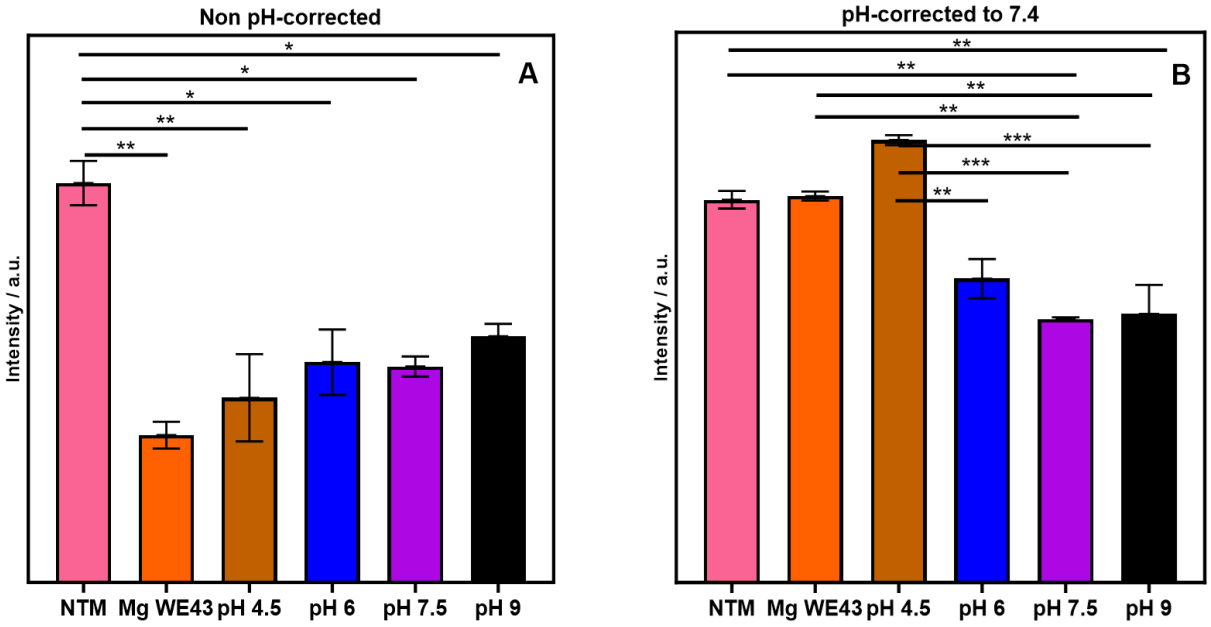

*Figure 4.40: Cell cytocompatibility test of varied electrolyte pH assessed using Neutral Red Assay: (A) treated DMEM media non pH-corrected (B) treated DMEM is pH-corrected to 7.4 to simulate body conditions. All values are mean values ± SEM (n=3). * - p<0.05, ** - p<0.01, *** - p<0.001*

was pH-corrected to pH 7.4, as denoted by Figure 4.40(B), there were improvements in cell viability across all sample types, however, the pH 6, 7.5 and 9 samples only saw slight improvements whereas the Mg WE43 alloy and pH 4.5 saw significant improvements to become statistically comparable to the NTM control suggesting that there were not a significant amount of toxic ions leaching out of the coating or the substrate into the media. Statistical differences were seen between the coated samples when pH-corrected such that there was a p value of $p < 0.01$ between the Mg WE43 alloy and both pH 7.5 and 9 samples, $p < 0.01$ between pH 4.5 and the pH 6 sample and $p < 0.001$ between the pH 4.5 and both pH 7.5 and 9 samples.

4.3.6 Potentiodynamic polarisation testing for varied electrolyte pH coatings

Figure 4.41 shows an example of the Tafel plots generated from PDP testing for each sample type of electrolyte pH variation. Each sample type was repeated in triplicate with the results being collated and listed below with calculated corrosion rate in Table 4.11.

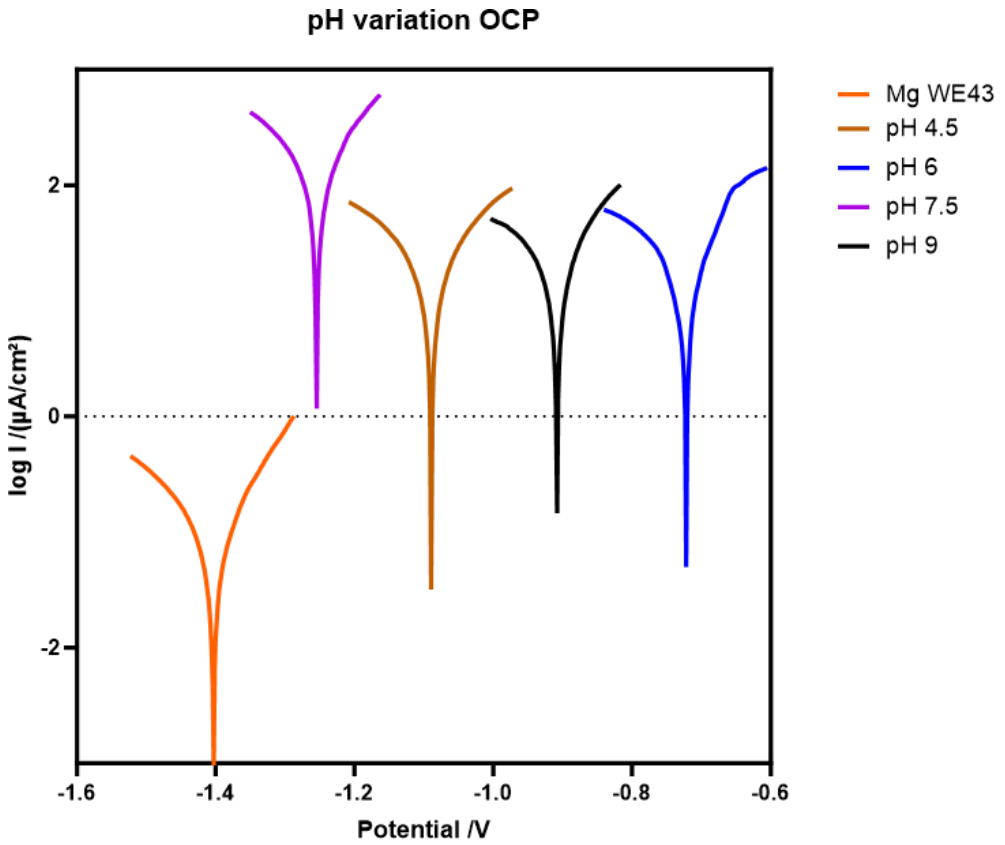

Figure 4.41: Electrochemical Corrosion Test Results for varied electrolyte pH coatings deposited on Mg WE43, in DMEM at 37°C

Table 4.11: Mean Ecorr and Icorr values for each electrolyte pH and the resultant corrosion rate calculated with standard error (n=3)

Sample type	Corrosion Potential E_{corr} / V	Corrosion Current Density i_{corr} / (mA/cm²)	Polarisation Resistance R_p / Ωcm²	Corrosion Rate v_{corr} / (mm/Y)
Mg WE43	-1.42 ± 0.01	0.097 ± 0.01	264.5 ± 39.62	2.22 ± 0.030
pH 4.5	-1.17 ± 0.01	0.025 ± 0.01	782.5 ± 30.20	0.57 ± 0.002
pH 6.0	-0.72 ± 0.29	0.053 ± 0.04	1179.9 ± 457.33	1.22 ± 0.023
pH 7.5	-1.26 ± 0.09	0.256 ± 0.17	201.5 ± 95.59	5.86 ± 0.028
pH 9.0	-0.92 ± 0.23	0.044 ± 0.02	886.4 ± 313.64	1.00 ± 0.017

Similar to the experiments where the samples varied by deposition time, for the variation in electrolyte pH, all of the coated samples have a more positive E_{corr} as compared to the Mg WE43 alloy control suggesting improvements on corrosion resistance by these coatings. There was no trend seen between the coated samples and the most positive E_{corr} was found for the pH

6 sample, with the most negative E_{corr} of the coated samples being recorded for the sample deposited at pH 7.5. The sample at pH 7.5 also showed the largest i_{corr} of 0.256 mA/cm^2 which translated to the highest corrosion rate of 5.86 mm/Y which was almost double the uncoated Mg WE43 alloy which exhibited a corrosion rate of 2.22 mm/Y. Despite the sample deposited at pH 6 having the most positive E_{corr}, it was outperformed in terms of corrosion rate by both samples deposited at pH 4.5 and 9 which showed calculated corrosion rates of 0.57 and 1.00 mm/Y as compared to that of 1.22 mm/Y exhibited by the pH 6 sample.

4.4 Manufacturing and Characterisation of Phosphate-based Glass Targets for RFMS deposition

To date there has been limited research into the sputtering of phosphate-based glasses and in extension research into the manufacturing of targets from these compositions. In recent years, greater interest has been focussed on researching the effects of lowering P content, changing the Q species of the glass and the influence this has on the biocompatibility of the material. To this end, this thesis will investigate three different phosphate-based glasses with varying P content and their compositions are listed below in Table 4.12.

Table 4.12: Selected target formulations for PBG targets in mol%

Target Name	Composition /mol%			
	P_2O_5	CaO	MgO	NaO
P30	30	26	24	20
P35	35	21	24	20
P40	40	16	24	20

The targets were to be designated P30, P35 and P40 based on the P_2O_5 content of the glass. The P_2O_5 content was substituted for the equivalent mol% of CaO for the variation of PBG formulations. The concentrations of MgO and NaO remained unchanged. The desired composition of the targets was converted into at.% of each constituent element for ease of

comparing the EDX results of the actual target composition with the values being listed in Table 4.13 below.

Table 4.13: Desired elemental composition of the P30, P35 and P40 targets converted into at%

Target	Elemental Composition / at.%					P:O ratio
	Ca	Mg	Na	O	P	
P30	7.03	6.49	10.81	59.46	16.22	0.27
P35	5.32	6.08	10.13	60.76	17.72	0.29
P40	3.81	5.71	9.52	61.90	19.05	0.31

4.4.1 Manufacturing development of PBG targets for RFMS deposition

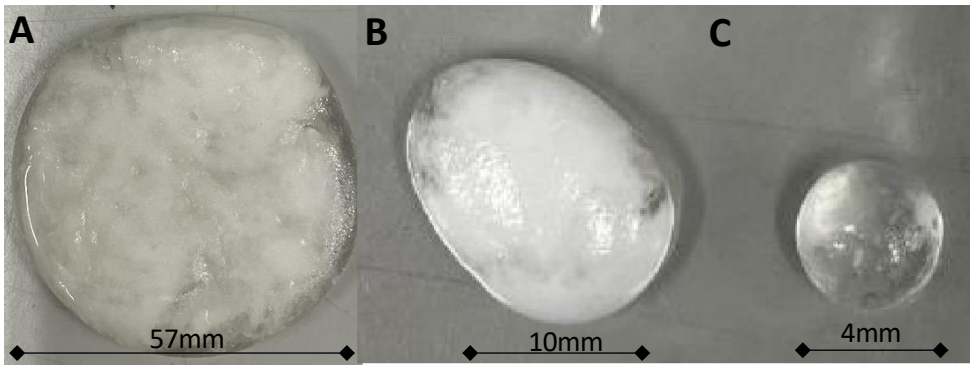

Figure 4.42: Examples of P30 PBG samples used for characterisation, development and deposition (A) RFMS target size (B) small pebbles cast for analysis

During the melt quenching process of target formation, there were challenges with the cooling of the glass being too slow, resulting in surface crystallisation of the glass castings for the P30 and P35 compositions. The method of splat quenching, described in *Section 3.2.4*, was utilised to address this issue. However, this does not counteract the stresses in the glass which cause the glass to shatter upon cooling. To get the PBG into a usable target form, the glass processing included several steps experimentally determined including remelting, recasting and annealing in a target mould which largely negated the effects of splat quenching, giving targets similar to that shown in Figure 4.42(A).

This surface crystallisation did not occur upon every recasting and so a usable target was able to be produced by repeating the production process with a successful target achievement rate of 1 in 3 attempts.

A secondary manufacturing issue was that the effervescence of the melting powders caused the contents of the melting crucible to spill over onto the alumina blocks being used to stabilise the crucible. This required multiple smaller batches to be melted and splat quenched, before combining the shards and continuing the recasting and annealing portion of target production. This resulted in the targets shown in Figure 4.43 being produced. The successful targets produced exhibited a consistency in thickness of ca. 6mm across the majority of the target surface for all target types. The slight variations in thickness were observed at the "missing edges" of the target at seen in Figure 4.43(A,B) with the target thickness reaching 6mm ca. 3mm from the edge.

It was observed after the RFMS deposition process that all 3 targets exhibited some cracking on the target surface. However, the targets did not shatter as the cracks did not propogate through the full body of the targets. This would allow reuse of the targets for multiple deposition runs until complete fracture.

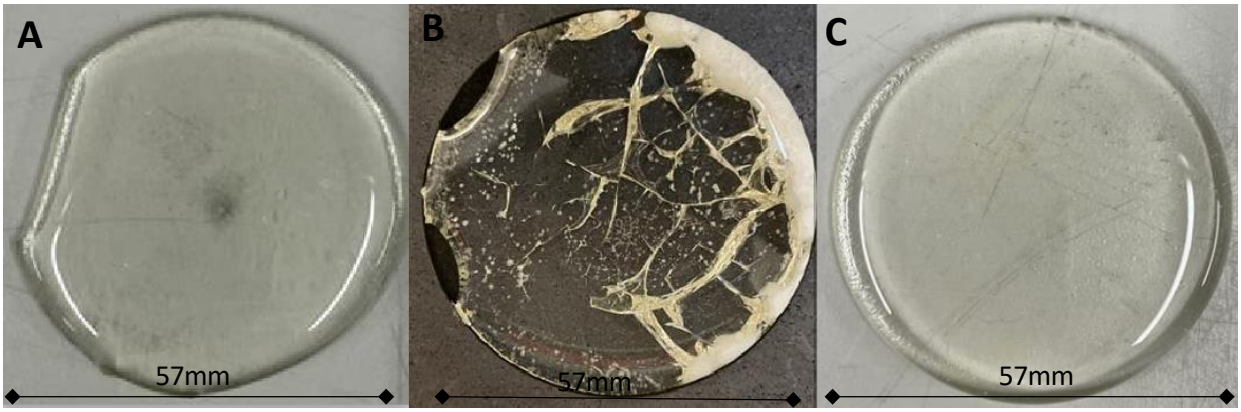

Figure 4.43: PBG targets used for RFMS deposition (A) P30 target (B) P35 target showing some surface crystallisation at the target edge (C) P40 target

4.4.2 SEM/EDX of bulk PBG pebbles

EDX data was collected for the samples of bulk PBG from the surface that would be used for sputtering, in order to assess the composition of the bulk targets for comparison against deposited coatings. The maximum deviation in at.% difference was revealed to be *ca.* 2.74 at.% for the P difference of the P35 sample. The largest variations were seen for the O and P contents but the majority of elemental compositions <1 at.% showing a good level of agreeability for the samples to the desired target formulations. The P:O ratios were all ca. 0.05 away from the desired composition, with the P35 and P40 samples exhibiting a lower ratio than expected and P30 showing a larger ratio than expected.

Table 4.14: Compositions of bulk PBG samples with varied P content as measured by EDX and difference from desired target formulation

Target	Elemental Composition / at.%					P:O ratio
	Ca	Mg	Na	O	P	
P30	5.64 ± 1.39	7.55 ± 1.06	10.03 ± 0.78	58.67 ± 0.79	18.10 ± 1.78	0.31
P35	4.48 ± 0.84	7.21 ± 1.13	10.11 ± 0.02	63.21 ± 2.45	14.98 ± 2.74	0.24
P40	2.97 ± 0.84	5.95 ± 0.24	10.52 ± 1.00	64.09 ± 2.19	16.47 ± 2.58	0.26

Table 4.15 Compositions of bulk PBG samples with varied P content as measured by EDX and difference from desired target formulation in mol.%

Target	Elemental Composition / mol.%			
	P_2O_5	CaO	MgO	NaO
P30	33.1 ± 3.1	20.7 ± 5.3	28.0 ± 4.0	18.3 ± 1.7
P35	30.8 ± 4.2	18.5 ± 2.5	30.0 ± 6.0	20.8 ± 0.8
P40	36.6 ± 3.4	13.2 ± 2.8	26.8 ± 2.8	23.4 ± 3.4

It can be noted that the P_2O_5 mol.% of P35 sample was closer to 30 than the P30 sample. This was attributed to the surface crystallization effects during annealing, changing composition over the scan area.

4.4.2.1 P30 bulk PBG

Figure 4.44 shows the topology of the P30 pebble cast for bulk material analysis purposes. The surface showed signs of surface crystallisation where there was deviation from the overall smooth texture. The area of crystallisation was similar to the white target edge in Figure

4.43(B). The P30 target shown in Figure 4.43(A) was smooth in texture, and clear which was characteristic of other pebble samples shown to be amorphous by XRD.

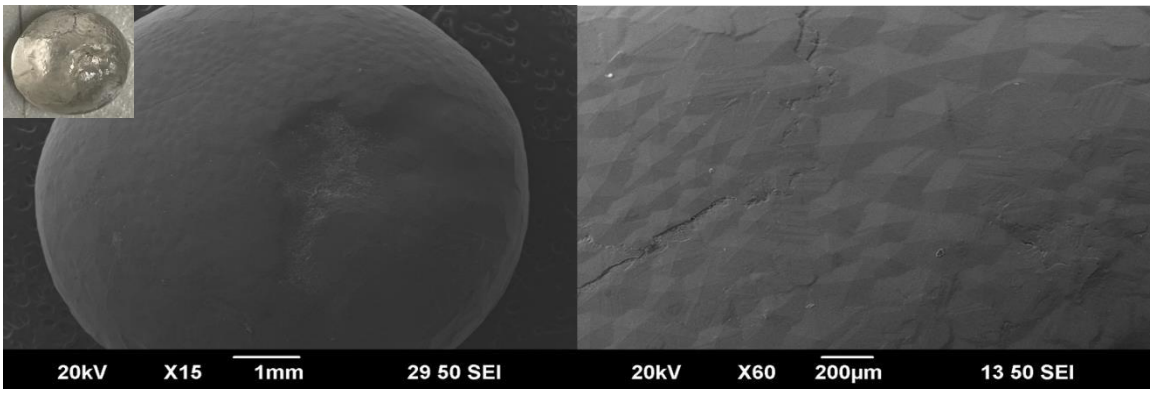

Figure 4.44: Micrograph images of the pebble cast for P30 PBG analysis showing signs of potential surface crystallisation

4.4.2.2 P35 bulk PBG

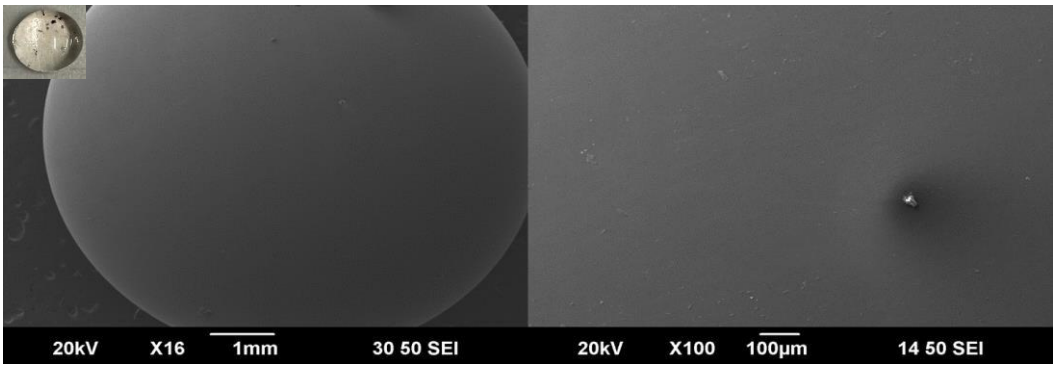

Figure 4.45: Micrograph images of the pebble cast for P35 PBG analysis

Figure 4.45 shows the smooth morphology of the P35 pebble for analysis, typical of PBG glass structures, confirmed to be amorphous by XRD Figure 4.47. There was a slight imperfection seen on the right of Figure 4.45 which suggests there may be a small degree of contamination from the melt quench and casting process.

4.4.2.3 P40 bulk PBG

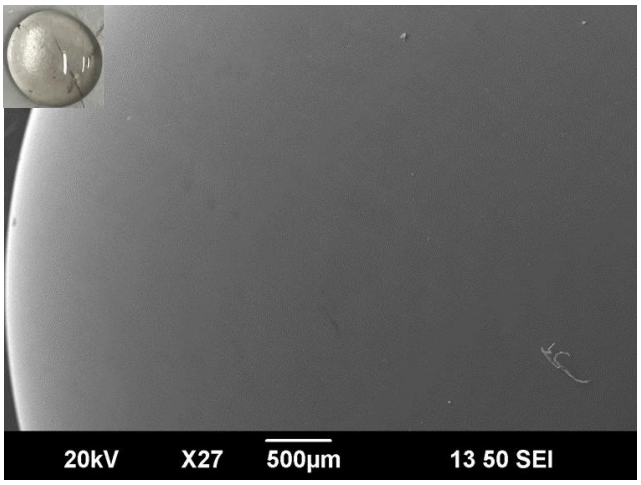

Figure 4.46: Micrograph image of the pebble cast for P40 PBG analysis

Figure 4.46 shows the smooth topology of the P40 pebble suggesting an amorphous structure of the glass. Other shapes visible in the micrograph located on top of the pebble, were discounted as a dust contamination.

4.4.3 XRD patterns of bulk PBG pebbles

Figure 4.47 shows the XRD patterns of the small PBG "pebbles" used for characterisation purposes. The P35 and P40 patterns show the glass to be amorphous materials. The P30 glass showed signs of surface crystallisation mentioned in *Section 4.4.1* with peaks matched to brushite, Mg, Na, P and $Na_2Ca(PO_4)$. However, through visual comparison with P30 target Figure 4.43(A), there was no apparent crystallisation of the P30 target and would likely give a similar pattern to those of P35 and P40 samples. The P35 target (Figure 4.43(B)) showed signs of crystallisation on the outer edge but as the sputtering process utilises material from around the centre of the target [231], the crystallisation was accepted and the target used for depositions.

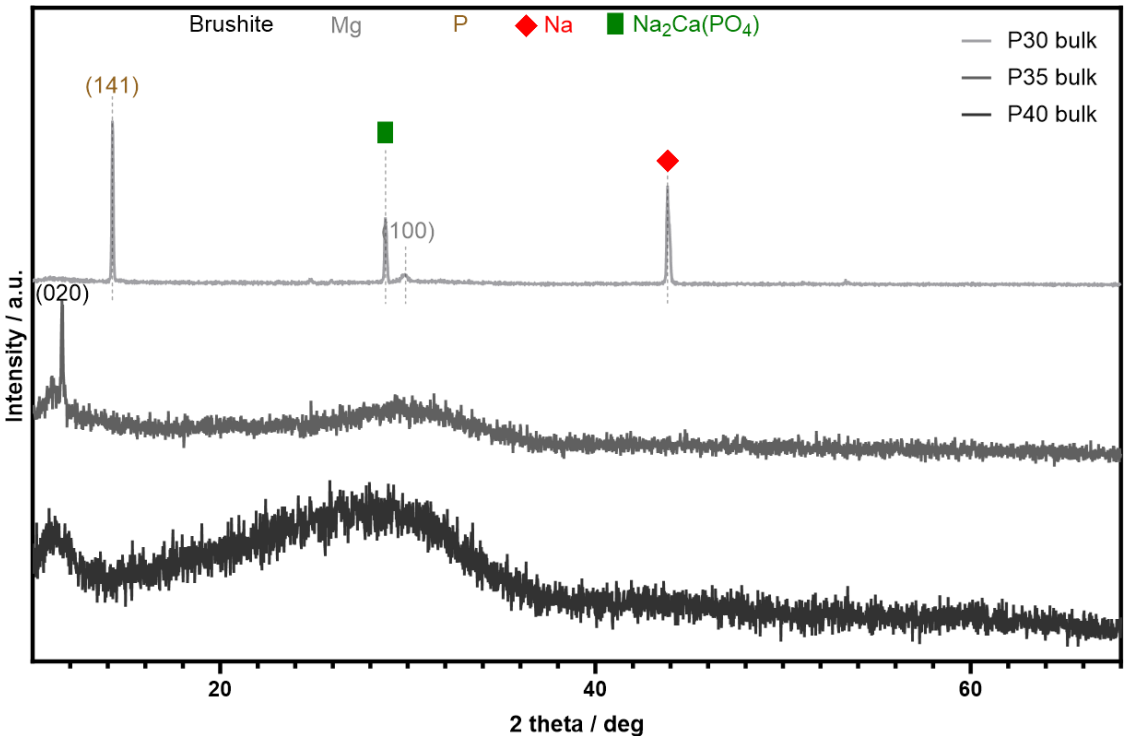

Figure 4.47: XRD patterns of the pebbles used for analysis of bulk PBG material. Peak deconvolutions are as follows: () – Mg:ICDD 00-004-0770, () – Brushite:ICDD 00-001-0395, () – P:ICDD 00-044-0906, ◊ - Na , □ – $Na_2Ca(PO_4)$

4.4.4 XPS spectra of bulk PBG pebbles

Figure 4.48 presents a survey scan and detailed high-resolution C 1s, Ca 2s, Mg 2s, Na 1s, O 1s and P 2p spectra for the bulk glass samples. Each glass formulation exhibited all of these peaks with little variation. The Mg 2s peaks were attributed to the same bonding despite a small variation in binding energy, within error tolerance for the Mg 2s peak. This error was attributed to the stresses caused in the sample by the surface crystallisation previously shown in *Sections 4.4.2.1* and *4.4.3* as compared to both other samples which were shown to be amorphous. All three samples exhibited a C 1s peak at 284.8 eV which was attributed to C=C bonding, indicative of adventitious carbon. However, the largest compositional variation of the samples, as detailed in Table 4.16, was exhibited by the C 1s peak, which was likely due to the use of a graphite mould during the casting and annealing processes.

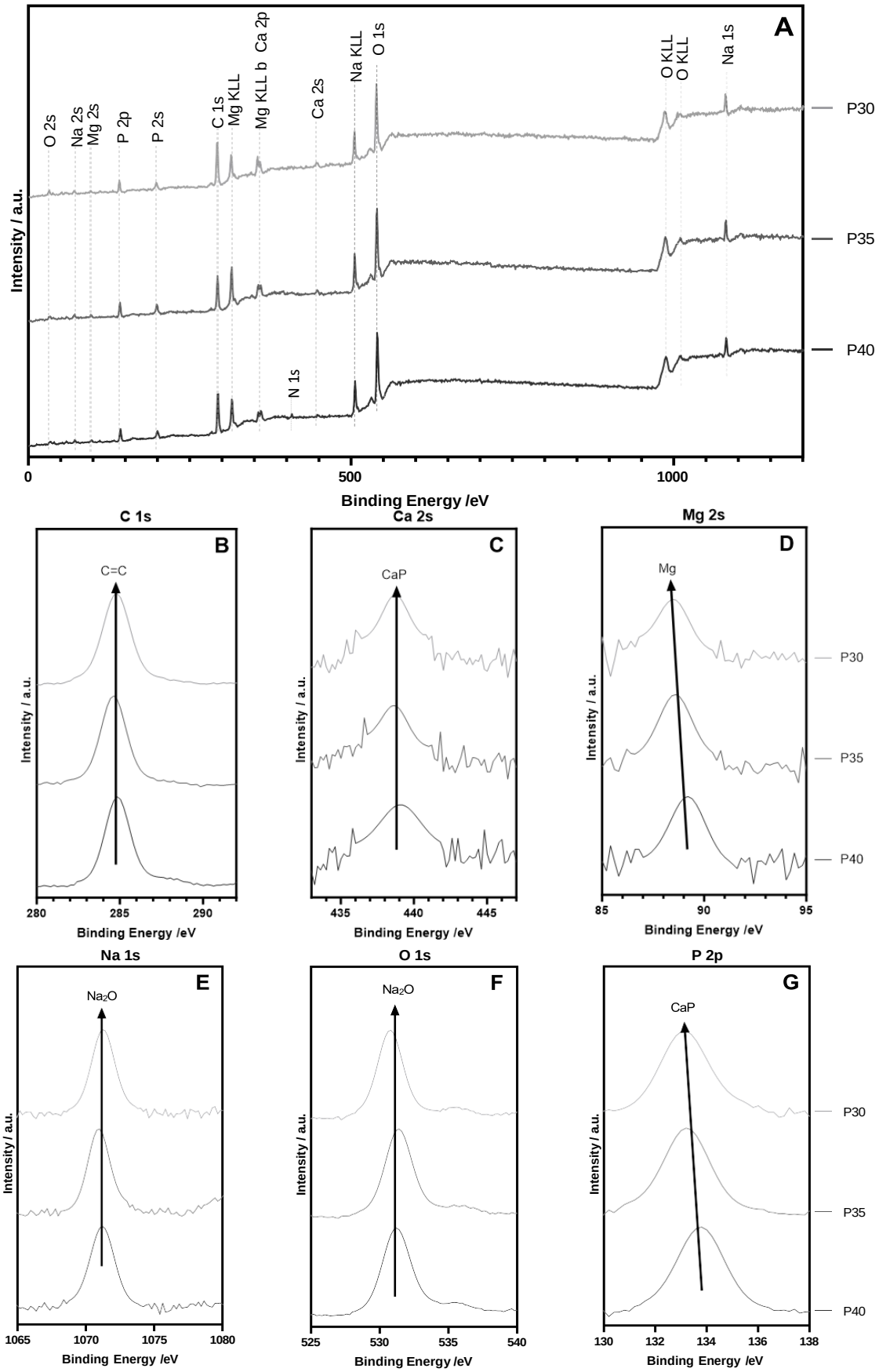

Figure 4.48: XPS spectra of the PBG only coatings deposited onto Mg WE43 discs (A) survey scan (B) C 1s high resolution spectra (C) Ca 2s high resolution spectra (D) Mg 2s high resolution spectra (E) Na 1s high resolution spectra (F) O 1s high resolution spectra (G) P 2p high resolution spectra

All of the glass samples exhibited a smaller P content as compared to the EDX analysis, suggesting the surface layer contains a lower P content due to P being the network former of the PBG. Similarly to EDX analysis, the P35 sample exhibited the highest P content, as shown by the P:O ratio, which may be caused by the variation of Q species exhibited by the glasses.

Table 4.16: Surface element compositional analysis for bulk glass samples by XPS

Sample Type	Elemental Composition /at.%						P:O ratio
	C	Ca	Mg	Na	O	P	
P30	47.7	1.6	2.4	5.9	31.7	10.8	0.34
P35	34.5	1.3	4.2	6.8	36.7	16.6	0.45
P40	41.8	1.2	4.0	5.8	34.8	12.3	0.35

4.5 Phosphate-based Glass coatings deposited onto Mg WE43 discs by RFMS

4.5.1 SEM/EDX of PBG coatings on Mg WE43 discs

Table 4.17 shows the EDX analysis for the PBG only coatings. The large Mg content of the PBG coatings suggest a relatively low sputtering rate of the glass. Furthermore, preferential sputtering of certain elements may also be occurring. A trend of P35 samples exhibit the highest P content in agreement with *Section 4.4.4* above. The Mg content maintains a high relative at.% ranging from 33 – 48 at.% across the varied PBG formulations, suggesting the coating thickness was quite thin (< 2 μm) as the underlying Mg WE43 alloy contributed to most of the elements peaks.

Table 4.17: Compositions of as-deposited PBG coatings by EDX calculated with SEM (n=3)

Target	Elemental Composition / at.%					P:O ratio
	Ca	Mg	Na	O	P	
P30 coat	0.87 ± 0.03	48.13 ± 3.64	2.73 ± 0.30	45.02 ± 3.16	2.40 ± 0.04	0.05
P35 coat	1.05 ± 0.03	42.03 ± 1.05	2.98 ± 0.14	49.48 ± 0.87	4.14 ± 0.25	0.08
P40 coat	0.55 ± 0.07	33.05 ± 1.11	1.87 ± 0.26	61.86 ± 0.83	2.58 ± 0.19	0.04

4.5.1.1 P30 PBG coating deposited on Mg WE43 by RFMS

Figure 4.49 shows the P30 sputtered deposition onto Mg WE43 alloy. There was a large Mg content from EDX suggesting the layer of PBG may not be very thick as the high Mg content was contributed by the underlying Mg WE43 alloy, with only a small contribution from the

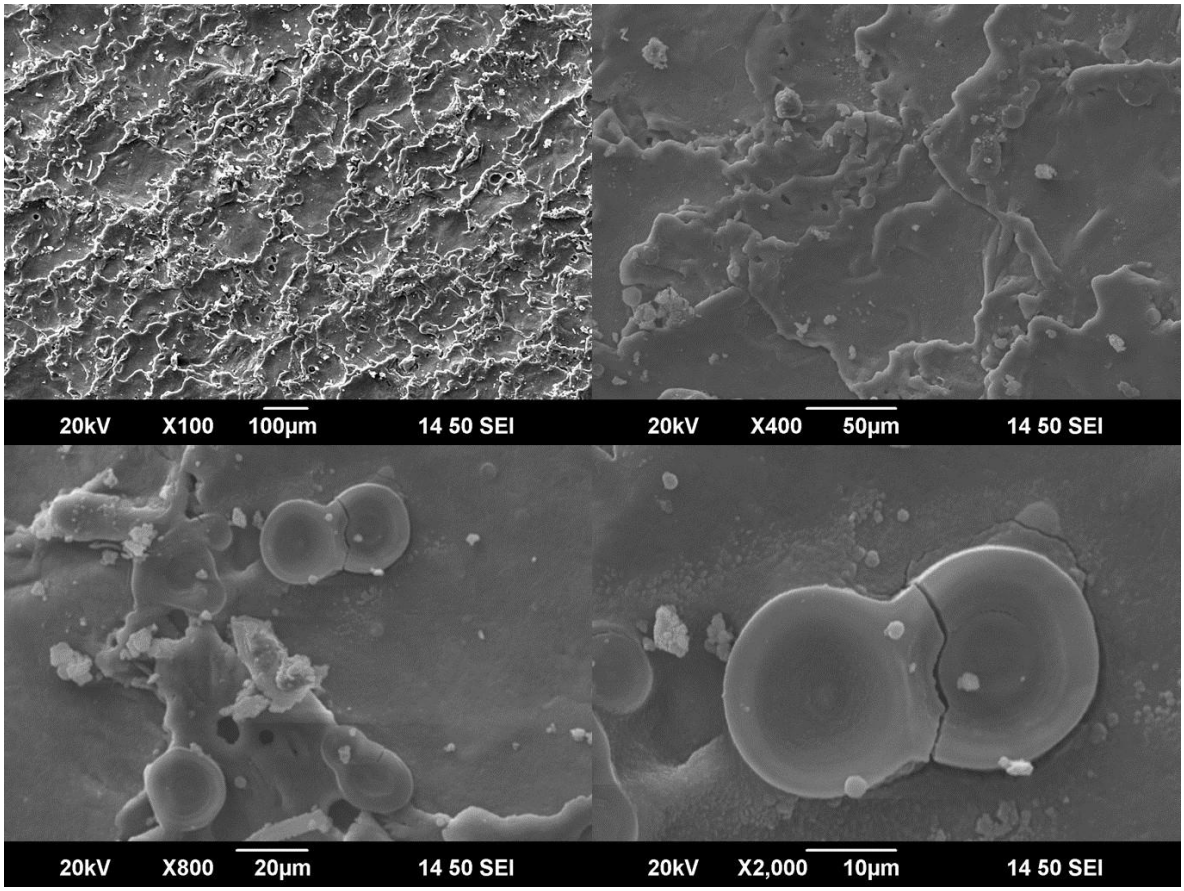

Figure 4.49: SEM images of Mg WE43 alloy coated with RFMS P30 PBG showing some globular deposits of PBG and relatively large concave disc structures deposited which may be large and brittle PBG deposits with observed cracks

sputtered glass. There were a variety of concave disc-like shapes deposited across the surface of the alloy which were only observed for the P30 and P35 coating types. Cracks were visible in the structure of some of these disc-like shapes, as pictured in Figure 4.49, suggesting that the deposited structure may be brittle in nature as would be expected of a glass layer, or that there was a non-uniform thermal expansion across the deposit. Each individual disc was *ca.* 20 µm in diameter however, there were also smaller globules which appear to be amorphous deposits *ca.* 1µm in length across the surface of both the disc shapes and the rest of the underlying alloy substrate.

4.5.1.2 P35 PBG coating deposited on Mg WE43 by RFMS

Figure 4.50 shows the surface of the Mg WE43 alloy after sputtering deposition of P35 PBG.

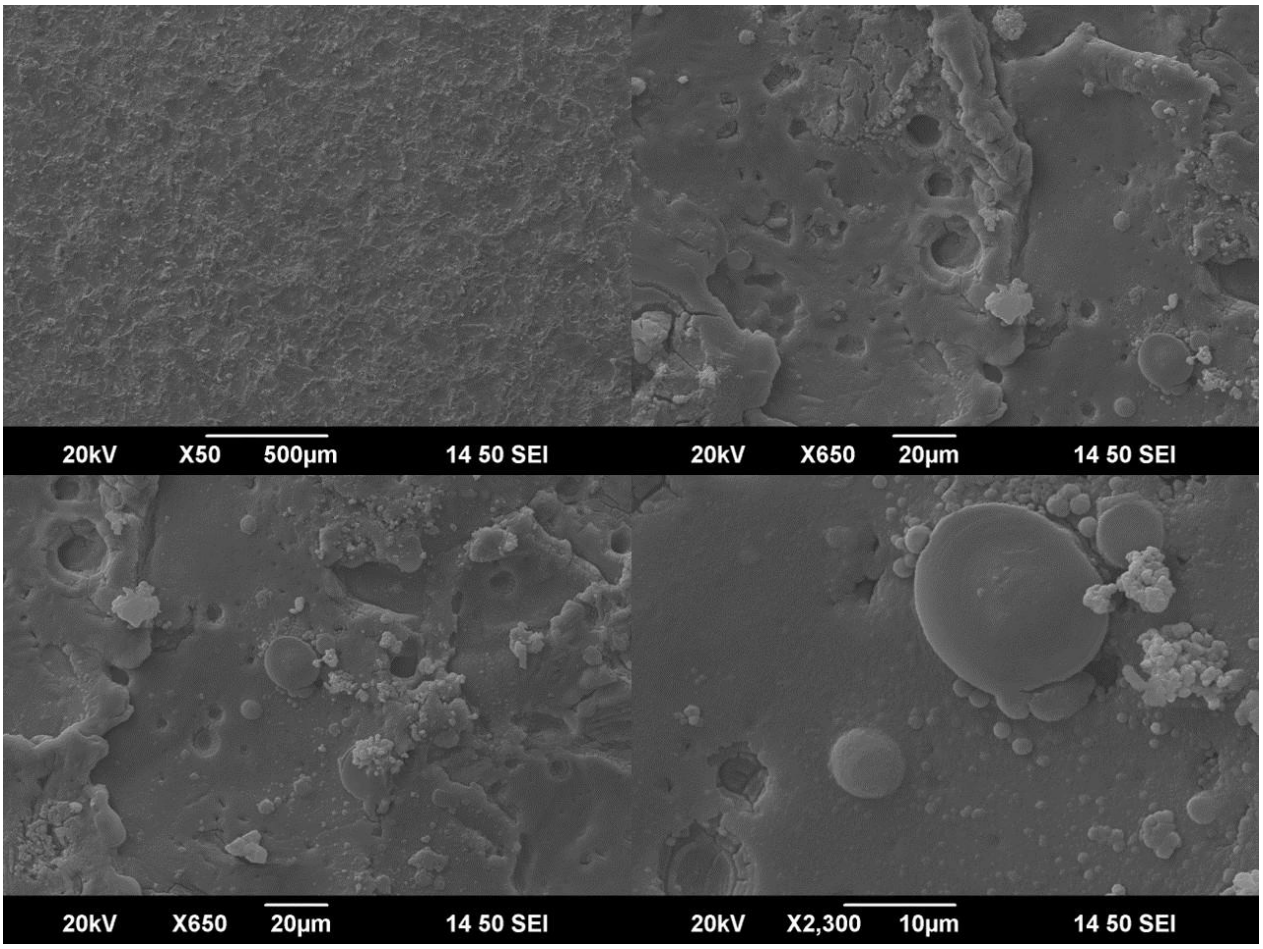

Figure 4.50: SEM images of Mg WE43 alloy coated with RFMS P35 PBG showing globular deposits of PBG, sites of potential cratering effects from the RFMS method and an increased amount of deposition features as compared to the P40 coat

Similarly to the P30 deposition, Figure 4.50 shows that there were disc-like shapes across the surface of the substrate *ca.* 20µm in diameter with smaller globules also widespread *ca.* 1µm in diameter. These deposits appear to be integrated with the surface suggesting a deposited PBG coating with areas of larger deposits within that coating. Conversely to that seen for the P30 deposition, there was a cratering effect observed at many areas across the alloy surface with cracking within the crater. These craters vary in size from *ca.* 5 to 20µm in diameter.

4.5.1.3 P40 PBG coating deposited on Mg WE43 by RFMS

Figure 4.51 shows the surface morphology of the as-deposited P40 PBG coating. Across the surface of the substrate, there were deposits varying in size from *ca.* 1 to 20 µm in diameter, similar to those deposits observed for the other PBG coatings integrating into the top surface. There were also craters observed however, to a lesser degree than that for the P35 PBG coating and there was not the same level of cracking within these craters. In a few areas there were large agglomerations formed which appeared to be a combination of the PBG depositions and a material similar to the alloy surface. There were no disc-like shapes similar to those pictured in Figure 4.49 and Figure 4.50 observed.

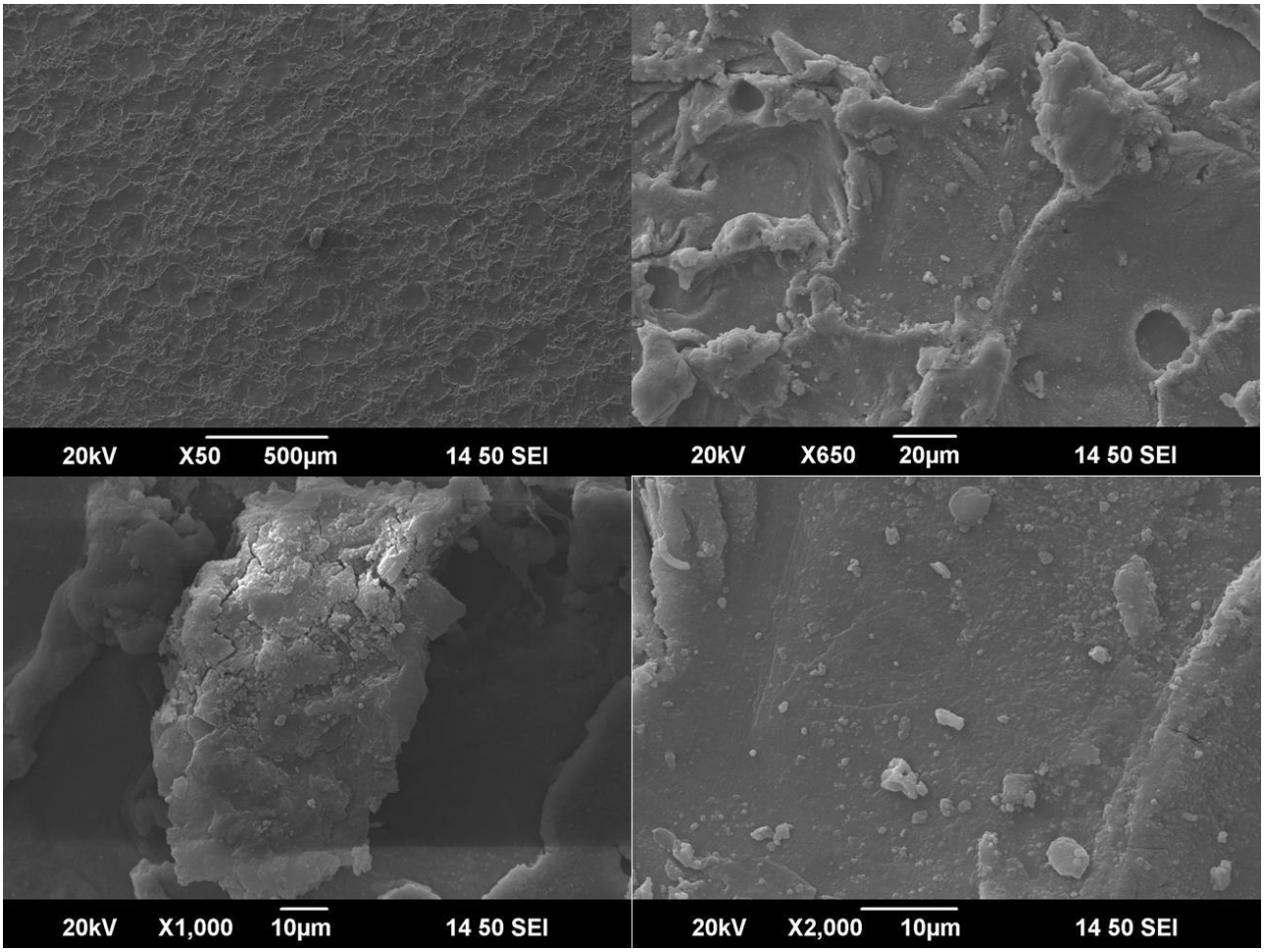

Figure 4.51: SEM images of Mg WE43 alloy coated with RFMS P40 PBG showing some globular deposits of PBG and a similar surface morphology to the uncoated disc due to the thin nature of the PBG coat

4.5.2 XRD patterns of PBG only and bi-layered coatings

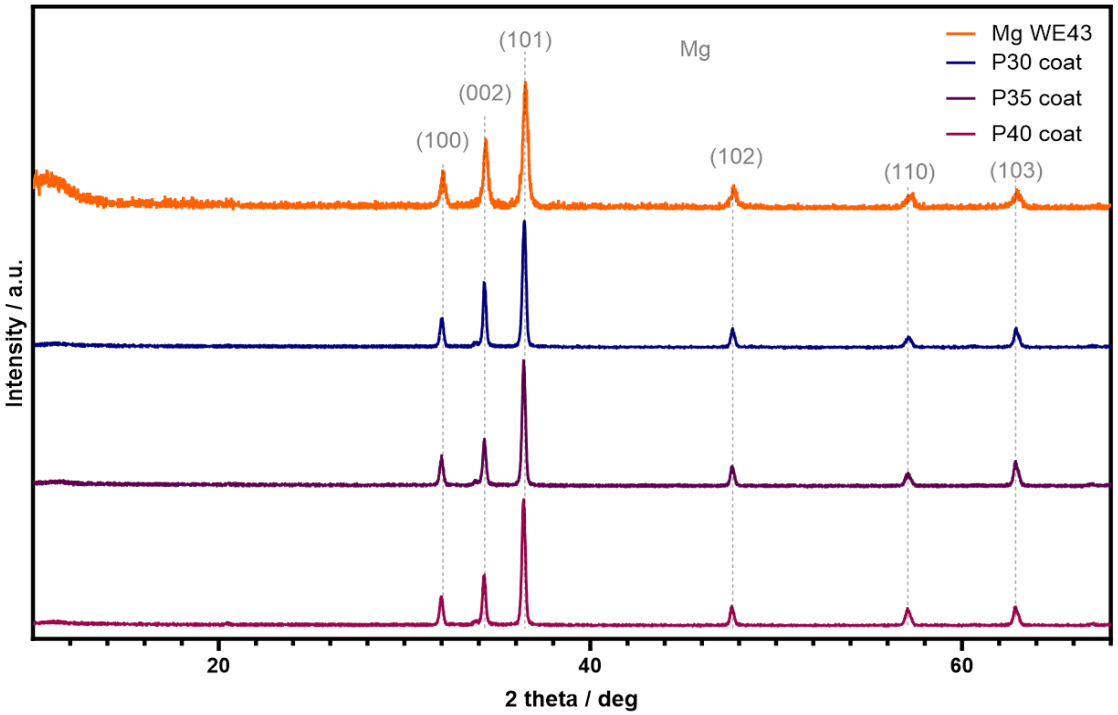

Figure 4.52: XRD patterns of as-deposited PBG coatings on Mg WE43 alloy substrate with varied PBG composition. Peak deconvolutions are as follows: () – Mg:ICDD 00-004-0770

Figure 4.52 depicts the XRD patterns of the PBG sputtered coatings deposited on the Mg WE43 alloy substrate surface. All three depositions exhibited the same six peaks at 32.1, 34.4 36.5, 47.7, 57.4 and 63.0º 2θ which match the Mg peaks seen for the Mg WE43 alloy (ICDD database 00-004-0770). They maintain a similar relative intensity across the target formulations with a small noticeable difference for the peak at 57.4º, which shows an increase in relative intensity for the P40 coating when compared to the P30 coating. Peak orientations can be found in *Section 4.1.2*. The lack of peaks representing other elements follows the trend with EDX analysis for these coatings where there was no other component contributing > 5 at.% to the surface coating with the majority of those elements contributing *ca.* 1 – 2 at.% to the coating compositions.

4.5.3 XPS spectra of PBG only coatings

Figure 4.53 presents a survey scan and detailed high resolution C 1s, Mg 2s, Na 1s, O 1s and P 2p spectra for the PBG coatings. Each glass formulation exhibited all of these peaks with little variation of binding energies with the exception of the P40 coating which exhibited two Mg 2s peaks representing Mg and MgO. The P 2p peaks at a binding energy of 134.6 eV were attributed to $(PO_3)^-$ bonding and were exhibited by each PBG sample type. As the Na and P peaks were contributed by the PBG coatings formulation, there was no peak observed for the Mg WE43 alloy at these binding energies. The slight distortion of the O 1s peak for the P40 coating suggests multiple bonds contributing to the shape which would follow with the P40 coating exhibiting MgO and $(PO_3)^-$ bonding in the sample. In the survey spectra, there was a peak observed for Cu which occurred from slight backsputtering of the Cu backing plate during the RFMS deposition. EDX confirmed this to be < 1 at.%. The elemental analysis by XPS for the PBG coatings are listed in Table 4.18. Due to the scanning penetration of XPS being lower than that of EDX (*ca.* 10 nm v 2 μm), the disparity between Mg content can be explained due to the thin film PBG coating applied meaning the majority of contributions of coating elements will be found in this top 10 – 15 nm layer scanned. All three coating types exhibited a lower P:O ratio than the respective glass targets, likely due to preferential sputtering and the lowest P content target of P30 exhibited the highest P content in the coating with a P:O ratio of 0.23.

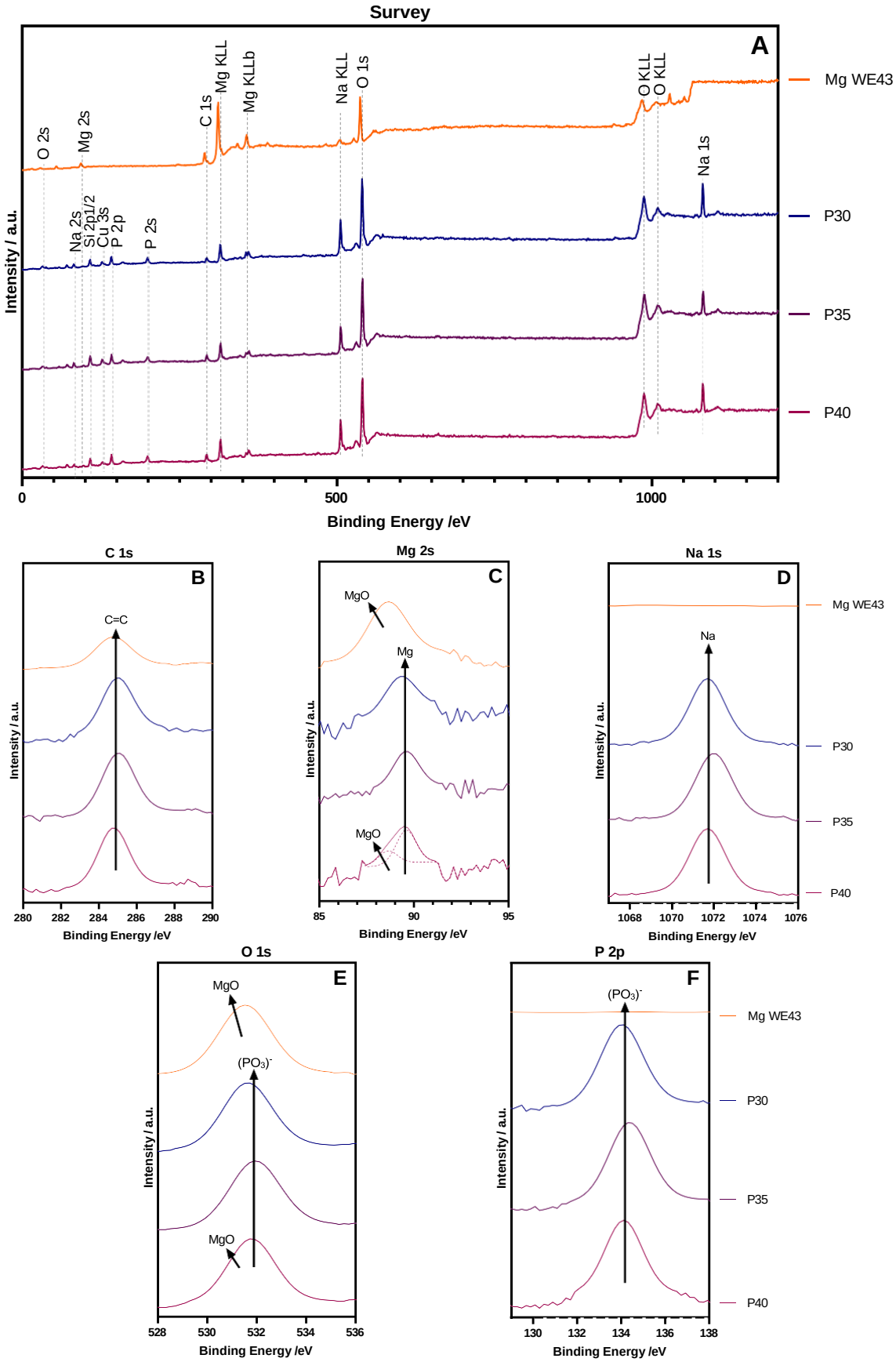

Figure 4.53: XPS spectra of the PBG only coatings deposited on Mg WE43 discs (A) survey scan (B) C 1s high resolution spectra (C) Mg 2s high resolution spectra (D) Na 1s high resolution spectra (E) O 1s high resolution spectra (F) P 2p high resolution spectra

Table 4.18: Surface element compositional analysis for varied PBG coating formulation by XPS

Sample Type	Elemental Composition /at%					P:O ratio
	C	Mg	Na	O	P	
Mg WE43	27.3	18.6	-	52.2	-	-
P30	10.4	2.3	16.5	56.9	12.9	0.23
P35	8.8	2.4	10.3	62.5	10.7	0.17
P40	10.7	2.0	13.5	59.6	11.7	0.20

4.5.4 Profilometry of RFMS sputtered PBG coatings for thickness measurements

4.5.4.1 P30 PBG coating deposited on polished Mg WE43 profilometry

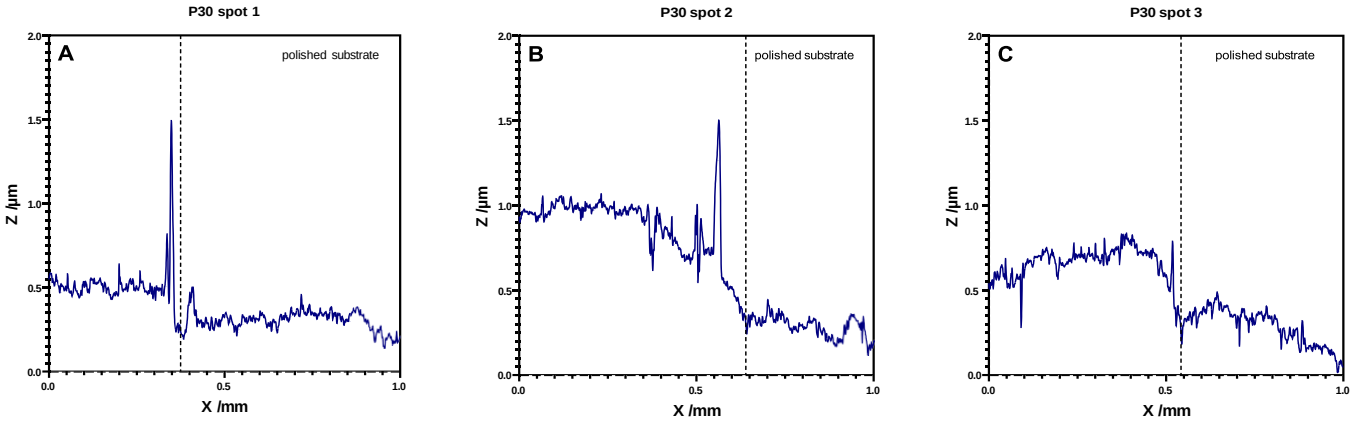

Figure 4.54: Profilometry of the P30 glass coating measured at 3 different points along the substrate-coating border taken at A) ca. 2.5mm from left B) ca. 5mm from left C) ca. 7.5mm from left

Figure 4.54 depicts the profilometry measured across 3 points along the substrate-coating border showing the PBG deposition thickness for the P30 target. As the deposition thickness of the glass was much smaller than that of the CaP, any variations in the morphology of the polished substrate are larger by comparison showing a higher relative roughness of the polished side of the samples compared to previous profilometry measurements for CaP. The P30 glass showed an average thickness of *ca.* 0.6 µm with a large deposit recorded to be just over 1 µm thick. There was a clear step difference between the PBG coated side and uncoated side in the order of ≤0.5 µm, which would fill voids left in a CaP coating due to the amorphous nature of

the glasses. As the deposition time for the PBG was 48 h, the average deposition rate was calculated to be 12.5 nm/h for the P30 sample.

4.5.4.2 P35 PBG coating deposited on polished Mg WE43 profilometry

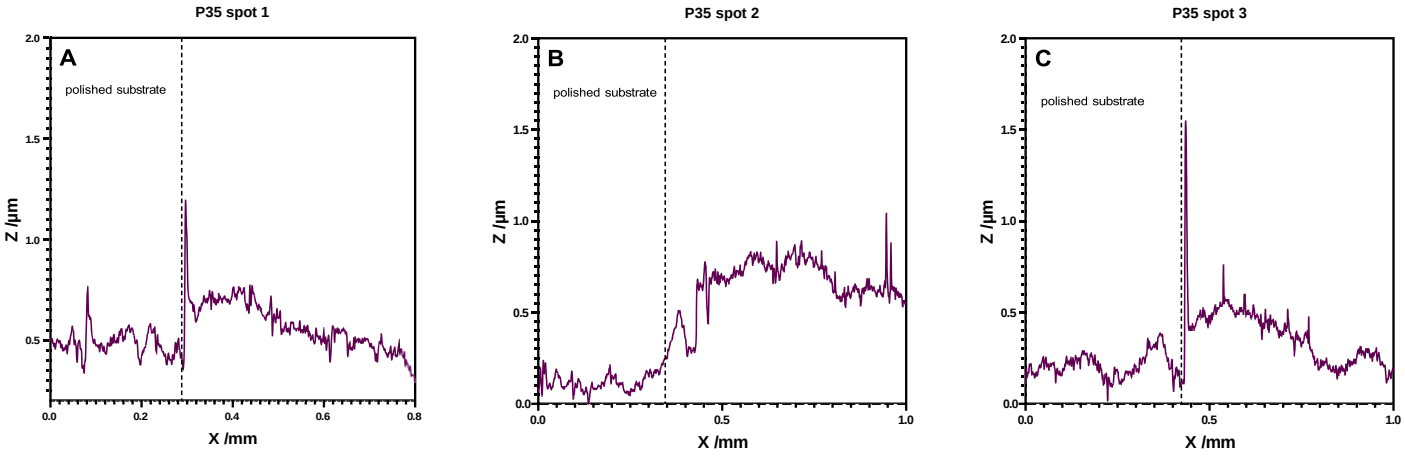

Figure 4.55: Profilometry of the P35 glass coating measured at 3 different points along the substrate-coating border taken at A) ca. 2.5mm from left B) ca. 5mm from left C) ca. 7.5mm from left

The profiles depicted in Figure 4.55 show the P35 deposition across the substrate-coating border. Similarly to the P30 sample, there was a base layer deposited although the P35 layer was slightly thinner (*ca.* 0.49 µm) with some individual peaks *ca.* 1 µm thick. As the variations in peak heights recorded was relatively small for the coated side of the substrate, this would support the suggestion that the PBG deposition was amorphous in nature and would likely be a complimentary coating to the electrodeposited CaP which exhibits voids in the coating. Taking the average deposition thickness as *ca.* 0.49 µm, the average deposition rate was calculated to be 10.2 nm/h under the conditions specified in *Section 3.2.5*.

4.5.4.3 P40 PBG coating deposited on polished Mg WE43 profilometry

Figure 4.56 shows the profiles recorded for the P40 sputtered deposition at 3 points along the substrate-coating border. Similarly to the other PBG depositions, a characteristically amorphous coating was deposited. The deposition rate of the P40 target was slower than that of the two lower P content glasses as an average thickness of 0.4 µm was deposited in the 48 h

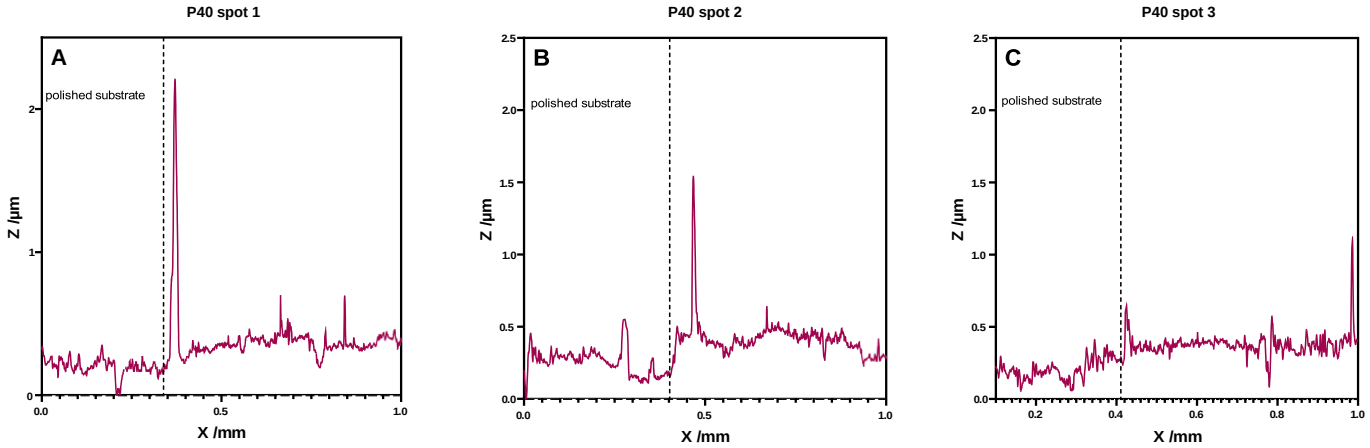

Figure 4.56: Profilometry of the P40 glass coating measured at 3 different points along the substrate-coating border taken at A) ca. 2.5mm from left B) ca. 5mm from left C) ca. 7.5mm from left

deposition time giving a calculated deposition rate of 8.3 nm/h. There were still large peaks observed for the PBG at the deposition border which were *ca.* 1 µm thick. The amorphous coating suggests that the P40 deposition would be complimentary to the CaP coating although there may be an issue due to the low thickness of the coating as compared to the lower P content formulations. The average thicknesses of the RFMS PBG coating profiles for the varied P content targets, were averaged across the 3 measurements and collated below in Table 4.19.

Table 4.19 PBG coating thickness and calculated deposition rate for varied P content target formulations with SEM (n=3)

PBG Target	Average Profile Thickness /µm	Deposition Rate / $^{nm}/_{h}$
P30	0.60 ± 0.10	12.5
P35	0.49 ± 0.07	10.2
P40	0.40 ± 0.02	8.3

4.5.5 Elution Cytocompatibility Testing for PBG coatings deposited on MgWE43

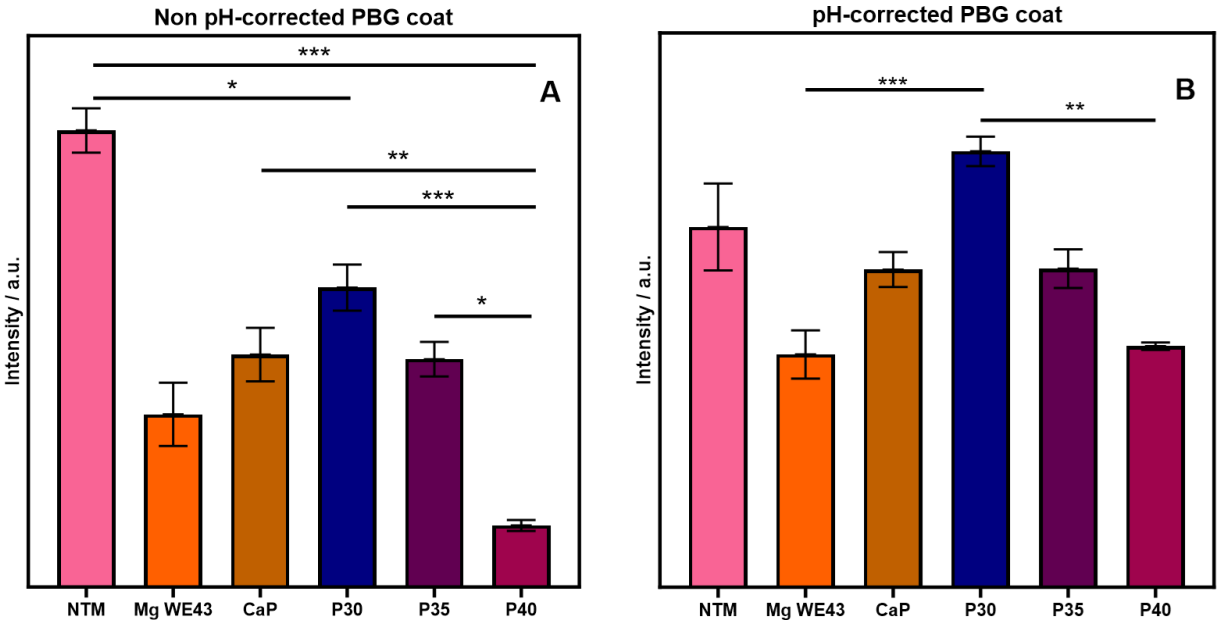

*Figure 4.57: Cell cytocompatibility test of PBG only coat and bi-layered PBG + CaP coatings assessed using Neutral Red Assay: (A) treated DMEM media non pH-corrected (B) treated DMEM is pH-corrected to 7.4 to simulate body conditions. All values are mean values ± SEM (n=3). * - p<0.05, ** - p<0.01, *** - p<0.001*

Figure 4.57 shows the cell viability of MG-63 cells after 24 hours exposure to DMEM treated with each sample type both as treated (Figure 4.57(A)) and pH-corrected to 7.4 (Figure 4.57(B)). For the treated media, there was a drop in performance of all sample types when compared to the NTM control. The drop in performance was statistically significant for all sample types with a $p < 0.001$ for all samples except the P30 coating which had a value $p < 0.05$. The lowest performing coating was the P40 only coating which performed significantly worse than any other coating type and the only statistically comparable sample was the uncoated Mg WE43 alloy. When the pH of the treated media was corrected to 7.4, there was an improvement in cell viability of all sample types to be comparable with the NTM control with no statistical significance in the cell viability, suggesting that there were not a significant amount of toxic ions leaching out of the coatings into the media and the drop of cell viability in the non pH-corrected test was due to the pH change during the media treatment process.

However, there was still some variation in performance between certain sample types with the highest performer being the P30 PBG coating. There was statistical significance between the performance of these samples and both the Mg WE43 alloy and the P40 PBG coating. The significance between the P30 coating and P40 coating gives $p < 0.01$ and a $p < 0.001$ for the Mg WE43 alloy.

4.5.6 Potentiodynamic polarisation testing for PBG only coatings deposited on Mg WE43

Figure 4.58 shows an example of the Tafel plots generated from PDP testing for each sample type of the PBG coatings respectively. The CaP was included as a reference comparison for the CaP coating deposited at 0.6 duty cycle, electrolyte pH 4.5 and a 20 min deposition time. Each sample type was repeated in triplicate with the results being collated and listed below with calculated corrosion rate in Table 4.20.

Table 4.20: Mean Ecorr and Icorr values for each PBG coating and the resultant corrosion rate calculated with SEM (n=3)

Sample type	Corrosion Potential E_{corr} / V	Corrosion Current Density i_{corr} / (mA/cm^2)	Polarisation Resistance R_p / Ωcm^2	Corrosion Rate v_{corr} / (mm/Y)
Mg WE43	-1.42 ± 0.01	0.097 ± 0.009	264.5 ± 39.62	2.22 ± 0.030
CaP	-1.17 ± 0.01	0.025 ± 0.011	782.5 ± 30.20	0.57 ± 0.002
P30	-1.21 ± 0.07	0.087 ± 0.044	680.4 ± 479.99	2.00 ± 0.022
P35	-1.08 ± 0.27	0.164 ± 0.098	1026.6 ± 639.68	3.74 ± 0.026
P40	-0.97 ± 0.26	0.128 ± 0.021	784.4 ± 347.82	2.92 ± 0.007

All of the PBG coatings exhibited a more positive E_{corr} than the Mg WE43 alloy suggesting a lower thermodynamic corrosion tendency. However, this did not translate to a lower corrosion rate for the P35 and P40 samples which both exhibited a higher i_{corr} and hence corrosion rates of 3.74 mm/Y and 2.92 mm/Y respectively as compared to 2.22 mm/Y for the Mg WE43 alloy.

For these coatings a trend was observed that the higher P content of the glass coatings gave a more positive corrosion potential although the lowest P content gave the lowest corrosion rate of 2.00 mm/Y.

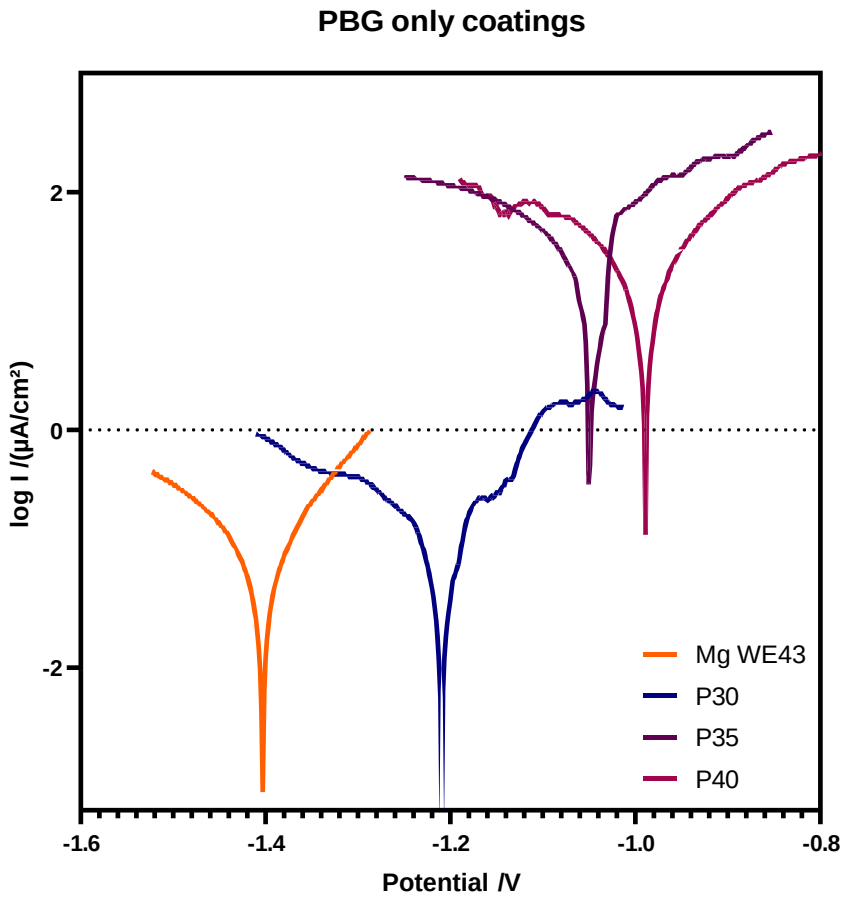

Figure 4.58: Electrochemical Corrosion Test Results for varied formulation sputtered PBG coatings deposited on Mg WE43, in DMEM at 37°C

4.6 Bilayered CaP + PBG coatings deposited on Mg WE43 alloy

Due to the voids in the coating surface of deposited CaP coatings giving a higher likelihood of early corrosion of the Mg WE43 alloy substrate, the bilayered coatings of electrodeposited CaP with a PBG layer sputtered directly on top were investigated aiming to utilise the benefits of both coating types whilst showing the two methods to deposit complimentary coatings. This section analyses and compares the performances of the novel, bi-layered CaP and PBG coatings with the Mg alloy substrate and the electrodeposited CaP coatings.

4.6.1 SEM/EDX of bilayered CaP + PBG coatings deposited on Mg WE43

Table 4.21 shows the EDX analysis for the bilayered PBG and CaP coatings. A similar trend of P35 CaP samples exhibiting the highest P content is in agreement with *Sections 4.4.4 and 4.5.1* above. The combination of CaP and PBG layers shows a drastic reduction in Mg content, from *ca.* 40 to 1.5 at.% (Table 4.17), suggesting the alloy surface was close to being completely covered as Mg content below 2 at.% may be entirely contributed by the Mg content of the PBG targets. The Ca and P content increased significantly as the EDX readings will penetrate deeper than just the topmost PBG layer and the underlying coating was composed of Ca and P.

Table 4.21: Mean compositions of as-deposited bi-layered coatings by EDX with SEM (n=3)

Target	Elemental Composition / at.%					Ca:P ratio
	Ca	Mg	Na	O	P	
P30 CaP	11.12 ± 1.03	2.03 ± 0.22	1.49 ± 0.37	75.18 ± 1.65	10.18 ± 1.27	1.09
P35 CaP	10.77 ± 1.01	1.69 ± 0.18	1.70 ± 0.31	74.51 ± 1.35	11.33 ± 0.74	0.95
P40 CaP	7.91 ± 0.55	4.03 ± 2.18	1.42 ± 0.28	77.56 ± 3.06	9.08 ± 0.53	0.87

4.6.1.1 SEM of Bi-layered CaP and P30 coating deposited on Mg WE43

Figure 4.59 depicts the combined architectures of the bi-layered P30 CaP coating deposited onto the Mg WE43 alloy. There was widespread coverage of similar crystals observed in the previous sections attributed to brushite crystals across the alloy surface. There were some disc-like shapes (example circled in white) across the deposition, which may be similar to the disc-shapes observed for previous glass depositions or may be contamination from charging and arcing during the sputter deposition process, but the majority of the glass deposits appear to be the smaller 1µm diameter globules.

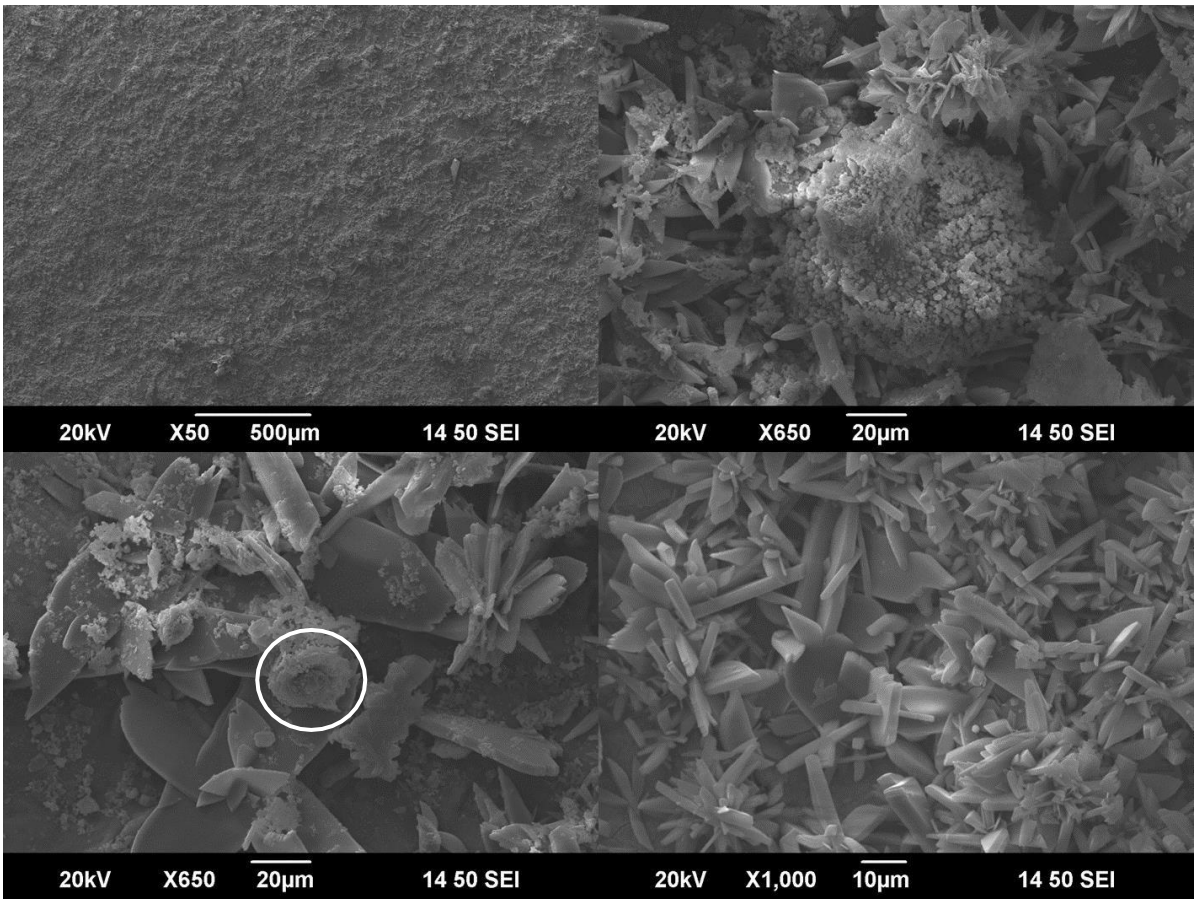

Figure 4.59: SEM images of the combined bi-layer CaP and P30 PBG coating with a disc-shaped PBG deposited circled in white, a large surface coating with few voids observed and densely packed clusters of small crystals typical of the bilayered coatings

4.6.1.2 SEM of Bi-layered CaP and P35 coating deposited on Mg WE43

Figure 4.60 shows the bi-layered CaP and P35 PBG coating as-deposited on the Mg WE43 alloy substrate. There was a large crystalline brushite-like deposition across the alloy surface with minimal voids however, in these voids there were signs of other features. The features were observed to be in a new form in this sample as a large conglomerate (circled in white) *ca.* 100µm in length as well as a flat amorphous leaf shape on top of the brushite deposition (circled orange). The large conglomerates were relatively uncommon when compared to the previous sample types but *ca.* 5 - 10 instances of this deposition type were observed across the viewsites of this coating. There appears to be an interaction between the brushite crystals and the PBG sputtered coating causing a rounded, globular deposit which give a larger depth to the coating. The needle-like brushite structures appear to have become smaller and more densely packed,

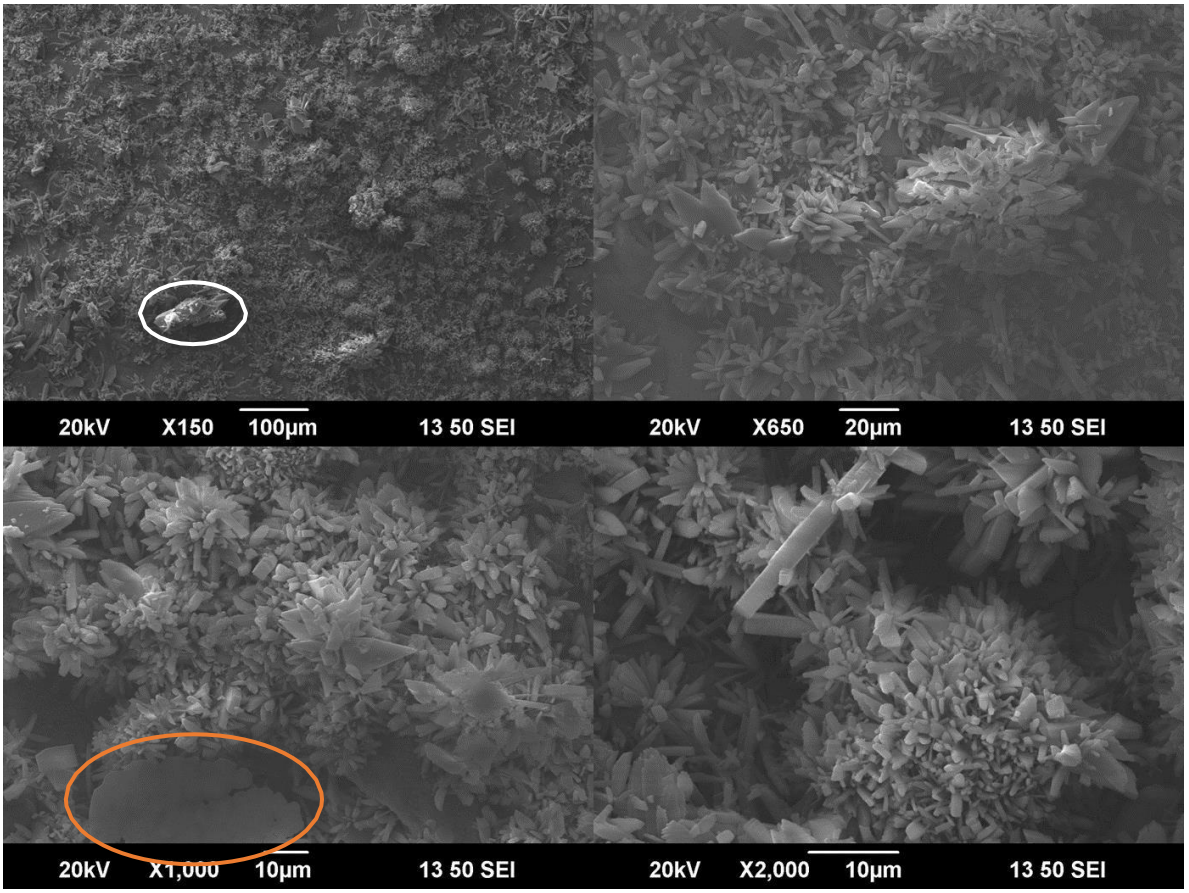

Figure 4.60: SEM images of the combined bi-layer CaP and P35 PBG coating with newly observed large conglomerates (circled white), amorphous leaf shape (circled orange) and clusters of densely packed small crystals being typical of the bilayered coating

as compared to the CaP only deposited coatings, with a needle size < 1µm thick in cross-section.

4.6.1.3 SEM of Bi-layered CaP and P40 coating deposited on Mg WE43

The bi-layered CaP and P40 coating depicted in Figure 4.61, shows many similarities with the other bi-layered coatings in that there was a wide coverage of the brushite crystals and smaller, globular structures. There was a tendency for the brushite crystals to be a needle-like shape and in some areas, the needles have become smaller. In the void areas of this coating, there were signs of the cratering effect previously seen for the PBG only coatings upon high magnification (circled white in Figure 4.61). Several plate-like crystals ≥ 100 µm in length, were observed in the coating, which appear to lay on top of the needle clusters instead of appearing around the edges of any voids in the coating. Some cracks were visible in the base layer, deposited in

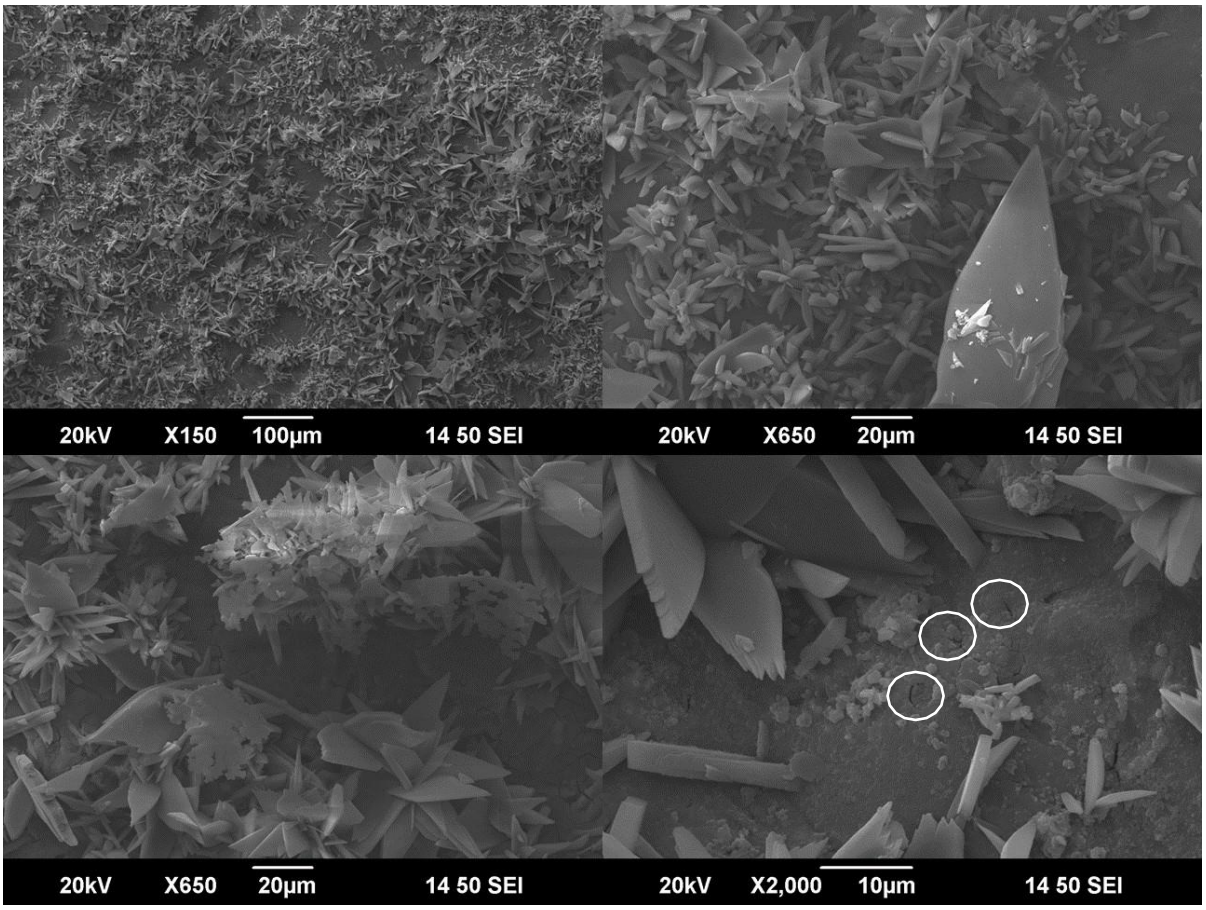

Figure 4.61: SEM images of the combined bi-layer CaP and P40 PBG coating with potential cratering sites circled white and large CaP crystals deposited on top of smaller needle-like structures as compared to previously observed around the edges of CaP layer voids

the coating voids possibly due to the brittle nature of the PBG coating although these seem to be only a few µm in length and appear to be shallow in depth.

4.6.2 XRD patterns of bi-layered coatings deposited on MG WE43 alloy

Figure 4.62 shows the XRD patterns of the bi-layered coatings as compared to the uncoated Mg WE43 alloy and the CaP coating used as standard. The bi-layered coatings exhibited the same peaks as the CaP control with Mg peaks (ICDD database 00-004-0770) at 32.1, 34.4 36.5, 47.7, 57.4 and 63.0º 2θ alongside the brushite peaks at 11.6, 21.0, 23.2, 29.3, 30.5 and 50.2º 2θ (ICCD database 00-001-0395). The phase orientation for these peaks has been reported previously in *Sections 4.1.2* and *4.2.2*. Comparing the three bi-layered coating patterns shows a similar relative intensity for the majority of recorded peaks with the exception of the brushite peak at 11.6º which increased in relative intensity as P content of the PBG formulation

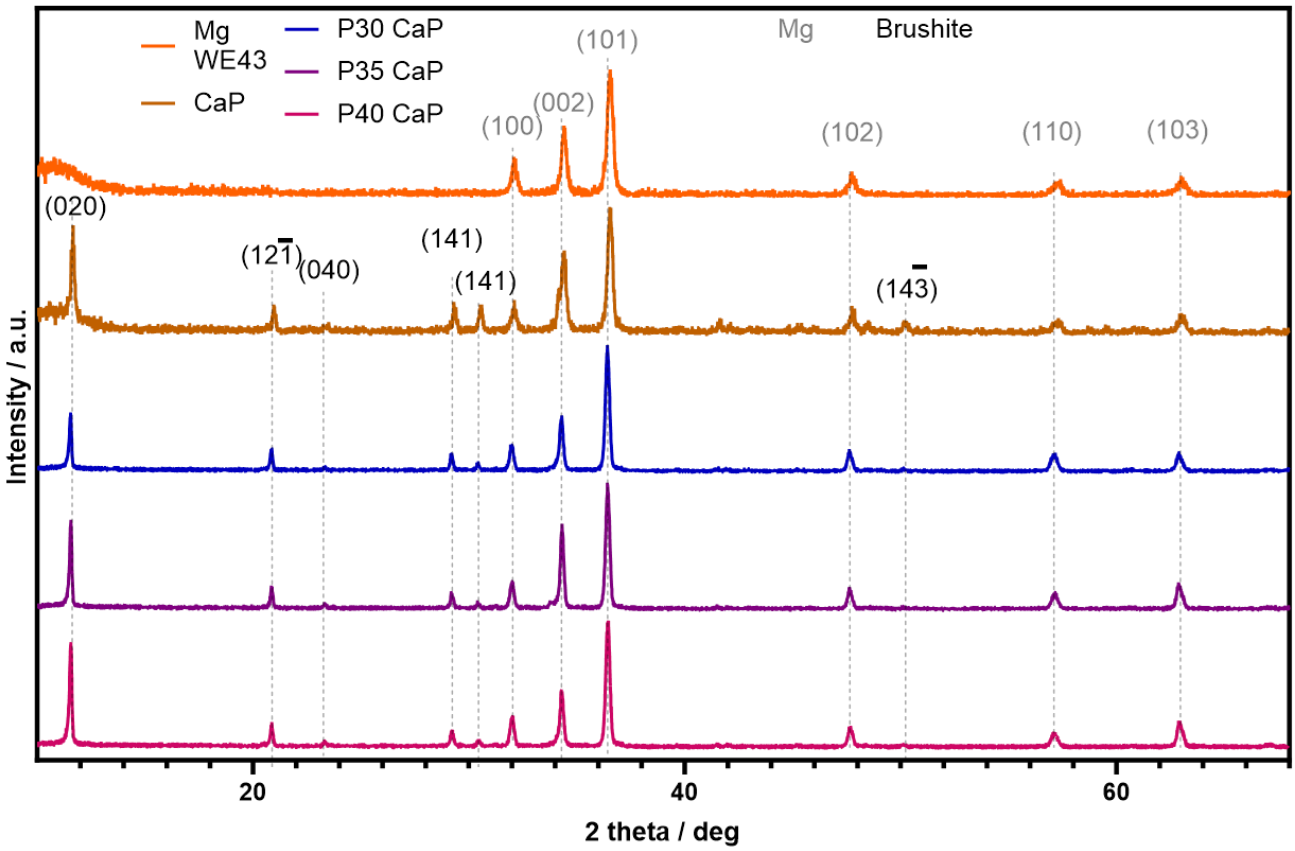

Figure 4.62: XRD patterns of as-deposited bi-layered CaP and PBG coatings on Mg WE43 alloy substrate with varied PBG composition. Peak deconvolutions are as follows: () – Mg:ICDD 00-004-0770, () – Brushite:ICDD 00-001-0395

increases. The P40 CaP brushite (020) phase at 11.6º was the only one of the three bi-layered coatings with a relative intensity comparable to that of the CaP only coating.

4.6.3 XPS spectra of bi-layered coatings deposited on Mg WE43 alloy

Figure 4.63 presents a survey scan and detailed high resolution C 1s, Ca 2s, Mg 2s, Na 1s, O 1s and P 2p spectra for the bi-layered PBG and CaP coatings. Each coating exhibited all of these peaks however, as expected the Mg WE43 alloy control did not exhibit Ca 2s, Na 1s or P 2p as these elements were fully contributed by the electrodeposition and sputtering coating methods. Similarly to the PBG only coatings, the survey spectra exhibited Cu 2s and Cu 3s peaks but the elemental analysis found this to contribute < 1 at.% so was assumed to be negligible. The elemental analysis of the bi-layered coatings by XPS is listed in Table 4.22. Despite exhibiting the lowest Ca at.%, the P35 CaP sample showed three components attributed to Ca, CaP and $Ca(PO_3)_2$ bonding.

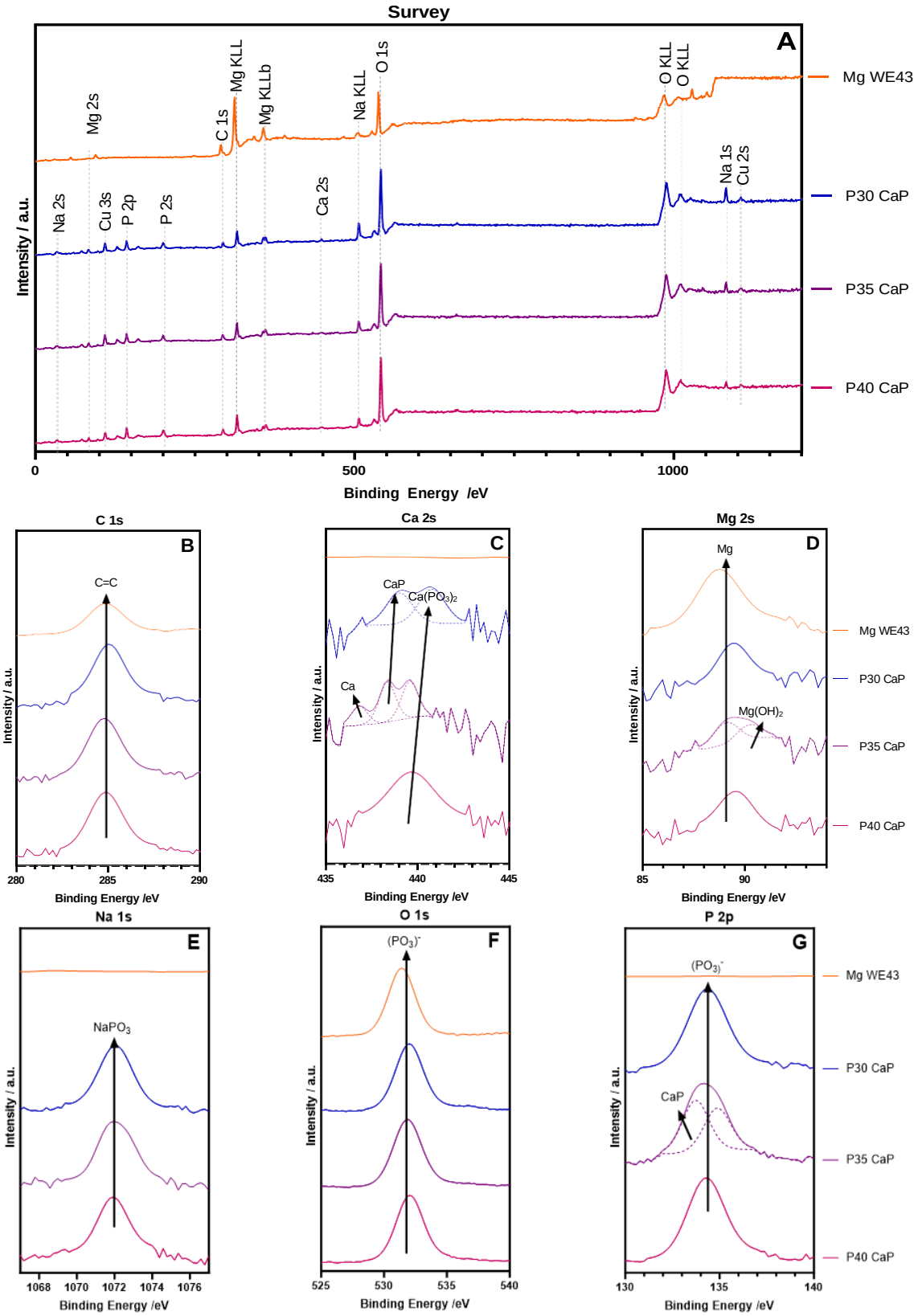

Figure 4.63: XPS survey spectra of the combined CaP and PBG coatings and high resolution scans (A) survey (B) C 1s high resolution spectra (C) Ca 2s high resolution spectra (D) Mg 2s high resolution spectra (E) Na 1s high resolution spectra (F) O 1s high resolution spectra (G) P 2p high resolution spectra

The P30 CaP sample also exhibited 2 components for the Mg 2s, Na 1s and P 2p spectra suggesting that hydroxide bonding was present in the sample with Na 1s binding energy of 1072.6 eV. The P 2p peak was attributed to $(PO_3)^-$ bonding due to the binding energy of 134.6 eV. This bonding type would be in agreement with the Na 1s peak suggesting $NaPO_3$ bonding with a binding energy of 1071.7 eV. The O 1s high resolution scan may have different bonding types affecting the peak of the P30 CaP sample as hydroxide bonding with metals would be expected at 531.3 eV and $(PO_3)^-$ bonding expected at 532.6 eV. Due to the energies being relatively close, they may have contributed to the same peak shown in Figure 4.63(F). Similarly to the P30 only coating, the P30 CaP bilayer contained the highest P proportion with a P:O ratio exhibited of 0.25 compared to 0.14 and 0.23 of the P35 CaP and P40 CaP coatings respectively.

Table 4.22: Surface element compositional analysis for bi-layered coatings formulation by XPS

Sample Type	Elemental Composition /at%						P:O ratio
	C	Ca	Mg	Na	O	P	
Mg WE43	27.3	-	18.6	-	52.2	-	-
P30 CaP	7.8	1.2	2.6	8.1	60.6	15.3	0.25
P35 CaP	9.1	0.8	1.7	3.9	69.2	9.7	0.14
P40 CaP	10.1	0.9	2.8	2.9	64.7	15.0	0.23

4.6.4 Thicknesses of bilayered CaP + PBG coatings

The bi-layered coatings are a combination of the profiles examined in *Sections 4.1.4.2* and *4.5.4.* From review of these profiles, the coating thicknesses deposited can be inferred and are listed below in Table 4.23. The average thickness of the CaP coating was taken to be 7.41µm, as measured previously in *Section 4.1.4*, accounting for the base layer and larger crystal peaks.

Table 4.23: Deposited bi-layer coating thicknesses and ratio of CaP to PBG layer thickness

Sample type	CaP thickness /µm	PBG thickness /µm	Combined thickness /µm	PBG contribution /%
P30 CaP	7.41 ± 0.84	0.60 ± 0.10	8.01 ± 0.94	7.49
P35 CaP		0.49 ± 0.07	7.90 ± 0.91	6.20
P40 CaP		0.40 ± 0.02	7.81 ± 0.86	5.12

4.6.5 Elution Cytocompatibility Testing for bi-layered coatings deposited on Mg WE43

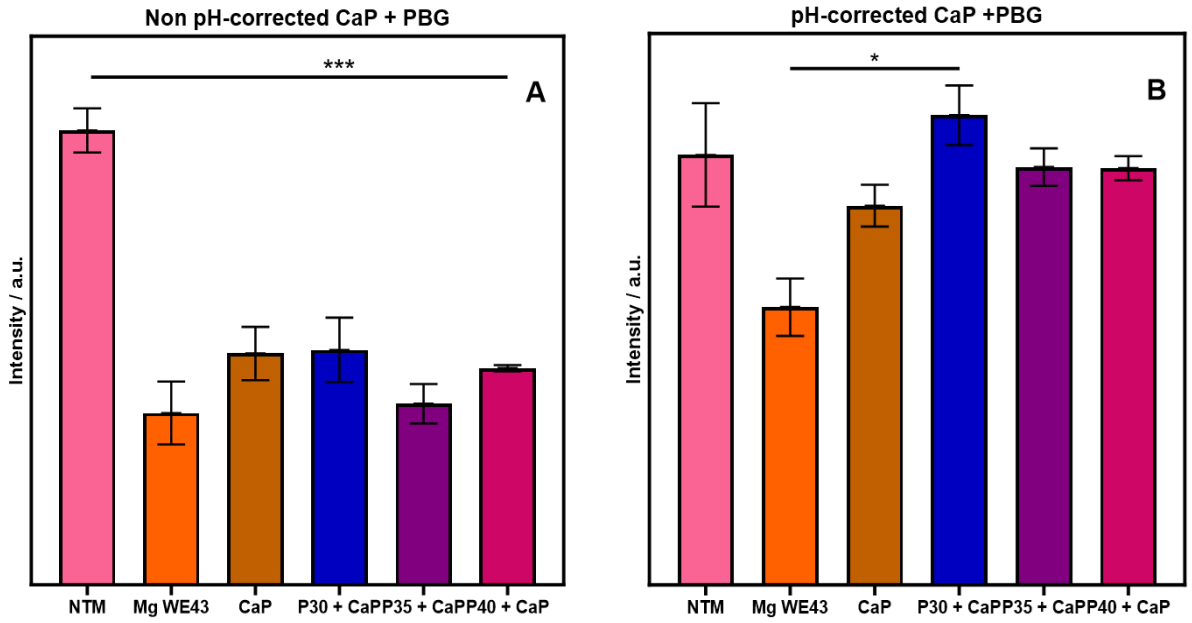

*Figure 4.64: Cell cytocompatibility test of bi-layered PBG + CaP coatings assessed using Neutral Red Assay: (A) treated DMEM media non pH-corrected (B) treated DMEM is pH-corrected to 7.4 to simulate body conditions. All values are mean values ± SEM (n=3). * - p<0.05, ** - p<0.01, *** - p<0.001*

Figure 4.64 shows the cell viability of MG-63 cells after 24 h exposure to DMEM treated with each sample type both as treated (Figure 4.64 (A)) and pH-corrected to 7.4 (Figure 4.64 (B)). For the treated media, there was a drop in performance of all sample types when compared to the NTM control. The drop in performance was statistically significant for all sample types with a $p < 0.001$ for all samples. When the pH of the treated media was corrected to 7.4, there was an improvement in cell viability of all sample types to be comparable with the NTM control with no statistical significance in the cell viability, suggesting that there were not a significant amount of toxic ions leaching out of the coatings into the media and the drop of cell viability in the non pH-corrected test was due to the pH change during the media treatment process. However, there was still some variation in performance between certain sample types with the highest performer being the P30 CaP bi-layered coating. There was statistical significance between the performance of these samples and the Mg WE43 alloy. The significance between the P30 CaP sample and the Mg WE43 alloy showed a $p < 0.05$. The bi-layered samples showed very similar levels of viability across both tests, whereas there was greater variation between

the PBG only coatings, suggesting that the CaP layer may act as a stabiliser that can be enhanced by the PBG depositions.

4.6.6 Potentiodynamic polarisation testing for bi-layered CaP + PBG coatings

Figure 4.65 shows an example of the Tafel plots generated from PDP testing for each sample type of the PBG coatings and bi-layered coatings respectively. Each sample type was repeated in triplicate with the results being collated and listed below with calculated corrosion rate in Table 4.24.

Table 4.24: Mean Ecorr and Icorr values for each PBG + CaP coating and the resultant corrosion rate calculated with SEM (n=3)

Sample type	Corrosion Potential E_{corr} / V	Corrosion Current Density i_{corr} / (mA/cm^2)	Polarisation Resistance R_p / Ωcm^2	Corrosion Rate v_{corr} / (mm/Y)
Mg WE43	-1.42 ± 0.01	0.097 ± 0.009	264.5 ± 39.62	2.22 ± 0.030
CaP	-1.17 ± 0.01	0.025 ± 0.011	782.5 ± 30.20	0.57 ± 0.002
P30 CaP	-0.71 ± 0.03	0.032 ± 0.006	1165.0 ± 44.91	0.74 ± 0.009
P35 CaP	-1.13 ± 0.22	0.129 ± 0.059	559.9 ± 370.09	2.94 ± 0.020
P40 CaP	-1.36 ± 0.01	0.204 ± 0.042	168.1 ± 17.05	4.67 ± 0.009

The three bi-layered coatings all exhibited more positive corrosion potentials than the Mg WE43 alloy while the P30 CaP and P35 CaP samples also had a more positive corrosion potential than the CaP control with the most positive E_{corr} of -0.71 V exhibited by the P30 CaP sample. The P30 CaP sample had the lowest corrosion rate of the bi-layered coatings of 0.74 mm/Y however, this was higher than the electrodeposited CaP layer alone which showed a corrosion rate of 0.57 mm/Y despite having a more negative corrosion potential than the P30 CaP sample.

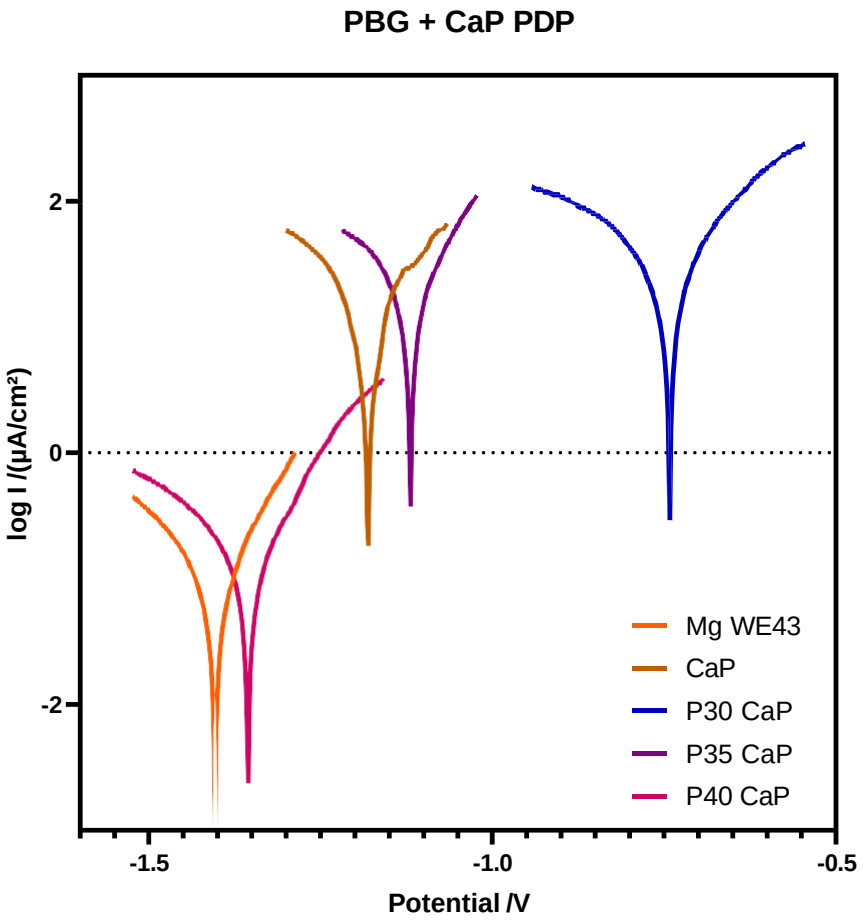

Figure 4.65: Electrochemical Corrosion Test Results for bilayered coatings deposited on Mg WE43 discs, in DMEM at 37°C

4.7 Chapter Summary

The effects of varying different electrodeposition parameters to influence the CaP deposition onto Mg WE43 alloy and developing a novel bi-layered CaP and PBG coating has been investigated as part of a strategy to improve cell response to Mg WE43 alloy and either inhibit or delay the onset of corrosion of the Mg WE43 alloy. Calcium phosphate during the electrodeposition process was deposited in the brushite phase with a transition from brushite to amorphous CaP with increasing duty cycle. However, there was a higher deposition rate of CaP with higher duty cycle so the duty cycle of 0.6 was taken to be optimal for further testing. The deposition time was then varied showing a greater deposition coverage with increased

deposition time as Mg content from elemental comparison methods decreased. However, this trend was not linear and there is a risk of starting the corrosion process of the underlying substrate exhibited by cracking at deposition times higher than 40 mins with the corrosion rate of the 20 min deposition sample being the lowest. The electrolyte pH was raised to attempt to encourage deposition of hydroxyapatite instead of brushite. However, this decreased the deposition rate of CaP to *ca.* 7.5 µm/min and only deposited small amounts of hydroxyapatite whilst maintaining majority brushite deposits and also small amounts of P deposits confirmed by XRD. The CaP coatings all improved the corrosion rate of the Mg WE43 alloy and shifted the corrosion potential to a more positive value despite the coatings all containing voids in the surface morphology of the coating.

The development of the novel bi-layered coatings saw a complimentary coating where voids originally left in the electrodeposited CaP were coated with PBG which also interacted with the CaP deposition to show areas of smaller, more crystalline brushite deposits. The corrosion performance of these bi-layered coatings all improved the corrosion potential as compared to the Mg WE43 alloy although only the P30 CaP and P35 CaP coatings were more positive than the CaP only coating. The corrosion rate of the CaP only coating was the lowest implying that the combination of the PBG and CaP bi-layer increases the corrosion rate of the sample but the P30 CaP coating only increases corrosion rate by 0.17 mm/Y but is still a reduction of 1.48 mm/Y compared to the uncoated Mg WE43 alloy. There were also significant benefits to the cytocompatibility through the addition of the lower P content PBG layers with the greatest benefit being found with the addition of a P30 layer. Overall with the aim of reducing corrosion rate, the P30 CaP bi-layer coating reduced the corrosion rate threefold compared to the uncoated Mg WE43 alloy and simultaneously improved the cytocompatibility a statistically significant amount.

Chapter 5 – Discussion

5.1 Introduction

The ability of biocompatible Mg alloys to degrade in a human body fluid environment without producing toxic byproducts makes them one of the best candidate materials for temporary biodegradable implants for a variety of orthopaedic applications [364]. However, despite clinical approval of the Magnezix screw [10], improvements of corrosion rate or the delay to the onset of degradation must still be made if Mg alloys are to be utilised for a wider variety of applications. As outlined in the literature review (*Section 2.8*), among the most popular strategies for improving corrosion rate of Mg alloys is the application of CaP coatings [16, 308] via the electrodeposition method. Yet with the benefits to corrosion rate exhibited by the coated alloys [315, 365], there are still some areas to be improved upon such as the early onset pitting corrosion due to gaps in the coating surface and the desire for increased levels of bioactivity at the bone/implant interface [366]. Due to the requirement for any additions to the implant to be resorbable in human environments, the addition of coatings such as Si-based glasses must be reconsidered. However, the hydration and hydrolysis reactions of the phosphate groups in PBGs enables these glasses to fully resorb in an aqueous human environment as described in *Section 2.6.3*. The brittle nature of these glasses prevents the use of the PBGs as a load-bearing material [219] but still shows potential for these glasses to be utilised as thin-film coatings at a bone remodelling site.

The aim of this work was to investigate the potential of combining two separate deposition methods, of CaP electrodeposition and PBG RFMS, to establish a complementary coating which would act as a sacrificial layer to delay the onset of corrosion to the Mg WE43 alloy and enhance the cytocompatibility of the substrate as a whole. As a first section of work, an investigation into the effects of varying the parameters used in the electrodeposition process

on the characteristics of the as-deposited CaP coatings was carried out to show whether these changes resulted in an improved corrosion resistance and cytocompatibility. As there were still expected issues to mitigate with an electrodeposited CaP coating alone, the second section of work proposed and investigated a novel PBG layer deposited by RFMS with the effects of lowering the P content of the glasses, in turn changing the respective Q^n species of the different glass formulations being examined. The two methods were then combined to determine whether a complimentary bilayered coating consisting of these two coating types could be established with a beneficial effect on the corrosion resistance and cytocompatibility of the Mg WE43 alloy.

5.2 Varying the Electrodeposition Parameters for Calcium Phosphate Coatings

5.2.1 Duty Cycle Variation for Calcium Phosphate Electrodeposition

Across the variations of duty cycle during the CaP electrodeposition process, there was seen to be a transitional effect from an amorphous coating at a duty cycle of 1 to a combination of amorphous and crystal deposition gradually decreasing with decreasing duty cycle, to a majority crystalline deposition at lower duty cycles such as 0.3 and 0.2. XRD analysis in *Section 4.1.2* identified the deposited crystal structure as brushite (DCPD) in agreement with Azem *et al.* [14] who utilised duty cycles of 0.1, 0.3 and 0.5 to deposit pulsed coatings which led to an improved corrosion resistance when compared to their underlying Ti alloy. As the deposition time was 20 min, a coating of 10 -20 μm was deposited. This allowed for preferential orientations of the deposited brushite structures to be determined, with the (020) brushite phase being preferred for any crystal deposition across the variation of duty cycle. It was expected that the relative intensity of brushite signals recorded would increase with decreasing duty cycle [367]. However, this was not strictly the case as the largest relative intensity of brushite was exhibited at a duty cycle of 0.6 and then showed a slight decrease in intensity with further

lowering of duty cycle (Figure 4.13). The variation of brushite intensities at lower duty cycles was relatively small but the presence of the $(12\bar{1})$, (141) and $(14\bar{3})$ brushite phases support the fact that brushite has a preferred orientation in this coating. Taking the XRD patterns into context with SEM there was an observed shift in the deposited form of CaP from multiple orientations of crystalline brushite at low duty cycles to an amorphous CaP hump at 1 duty cycle. The deposited coating at 1 duty cycle exhibited an amorphous sheet like structure of which similar structures were observed in decreasing amount as the duty cycle also decreased, where there was also a mixture of both the amorphous CaP and crystalline brushite at intermediary duty cycle depositions. This likely occurs due to the lack of relaxation time during the electrodeposition process which has been shown to promote nucleation and propagation of CaP crystal structures [368].

SEM analysis of the coatings (*Section 4.1.1*) showed the pulsed coatings, duty cycle less than 1, to be porous in nature. Porosity of the coating is beneficial to the development of bone substitutes due to their large surface area promoting the tendency to bioresorb, inducing bioactivity and the provision of a framework for cellular attachment to the implant for integration, anchoring the implant to the surrounding bone structure [369]. However, the coating porosity simultaneously provides a route to the Mg alloy surface which may allow the corrosion of the alloy to begin earlier than desired. Depending on the crystal morphology and coating structure, different degradation rates may be observed and so there is potential to improve the coating's protective properties by depositing specific phases of CaP or an amorphous CaP layer. Also observed of the coatings was that there was an increase in the size of the crystal deposits with increasing duty cycle. It was postulated by Dev *et al.* [370] that morphological control of the deposited coatings is seen through the mechanism of the reduction of accumulated H_2 bubbles around the substrate, allowing the recovery of depleted ions in the area surrounding the cathode in electrolyte solution. The work in this thesis would support that

statement as the increasing relaxation time with decreasing duty cycle allowed recovery of the ionic concentration, causing current density spikes which resulted in the formation of needle-like structures growing outwards compared to the larger plate-like structures. This formation may also be influenced by the addition of H_2O_2 to the electrolyte solution which was shown by Chen *et al.* to promote the needle-like structure formation over the plate-like formation [16]. However, the main effect achieved by this is promoting the deposition of needle-like structures at a higher duty cycle which may allow for a greater deposition rate as it has been shown that there is no correlation between porosity values and applied duty cycle by Azem et al [14]. Ca:P ratios calculated using data from EDX suggested the phases of CaP deposited could vary from brushite (ratio ca. 1) to amorphous CaP (ratio ca. 1.2-2.2) [361], which would support the inferences of XRD that the two phases of CaP deposition were brushite and amorphous CaP.

Analysis of XPS showed there to be minimal variation between the varied duty cycle samples as the majority of high resolution peaks were attributed to a single deconvolution of each element. However, due to XPS being a surface scanning technique [371], there were no Mg 2s peaks exhibited by samples of 0.2 duty cycle and all duty cycles from 0.8 and above, suggesting a potentially more continuous coating with the 0.2 duty cycle sample being an outlier. The 0.2 duty cycle sample may have been densely packed with brushite crystals in the scanning region which would account for the lack of a scanned Mg 2s high resolution peak. However, when comparing the CaP coated samples with the Mg WE43 alloy, there was seen to be an effect on the O 1s peak, where the coated samples exhibited a new deconvolution due to the addition of C-O-C bonding at 286.8 eV [372] and a proportion of Ca=O bonding for the 0.4 duty cycle sample. Minor variations were observed in the binding energies of the P 2p peaks across the varied duty cycles. However, the variation was *ca.* ±0.1 eV and is likely caused by small stresses in the coating which may arise from a dehydration effect during the deposition [373]. Ca:P ratios calculated using XPS characterisation suggest that the top surface layer of the

coatings were of the MCP phase as their ratios were in the region of 0.5-0.6 [361]. Due to the nature of XPS analysis only scanning the top 10-15 nm of a coating, these ratios are likely due to the internal structure of the crystals formed which are in the micrometer scale and so the full structure of the CaP crystal is not encapsulated. The coating characterisation techniques showed a good level of agreement for the deposited CaP coatings, suggesting the main effect that duty cycle has on the deposited coatings was the morphology of the CaP deposits, whether the deposit is crystalline at a low duty cycle or amorphous at a high duty cycle, with some degree of transition between these two states. The effects of both the crystalline and amorphous deposits on the cellular and corrosion responses are to be examined as the amorphous coatings cover a larger area of the Mg WE43 alloy surface but may degrade faster than the crystalline depositions which tend to be more insoluble in body conditions [374].

Monasterio *et al.* [367] stated there is a correlation between increasing duty cycle and increasing coating thickness. However, profilometry of varying duty cycles presented in *Section 4.1.4* would suggest that this is not the case. An argument could be made that this correlation is made due to the amorphous nature of direct deposition coatings at 1 duty cycle lacking the porosity exhibited by coatings of a lower duty cycle. However, the peak variations recorded for both the amorphous deposition and crystalline depositions exhibited a relatively similar z differential. This could be affected by the accuracy to which the profilometer could record but may suggest more about the deposition rate from solution whether the deposits are crystalline or not. One of the main factors in the deposition process is the zeta potential, which is defined as the difference in potential between the surface of a solid particle immersed in solution and the bulk of the solution [375]. The zeta potential can be related to the electrophoretic mobility (EPM) through the Helmholtz-Smoluchowski formula [376]:

Equation 5.1

$$\zeta = {}^{4\pi\mu\eta}/_{\epsilon}$$

Where ζ is the zeta potential in mV, μ is the EPM in $(\mu m.cm/V.s)$, η is the fluid viscosity and ϵ is the dielectric constant.

For the electrodeposition of CaP to occur, a negative charge must be induced locally to the surface of the substrate in order to attract the positively charged Ca and PO_4 ions from the bulk solution. Makiewicz *et al.* [373] examined the amperage during the electrodeposition process and noticed a sharp drop within the early stages of the deposition process. It was theorised that this was due to adhesion of hydrogen bubbles to the cathode surface, forming a resistance barrier between the electrodes, limiting the current flow and impeding the deposition of positive ions. As the coating was characterised to show brushite deposition, it can be stated that the Ca and PO_4 ions had the largest absolute value of zeta potential in the electrolyte solution [377], making their movement towards the cathode strongly favoured in comparison to the rest of the electrolyte during the electrodeposition process. Simultaneously, during the deposition of brushite crystals on top of the earliest deposited crystals, a proportion of the Ca ions derived from the earliest-deposited brushite may react with hydroxide ions, created in the electrochemical reaction of water reduction, to form calcium hydroxide ($Ca(OH)_2$) at the deposit interface. The forming layer serves as a base for further crystal growth and deposition which starts to gradually replace the hydrogen bubbles on the surface of the substrate [373]. These hydrogen bubbles may form from water reduction or also the degradation of the Mg-alloy substrate surface. However, with increasing deposition thickness there is also an increase in the resistance of the solution, due to the deposited layer hindering the transport of hydroxide and calcium ions in the solution which promote further thickness growth [373]. This would suggest that there will be a point where a maximum deposition thickness is reached due to the deposition lowering the zeta potential of ions to be adsorbed to the substrate. Due to the applied voltage being -3 V, it was likely that the zeta potential induced by the supplied voltage was counteracted by the resistance caused by the CaP deposition, giving a net potential of 0 V. If a

thicker coating is required, a more negative applied voltage will likely increase the zeta potential of the ions in the bulk electrolyte to overcome the resistance induced by the brushite coating layer at *ca.* 15 – 20 µm thick [378]. However, the variation of applied deposition voltage was not investigated in this work to aid in comparison to work previously completed by Saremi et al [330]. As there was little variation between the thicknesses of the coatings with varying duty cycle, it can be assumed that the duty cycle has little to no effect on the zeta potential and the deposition is more strongly dominated by other factors such as pH [375], ion concentration strength [379] and potentially applied voltage.

Indirect contact cellular testing showed improved cytocompatibility for all duty cycle samples tested as compared to the uncoated Mg WE43 alloy. The improvement shown is likely due to a combination of the coatings providing a beneficial Ca and PO_4 ions which have been shown to improve cell adhesion [380], and the lower corrosion rate reducing the hydrogen evolution which in turn affects the viability and function of cells [381]. There was no significant difference observed with varying duty cycle however, these tests must be looked at in a wider context that due to the nature of rapid onset Mg alloy corrosion from reaction with Cl^- rich supplemented DMEM [382], the test parameters were adapted to a shorter media exposure time than the 24 h suggested by the ISO 10993-5 and a decreased SA:V ratio. From this it can be stated that during the shortened exposure period, there was not a release of toxic ions into the culture media suggesting that if there is a large supply of media to dilute the H evolution effects, a good level of cell cytocompatibility can be obtained by the deposited CaP coatings. Previous literature has also detailed beneficial effects of CaP coatings as a corrosion inhibitor due to their preferential degradation as a sacrificial layer compared to Mg alloy [176, 383] and the enhancement of passivating oxide formation through the mechanism of solution treatment [384].

5.2.2 Deposition Time Variation for Calcium Phosphate Electrodeposition

As the duty cycle directly affects the crystal deposition morphology, the variation of deposition times would generally be expected to affect the thickness and density of the deposited coating as opposed to crystal morphology. SEM analysis showed a good agreement with the statement that deposition time does not affect the crystal morphology as the deposited crystals maintained the expected plate-like and needle-like brushite crystals confirmed with XRD. However, previous literature has shown the ability to tune crystal orientation, adhesive strength, crystal morphology and coating porosity through the variation of deposition time [370]. This could occur due to the nucleation modes varying with increased loading time as initial nucleation and crystal growth occur horizontally on the cathode to cover the substrate [385]. Whilst in this nucleation stage, the rate of crystal growth will be less than the rate of nucleation site formation until the substrate surface is covered and the rate of crystal growth becomes predominant compared to the nucleation site formation rate. This point is where the coating thickness tends to grow upwards until other factors such as zeta potential become dominant. However, Nam *et al.* [386] observed a drop in overall mass of the CaP coating due to the reduction in adhesion strength of weaker nucleated crystals deposited in a thicker coating. Similarly, increased deposition time showed a higher relative intensity of non-dominant brushite orientations such as the $(12\bar{1})$, (040), (141), $(15\bar{2})$ and $(14\bar{3})$ phase orientations. However, a maximum was reached at 60 min deposition and a decrease shown for the 120 min deposition suggesting a weaker coating adhesion of the brushite crystals when deposited in these orientations [386]. XPS showed a general agreement with XRD as for increased deposition time, there was no Mg 2s high resolution peak and a greatly reduced Mg KLL auger peak observed suggesting a good substrate coating coverage.

When examining the coatings via XRD in regards to potential thickness variation, the relative intensity of Mg peaks attributed to the underlying substrate significantly decreased for all

deposition times above 20 mins however, this was not a linear trend as there was minimal difference between the 40 min, 60 min and 120 min patterns. This would suggest that the coatings would be thicker with increased deposition time as the brushite coatings were thick enough to dampen the X-ray penetration into the underlying substrate surface [370]. The apparent thickness increase can be attributed to the increased availability of Ca and PO_4 ions in the electrode vicinity for an extended period of time over the increased deposition period. Despite this, profilometry measurements (*Section 4.2.4*) showed no evidence of a larger deposition thickness with the coatings tending towards the 10 – 15 µm range, similar to that of the 20 min deposition time sample. However, the deposited coatings appear to be more densely packed with increased deposition time, which would explain the lower intensities of Mg peaks exhibited by XPS and XRD. Similarly, this would agree with the suggestion that the deposited crystals at increased deposition times would tend towards the smaller, needle-like morphology as the largest depositions recorded for the 40 min deposition was in the region of 10 µm. The calculated Ca:P ratio of the coatings were similar to that observed for the varied duty cycle coatings suggesting the crystals deposited were of a similar nature. The increased deposition thickness of the 60 and 120 min samples would likely be a crystal deposition growing on top of the smaller needle crystals, creating a packing effect where the deposition density of the smaller crystals are increased. An explanation for this could be that the zeta potential becomes zero after a certain thickness of coating is deposited due to the kinetic resistance of the already deposited coating [377]. But due to the nature of the deposited brushite coatings being porous and non-uniform, there would be a variation of zeta potential across the substrate surface causing the rate of nucleation site formation to once again overtake the rate of crystal growth in the pore sites of the coating after the thickness plateau is reached for the deposition parameters after 20 mins [373]. In their work, Makiewicz *et al.* [373] found that applied charge drops with increasing deposition time but simultaneously showed a denser suspension layer

near the cathode which may account for some of the denser packing of crystals observed in this work (*Section 4.2.1*). An issue with increasing deposition thickness is that the same current density is difficult to maintain throughout the deposition process and as such the deposition is non-linear [387] due to the resistance to ion diffusion increasing and subsequent zeta potential decrease as distance from the cathode increases. This could be addressed by optimising the ionic strength of suspension, which can reduce the EPM of the of suspended particles if either too resistive or too conductive [378]. Similarly, applied a larger potential to the cathode surface would also overcome the resistance barrier and induce a zeta potential for further growth during the deposition time. Another observation of Makiewicz *et al.* [373] was that average deposit thickness over time was a constant increase during the initial growth period, but shrinkage was observed after reaching a maximum thickness potentially caused by hydrogen detaching from the bulk of the deposited layer, leading to partial dissolution of the deposited layer. The deposition thickness was not seen to increase after 20 min and a steady current was reached.

The cytocompatibility testing showed a significant increase in cell viability for the 120 min deposition compared to both the Mg alloy substrate and the 20 min deposition, suggesting that increasing the deposition time has benefits caused by the denser packing of brushite crystals in the coating. However, despite the 40 min deposition showing significant improvement over the Mg alloy, the 60 min deposition time did not. This may be due to the preferred phase orientation of brushite as mentioned previously, the non-dominant crystal orientations reduced from the 60 min deposition to 120 min deposition likely due to poorer adhesion strength to the substrate in these orientations [386] which may have simultaneously affected viability by the proportion of CaP likely to leach from the samples into culture media. Since the cell viability of the Mg alloy remained similar for both the non pH-corrected and pH-corrected tests, whilst the coated samples all showed improvement when pH-corrected, it would suggest that the pH change during media treatment was responsible for the lower cell viability. It would follow that there

were likely no toxic ions leaching out of the coated samples into the cell media as all coated samples performed similarly to the TCP control when pH-corrected. The beneficial performance of the 40 min deposition over the 60 min deposition could potentially be explained by the lower proportion of the non-dominant orientations propagated by the electrodeposition process as the highest proportion of these orientations was observed by XRD for the 60 min deposition. The benefits shown through cytocompatibility testing also generally translated to improvements in the corrosion rate of the substrate with the most positive E_{corr} values being exhibited by the 40 min and 120 min depositions showing a preferable coating for corrosion resistance [388] and a greatly reduced corrosion rate compared to that of the Mg WE43 alloy. However, these corrosion rates exhibited were larger than the 20 min deposition time so the benefits of a more densely packed coating can be examined against the benefit of a further reduced corrosion rate and a selection made based on the impact factors of each beneficial property exhibited by the various coating deposition times.

5.2.3 Electrolyte pH Variation for Calcium Phosphate Electrodeposition

The variation of electrolyte pH is known to be very influential on the deposition of CaP [389, 390, 391], affecting factors such as deposited phase and deposition rate etc. It is generally considered that the lower the electrolyte pH value, the higher the deposition rate [373]. The previous work of this thesis has shown that using a pH value of 4.5 will deposit the brushite phase of CaP, however, ideally the deposited phase of CaP would be hydroxyapatite due to its superior mechanical properties such as tensile strength (3.5 MPa for HA, 1.3 MPa for brushite [392]), shear strength (9.8 MPa for HA, 2.9 MPa for brushite [392]) and decreased solubility under human body conditions [393]. Although brushite is a precursor to HA, in attempt to remove a secondary transformation stage, the electrolyte pH during deposition was increased to attempt to induce a phase change of deposition where HA is more preferentially formed under neutral or basic conditions. It must also be considered that there may be a balance found

between maintaining as high a deposition as possible, by having as low an electrolyte pH as possible, whilst raising the electrolyte pH in attempt to deposit HA by electrodeposition. The work of this thesis explored the increase of electrolyte pH to determine whether HA would be beneficial on a cellular level and is useful in comparing the in vitro responses of a deposited HA coating, with brushite coatings which will likely transition towards HA in human conditions.

SEM analysis of depositions at varied electrolyte pH showed a good agreement with the earlier statement that deposition rate decreases with increasing solution pH as there was visibly a more sparse deposition with larger pores in the coating and significant cracking of the underlying substrate exposed to the electrolyte during the deposition process. The reason for this reduction is deposition rate is likely due to increased difficulty inducing a pH gradient local to the cathode in comparison to the bulk solution and as such the zeta potential for deposition would be decreased [389]. If the bulk solution is at a high pH, the concentration of hydroxide ions local to the cathode would be relatively smaller than in a solution with a more acidic pH, meaning there would be a lower diffusion gradient for CaP particles to deposit onto the cathode substrate surface. Another issue presented by Ducheyne *et al.* [394] was the difficulty of HA deposition from aqueous solution to due water adsorption to the HA molecules. However, XRD confirmed there was HA deposited in the (002) and (221) phase orientations using an electrolyte pH of 7.5 or greater whilst also showing a reduced deposition of brushite. It is likely that the largest HA deposition was observed for the pH 7.5 samples due to the similarity to human body pH where HA is the preferred CaP phase. Despite preferred conditions for HA deposition there simultaneously was shown to be deposits of pure P, suggesting that due to the precipitation of HA in bulk solution of electrolyte, there is likely to be formation of calcium-deficient apatites [393], which may have led to the deposition of P by Ca deficiency in the localised area of the cathode. XPS data showed a lower Ca:P ratio for the higher electrolyte pH, suggesting there

may be a slight inhibiting factor to the deposition of CaP at higher electrolyte pH. This could also suggest that there is a decrease in the deposition rate which would show agreement with SEM images with sparser depositions at higher pH. Contrary to the conclusions of some previous literature where it was claimed that HA can only be deposited in non-water solvents [395, 394, 396] via electrodeposition, this work has shown evidence of HA deposition from a water-based electrolyte by raising the pH of the bulk electrolyte.

It has been reported that electrolyte pH is the most high impact factor in controlling the electrophoretic mobility and conductivity of the electrolyte [390, 391], which in turn has already been shown to affect the zeta potential by Equation 5.1. This would lend credence to the use of electrolyte pH variance to achieve increased deposition rate and coating uniformity which has been shown to be possible by Rojaee *et al.* [378], although the isoelectric point of each phase to be deposited must be considered in the evaluation of electrolyte pH as some precursors are unable to be deposited by electrodeposition due to never reaching a sufficient zeta potential for deposition. For the deposition process to occur, the zeta potential must be of sufficient magnitude that the particles in the electrolyte would tend to repel each other and not easily agglomerate [377], creating a better dispersion allowing for a continuous deposition and recovery process. If the zeta potential is too low, this indicates the instability of the electrolyte suspension with low electrostatic repulsive forces and at this stage, van der Waal's forces take over and cause particles to aggregate and agglomerate, further increasing the resistance to deposition [397]. Also seen in literature is the influence of electrolyte pH on the crystallinity of deposited coatings [385], where an increase in electrolyte pH was seen to increase the crystallinity of deposited CaP and a reduction of pH below pH 2.5 reduced CaP crystallinity. This microstructural change can be attributed to the supersaturation of OH^- ions close to the cathode caused by the shift in pH [385], suggesting that there will be an optimal electrolyte pH to increase the degree of CaP crystallinity whilst ensuring a maximum deposition rate for this

crystallinity. However, the results of this thesis show that the increase in electrolyte pH in steps of 1.5 pH above pH 4.5 all significantly reduce the deposition rate as the measured coating thicknesses for electrolyte pHs 6.0 – 9.0 varied between *ca.* 0.1 – 0.2 µm, which is a *ca.* 37-fold decrease in coating thickness compared to the CaP coating deposited at electrolyte pH 4.5. This would indicate that the resistance to deposition was significantly increased for any CaP electrodeposition carried out with a pH above 6 and the van der Waal's forces have become dominant due to the instability of the solution, where particles have agglomerated and are less readily attracted to the Mg WE43 alloy surface during the electrodeposition process.

The cytocompatibility assessment showed a clear trend that the increase in electrolyte pH showed a significant decrease in cell viability as compared to the lower pH 4.5 electrolyte solution. This is most likely due to the lower thickness of the deposited coating providing less corrosion protection as the deposition rate is generally higher at a more acidic pH [373]. Another contributing factor to the cell viability is likely that the significant cracking seen on the surface of the underlying Mg alloy substrate acted as a propagating surface for pitting corrosion [152], which in turn causes a severe pH change [153] in the supplemented media to a more basic pH which has a toxic effect on the cultured cells causing cell death [398]. However, despite this lowering of cell viability, there was a reduction in the corrosion rate as compared to the Mg alloy, suggesting there may be variations in the coating depositions at increased electrolyte pH due to the precipitation of Ca salts in the bulk electrolyte and the reduced zeta potential for deposition caused by this phenomena [393]. This shows some agreement with the standard error of mean calculated across the 3 repeats of the corrosion testing as the errors observed for the elevated electrolyte pH samples above pH 4.5 were an order of magnitude larger than that observed for electrolyte pH 4.5. The corrosion rate of the pH 9 sample was *ca.* two times lower than the uncoated Mg alloy, suggesting that the deposition of HA had a significant effect on the sample, despite the low deposition rate. Despite this, the

control sample deposited using electrolyte pH of 4.5 had an *ca.* two-fold further reduction of corrosion rate compared to the electrolyte pH 9 sample, suggesting that coating thickness is the most important factor for a 20 min deposition. Even with the brushite deposited at pH 4.5 being known to be more soluble in media than deposited HA [399].

5.2.4 Calcium Phosphate electrodeposition overview for next steps

The electrodeposition of CaP coatings onto a metallic substrate via the cathodic deposition method has been utilised to deposit homogenous coatings by a number of authors [400, 401, 402] with varying deposition parameters focusing on improving biocompatibility and corrosion resistance of the underlying metal substrate. Various crystalline phases of CaP have been successfully produced such as octacalcium [403], HA [404] and brushite [405], with the coatings described as porous or microporous. The findings of this work agree that the application of a pulsed potential produces a superior CaP coating to that of a constantly applied potential [406] in terms of crystallinity, corrosion resistance and a higher cell viability. Varying the duty cycle between 0.2 and 1 resulted in a transitional deposition with the reduction of duty cycle generally resulting in a higher degree of crystalline deposition as compared to globular deposits of amorphous CaP with higher duty cycles. Increasing the deposition time resulted in the denser packing of CaP crystals through the consistent application of charge once the maximum coating thickness was reached for the zeta potential to become zero due to the thickest parts of the coating providing a resistance to potential difference [373]. This denser packing showed an improved cytocompatibility due to the saturation of Ca and PO_4 ions available to interact with the cells which has been proven to induce an increased level of osseointegration both *in vitro* [374, 407] and *in vivo* [408, 409]. However, there was a slight increase in the corrosion rate compared to the 20 min deposition which would suggest that there was potentially a degree of corrosion initiated during the extended immersion period of deposition which was exposed as the dissolution rate of the brushite from a similar thickness

remains the same. The variation of electrolyte pH to attempt to deposit the preferable HA CaP phase was successful in depositing small amounts of HA. But these coatings were largely unsuccessful when it came to performance as there was an increased corrosion rate, decreased level of cell viability and a thinner coating deposited with areas of pure P also observed within the coating. From this it would be concluded that a higher deposition rate of a less favourable CaP phase in brushite [320] would still be preferable to a lower deposition rate of the preferred HA phase as the benefits of osseointegration [407] and coating thickness [367] providing a layer of protection showed a marked improvement in corrosion and cell viability tests.

The electrodeposition of brushite crystals has often been utilised due to its inexpensive nature [410] and high deposition rate [411] despite demonstrating a greater solubility than the majority of CaP phases [412]. As a thick coating is generally required for adequate protection of Mg alloys, it is thought that it may be more advantageous to obtain a thick brushite coating and add a conversion step where the brushite is converted into the more favourable HA phase. As observed in the work of this thesis, the deposition of HA is possible by increasing the pH of the electrolyte solution to 7.5 and above, as HA is more stable at pH greater than 6-7 [407]. However, as the deposition rate of HA is too low and potentially inconsistent from batch to batch, a brushite deposition and further conversion will be more effective than a direct HA deposition. This conversion has been achieved through methods such as a 2 h treatment in 1M NaOH [413] and post-deposition sintering and annealing [385] with the benefit of post-deposition treatment reducing substrate corrosion during the coating process as compared to conversion attempts by deposition parameter variation [414].

As the nature of deposited brushite coatings is porous, leaving potential sites for early onset pitting corrosion to occur, there is an opportunity for the improvement of corrosion resistance and biocompatibility via the deposition of a complimentary layer, developing a new composite bi-layered coating. The implications of which are discussed below.

5.3 Radio Frequency Magnetron Sputtered Phosphate-Glass Coatings on Mg WE43 alloy

Recent investigations into the utilisation of melt quenched PBGs has shown the ability to be tailored both structurally and compositionally [105, 415, 106] for applications such as the controlled release of ionically bound elements to promote angiogenesis [227], tailoring of coatings to bone defects in individual patients and the increase in bioactivity levels around an implant surface [416].

Variations were seen between the target compositions and the as prepared compositions measured by EDX analysis (Table 4.7 and 4.8) with the largest differences of 1.39-Ca 1.13-Mg 1-Na 2.45-O 2.74-P %at. These variations were attributed to absorption of moisture from the atmosphere, accuracy of the EDX instrument and precursor purity as P_2O_5 is known to absorb atmospheric moisture [106] and increase in mass during the preparation of precursors for the melt-quench process. Similar compositional variations have been observed by Ahmed *et al.* [417] and Stuart *et al.* [106] attributed to similar factors during the preparation process. The splat quench method was used in attempt to prevent surface crystallisation of the glasses which are amorphous by definition, as further disparities may occur pertaining to difficulty in depositions as more energy would be required to break the ordered lattice bonds of a crystalline structure [418]. The surface crystallisation is generally related to the undesired glass vitrification or crystallisation of glass powders [418] which becomes prevalent when using PBGs with a low P content, specifically with high proportions of the orthophosphate and pyrophosphate species [262]. However, due to the requirement for PBG targets to be cast into a mould and annealed to prevent stress cracking during RFMS depositions, there is a second opportunity for surface crystallisation to occur which was observed around the edges of the P35 target and the P30 “pebble” cast alongside the P30 target for analysis purposes. However, due to the P30 target macroscopically showing no signs of crystallisation compared to the

"pebbles", and the central "racetrack" area of the P35 target, where the RFMS process deposits from, showing little to no signs of crystallisation, these were treated as amorphous PBG targets despite the XRD analysis of separate samples suggesting the P30 target may be crystalline.

Stuart *et al.* [100] have established that there is a linear relationship between the deposition power and deposition rate where an increase in power will increase the deposition rate due to increased kinetic energy of the bombarding atoms. However, applied power often needs to be restricted to below 100W as crystallisation of the targets can occur due to the thermal heating induced by atom bombardment [419], as well as the brittle nature of the glass causing cracking and destruction of the target at higher powers. With this in mind, a backing layer of Kapton tape was applied to hold the target together if it were to crack, as had been observed with initial target testing (data not shown). During the depositions detailed in the work of this thesis, some cracking was observed in all of the PBG targets, however, none of the targets cracked through the whole thickness and the cracks were likely along lines of self-contained internal stresses.

XRD analysis of the sputtered PBG only coatings was inconclusive as to characterising the coatings due to the thin-film nature of the coatings and the low deposition rate depositing coatings of *ca.* ≤ 500 nm which would be difficult to see in an XRD pattern due to the penetration depth of the scan being much larger than the PBG thickness. In this case XPS is a more valuable characterisation method due to its ability to detect much thinner coatings on the surface of a substrate. XPS analysis showed the expected components deposited with similar bonding types across the target formulation variations with the exception of the P40 coating having an oxidised Mg deconvolution. The spectra is likely to show similarities due to the targets being composed of the same elements, but also exhibit variations in the relative intensities of individual elements, as the coatings will be affected by the phenomena of preferential sputtering [100] which would deposit some elements more readily than others. The sputtering yield of targets comprised of multiple elements are governed by two main cascade

effects of momentum transfer and ion penetration within the surface layers of the sputtering target [420, 421]. Stuart *et al.* [100] observed a preferential sputtering order under similar deposition parameters of Na > Mg > Ca > P by comparison of target formulations and coating compositions deposited. Elemental analysis through XPS would suggest a preferential sputtering order of Na > P > Mg > Ca with the P being more preferential than seen by Stuart. The PBG coatings exhibited an absence of Ca with no peaks detected by XPS analysis which would show agreement with a lower preferential sputtering. The increased preferential sputtering of P observed may be due to the positioning of P within the PBG target internal structure as there may have been a higher proportion of P concentrated in the central "racetrack" area of the targets compared to both Mg and Ca due to the disorganised structure of the glass. Stan *et al.* [422] and Berbecaru *et al.* [291] observed lower rates of sputtering for network forming elements such as Si and P and higher sputtering rates for network modifying elements such as Na, Mg and *Ca.* The increase in P sputtering yield may be due to the presence of atmospheric moisture within the composition, absorbed during the melt-quench production process, which can form P-OH bonds leading to depolymerisation of the glass [423] potentially occurring during deposition and thus an easier dislocation from the bulk glass target to be deposited. This theory is supported by the deposition of disc-like glass shapes observed using SEM. These discs appeared to be concave and brittle as shown in Figure 4.47 to have cracked significantly into the depth of the deposit. Under the assumption that these disc-shaped deposits are larger P-containing structures caused by the delamination from P-OH bonds, the unexpectedly high sputtering yield of P, as measured by XPS, could be explained. However, this needs further investigation.

Cytocompatibility testing of the PBG coatings showed a trend of increased levels of cell viability with decreasing P content. This shows a good level of agreement with previous work by de Melo *et al.* [262] who tested green fluorescence protein (GFP)-labelled mesenchymal

stem cells (MSCs), finding significant increases in the cell adherence levels by the reduction of P content of PBG coatings. Many of the cells which did attach to the P40 coating were observed to have a rounded morphology, which has been shown to be indicative of cells with a low degree of substrate attachment [424]. This trend has now been repeated using MG63 osteoblast-like cells showing that increasing the proportion of orthophosphates and pyrophosphates within the glass structure shows a benefit to the cytocompatibility levels of the substrates as there was a significant improvement of cell viability observed for the P30 coating, which has a higher proportion of orthophosphate, compared to both the Mg WE43 alloy and P40 coating with no orthophosphates in the glass structure. This trend can be attributed to the established roles of pyrophosphates and orthophosphates within the bone resorption and formation cycle, which can aid in the generation of new bone and crystallisation of HA [425, 426]. Complimenting these roles, Kasuga *et al.* [427] found that lower P content glasses exhibited a much lower ion release rate than typical metaphosphate glasses, suggesting favourable dissolution rates and a more stable surface integrity, local pH and osmolarity levels [428]. However, there was a slight variation in this trend found via corrosion testing with an agreement that the highest proportion of orthophosphates in the P30 coating, as stated by De Melo et al [262], provided the best protection of the PBG coating formulations with a slight improvement as compared to the uncoated Mg WE43 alloy. But the P40 coating exhibited a lower corrosion rate than that of the P35 coating with both showing an increase in corrosion rate as compared to the uncoated alloy. Further work would be required to obtain actual dissolution rates of these glasses as both bulk glasses and coatings to help determine the reasons for increased corrosion rates. It is likely there would be a more vigorous reaction between the glass and the DMEM used for corrosion testing in this work than the distilled water used by Tošić et al [429] due to the high reactivity of Mg with the Cl ions in the DMEM [430]. Also to be taken into consideration is the thickness of these PBG coatings in relation to the corrosion

rate and protection of the underlying alloy. During the corrosion testing, the corrosion rate seen will be that of the outer surface coating, which will degrade as a sacrificial layer of protection to the underlying Mg alloy, so despite the higher corrosion rates seen for the P35 and P40 coatings, there will still be a delay to the degradation onset of the underlying alloy. Depending on the dissolution rates of the PBG coatings, the corrosion of the underlying Mg alloy may not have begun during the PDP testing period, which lasted ca. 35 min in 1 L DMEM at 37 ºC. None of the PBG coatings showed an improvement in corrosion rate compared to the electrodeposited CaP coating likely due to the coating being *ca.* 20 times as thick as the thickest PBG coat and the relative insolubility of the deposited brushite crystals by comparison to PBG [431, 21]. Interestingly, the P30 coating contained the highest proportion of P of the 3 PBG coatings exhibiting a P:O ratio of 0.23 as compared to 0.17 and 0.20 for the P35 and P40 coats respectively. This may have occurred due to the structure of the Q species within the glass and may be an aid to the cytocompatibility levels exhibited. As the P30 coating has shown both an improvement of the cytocompatibility, compared to the CaP coatings, and the corrosion rate compared to the Mg WE43 alloy, this coating may show the most promise as part of a bi-layered composite coating which will be discussed in the following section.

5.4 Novel Bi-layered Calcium Phosphate and Phosphate Glass coatings

The bi-layered composite CaP and PBG coatings theoretically show much promise for use in orthopaedic applications due to the combination of benefits shown by both layers of the deposited coatings. The electrodeposited CaP layer provides a relatively thick protection layer to the underlying substrate which has been shown in previous sections to reduce the corrosion rate of the alloy and improve the cell viability by providing a structure for cells to adhere to and proliferate on [367]. Whilst the relatively thin-film of PBG sputtered on top of the CaP layer would add a layer of protection to the porous sections of the underlying coat, due to the amorphous nature of the deposition [231], and would further functionalise the coating to

promote osseointegration and an improved cytocompatibility [426]. Despite the top layer the cells would attach to being the PBG, the underlying morphology of the CaP coating would still be contributing largely to the overall surface roughness due to the CaP thickness being *ca*. 20 times larger than the PBG layer, with variations in peak heights from profilometry showing to be much larger than the PBG layer thickness.

As with the XRD analysis of the PBG coating only, the underlying structures are visible in the spectra due to the penetration thickness of XRD analysis, recording similar patterns to that observed for the electrodeposited CaP layer alone. The cratering effect observed for the P35 and P40 coatings may be caused by the impact of sputtered atoms or molecules colliding with the surface of the alloy during deposition and dislodging a weak portion of the alloy matrix similarly observed during the physical vapour deposition process by Panjan et al [432]. The P30 deposition has a tendency to interact with the coating in two ways. Firstly, there are clusters which appear to be amorphous, representative of the P30 glass deposition deposited in the voids of the CaP layer and secondly there is an interaction between the brushite crystals and the P30 deposits where the amorphous clusters sit on top of the brushite needles and in some areas the density of these clusters is large enough that the brushite crystals are completely covered by the glass. With both of these interaction types being exhibited across the surface, transitioning from the areas of high density CaP deposition and voids of low CaP deposition density, it can be assumed the bilayered coating achieves a complete coating across the surface of the alloy, with the PBG layer integrating with the brushite crystals and covering the voids left from the CaP electrodeposition process. However, there may be some contribution to the degree of crystallinity of the underlying brushite layer from the sputtering process as a heating effect is observed due to the plasma and bombardment mechanisms of the sputtering process where the kinetic energy of the bombarding species, typically in the region of 100 eV has been shown to deposit denser coatings with lower O content [433]. This may explain why the slight

amorphous hump observed for the CaP only sample around 11º 2θ has disappeared in the XRD patterns of the bi-layered coatings due to the potential annealing of the CaP structures caused by this heating [434]. However, the chemical interaction between the coating layers can be more accurately observed via XPS analysis (Figure 4.56), where the P35 CaP coating exhibited a number of varying bonding deconvolutions for the Ca 2s, Mg 2s, Na 1s and P 2p peaks. This would suggest that lowering the P content may have an effect on the bonding interactions between the deposited PBG and CaP alongside the heating effect observed from the sputtering process. But these interactions may be due to the predominance of invert Q^0 and Q^1 species in the glass as the P35 CaP coating showed the largest amount of deconvolutions with *ca.* 94% of Q^1 species distribution, P30 CaP with 39% Q^0 and 61% Q^1 species distribution and the least variation from the P40 CaP with 51% Q^1 distribution [262].

Comparison of the corrosion rates and coating thicknesses of the bi-layered coatings against the Mg WE43 and CaP coating controls can be used to give an indication of the effects of the composite coatings and whether the PBG layer sputtered on top of the CaP actually provides a beneficial effect in terms of bioactivity and corrosion protection. Table 4.13 shows the largest contribution of PBG to the bi-layered coatings is *ca.* 6% of the total thickness. Therefore, it would be expected that the CaP layer would have the largest influence on the properties of the combined coatings and may act as a bulk material that provides a base layer of protection adjusted by the PBG properties. The cytocompatibility testing would support this theory as there was no significant difference in the performances of the bi-layered coatings in terms of cell viability and similarly no significant difference between the bi-layered coatings and the CaP only coating. When considering that the biological performances of the PBG only coatings varied significantly, it can be assumed that the bulk CaP acts as a performance stabiliser with small variations caused by the thin-film glasses. However, the P30 CaP bi-layered coating showed a significant improvement in the cell viability over the uncoated Mg alloy, showing

agreement with de Melo *et al.* [262] on the beneficial effects of the P30 coating over the higher P content glasses. However, it would also suggest that the effect of the PBG coatings on the cell viability is the dominating factor as the trend observed of highest performance with lowest P content tracked across both of the PBG only coatings and the bi-layered PBG and CaP coatings. This would show that the structural roughness of the CaP coating, which was shown to provide beneficial effects for osseointegration [435, 436], was not as dominant as the cytocompatibility effects of the PBG glass depositions, which is likely due to the first media reaction being with the top layer of PBG. A similar trend was observed in the corrosion testing where, the best performing coating of the bi-layered coatings was the P30 CaP coating which exhibited a corrosion rate relatively similar to the CaP only coating and was a vast improvement over the uncoated alloy, whereas the other bi-layered coatings showed an increase in corrosion rate potential due to a rapid dissolution rate of the top PBG layer. This would be in support of the findings of Kasuga *et al.* [427] who showed the dissolution rates of inverse PBGs to be much lower than that of metaphosphates such as the P40 coatings.

Further work would be beneficial into the magnetron sputtering of invert phosphate glasses as there is a gap in the literature regarding the manufacture of glass targets which require a splat quench and the reliability of remelting and recasting into target moulds for an annealing treatment. The preferential sputtering effects seemed to change from expected in the literature with a high P content deposited when expected to be the lowest sputtering yield of the target elemental composition [291]. There is still an improvement to be made in regards to achieving a desired corrosion rate of 0.5 mm/year [35] for the bi-layered coatings to be used in clinical applications. However, there is potential to deposit a thick enough layer of PBG on top of the relatively thick CaP layer and the combined protective effect may be sufficient to delay the onset of degradation of the Mg alloy for a sufficient time in a variety of applications. Similarly, with the beneficial effects on cell viability and proliferation caused by the PBGs [435], the

increased speed of bone integration may reduce the required time for the healing process to occur in clinical applications.

The novel bi-layered PBG and CaP coatings have shown promise for their use in clinical applications of bioresorbable implants due to improvements in cytocompatibility and corrosion rate reduction of Mg WE43 alloys. The next section will discuss a variety of potential applications that would likely suit the use of these novel coatings.

5.5 Potential clinical applications of novel Calcium Phosphate and Phosphate Glass bi-layered coatings

Peltoniemi [437] theorised that the ideal biodegradable material would provide appropriate strength whilst degrading in a predictable fashion, without causing adverse reactions throughout the healing process. As the components used in the CaP and PBG coatings are all found naturally within the human body [428, 438], the bi-layered coatings would degrade without causing adverse reactions and the products could be naturally repurposed or disposed of by the body. Similarly, the tailorability of the PBGs allow for individual design for the desired timescales of healing , although more work showing property variation with thicker coatings would be of benefit. The limitations of the coating techniques must also be taken into consideration when looking to apply these coatings. As stated previously, it is relatively easy to deposit a thick layer of CaP in terms of getting ions from the bulk electrolyte to deposit onto a Mg WE43 substrate, but due to the requirement of maintaining an electrical contact for potential to be applied, there often is an uncoated ring on the substrate where a sample is being held against the electrode. There is potential for improvement of this by manufacturing a sample holder which maintains electrical contact by a slimmer margin, such as a wire hook which may also allow the coating of two sides at once. Similarly, a drawback of the RFMS method is that deposition can only be made in line of sight which may cause issues if the desired implant is of a complex geometrical nature and a full coating is to be applied. This could

potentially be addressed by the optimisation of the RFMS process, manufacturing a substrate holder which rotates during the deposition process to make sure as much of the surface as possible faces the sputtering target. However, if these issues are addressed, then there is an array of potential for these bi-layered coatings to be applied to clinical applications, of which some are discussed below.

One of the main areas for the use of these coatings would be as fracture fixation implants as the Mg alloy substrate would provide similar structural support to human bone [159, 27] at installation and then would interact with the bone, slowing the implant degradation so the bone can regenerate to its previous mechanical properties [439]. The main goals for fracture treatments are to align the fractured fragments, reduce the fracture size and preserve this reduction through immobilisation of the bone [440]. This immobilisation often occurs through the conjunctive use of either internal or external fixation usually in the form of pins, screws, wires, nails, rods and plates [441]. Bioresorbable materials and coatings aim to be used for internal fixation to prevent the need for removal after the healing process is complete. Internal fixation is accomplished by the implantation of fixtures to hold together bone fracture fragments of which the most common and likely applicable function of the bi-layered coatings would be on a plate [442] used to secure the bone fragments as the shear stress applied when sinking screws into bone may use enough force to damage the coating before the beneficial effects can be seen.

Another potential use would be in cardiovascular applications as structures such as stents which are only required for a maximum of 6 months clinically [443], to allow the healing process to occur. As iron structures were shown to take too long to degrade in body conditions [444], Mg alloys become a potential replacement due to their faster degradation rate. The degradation rate of the Mg alloys alone were too fast so the use of the novel bi-layered coatings could be utilised in this application to slow and delay degradation onset whilst maintaining the required

structural properties for the healing process. However, this would still require further optimisation to lower the corrosion rate to the acceptable limit for stents of 0.02 mm/year [445], but the bi-layered coatings have shown promise to prevent the onset of degradation and promote cellular activity to speed the healing processes.

A third application would be in laryngeal surgery, where Mg alloys are currently used as microclips to securely fasten vocal holds [446]. Bioabsorbable clips are preferred as they reduce the level of risk taking during the surgery of damaging the vocal folds whilst suturing to seal the epithelial microflaps [447]. Haenzi *et al.* [448] have published work on the degradation of magnesium tipped rivets for wound closure in gastrointestinal interventions and reported feasibility for the use of Mg. As the bi-layered coatings serve as a functional and sacrificial layer, the application of them to a Mg alloy could be used for these wound closure applications to tailor the degradation profile to the desired rate.

5.6 Chapter Summary

The use of the electrodeposition method to deposit CaP coatings onto Mg WE43 alloy substrates has been investigated, with the parameters of duty cycle, deposition time and electrolyte pH being varied as part of a two pronged-strategy for the development of a novel bi-layered coating which protects and functionalises Mg-based alloys. The second part of this strategy was the investigation of PBG coatings deposited by Radio Frequency Magnetron Sputtering, where the P content of the glasses was varied to increase the bioactivity and act as a complimentary top layer to the porous microstructure of the CaP bottom layer. The RFMS process saw a side effect that the characteristic induced heating annealed the small proportion of deposited amorphous CaP, crystalising the amorphous structures to the brushite phase as confirmed by XRD observations. The cytocompatibility of the various coatings were assessed via an indirect contact elution test for cell viability, with the best performing coatings

containing the P30 PBG layer. Under the conditions here, it was shown that lowering the Q^n species distribution of the glass improved the biocompatibility and degree of cell proliferation.

In addition, the corrosion performances of these coatings were assessed. The E_{corr} values of the bi-layered coatings were all observed to shift positively compared to the Mg WE43 alloy potentials, again with the P30 CaP bi-layer coating showing the most positive value of E_{corr} for the composite coatings. This translated to the P30 CaP coating also exhibiting the lowest corrosion rate of the bi-layered samples, although a slight further reduction would be preferred for clinical applications. Due to the deposition rate being very low for PBGs, the RFMS deposition parameters should be investigated to improve the deposited PBG layer thickness.

Orthopaedic applications such as bone fracture fixation are the closest to being achieved using these novel bi-layered coatings on a Mg alloy due to the good levels of bioactivity and corrosion rate being close to the required 0.5 mm/year. Some further work into the sputtering of low P glasses and a potential conversion step of brushite to HA would be a likely step to achieving the lower corrosion rates required for cardiovascular and laryngeal applications.

Chapter 6 – Conclusions and Future Work

This Chapter summarises the general conclusions drawn, based on the work investigated in this Thesis, into the development of a novel bilayered coating for the protection and functionalization of Mg-based alloys. The second section suggests aspects which may require further investigation and some further points of research which extend from this work and would be beneficial for the field.

6.1 Conclusions

A literature review was completed, identifying the coating deposition methods of CaP electrodeposition and RFMS of PBG as coating methods with the potential to be complimentary to each other for the protection and functionalization of the underlying Mg WE43 alloy substrate. Particular interest was identified for the cytocompatibility effects of lowering the phosphate content of the PBG targets whilst maintaining a bulk layer of CaP.

The structural properties of electrodeposited CaP were determined using complementary topographical, structural and chemical characterization techniques, which allowed further investigation into the optimization of the coating technique by varying deposition parameters of duty cycle, deposition time and electrolyte pH. Variation of the duty cycle and deposition time parameters showed that brushite was the preferred phase of CaP deposited with a preferential orientation in the (020) plane. Increasing the electrolyte pH from 4.5 to 9 showed the possibility to deposit small amounts of HA with a pH of 7.5 at the expense of coating density and thickness. Typical crystals deposited were of two main classifications: Larger plate-like crystals which ranged in size from *ca.* 10 – 50 μm and smaller needle-like crystals typically in the range of 2 – 5 μm. There were voids observed in the coating structure which generally increased in size with decreasing duty cycle. Profilometry showed that in a 20 min deposition period, an average coating thickness of *ca.* 8 μm is achieved across the varied duty cycles, showing that the gradual phase change from crystalline brushite to amorphous CaP with increasing duty cycle is the main difference between the coatings. The increasing deposition time exhibited an increase in the proportion of the needle-like crystals and a decrease in void size of the coating. Through investigation of corrosion properties and cellular activity, it was observed that the optimum duty cycle was 0.6 as the Mg alloy samples coated with CaP at this duty cycle, corresponded to the highest degree of cell viability after 24 hours in treated media and the lowest corrosion rate of 0.57 mm/Y whilst improving the E_{corr} of the Mg WE43 alloy from -1.42 to -1.17 V. Increasing the deposition time to 120 min also showed a significant

improvement in cell viability but had a slightly increased corrosion rate of 0.88 mm/Y as compared to the 20 min coating. Increasing the electrolyte pH did not show an overall improvement as compared to pH 4.5 so likely the optimum electrodeposition parameters are duty cycle 0.6, deposition time 120 min, due to the balance of coating thickness and cell viability, and electrolyte pH of 4.5.

Three compositions of PBG glass targets were manufactured, overcoming issues of surface crystallisation during processing and annealing into target form. Some small signs of crystallisation were observed but deemed insignificant to the RFMS deposition process. The P content was lowered from 40 – 30 mol%, changing the Q^n species of the glass targets with the aim of gaining the biocompatibility benefits associated with Q^0 orthophosphate glasses. Thin-film coatings of PBG ranged in thickness from 0.4 – 0.6 µm with the P30 coating being the thickest and P40 the thinnest of the coatings. Corrosion testing showed no improvement of the P35 and P40 sample corrosion rates. A small improvement was observed for the P30 coating reducing the Mg WE43 alloy corrosion rate from 2.22 – 2.00 mm/Y. Alone the PBG coatings do not provide significant corrosion protection to the Mg WE43 alloy due to the thin nature of the coatings. However, elution testing showed a significant improvement in the cell viability of MG-63 cells exposed to the P30 coated sample as compared to both the Mg WE43 alloy and the P40 coated sample. The P30 coated sample also exhibited a greater cell viability than the CaP coatings investigated. Combining this with the amorphous nature of the PBG coatings, it was determined that the PBG thin films would be complimentary to the base CaP layer to fill voids in the CaP coating whilst also improving the biocompatibility of the samples.

Novel bilayered coatings consisting of a base CaP layer and a top PBG layer were successfully deposited onto Mg WE43 discs. The RFMS deposition of PBG also induced a reaction in the brushite layer, modifying the large plate-like brushite crystals to become smaller clusters of brushite crystals. This was attributed to the heat generated during the RFMS process which was

assumed to have an annealing effect on the deposited CaP crystals. The thickness of the bilayered coatings was in the region of 8 µm thick with the higher PBG contribution seen by the P30 CaP sample which contributed to *ca.* 7.49 % of the total coating thickness. Examination of elution testing showed similar trends to that of the PBG only coatings, where the P30 CaP sample showed the highest levels of cell viability of all samples and a significant improvement over the Mg WE43 alloy. However, the base CaP coating had a buffering effect on the cell viability of the PBG layers, improving the performance of the P40 coating whereas previously the P40 only coating had performed significantly worse than the P30 coating. Corrosion testing showed that the P30 CaP coating significantly lowered the corrosion rate of the Mg WE43 alloy from 2.22 - 0.74 mm/Y. The higher P content glasses did not improve the corrosion rate of the underlying Mg WE43 alloy but did exhibit more positive E_{corr} values suggesting an improved corrosion resistance.

The novel bilayered coatings, especially the P30 CaP bilayer, proved their potential to be utilised in orthopaedic applications as the coatings covered the Mg WE43 alloy surface and would act as a sacrificial layer, delaying the onset of corrosion and exhibited a lower corrosion rate than that of the Mg alloy. They also showed benefits in terms of cell viability under elution testing being improved with these bilayered coatings. Another benefit shown was the ability of the coatings to be tailored based on the variation of electrodeposition parameters and the composition of PBG targets.

6.2 Recommendations for Future Work

This project covered the development of a novel bilayered coating for the functionalisation and protection of Mg WE43 alloy, however further work would be beneficial for additional

improvements of the corrosion performance and the manufacturing of PBG targets for the RFMS deposition of the top layer.

Following the deposition of a brushite CaP layer, an improvement could be made by performing a treatment which would convert the brushite crystals into a more insoluble HA phase of CaP. Literature has previously seen this achieved using a dissolution-precipitation process in alkaline solutions due to the higher solubility of brushite leading to ready hydrolysis and remodelling. This conversion process would likely be beneficial to the eventual osseointegration and corrosion protection of coated alloys. However, the method of laser flash annealing shows promise as a dry method to alter the CaP phase deposited without affecting the Mg alloy beneath the coating by controlling the power and penetration of the laser.

This work identified some difficulties in the manufacturing of low P content glass targets, especially in relation to the surface crystallisation of the glass during quenching and annealing processes. As low P glasses are a relatively new concept, there is currently no work on the processability of these glasses to obtain a large target *ca.* 57 mmØ x 6 mm thickness. The process of manufacturing employed in this work achieved one P30 target with no signs of surface crystallisation in 3 attempts, utilising splat quenching for rapid cooling of the molten glass. However, remelting the glass for casting into an annealing furnace appeared to negate some of the effects of the splat quench.

The concept of RFMS of PBG targets has only begun to be investigated in the last decade and currently has not extended into the sputtering of low P content glasses. The thicknesses achieved in this work were *ca.* 0.6 μm in a 48 h deposition period which leaves room for significant improvement of deposition rate. Optimisation of the RFMS process would be beneficial to achieve thicker PBG layers in a shorter deposition period. However, care must be

taken due to the brittle nature of the bulk PBG targets as they often crack under the stresses induced during the RFMS process.

This study has investigated the novel bilayered coatings from a characterisation, corrosion and cellular standpoint. As potential orthopaedic applications are likely to come under stress and mechanical forces, it would be beneficial to understand the mechanical properties of the bilayered coatings and examine the degradation profiles under stress by utilising mechanical testing techniques such as tensile, adhesion and shear testing which would in turn provide a greater knowledge base for potential applications.

Wider literature contains many studies on the use of various physiological solutions. In this research, DMEM was used for corrosion testing and as culture media, with the conclusion that the Mg WE43 alloy would react aggressively in this medium due to the high concentration of chloride ions. Therefore, it would be useful to investigate the effects of the bilayered coatings on the corrosion performance in a variety of test solutions and examine the corrosion products formed during these tests for characterisation purposes. In particular, further *in vitro* studies of cellular response to the bilayered coatings would be beneficial to aid in the determination of functional properties of the coated alloy, which may increase the potential for progression of the coated alloys for future use *in vivo*.

References

[1] M. Geetha, A. K. Singh, R. Asokamani and A. K. Gogia, “Ti based biomaterials, the ultimate choice for orthopaedic implants - a review,” *Progress in Materials Science,* vol. 54, no. 3, 2009.

[2] B. D. Ratner, A. S. Hoffman, F. J. Schoen and J. E. Lemons, Biomaterials Science - an Introduction to Materials in Medicine (2nd edition), Elsevier, 2004.

[3] H. S. Brar, M. O. Platt, M. Sarntinoranont, P. I. Martin and M. V. Manuel, “Magnesium as a biodegradable and bioabsorbable material for medical implants,” *Journal of Materials,* vol. 61, no. 9, pp. 31-34, 2009.

[4] R. Nilsen, “Elimination of secondary surgery for removal of internal fixations of fractured bones,” Cordis, Oslo, 2008.

[5] M. O. Agerbaek, E. F. Eriksen, J. Kragstrup, L. Mosekilde and F. Melsen, “A reconstruction of the remodelling cycle in normal human cortical iliac bone,” *Bone Minerals,* vol. 12, pp. 101-112, 1991.

[6] O. Bostman and H. Pihlajamki, “Routine implant removal after fracture surgery: a potentially reducible consumer of hospital resources in trauma units,” *Journal of Trauma and Acute Care Surgery,* vol. 41, no. 5, pp. 846-849, 1996.

[7] M. Moravej and D. Mantovani, “Biodegradable metals for cardiovascular stent application: Interests and new opportunitites,” *International Journal of Molecular Sciences,* vol. 12, no. 7, pp. 4250-4270, 2011.

[8] S. Garg and P. W. Serruys, “Coronary stents looking forward,” *Journal of the American College of Cardiology,* vol. 56, no. 10, pp. S43-S48, 2010.

[9] F. Witte, “The history of biodegradable magnesium implants: a review,” *Acta Biomaterialia,* vol. 6, pp. 1680-1692, 2010.

[10] R. Biber, J. Pauser, M. Geßlein and H. Bail, “Magnesium-Based Absorbable Metal Screws for Intra-Articular Fracture Fixation,” *Case Rep Orthop,* p. 9673174, 2016.

[11] Z. N. I. Abidin, A. D. Atrens, D. Martin and A. Atrens, “Corrosion of high purity mg, mg2zn0.2mn, ze41 and az91 in hank's solution at 37C,” *Corrosion Science,* vol. 53, no. 11, pp. 3542-3556, 2011.

[12] Y. Chen, Z. Xu, C. Smith and J. Sankar, “Recent advances on the development of magnesium alloys for biodegradable implants,” *Acta Biomaterialia,* vol. 10, no. 11, pp. 4561-4573, 2014.

[13] A. Zielinski and M. Bartmanski, “Electrodeposited Biocoatings, Their Properties and Fabrication Technologies: A Review,” *Coatings*, vol. 10, p. 782, 2020.

[14] F. A. Azem, T. K. Delice, G. Ungan and A. Cakir, “Investigation of duty cycle effect on corrosion properties of electrodeposited calcium phosphate coatings,” *Materials Science and Engineering C,* vol. 68, pp. 681-686, 2016.

[15] J. Buchanan, D. Fletcher and P. Linsley, “Review of hydroxyapatite ceramic coated hip implants: A clinical and radiological evaluation with up to twenty year follow up,” *J Bone Joint Surg Br,* vol. 94, p. 113, 2012.

[16] X. Y. Chen, Z. W. Zhao, A. L. Chen and H. G. Li, “Pulsed electrodeposition of hydroxyapatite on titanium substrate in solution containing hydrogen peroxide,” *Trans Nonferrous Met Soc,* vol. 17, pp. 617-621, 2007.

[17] B. Clarke, “Normal bone anatomy and physiology,” *Clinical Journal of the American Society of Nephrology,* vol. 3, pp. 131-139, 2008.

[18] H. A. Jehn and B. Rother, “Homogeneity of multi-component PVD hard coatings deposited by multi-source arrangements,” *Surface and Coatings Technology,* vol. 112, no. 3, pp. 103-107, 1999.

[19] L. Le Guehennec, A. Soueidan, P. Layrolle and Y. Amouriq, “Surface treatments of titanium dental implants for rapid osseointegration,” *Dental Materials,* vol. 23, no. 7, pp. 844-854, 2007.

[20] I. Ahmed, M. Lewis, I. Olsen and J. C. Knowles, “Phosphate glasses for tissue engineering: Part 1. Processing and characterisation of a ternary-based P2O5-CaO-Na2O glass system,” *Biomaterials,* vol. 25, no. 3, pp. 491-499, 2004.

[21] A. A. Ahmed, A. A. Ali and A. E. El-Fiqi, “Glass-forming compositions and physiochemical properties of degradable phosphate and silver-doped phosphate glasses in the P2O5-CaO-Na2O-Ag2O system,” *Journal of Materials Research and Technology,* vol. 8, no. 1, pp. 1003-1013, 2019.

[22] S. Lee, H. Maeda, A. Obata, K. Ueda, T. Narushima and T. Kasuga, “Structure and dissolution behaviour of MgO-P2O5-TiO2/Nb2O5 (Mg/P>1) Invert Glasses,” *Journal of the Ceramics Society of Japan,* vol. 123, pp. 942-948, 2015.

[23] X. Lin, Q. Chen, Y. Xiao, Y. Gao, I. Ahmed, M. Li, H. Li, K. Zhang, W. Qiu, X. Liu, A. R. Boccaccini and A. Qian, “Phosphate glass fibers facilitate proliferation and osteogenesis through Runx2 transcription in murine osteoblasic cells,” *Journal of Biomedical Materials Research,* vol. 108, pp. 316-326, 2020.

[24] F. Foroutan, A. Nikolaou, B. A. Kyffin, R. M. Elliott, M. Felipe-Sotelo, J. Gutierrez-Merino and D. Carta, “Multifunctional Phosphate-Based Glass Fibers Prepared via Electrospinning of Coacervate Precursors: Controlled Delivery, Biocompatibility and Antibacterial Activity,” *Materialia,* vol. 14, p. 100939, 2020.

[25] T. A. Turvey, W. P. Proffit and C. Phillips, “Biodegradable fixation for craniomaxillofacial surgery: a 10-year experience involving 761 operations and 745 patients,” *Int J Oral Maxillofac Surg,* vol. 40, pp. 244-249, 2011.

[26] E. Ghali, Corrosion resistance of aluminum and magnesium alloys: Understanding, performance, and testing, New Jersey: Wiley, 2010.

[27] J. Rho, T. Y. Tsui and G. M. Pharr, “Elastic properties of human cortical and trabecular lamellar bone measured by nanoindentation,” *Biomaterials,* vol. 18, no. 20, pp. 1325-1330, 1997.

[28] A. Atrens, Z. Shi, S. U. Mehreen, S. Johnston, G. Song, X. Chen and F. Pan, “Review of Mg alloy corrosion rates,” *Journal of Magnesium and Alloys,* vol. 8, pp. 989-998, 2020.

[29] C. Kammer, Magnesium Taschenbuch, Dusseldorf: Aluminium-Verlag, 2000.

[30] S. N. Mathaudhu, Magnesium Technology, Hoboken: Wiley, 2012.

[31] S. Graff, W. Bricks and D. Steglich, “Yielding of Magnesium: from single crystal to polycrystalline aggregates,” *Int J Plasticity,* vol. 23, pp. 1957-78, 2005.

[32] F. H. Hosford, Mechanical Behaviour of Materials, New York: Cambridge University Press, 2005.

[33] J. Gray and B. Luan, “Protective coatings on magnesium and its alloys - a critical review,” *J Alloys Compd,* vol. 336, pp. 88-113, 2002.

[34] V. Tsakiris, C. Tardei and F. M. Clicinshi, “Biodegradable Mg alloys for orthopedic implants - A review,” *Journal of Magnesium and Alloys,* vol. 9, pp. 1884-1905, 2021.

[35] Y. Wen, Q. Liu, J. Wang, Q. Yang, W. Zhao, B. Qiao, Y. Li and D. Jiang, “Improving in vitro and in vivo corrosion resistance and biocompatibility of Mg-1Zn-1Sn alloys by microalloying with Sr,” *Bioactive Materials,* vol. 6, no. 12, pp. 4654-4669, 2021.

[36] G. Song, A. Atrens, X. Wu and B. Zhang, “Corrosion behaviour of AZ21, AZ501 and AZ91 in sodium chloride,” *Corrosion Science,* vol. 40, no. 10, pp. 1769-1791, 1998.

[37] H. Hornberger, S. Virtanen and A. R. Boccaccini, “Biomedical coatings on magnesium alloys - A review,” *Acta Biomaterialia,* vol. 8, pp. 2442-2455, 2012.

[38] O. Hoog, N. Birbilis, M. Zhang and Y. Estrin, “Surface grain size effects on the corrosion of magnesium,” *Key Eng Mater,* vol. 384, pp. 229-240, 2008.

[39] H. Wang, Y. Estrin and Z. Zuberova, “Bio-corrosion of a magnesium alloy with different processing histories,” *Materials Letters,* vol. 62, pp. 2476-2479, 2008.

[40] R. Xin, M. Wang, J. Gao, P. Liu and Q. Liu, “Effect of microstructure and texture on corrosion resistance of magnesium alloys,” *Mater Sci Forum,* Vols. 610-613, pp. 1160-1163, 2009.

[41] V. Kaesel, P. Tai, F. Bach, H. Haferkamp, F. Witte and H. Windhagen, "Approach to control the corrosion of magnesium by alloying," in *Proceedings of the sixth international conference magnesium alloys and their applications,* New York, 2004.

[42] E. F. Emley, "Principles of Magnesium Technology," *Elsevier Science & Technology,* p. 1013, 1966.

[43] G. Song, "Understanding magnesium corrosion: A framework for improved alloy performance," *Advanced Engineering Materials,* vol. 5, no. 12, pp. 837-858, 2003.

[44] E. C. Huse, "A new ligature?," *Chicago Med J Exam,* vol. 2, p. 172, 1878.

[45] E. Payr, " Beiträge zur Technik der Blutgefäss- und Nervennaht nebst Mittheilungen über die Verwendung eines resorbirbaren Metalles in der Chirurgie," *Arch Kin Chir,* vol. 62, pp. 67-93, 1900.

[46] E. Payr, "Blutgefäß- und Nervennaht (nebst Mittheilung über die Verwendung eines resorbirbaren Metalles in der Chirurgie," *Centralblatt für Chirurgie,* Vols. 18-21, pp. 31-37, 1900.

[47] S. Vordemann, Ueber die Resorption von Magnesium und Magnesium-Zirkoniumfäden unter Berücksichtigung der bisherigen Anwendung von Magnesium zu chirugischen Zwecken, Gottingen: Georg-August-Universitat zu Gottingen, 1939.

[48] E. W. Andrews, "Absorable metal clips as substitutes for ligatures in wound closure," *JAMA,* vol. 28, pp. 278-281, 1917.

[49] E. Höpfner, " Ueber Gefässnaht, Gefässtransplantation und Replantation von amputirten Extremitaten," *Arch Klin Chir,* vol. 70, pp. 417-471, 1903.

[50] M. G. Seelig, "A study of magnesium wire as an absorbable suture and ligature material," *Arch Surg,* vol. 8, no. 2, pp. 669-680, 1924.

[51] V. D. Lespinasse, "A practical mechanical method of end-to-end anastomosis of blood-vessels: using absorbable magnesium rings," *JAMA,* vol. 55, pp. 1785-1790, 1910.

[52] G. Gossrau, "Nähmaterial aus Magnesiumdrähten für chirurgische Zwecke". Germany 1935.

[53] P. Stone and J. W. Lord Jr, "An experimental study of the thrombogenic properties of magnesium and magnesium-aluminum wire in the dog's aorta," *Surgery,* vol. 30, no. 6, pp. 987-993, 1951.

[54] R. Jorgensen, "Bio-absorbable metal hemostatic clip". US Patent 4.602.632, 29 July 1986.

[55] E. Payr, "Zur Verwendung des Magnesiums für resorbirbare Darmknöpfe und andere chirurgisch-technische Zwecke," *Centralblatt Chir,* vol. 28, no. 20, pp. 513-515, 1901.

[56] P. Rostock, “Ist das Magnesium als Naht- und Schienungsmaterial fur Knochenoperationen geeignet?,” *Arch Orthop Trauma Surg,* vol. 38, no. 3, pp. 486-492, 1937.

[57] V. Chlumsky, “Über die Wiederherstellung der Beweglichkeit des Gelenkes bei Ankylose,” *Centralblatt Chir,* vol. 27, no. 37, pp. 921-925, 1900.

[58] A. Lambotte, “L'utilisation du magnesium comme materiel perdu dans l’ostéosynthèse,” *Bull Mem Soc Nat Cir,* vol. 28, pp. 1325-1334, 1932.

[59] J. Verbrugge, “Le matériel métallique résorbable en chirurgie osseuse,” *Presse Med,* vol. 23, pp. 460-465, 1934.

[60] E. Groves, “An experimental study of the operative treatment of fractures,” *Br J Surg,* vol. 1, no. 3, pp. 438-501, 1913.

[61] A. A. Zierold, “Reaction of bone to varous metals,” *Arch Surg,* vol. 9, no. 2, pp. 365-412, 1924.

[62] J. Verbrugge, “La tolérance du tissu osseux vis-à-vis du magnésium métallique,” *Presse Med,* vol. 55, pp. 1112-1114, 1933.

[63] J. Verbrugge, “L’utilisation du magnésium dans le traitement chirurgical des fractures,” *Bull Mem Soc Nat Cir,* vol. 59, pp. 813-823, 1937.

[64] E. D. McBride, “Magnesium screw and nail transfixion in fractures,” *South Med J,* vol. 31, no. 5, pp. 508-515, 1938.

[65] E. D. McBride, “Absorbable metal in bone surgery,” *JAMA,* vol. 111, pp. 2464-2467, 1938.

[66] W. L. Tpobwrbq BB, “Osteosynthesis with metal alloy as a material for bonding bone in fractures.,” *Xbpypubz,* vol. 8, pp. 41-44, 1948.

[67] E. Payr and A. Martina, “Experimentelle und klinische Beiträge zur Lebernaht und leberresection (Magnesiumplattennaht).,” *Arch Klin Chir,* vol. 77, no. 4, pp. 962-998, 1905.

[68] E. Payr, “Ueber Verwendung von Magnesium zur Behandlung von Blutgefässerkrankungen,” *Deut Z Chir,* vol. 63, pp. 503-511, 1902.

[69] E. Payr, “Zur Technik der Behandlung kavernöser Tumoren,” *Zentralblatt Chir,* vol. 30, pp. 233-234, 1903.

[70] P. Wilflingseder, R. Martin and C. Papp, “Magnesium seeds in the treatment of lymph- and haemangiomata,” *Chir Plastica,* vol. 6, pp. 105-116, 1981.

[71] S. Hoffheinz and N. Dimitroff, “Experimentelle Studie über die resorption parental zugeführten metallischen Magnesiums.,” *Deut Z Chir,* vol. 208, pp. 346-353, 1928.

[72] V. Chlumsky, “Beiträge zur Darmknopffrage,” *Mitt Grenzgebieten Med Chir,* vol. 3, pp. 416-451, 1907.

[73] G. Fontenier, R. Freschard and M. Mourot, “Study of the corrosion in vitro and in vivo of magnesium anodes involved in an implantable bioelectric battery,” *Med Biol Eng,* vol. 13, no. 5, pp. 683-689, 1975.

[74] H. E, “Ueber Gefässnaht, Gefässtransplantation und Replantation von amputirten Extremitäten,” *Arch Klin Chir,* vol. 70, pp. 417-471, 1903.

[75] G. Nogara, “Sulla tolleranza dell' osso verso i metalli riassorbibili magnesio ed electron,” *Arch Ital Chir,* vol. 56, no. 5, pp. 459-478, 1939.

[76] B. C. Wexler, “Pathophysiologic responses of spontaneously hypertensive rats to arterial magnesium-aluminium wire implants,” *Atherosclerosis,* vol. 36, no. 4, pp. 575-587, 1980.

[77] A. Tahmasebifar, S. M. Kayhan, Z. Evis, A. C. H. Tezcaner and M. Koc, “Mechanical, electrochemical and biocompatibility evaluation of AZ91D magnesium alloy as a biomaterial,” *Journal of Alloys and Compounds,* vol. 687, pp. 906-919, 2016.

[78] S. E. Henderson, K. Verdelis, S. Maiti, S. Pal, W. L. Chung, D. Chou, P. N. Kumta and A. J. Almarza, “Magnesium alloys as a biomaterial for degradable craniofacial screws,” *Acta Biomaterialia,* vol. 10, pp. 2323-2332, 2014.

[79] F. Witte, J. Fischer, J. Nellesen, H. A. Crostack, V. Kaese, A. Pisch, F. Beckmann and H. Windhagen, “In vitro and in vivo corrosion measurements of magnesium alloys,” *Biomaterials,* vol. 27, no. 7, pp. 1013-1018, 2006.

[80] H. Sigel, Metal ions in biological system, New York: Marcel Dekker Inc, 1986.

[81] M. Jiang, G. Monnet and B. Devincre, “On the origin of the Hall-Petch law: A 3d-dislocation dynamics simulation investigation,” *Acta Biomaterialia,* vol. 209, p. 116783, 2021.

[82] Z. Li, X. Gu, S. Lou and Y. Zheng, “The development of binary Mg-Ca alloys for use as biodegradable materials within bone,” *Biomaterials,* vol. 29, no. 10, pp. 1329-1344, 2008.

[83] Y. Wan, G. Xiong, H. Luo, F. He, Y. Huang and X. Zhou, “Preparation and characterization of a new biomedical magnesium-calcium alloy,” *Materials & Design,* vol. 29, no. 10, pp. 2034-2037, 2008.

[84] Y. S. Jeong and W. J. Kim, “Enhancement of mechanical properties and corrosion resistnace of Mg-Ca alloys through microstructural refinement by indirect extrusion,” *Corrosion Science,* vol. 82, pp. 392-403, 2014.

[85] M. Bornapour, N. Muja, D. Shum-Tim, M. Cerruti and M. Pekguleryuz, "Biocompatibility and biodegradability of Mg-Sr alloys: The formation of Sr-substituted hydroxyapatite," *Acta Biomaterialia,* vol. 9, no. 2, pp. 5319-5330, 2013.

[86] W. Zhang, Y. Shen, H. Pan, K. Lin, X. Liu, B. W. Darvell, W. W. Lu, J. Chang, L. Deng, D. Wang and W. Huang, "Effects of strontium in modified biomaterials," *Acta Biomaterialia,* vol. 7, no. 2, pp. 800-808, 2011.

[87] M. M. Avedasian and H. Baker, ASM Specialty Handbook - Magnesium and Magnesium Alloys, Ohio: ASM International, 1999.

[88] B. A. Bowman and R. M. Russell, Present knowledge in nutrition 9th ed., Washington DC: International Life Sciences Institute Press, 2006.

[89] P. Yin, N. Li, T. Lei, L. Liu and C. Ouyang, "Effects of Ca on microstructure, mechanical and corrosion properties and biocompatibility of Mg-Zn-Ca alloys," *Journal of Materials Science: Materials in Medicine,* vol. 24, no. 6, pp. 1365-1373, 2013.

[90] F. S. Pierce, S. J. Poon and Q. Guo, "Electron localization in metallic quasicrystals," *Science,* vol. 261, no. 5122, pp. 737-739, 1993.

[91] H. G. Seiler, H. Sigel and A. Sigel, A handbook of toxicity of inorganic compounds, New York: Marcel Dekker Inc, 1988.

[92] F. Feyerabend, J. Fischer, J. Holtz, F. Witte, R. Willumeit, H. Drucker, C. Vogt and N. Hort, "Evaluation of short-term effects of rare earth and other elements used in magnesium alloys on primary cells and cell lines," *Acta Biomaterialia,* vol. 6, no. 5, pp. 1834-1842, 2010.

[93] N. Birbilis, M. A. Easton, A. D. Sudholz, S. M. Zhu and M. A. Gibson, "On the corrosion of binary magnesium-rare earth alloys," *Corrosion Science,* vol. 51, no. 3, pp. 683-689, 2009.

[94] L. Yang, Y. Huang, F. Feyerabend, R. Willumeit, C. Mendis, K. U. Kainer and N. Hort, "Microstructure, mechanical and corrosion properties of Mg-Dy-Gd-Zr alloys for medical applications," *Acta Biomaterialia,* vol. 9, no. 10, pp. 8499-8508, 2013.

[95] J. Seitz, A. Lucas and M. Kirschner, "Magnesium-based compression screws: A novelty in the clinical use of implants," *JOM,* vol. 68, pp. 1177-1182, 2016.

[96] A. Hänzi, P. Gunde, M. Schinhammer and P. Uggowitzer, "On the biodegradation performance of an Mg-Y-RE alloy with various surface conditions in simulated body fluid," *Acta Biomaterialia,* vol. 5, pp. 162-171, 2009.

[97] B. Zberg, P. J. Uggowitzer and J. F. Loffler, "MgZnCa glasses without clinically observable hydrogen evolution for biodegradable implants," *Nature Materials,* vol. 8, no. 11, pp. 887-891, 2009.

[98] X. Gu, Y. Zheng, S. Zhong, T. Xi, J. Wang and W. Wang, "Corrosion of, and cellular responses to Mg-Zn-Ca bulk metallic glasses," *Biomaterials,* vol. 31, no. 6, pp. 1093-1103, 2010.

[99] X. Sun, H. Lin, C. Zhang, J. Jin and S. Di, "Electrochemical studies on CaP electrodeposition on three dimensional surfaces of selective laser melted titanium scaffold," *Coatings (Basel),* vol. 9, no. 10, p. 667, 2019.

[100] B. Stuart, M. Gimeno-Fabra, J. Segal, I. Ahmed and D. M. Grant, "Preferential sputtering in phosphate glass systems for the processing of bioactive coatings," *Thin Solid Films,* vol. 589, pp. 534-542, 2015.

[101] E. Salahinejad, M. J. Hadianfard, D. D. Macdonald, M. Mozafari, D. Vashaee and L. Tayebi, "Multilayer zirconium titanate thin films prepared by a sol-gel deposition method," *Ceramics International,* vol. 39, no. 2, pp. 1271-1276, 2013.

[102] Y. Wang, M. Wei and J. Gao, "Improve corrosion resistance of magnesium in simulated body fluid by dicalcium phosphate dihydrate coating," *Mater Sci Eng C Biomimetic Supramol Syst,* vol. 29, pp. 1311-1316, 2009.

[103] H. Yoshikawa, N. Tamai, T. Murase and A. Myoui, "Interconnected porous hydroxyapatite ceramics for bone tissue engineering," *J R Soc Interface,* vol. 6, pp. 341-348, 2009.

[104] L. Xu, F. Pan, G. Yu, L. Yang, E. Zhang and K. Yang, "In vitro and in vivo evaluation of the surface bioactivity of a calcium phosphate coated magnesium alloy," *Biomaterials,* vol. 30, pp. 1512-1523, 2009.

[105] B. W. Stuart, M. Gimeno-Fabra, J. Segal, I. Ahmed and D. M. Grant, "Degradation and characterization of resorbable phosphate-based glass thin-film coatings applied by radio-frequency magnetron sputtering," *ACS Appl. Mater. Interfaces,* vol. 7, no. 49, pp. 27362-27372, 2015.

[106] B. W. Stuart, M. Gimeno-Fabra, J. Segal, I. Ahmed and D. M. Grant, "Mechanical, structural and dissolution properties of heat treated thin-film phosphate based glasses," *Applied Surface Science,* vol. 416, pp. 605-617, 2017.

[107] H. Tanvir, "A study of bonding mechanisms and corrosion behaviour of cold sprayed coatings in Material Engineering," The University of Nottingham, Nottingham, 2011.

[108] W. S. Tait, An introduction to elctrochemical corrosion testing for practicing engineers and scientists, PairODocs Publications, 1994.

[109] Z. C. Zeng, "Review of studies on corrosion of magnesium alloys," *Transactions of Nonferrous Metals Society of China,* vol. 16, 2006.

[110] H. Mraied, W. Wang and W. Cai, "Influence of Chemical Heterogeneity and Microstructure on the Corrosion Resistance of Biodegradable WE43 Magnesium Alloys," *Journal of Materials Chemistry B,* 2019.

[111] J. Liao and M. Hotta, “Corrosion products of field-exposed Mg-Al series magnesium alloys,” *Corrosion Science,* vol. 112, pp. 276-288, 2016.

[112] Z. Cui, X. Li, K. Xiao and C. Dong, “Atmospheric corrosion of field-exposed AZ31 magnesium in a tropical marine environment,” *Corrosion Science,* vol. 76, pp. 243-256, 2013.

[113] G. Song, A. Atrens and M. Dargusch, *Corrosion Science,* vol. 41, p. 249, 1999.

[114] G. L. Makar, J. Kruger and A. Joshi, *International Materials Review,* vol. 38, no. 3, p. 138, 1993.

[115] G. L. Makar and K. Kruger, *Journal of the Electrochemical Society,* vol. 137, no. 2, p. 414, 1990.

[116] H. H. Uhlig and R. W. Reviw, Ch 20, New York: Wiley, 1985.

[117] B. N. Popov, Corrosion Engineering Principles and Solved Problems Ch 10, Elsevier, 2015.

[118] Z. Shi, J. X. Jia and A. Atrens, “Galvanostatic anodic polarisation curves and galvanic corrosion of high purity mg in 3.5% nacl saturated with mg(oh)2,” *Corrosion Science,* vol. 60, pp. 296-308, 2012.

[119] S. Bender, J. Goellner, A. Heyn and S. Schmigalla, “A new theory for the negative difference effect in magnesium corrosion,” *Materials and Corrosion,* vol. 63, no. 8, p. 707, 2012.

[120] G. L. Song and A. Atrens, *Advanced Engineering Materials,* vol. 5, p. 837, 2003.

[121] G. L. Song and A. Atrens, “Corrosion Mechanisms of Magnesium Alloys,” *Advanced Engineering Materials,* vol. 1, p. 11, 1999.

[122] G. Williams, N. Birbilis and H. N. McMurray, “The source of hydrogen evolved from a magnesium anode,” *Electrochemistry Communications,* vol. 36, p. 1, 2013.

[123] Z. Shi, M. Liu and A. Atrens, “Measurement of the corrosion rate of magnesium alloys using tafel extrapolation,” *Corrosion Science,* vol. 52, no. 2, pp. 579-588, 2010.

[124] G. Williams and H. N. McMurray, “Localized Corrosion of Magnesium in Chloride-Containing Electrolyte Studied by a Scanning Vibrating Electrode Technique,” *Journal of the Electrochemical Society,* vol. 155, no. 7, p. 340, 2008.

[125] G. Williams, H. Llwyd Dafydd and R. Grace, “The localized corrosion of Mg alloy AZ31 in chloride containing electrolyte studied by a scanning vibrating electrode technique,” *Electrochimica Acta,* vol. 109, p. 489, 2013.

[126] M. E. Straumanis and B. Bhatia, “Disintegration of Magnesium While Dissolving Anodically in Neutral and Acidic Solutions,” *Journal of the Electrochemical Society,* vol. 110, no. 5, p. 357, 1963.

[127] G. R. Hoey and M. Cohen, "Corrosion of anodically and cathodically polarized magnesium in aqueous media," *Journal of the Electrochemical Society,* vol. 105, no. 5, p. 245, 1958.

[128] G. Song, A. Atrens, D. Stjohn, J. Nairn and Y. Li, "The electrochemical corrosion of pure magnesium in 1 N NaCl," *Corrosion Science,* vol. 29, no. 5, p. 855, 1997.

[129] E. Gulbrandsen, "Anodic behaviour of Mg in HCO-3/CO2-3 buffer solutions. Quasi-steady measurements," *Electrochimica Acta,* vol. 37, no. 8, p. 1403, 1992.

[130] E. Gulbrandsen, J. Taftø and A. Olsen, "The passive behaviour of Mg in alkaline fluoride solutions. Electrochemical and electron microscopical investigations," *Corrosion Science,* vol. 34, no. 9, p. 1423, 1993.

[131] G. G. Perrault, "Potentiostatic study of the magnesium electrode in aqueous solution," *Journal of Electroanalytical Chemistry and Interfacial Electrochemistry,* vol. 27, no. 1, p. 47, 1970.

[132] Z. Shi, F. Cao, G. Song and A. Atrens, "Low apparent valence of Mg during corrosion," *Corrosion Science,* vol. 88, p. 434, 2015.

[133] A. D. Atrens, I. Gentle and A. Atrens, *Corrosion Science,* vol. 92, pp. 173-181, 2015.

[134] G. Song, A. Atrens, D. S. John, X. Wu and J. Nairn, "The anodic dissolution of magnesium in chloride and sulphate solutions," *Corrosion Science,* vol. 39, no. 10, pp. 1981-2004, 1997.

[135] G. S. Frankel, A. Samaniego and N. Birbilis, "Evolution of hydrogen at dissolving magnesium surfaces," *Corrosion Science,* vol. 70, p. 104, 2013.

[136] K. S. Williams, V. Rodriguez-Santiago and J. W. Andzelm, "Enhanced hydrogen evolution on Mg(OH)2 covered Mg surfaces," *Electrochimica Acta,* vol. 210, p. 261, 2016.

[137] J. A. Yuwono, N. Birbilis, K. S. Williams and N. V. Medhekar, "Electrochemical stability of magnesium surfaces in an aqueous environment," *The Journal of Physical Chemistry C,* vol. 120, no. 47, p. 26922, 2016.

[138] K. Limmer, K. Williams, J. Labukas and J. Andzelm, *Corrosion,* vol. 73, no. 5, p. 506, 2017.

[139] K. S. Williams, J. P. Labukas, V. Rodrigues-Santiago and J. W. Andzelm, "First principles modelling of water dissociation on Mg(001) and development of a Mg surface pourbaix diagram," *Corrosion,* vol. 71, no. 2, p. 209, 2015.

[140] C. D. Taylor, "A first-principles surface reaction kinetic model for hydrogen evolution under cathodic and anodic conditions on magnesium," *Journal of the Electrochemical Society,* vol. 163, no. 9, p. 602, 2016.

[141] E. McCafferty, Introduction to corrosion science 2nd edition, New York: Springer International Publishing, 2010.

[142] H. A. Miley, "Fundamentals of oxidation and tarnish," in *The corrosion handbook*, New York, John Wiley, 1948, pp. 11-20.

[143] K. Asami and S. Ono, "Quantitative X-ray photoelectron spectroscopy characterisation of magnesium oxidised in air," *Journal of the Electrochemical Society,* vol. 147, no. 4, pp. 1408-1413, 2000.

[144] M. Santamaria, F. DiQuarto, S. Zanna and P. Marcus, "Initial surface film on magnesium metal: a characterisation by X-ray photoelectron spectroscopy (XPS) and photocurrent spectroscopy (PCS)," *Electrochimica,* vol. 53, no. 3, pp. 1315-1325, 2007.

[145] A. Seyeux, M. Liu, P. Schmutz, G. Song, A. Atrens and P. Marcus, "ToF-SIMS depth profile of the surface film on pure magnesium formed by immersion in pure water and the identification of magnesium hydride," *Corrosion Science,* vol. 51, pp. 1883-1886, 2009.

[146] M. Liu, S. Zanna, H. Ardelean, I. Frateur, P. Schmutz, G. Song, A. Atrens and P. Marcus, "A first quantitative xps study of the surface films formed, by exposure to water, on mg and on the mg-al intermetallics: Al 3mg 2 and mg 17al 12," *Corrosion Science,* vol. 51, no. 5, pp. 1115-1127, 2009.

[147] M. P. Brady, G. Rother, L. M. Anovitz, K. C. Littrell, K. A. Unocic, H. H. Elsentriecy, G. L. Song, J. K. Thomson, N. C. Gallego and B. Davis, "Film breakdown and naoporous mg(oh)(2) formation from corrosion of magnesium alloys in salt solutions," *Journal of the Electrochemical Society,* vol. 162, no. 4, pp. 140-149, 2015.

[148] J. Chen, J. Wang, E. Han and W. Ke, "In situ observation of pit initiation of passivated AZ91 magnesium alloy," *Corrosion Science,* vol. 51, pp. 477-484, 2009.

[149] Y. Xin, T. Hu and P. K. Chu, "In vitro studies of biomedical magnesium alloys in a simulated physiological environment: A review," *Acta Biomaterialia,* vol. 7, no. 4, pp. 1452-1459, 2011.

[150] R. Zeng, W. Dietzel, F. Witte, N. Hort and C. Blawert, "Progress and challenge for magnesium alloys as biomaterials," *Advanced Engineering Materials,* vol. 10, no. 8, pp. 3-14, 2008.

[151] A. G82-98, "Standard guide for development and use of a galvanic series for predicting galvanic corrosion performance," *ASTM,* vol. 3.02, pp. 356-361, 1998.

[152] G. E. J. Poinern, S. Brundavanam and D. Fawcett, "Biomedical magnesium alloys: A review of material properties, surface modifications and potential as a biodegradable orthopaedic implant," *American Journal of Biomedical Engineering,* vol. 2, no. 6, pp. 218-240, 2012.

[153] R. Zeng, E. Han and W. Ke, "Corrosion of artificial aged magnesium alloy AZ80 in 3.5 wt pct NaCl solutions," *Journal of Materials Science and Technology,* vol. 23, no. 3, pp. 353-358, 2007.

[154] R. Ambat, N. N. Aung and W. Zhou, "Evaluation of micro-structural effects on corrosion behaviour of AZ91D magnesium alloy," *Corrosion Science,* vol. 42, pp. 1433-1455, 2000.

[155] L. J. Liu and M. Schlesinger, "Corrosion of magnesium and its alloys," *Corrosion Science,* vol. 51, pp. 1733-1737, 2009.

[156] M. G. Fontana and N. D. Greene, Corrosion Engineering, New York: McGraw-Hill, 1987.

[157] G. M. Hoch, "National Association," in *Int. Corr. Conf. Ser*, Houston, 1974.

[158] E. Ghali, "Testing of general and localized corrosion of magnesium alloys: A critical review," *Journal of materials engineering and performance,* vol. 13, no. 5, pp. 517-529, 2004.

[159] E. Ghali, W. Dietzel and K. U. Kainer, "General and localized corrosion of magnesium alloys: A critical review," *Journal of Materials Engineering and Performance,* vol. 22, no. 10, pp. 2875-2891, 2013.

[160] L. L. Shreir, "Corrosion," in *Metal/ Environment Reactions*, Newnes-Butterworths, 1965, pp. 86-100.

[161] D. L. Albright, "Advances in Magnesium Alloys and Composites," Phoenix, International Magnesium Association and the Non-Ferrous Metals Committee, 1988, pp. 57-75.

[162] R. Zeng, Z. Yin, X. Chen and D. Xu, "Corrosion Types of Magnesium Alloys," *Magnesium Alloys - Selected Issue,* 2018.

[163] N. T. Kirkland, N. Birbilis and M. P. Staiger, "Assessing the corrosion of biodegradable magnesium implants: A critical review of current methodologies and their limitations," *Acta Biomaterialia,* vol. 8, no. 3, pp. 925-936, 2012.

[164] ASTM, Standard guide for laboratory immersion corrosion testing of metals astmg31-12a, PA, USA: ASTM International, 2012.

[165] Z. Shi and A. Atrens, "An innovative speciment configuration for the study of Mg corrosion," *Corrosion Science,* vol. 53, pp. 226-246, 2011.

[166] L. Yang and E. Zhang, "Biocorrosion behaviour of magnesium alloy in different simulated fluids for biomedical application," *Mater. Sci. Eng. C,* vol. 29, pp. 1691-1696, 2009.

[167] W. Ng, K. Chiu and F. Cheng, "Effect of pH on the in vitro corrosion rate of magnesium degradable implant material," *Mater Sci Eng C,* vol. 30, pp. 898-903, 2010.

[168] B. Shaw and R. Wolfe, "Corrosion of magnesium and magnesium-base alloys," in *Corrosion of materials*, Metals Park, OH, ASM International, 2005, pp. 205-227.

[169] Y. Xin, C. Liu, X. Xhang, G. Tang, X. Tian and P. Chu, "Corrosion behaviour of biomedical AZ91 magnesium alloy in simulated body fluids," *J Mater Res,* vol. 22, pp. 2004-2011, 2007.

[170] C. Zhang, R. Zeng, C. Liu and J. Gao, "Comparison of calcium phosphate coatings on Mg-Al and Mg-Ca alloys and their corrosion behaviour in Hank's solution," *Surf Coat Technol,* vol. 204, pp. 3636-3640, 2010.

[171] L. Li, J. Gao and Y. Wang, "Evaluation of cyto-toxicity and corrosion behaviour of alkali-heat-treated magnesium in simulated body fluid," *Surf Coat Technol,* vol. 185, pp. 92-98, 2004.

[172] C. Liu, Y. Xin, G. Tang and P. Chu, "Influence of heat treatment on degradation behaviour of bio-degradable die-cast AZ63 magnesium alloy in simulated body fluid," *Mater Sci Eng A,* vol. 456, pp. 350-357, 2007.

[173] G. Song and S. Song, "A possible biodegradable magnesium implant material," *Advanced Engineering Materials,* vol. 9, no. 4, pp. 298-302, 2007.

[174] E. Widmaier, H. Raff and K. Strang, Vander's human physiology: the mechanisms of body function, Boston, MA: WCB McGraw-Hill, 2010.

[175] ASTM, Standard practice for calculation of corrosion rates and related information from electrochemical measurements, ASTM International, 2015.

[176] N. Kirkland, N. Birbilis, J. Walker, T. Woodfield, G. Dias and M. Staiger, "In vitro dissolution of magnesium-calcium binary alloys: clarifying the unique role of calcium additions in bioresorbable magnesium implant alloys," *J Biomed Mater Res B Appl Biomater,* vol. 95B, pp. 91-100, 2010.

[177] J. Levesque, H. Hermawan, D. Dube and D. Mantovani, "Design of a pseudo-physiological test bench specific to the development of biodegradable metallic biomaterials," *Acta Biomaterialia,* vol. 4, no. 2, pp. 284-295, 2008.

[178] T. K. Bergersen and L. Walloe, "Acral Coldness - severely reduced blood flow to fingers and toes," *Handbook of Clinical Neurology,* vol. 157, pp. 677-685, 2018.

[179] T. Osada and G. Radegran, "Femoral artery blood flow and its relationship to spontaneous fluctuations in rhythmic thigh muscle workload," *Clin Physiol Funct Imaging,* vol. 29, pp. 277-292, 2009.

[180] Y. Sun, H. Helmholz and R. Willumei-Romer, "Preclinical in vivo research of magnesium-based implants for fracture treatment: A systematic review of animal

model selection and study design," *Journal of Magnesium and Alloys,* vol. 9, pp. 351-361, 2021.

[181] A. Chaya, S. Yoshizawa, K. Verdelis, N. Myers, B. J. Costello, D. T. Chou, S. Pal, S. Maiti and P. N. Kumta, *Acta Biomaterialia,* vol. 18, pp. 262-269, 2015.

[182] A. Chaya, S. Yoshizawa, K. Verdelis, S. Noorami, B. J. Costello and C. Sfeir, *J Oral Maxillofac Surg,* vol. 73, pp. 295-305, 2015.

[183] C. C. Hung, A. Chaya, K. Liu, K. Verdelis and C. Sfeir, *Acta Biomaterialia,* vol. 98, pp. 246-255, 2019.

[184] J. Reinfrath, C. Roessig, L. Wolters, J. M. Seitz, P. Helmecke and N. Angrisani, "Implant location strongly influences degradation and applicability of magnesium alloys for orthopaedic application," *Eur Cells Mater,* vol. 26, no. 51, 2013.

[185] S. F. Fischerauer, T. Kraus, X. Wu, S. Tangl, E. Sorantin, A. C. Hanzi, J. F. Loffler, P. J. Uggowitzer and A. M. Weinberg, "In vivo degradation performance of micro-arc-oxidised magnesium implants: a micro-CT study in rats," *Acta Biomaterialia,* vol. 9, no. 54, pp. 11-20, 2013.

[186] B. Ullman, J. Reinfrath, D. Dziuba, J. Seitz, D. Bormann and A. Meyer-Lindenberg, "In vivo degradation behaviour of the magnesium alloy LANd442 in rabbit tibiae," *Materials,* vol. 4, no. 2, pp. 197-218, 2011.

[187] T. Kraus, S. F. Fischerauer, A. C. Hanzi, P. J. Uggowitzer, J. F. Loffler and A. M. Weinberg, "Magnesium alloys fo rtemporary implants in osteosynthesis: in vivo studies of their degradation and interaction with bone," *Acta Biomaterialia,* vol. 8, pp. 1230-1238, 2012.

[188] T. A. Huehnerschulte, N. Angrisani, D. Ritterhaus, D. Bormann, H. Windhagen and A. Meyer-Lindenberg, "In vivo corrosion of two novel magnesium alloys ZEK100 and AX30 and their mechanical suitability as biodegradable implants," *Materials,* vol. 4, pp. 1144-1167, 2011.

[189] A. H. M. Sanchez, B. J. C. Luthringer, F. Feyerabend and R. Willumeit, "Mg and Mg alloys: how comparable are in vitro and in vivo corrosion rates? - a review," *Acta Biomaterialia,* vol. 13, pp. 16-31, 2015.

[190] J. Reinfrath, A. Marten, N. Angrisani, R. Eifler and A. Weizbauer, "In vitro and in vivo corrosion of the novel magnesium alloy Mg-La-Nd-Zr: influence of the measurement technique and in vivo implant location," *Biomedical Materials,* vol. 10, p. 045021, 2015.

[191] L. N. Zhang, Z. T. Hou, X. Ye, Z. B. Xu, X. L. Bai and P. Shang, "The effect of selected alloying element additions on properties of mg-based alloy as bioimplants: A literature review," *Frontiers of Materials Science,* vol. 7, no. 3, pp. 227-236, 2013.

[192] Q. Wang, L. Tan, W. Xu, B. Zhang and K. Yang, "Dynamic behaviours of a Ca-P coated AZ31B magnesium alloy during in vitro and in vivo degradations," *Mater Sci Eng B,* vol. 176, pp. 1718-1726, 2011.

[193] P. Lu, L. Cao, Y. Liu, X. Xu and X. Wu, "Evaluation of magnesium ions release, biocorrosion, and hemocompatibility of MAO/PLLA-modified magnesium alloy WE42," *J Biomed Mater Res Part B: Appl Biomater,* vol. 96, pp. 101-109, 2011.

[194] X. Gu, Y. Zheng, Y. Cheng, S. Zhong and T. Xi, "In vitro corrosion and biocompatibility of binary magnesium alloys," *Biomaterials,* vol. 30, pp. 484-498, 2009.

[195] D. Wang, Y. Cao, H. Qiu and Z. Bi, "Improved blood compatibility of Mg-1.0Zn-1,0Ca alloy by micro-arc oxidation," *J Biomed Mater Res Part A,* vol. 99, pp. 166-172, 2011.

[196] Y. Wang, Y. He, Z. Zhu, Y. Jiang, J. Zhang, J. Niu, L. Mao and G. Yuan, "In vitro degradation and biocompatibility of Mg-Nd-Zn-Zr alloy," *Chin Sci Bull,* vol. 57, pp. 2163-2170, 2012.

[197] J. Fischer, D. Profrock, N. Hort, R. Willumeit and F. Feyerabend, "Reprint of: Improved cytotoxicity testing of magnesium materials," *Mater Sci Eng B,* vol. 176, pp. 1773-1777, 2011.

[198] J. Fischer, M. H. Prosenc, M. Wolff, N. Hort, R. Willumeit and F. Feyerabend, "Interference of magnesium corrosion with tetrazolium-based cytotoxicity assays," *Acta Biomaterialia,* vol. 6, pp. 1813-1823, 2010.

[199] C. Lorenz, J. Brunner, P. Kollmannsberger, L. Jaafar, B. Fabry and S. Virtanen, "Effect of surface pre-treatments on biocompatibility of magnesium," *Acta Biomaterialia,* vol. 5, pp. 2783-2789, 2009.

[200] Y. Zhao, G. Wu, J. Jiang, H. Wong, K. Yeung and P. Chu, "Improved corrosion resistance and cytocompatibility of magnesium alloy by two-stage cooling in thermal treatment," *Corrosion Science,* vol. 59, pp. 360-365, 2012.

[201] J.-H. Jo, B.-G. Kang, K.-S. Shin, H.-E. Kim, B.-D. Hahn and D.-S. e. a. Park, "Hydroxyapatite coating on magnesium with MgF(2) interlayer for enhanced corrosion resistance and biocompatibility," *J Mater Sci Mater Med ,* vol. 22, pp. 2437-2447, 2011.

[202] A. Loos, R. Rohde, A. Haverich and S. Barlach, "In vitro and in vivo biocompatibilitytesting of absorbable metal stents," *Macromol Symp,* vol. 253, pp. 103-108, 2007.

[203] C. Yang, G. Yuan, J. Zhang, Z. Tang, X. Zhang and K. Dai, "Effects of magnesium alloys extracts on adult human bone marrow-derived stromal cell viability and osteogenic differentiation," *Biomed Mater,* vol. 5, p. 045005, 2010.

[204] S. Miret, E. M. de Groene and W. Klaffke, “Comparison of in vitro assays of cellular toxicity in the human hepatic cell line hepG2,” *Journal of Biomolecular Screening,* vol. 11, no. 2, 2006.

[205] L. Cobb, “Cell Proliferation Assays and Cell Viability Assays,” *Mater Methods,* vol. 3, p. 2799, 2013.

[206] H. N. Fernley, Mammalian alkaline phosphatases, New York: Academic Press, 1971.

[207] G. Taju, S. A. Majeed, K. S. N. Nambi, V. S. Babu, S. Vimal, S. Kamatchiammal and A. S. S. Hameed, “Comparison of in vitro and in vivo acute toxicity assays in etroplus suratensis (Bloch 1790) and its three cell lines in relation to tannery effluent,” *Chemosphere,* vol. 87, pp. 55-61, 2012.

[208] G. N. Eick, F. C. Madimenos, T. J. Cepon-Robins, M. J. Devlin, P. Kowal, L. S. Sugiyama and J. J. Snodgrass, “Validation of an enzyme-linked immunoassay assay for osteocalcin, a marker of bone formation in dried blood spots,” *American Journal of Human Biology,* vol. 32, 2020.

[209] G. Tolun and R. S. Myers, “A real-time DNase assay (ReDA) based on PicoGreen fluorescence,” *Nucleic Acids Research,* vol. 31, no. 18, 2003.

[210] V. Wagener and S. Virtanen, “Influence of electrolyte composition (simulated body fluid vs. dulbecco's modified eagle's medium), temperature, and solution flow on the biocorrosion behaviour of commercially pure Mg,” *Corrosion,* vol. 73, no. 12, pp. 1413-1422, 2017.

[211] A. Z. Pevec, Z. Slejkovec, J. T. van Elteren and I. Falnoga, “As2O3 oxidation by vitamin C: cell culture studies,” *Biometals,* vol. 25, pp. 103-113, 2012.

[212] R. A. Kopher, V. R. Penchev, M. S. Islam, K. L. Hill, S. Khosla and D. S. Kaufman, “Human embryonic stem cell-derived CD34+ cells function as MSC progenitor cells,” *Bone,* vol. 47, pp. 718-728, 2010.

[213] R. G. Ham, “Clonal growth of mammalian cells in a chemically defined, synthetic medium,” *National Academy of Sciences,* vol. 53, no. 2, pp. 288-293, 1965.

[214] H. Eagle, “Amino acid metabolism in mammalian cell cultures,” *Science,* vol. 130, no. 3373, pp. 432-437, 1959.

[215] K. Fosgerau, J. Breinholt, J. G. McCormack and N. Westergaard, “Evidence against glycogen cycling of gluconeogenic substrates in various liver preparations,” *J Biol Chem,* vol. 277, no. 32, pp. 28648-28655, 2002.

[216] K. Maheshwari, A. Turan, N. Makarova, C. Ma, W. A. S. Esa, K. Ruetzler, S. Barsoum, A. G. Kuhel, M. R. Ritchey, C. Higuera-Rueda, T. Kopyeva, L. Stocchi, H. Essber, B. Cohen, I. Suleiman, G. R. Bajracharya, D. Chelnick, E. J. Mascha, A. Kurz and D. Sessler, “Saline versus lactated ringer's solution: The saline or lactated ringer's (SOLAR) trial,” *Anesthesiology,* vol. 132, no. 4, pp. 614-624, 2020.

[217] N. Kirkland, J. Lespagnol, N. Birbilis and M. Staiger, "A survey of bio-corrosion rates of magnesium alloys," *Corrosion Science,* vol. 52, pp. 287-291, 2010.

[218] H. Sasaki, J. Enomoto, Y. Ikeda, H. Honda, J. Fukuda and R. Kato, "Comparisons of cell culture medium using distribution of morphological features in microdevice," *Journal of Bioscience and Bioengineering,* vol. 121, no. 1, pp. 117-123, 2016.

[219] E. A. Abou Neel, D. M. Pickup, S. P. Valappil, R. J. Newport and J. C. Knowles, "Bioactive functional materials: a perspective on phosphate-based glasses," *Journal of Materials Chemistry,* vol. 19, no. 6, pp. 690-701, 2009.

[220] I. Ahmed, D. Ready, M. Wilson and J. C. Knowles, "Antimicrobial effect of silver-doped phosphate-based glasses," *J. Biomed. Mater. Res, Part A,* vol. 79A, no. 3, pp. 618-626, 2006.

[221] J. C. Knowles, "Phosphate based glasses for biomedical applications," *Journal of Materials Chemistry,* vol. 13, no. 10, pp. 2395-2401, 2003.

[222] X. L. Liu, D. M. Grant, A. J. Parsons, L. T. Harper, C. D. Rudd and I. Ahmed, "Magnesium coated bioresorbable phosphate glass fibres: investigation of the interface between fibre and polyester matrices," *BioMed. Res. Int,* vol. 13, pp. 1-10, 2013.

[223] N. Sharmin, M. S. Hasan, A. J. Parsons, D. Furniss, C. A. Scotchford, I. Ahmed and C. D. Rudd, "Effect of Boron addition on the thermal, degradation and cytocompatibility properties of phosphate based glasses," *BioMed. Res. Int,* pp. 1-12, 2013.

[224] I. Ahmed, C. A. Collins, M. P. Lewis, I. Olsen and J. C. Knowles, "Processing, characterisation and biocompatibility of iron-phosphate glass fibres for tissue engineering," *Biomaterials,* vol. 25, no. 16, pp. 3223-3232, 2004.

[225] N. Sharmin and C. D. Rudd, "Structure, thermal properties, dissolution behaviour and biomedical applications of phosphate glasses and fibres: a review," *Journal of Materials Science,* vol. 52, pp. 8733-8760, 2017.

[226] J. Jones and A. Clare, Bio-Glasses: An Introduction, John Wileys and Sons Ltd, 2012.

[227] A. Hoppe, N. S. Guldal and A. R. Boccaccini, "A review of the biological response to ionic dissolution products from bioactive glasses and glass ceramics," *Biomaterials,* vol. 32, no. 11, pp. 2757-2774, 2011.

[228] B. C. Bunker, G. W. Arnold and J. A. Wilder, "Phosphate Glass Dissolution in Aqueous Solution," *Journal of Non-Crystalline Solids,* vol. 64, no. 3, pp. 291-316, 1984.

[229] R. K. Brow, "Review: the structure of simple phosphate glasses," *Journal of Non-Crystalline Solids,* pp. 1-28, 2000.

[230] M. S. Hasan, I. Ahmed, A. J. Parsons, G. S. Walker and C. A. Scotchford, "Material characterisation and cytocompatibility assessment of quinternary phosphate glasses," *Journal of Materials Science,* vol. 23, pp. 2531-2541, 2012.

[231] B. W. Stuart, Deposition and Characterisation of RF Magnetron Sputtered Phosphate Based Glasses, Doctor of Philosophy Thesis: University of Nottingham, 2016.

[232] I. Ahmed, E. A. Abou Neel, S. P. Valappil, S. N. Nazhat, D. M. Pickup, D. Carta, D. L. Carroll, R. J. Newport, M. E. Smith and J. C. Knowles, "The structure and properties of silver-doped phosphate-based glasses," *Journal of Materials Science,* vol. 42, no. 23, pp. 9827-9835, 2007.

[233] I. Ahmed, P. S. Cronin, E. A. Abou Neel, A. J. Parsons, J. C. Knowles and C. D. Rudd, "Retention of mechanical properties and cytocompatibility of a phosphate-based glass fiber/polylactic acid composite," *Journal of Biomedical Materials Resources B,* vol. 89B, pp. 18-27, 2009.

[234] J. Gough, P. Christian, C. A. Scotchford, C. D. Rudd and I. A. Jones, "Synthesis, degradation, and in vitro cell responses of sodium phosphate glasses for craniofacial bone repair," *Journal of Biomedical Materials Resources,* vol. 59, no. 3, pp. 481-489, 2002.

[235] A. Parsons, M. Evans, C. D. Rudd and C. A. Scotchford, "Synthesis and degradation of sodium iron phosphate glasses and their in vitro cell response," *Journal of Biomedical Materials Research,* vol. 71A, no. 2, pp. 283-291, 2004.

[236] E. Abou Neel, I. Ahmed, J. J. Blaker, A. Bismarck, A. R. Boccaccini, M. P. Lewis, S. N. Nazhat and J. C. Knowles, "Effect of iron on the surface, degradation and ion release properties of phosphate-based glass fibres," *Acta Biomaterialia,* vol. 1, no. 5, pp. 553-563, 2005.

[237] X. Yu, D. E. Day, G. J. Long and R. K. Brow, "Properties and structure of sodium-iron phosphate glasses," *Journal of Non-Crystalline Solids,* vol. 215, pp. 21-31, 1997.

[238] M. Nogami, Y. Hosoi, T. Kasuga and T. Fujimoto, "Calcium phosphate invert glasses and glass-ceramics with apatite-forming ability," *Bioceramics,* vol. 240, no. 2, pp. 265-268, 2003.

[239] A. Kiani, N. J. Lakhkar, V. Salih, M. E. Smith, J. V. Hanna, R. J. Newport, D. M. Pickup and J. C. Knowles, "Titanium-containing bioactive phosphate glasses," *Philos Trans A Math Phys Eng Sci,* vol. 370, pp. 1352-1375, 2012.

[240] T. Kasuga, T. Hattori and M. Niinomi, "Phosphate glasses and glass-ceramics for biomedical applications," *Phosphorous Research Bulletin,* vol. 26, pp. 8-15, 2012.

[241] E. Abou Neel, I. Ahmed, J. Pratten, S. N. Nazhat and J. C. Knowles, "Characterisation of antibacterial copper releasing degradable phosphate glass fibres," *Biomaterials,* vol. 26, no. 15, pp. 2247-2254, 2005.

[242] A. G. Avent, C. N. Carpenter, J. David Smith, D. M. Healy and T. Gilchrist, "The dissolution of silver-sodium-calcium-phosphate glasses for the control of urinary tract infections," *Journal of Non Crystalline Solids,* vol. 328, pp. 31-39, 2003.

[243] R. O. Omrani, A. Kaoutar, A. El Jazouli, S. Krimi, I. Khattech, M. Jemal, J. J. Videau and M. Couzi, "Structural and thermochemical properties of sodium magnesium phosphate glasses," *Journal of Alloys and Compounds,* vol. 632, pp. 766-771, 2015.

[244] I. Ahmed, A. Parsons, A. Jones, G. Walker, C. Scotchford and C. Rudd, "Cytocompatibility and effect of increasing MgO content in a range of quaternary invert phosphate-based glasses," *J Biomater Appl,* vol. 24, no. 6, pp. 555-575, 2010.

[245] E. Abou Neel, A. Ensanya, W. Chrzanowski, S. P. Valappil, L. A. O'Dell, D. M. Pickup, M. E. Smith, R. J. Newport and J. C. Knowles, "Doping of a high calcium oxide metaphosphate glass with titanium dioxide," *Journal of Non Crystalline Solids,* vol. 355, no. 16, pp. 991-1000, 2009.

[246] E. Abou Neel, W. Chrzanowski, D. M. Pickup, L. A. O'Dell, N. J. Mordan, R. J. Newport, M. E. Smith and J. C. Knowles, "Structure and properties of strontium-doped phosphate-based glasses," *Journal of the Royal Society Interface,* vol. 6, no. 34, pp. 435-446, 2009.

[247] J. Massera, L. Petit, T. Cardinal, J. J. Videau, M. Hupa and L. Hupa, "Thermal properties and surface reactivity in simulated body fluid of new strontium ion-containing phosphate glasses," *Journal of Materials Science: Materials in Medicine,* vol. 24, no. 6, pp. 1407-1416, 2013.

[248] D. S. Brauer, M. N. Anjum, M. Mneimne, R. M. Wilson, H. Doweidar and R. G. Hill, "Fluoride-containing bioactive glass ceramics," *Journal of Non Crystalline Solids,* vol. 358, pp. 1438-1442, 2012.

[249] M. Bitar, V. Salih, V. Mudera, J. C. Knowles and M. P. Lewis, "Soluble phosphate glasses: in vitro studies using human cells of hard and soft tissue origin," *Biomaterials,* vol. 25, no. 12, pp. 2283-2292, 2004.

[250] K. Skelton, J. V. Glenn, S. A. Clarke, G. Georgiou, S. P. Valappil, J. C. Knowles, S. N. Nazhat and G. R. Jordan, "Effect of ternary phosphate-based glass compositions on osteoblast and osteoblast-like proliferation, differentiation and death in vitro," *Acta Biomaterialia,* vol. 3, no. 4, pp. 563-572, 2007.

[251] D. Brauer, C. Russel, W. Li and S. Habelitz, "Effect of degradation rates of resorbable phosphate invert glasses on in vitro osteoblast proliferation," *Journal of Biomedical Materials Resources A,* vol. 77A, no. 2, pp. 213-219, 2006.

[252] L. L. Hench, "The story of bioglass," *J Mater Sci Mater Med,* vol. 17, no. 11, pp. 967-978, 2006.

[253] Y. C. Fredholm, N. Karpukhina, D. S. Brauer, J. R. Jones, R. V. Law and R. G. Hill, "Influence of strontium for calcium substitution in bioactive glasses on degradation, ion release and apatite formation," *J R Soc Interface,* vol. 9, no. 70, pp. 880-889, 2012.

[254] E. Gentleman, Y. C. Fredholm, G. Jell, N. Lotfibakhshaiesh, M. D. O'Donnell, R. G. Hill and M. M. Stevens, "The effects of strontium-substituted bioactive glasses on osteoblasts and osteoclasts in vitro," *Biomaterials,* vol. 31, no. 14, pp. 3949-3956, 2010.

[255] Y. Lu, L. Tan, B. Zhang, J. Lin and K. Yang, "Synthesis and characterisation of Ca-Sr-P coating on pure magnesium for biomedical application," *Ceramics International,* vol. 40, no. 3, pp. 4559-4565, 2014.

[256] C. A. Tas, "X-ray amorphous calcium phosphate (ACP) synthesis in a simple biomineralisation medium," *Journal of Materials Chemistry B,* vol. 35, pp. 4511-4520, 2013.

[257] H. P. H. Ding, X. Xu and R. Tang, "Toward a detailed understanding of magnesium ions on hydroxyapatite crystallisation inhibition," *Crystal Growth and Design,* vol. 14, no. 2, pp. 763-769, 2014.

[258] P. Shih, S. Yung and T. Chin, "FTIR and XPS studies of P2O5-Na2O-CuO glasses," *Journal of Non Crystalline Solids,* vol. 244, no. 2, pp. 211-222, 1999.

[259] V. Simon, D. Muresan, A. F. Takacs, M. Neumann and S. Simon, "Local order changes induced in calcium-sodium-phosphate glasses by transition metals," *Solid State Ionics,* vol. 178, no. 3, pp. 221-225, 2007.

[260] A. Eisenberg, H. Farb and L. Cool, "Glass transitions in ionic polymers," *J Polym Sci A-2 Polym Phys,* vol. 4, no. 6, pp. 855-868, 1966.

[261] J. Hudgens and S. Martin, "Glass transition and infrared spectra of low-alkali, anhydrous lithium phosphate glasses," *Journal of American Ceramics Society,* vol. 76, no. 7, pp. 1691-1696, 1993.

[262] N. De Melo, L. Murrell, M. T. Islam, J. J. Titman, L. Macri-Pellizzeri, I. Ahmed and V. Sottile, "Tailoring pyro- and orthophosphate species to enhance stem cell adhesion to phosphate glasses," *International Journal of Molecular Sciences,* vol. 22, no. 2, p. 837, 2021.

[263] H. Gao, T. Tan and D. Wang, "Dissolution mechanism and release kinetics of phosphate controlled release glasses in aqueous medium," *J Control Release,* vol. 96, no. 1, pp. 29-36, 2004.

[264] T. Kokubo and H. Takadama, "How useful is SBF in predicting in vivo bone bioactivity?," *Biomaterials,* vol. 27, no. 15, pp. 2907-2915, 2006.

[265] A. C. Tas, "The use of physiological solutions or media in calcium phosphate synthesis and processing," *Acta Biomaterialia,* vol. 10, no. 5, pp. 1771-1792, 2014.

[266] H. Gao, T. Tan and D. Wang, "Effect of composition on the release kinetics of phosphate controlled release glasses in aqueous medium," *J Control Release,* vol. 96, no. 1, pp. 21-28, 2004.

[267] F. Delahaye, L. Montagne, G. Palavit, J. Claude Touray and P. Baillif, "Acid dissolution of sodium-calcium metaphosphate glasses," *J Non-Cryst Solids,* vol. 242, no. 1, pp. 25-32, 1998.

[268] J. Knowles, K. Franks and I. Abrahams, "Investigation of the solubility and ion release in the glass system K2O-Na2O-CaO-P2O5," *Biomaterials,* vol. 22, no. 23, pp. 3091-3096, 2001.

[269] D. Brauer, N. Karpukhina, R. V. Law and R. G. Hill, "Effect of TiO2 addition on structure, solubility and crystallisation of phosphate invert glasses for biomedical applications," *J Non-Cryst Solids,* vol. 356, no. 44, pp. 2626-2633, 2010.

[270] E. Abou Neel, W. Chrzanowski and J. Knowles, "Effect of increasing titanium dioxide content on bulk and surface properties of phosphate-based glasses," *Acta Biomaterialia,* vol. 4, no. 3, pp. 523-534, 2008.

[271] X. Yu, D. Day, G. Long and R. Brow, "Properties and structure of sodium-iron phosphate glasses," *J Non-Cryst Solids,* vol. 215, no. 1, pp. 21-31, 1997.

[272] U. Hoppe, M. Karabulut, E. Metwalli, R. K. Brow and P. Jovari, "The Fe-O coordination in iron phosphate glasses by x-ray diffraction with high energy photons," *Journal of Physics-Condensed Matter,* vol. 15, no. 36, pp. 6143-6153, 2003.

[273] U. Hoppe, D. Stachel and D. Beyer, "The oxygen coordination of metal ions in phosphate and silicate glasses studied by a combination of x-ray and neutron diffraction," *Physica Scripta,* vol. 157, pp. 122-126, 1995.

[274] N. Sharmin, M. S. Hasan, C. D. Rudd, D. Boyd, U. Werner-Zwanziger, I. Ahmed and A. J. Parsons, "Effect of boron oxide addition on the viscosity-temperature behaviour and structure of phosphate-based glasses," *J Biomed Mater Res Part B,* 2016.

[275] K. V. Shah, M. Goswami, M. N. Deo, A. Sarkar, S. Manikandan, V. K. Shrikhande and G. P. Kothiyal, "Effect of B2O3 addition on micro-hardness and structural features of 40Na2O-10BaO-xB2O3-(50-x)P2O5; glass system," *Bull Mater Sci,* vol. 29, no. 1, pp. 43-48, 2006.

[276] F. ElBatal and A. ElKheshen, "Preparation and characterisation of some substituted bioglasses and their ceramic derivatives from the system SiO2-Na2O-CaO-P2O5 and effect of gamma irradiation," *Mater Chem Phys,* vol. 110, no. 2, pp. 352-362, 2008.

[277] D. Brauer, S. Russel and J. Kraft, "Solubility of glasses in the system P2O5-CaO-MgO-Na2O-TiO2: experimental and modelling using artificial neural networks," *J Non-Cryst Solids,* vol. 353, no. 3, pp. 263-270, 2007.

[278] F. Dohler, A. Mandlule, L. van Wullen, M. Friedrich and D. S. Brauer, "31P NMR characterisation of phosphate fragments during dissolution of calcium sodium phosphate glasses," *J Mater Chem B,* vol. 3, no. 6, pp. 1125-1134, 2015.

[279] J. Rinehart, T. D. Taylor, Y. Tian and R. A. Latour Jr, "Real-time dissolution measurement of sized and unsized calcium phosphate glass fibers," *J Biomed Mater Res,* vol. 48, no. 6, pp. 833-840, 1999.

[280] W. Otto, "Compaction effects in glass fibers," *J Am Ceram Soc,* vol. 44, no. 2, pp. 68-72, 1961.

[281] K. S. Sree Harsha, Principles of physical vapour deposition of thin films, Great Britain: Elsevier, 2006.

[282] J. G. Wolke, K. van Dijk, H. G. Schaeken, K. de Groot and J. A. Jansen, "Study of the surface characterisics of magnetron-sputter calcium phosphate coatings," *J. Biomed. Mater. Res,* vol. 28, pp. 1477-1484, 1994.

[283] Y. Yongyang, J. G. C. Wolke, L. Yubao and J. A. Jansen, "Preparation and characterization of RF magnetron sputtered calcium pyroposphate coatings," *J. Biomed. Mater. Res. A,* vol. 76A, pp. 744-752, 2006.

[284] J. Z. Shi, C. Z. Zhen, H. J. Yu and S. J. Zhang, "Application of magnetron sputtering for producing bioactive ceramic coatings on implant materials," *Bull. Mater. Sci,* vol. 31, pp. 877-884, 2008.

[285] C. C. Mardare, A. I. Mardare, J. R. F. Fernandes, E. Joanni, S. C. A. Pina, M. H. V. Fernandes and R. N. Correia, "Deposition of bioactive glass-ceramic thin-films by RF magnetron sputtering," *Journal of the European Ceramic Society,* vol. 23, no. 7, pp. 1027-1030, 2003.

[286] G. E. Stan, C. O. Morosanu, D. A. Marcov, I. Pasuk, F. Miculescu and G. Reumont, "Effect of annealing upon the structure and adhesion properties of sputtered bio-glass/titanium coatings," *Applied Surfaces Science,* vol. 255, pp. 9132-9138, 2009.

[287] G. E. Stan, S. Pina, D. U. Tulyagonov, J. M. F. Ferreira, I. Pasuk and C. O. Morosanu, "Biomineralization capability of adherent bio-glass films prepared by magnetron sputtering," *J Mater. Sci. -Mater Med,* vol. 21, pp. 1047-1055, 2010.

[288] G. E. Stan and D. Bojin, "Adherent glass-ceramic thin layer with bioactive potential deposited by magnetron sputtering techniques," *U. P. B Sci. Bull. Series B,* vol. 72, no. 2, pp. 187-196, 2010.

[289] G. E. Stan, D. A. Marcov, I. Pasuk, F. Miculescu, S. Pina, D. U. Tulyaganov and J. M. F. Ferreira, "Bioactive glass thin films deposited by magnetron sputtering technique: the role of working pressure," *Applied Surface Science,* vol. 256, no. 23, pp. 7102-7110, 2010.

[290] G. E. Stan, A. C. Popescu, I. N. Mihailescu, D. A. Marcov, R. C. Mustata, L. E. Sima, S. M. Petrescu, A. Ianculescu, R. Trusca and C. O. Morosanu, "On the bioactivity of adherent bioglass thin films synthesized by magnetron sputtering techniques," *Thin Solid Films,* vol. 518, no. 21, pp. 5955-5964, 2010.

[291] C. Berbecaru and G. E. Stan, "The bioactivity mechanism of magnetron sputtered bioglass thin films," *Applied Surface Science,* vol. 258, no. 24, pp. 9840-9848, 2012.

[292] L. L. Hench and J. Wilson, An Introduction to Bioceramics, 1st ed, Singapore: World Scientific Publising Company, 1993.

[293] L. L. Hench, "Bioceramics: from concept to clinic," *J. Am. Ceram. Soc.,* vol. 74, pp. 1487-1510, 1991.

[294] J. Serra, P. Gonzalez, S. Liste, S. Chiussi, B. Leon, M. Perez-Amor, H. O. Ylanen and M. Hupa, "Influence of the non-bridgin oxygen groups on the bioactivity of silicate glasses," *J. Mater. Sci. -Mater. Med,* vol. 13, pp. 1221-1225, 2002.

[295] Y. Zhao, M. Song, C. Chen and J. Liu, "The role of pressure in pulsed laser deposition of bioactive glass films," *J. Non-Cryst. Solids,* vol. 354, pp. 4000-4004, 2008.

[296] G. E. Stan, I. Pasuk, M. A. Husanu, I. Enculescu, S. Pina, A. F. Lemos, D. U. Tulyagonov, K. El Mabrouk and J. M. F. Ferreira, "Highly adherent bioactive glass thin films synthesized by magnetron sputtering at low temperature," *J. Mater. Sci. - Mater. Med,* vol. 22, pp. 2693-2710, 2011.

[297] J. Massera, S. Fagerlund, L. Hupa and M. Hupa, "Crystallisation mechanism of the bioactive glasses, 45S5 and S53P4," *Journal of the American Ceramic Society,* vol. 95, no. 2, pp. 607-613, 2012.

[298] A. Obeydavi, A. Shafyei, A. Rezaeian, P. Kameli and J. Lee, "Fabrication and properties evaluation of novel Fe46-XCr23Mo14Co7PXB5Si5 (X=0, 6) m metallic glasses deposited by DC magnetron sputtering," *Intermetallics,* vol. 131, pp. 107-120, 2021.

[299] T. Tite, A. C. Popa, I. M. Chirica, B. W. Stuart, A. C. Galca, L. M. Balescu, G. Popescu-Pelin, D. M. Grant, J. M. F. Ferreira and G. E. Stan, "Phosphate bioglass thin-films: cross-area uniformity, structure and biological performance tailored by the simple modification of magnetron sputtering gas pressure," *Applied Surface Science,* vol. 341, 2021.

[300] G. V. Rao and H. D. Shashikala, "Optical and mechanical properties of calcium phosphate glasses," *Glas. Phys. Chem,* vol. 40, pp. 303-309, 2014.

[301] A. Arora, D. B. Marshall, B. R. Lawn and M. V. Swain, "Indentation deformation/fracture of normal and anomalous glasses," *Journal of Non-Crystalline Solids,* vol. 31, pp. 415-428, 1979.

[302] B. W. Stuart, J. J. Titman, M. Gimeno-Fabra, I. Ahmed and D. M. Grant, "Insights into structural characterisation and thermal properties of compositionally equivalent vapour-condensed and melt-quenched glasses," *Materials and Design,* vol. 111, pp. 174-184, 2016.

[303] S. Zhang, Biological and Biomedical Coatings Handbook Processing and Characterization, Florida: CRC Press, 2011.

[304] D. Rode, V. Gaddam and J. H. Yi, "Subnanometer surface roughness of dc magnetron sputtered Al films," *J. Appl. Phys.,* vol. 102, no. 2, 2007.

[305] K. J. Rao, Structural Chemistry of Glasses, Elsevier, 2002.

[306] A. Boyd, M. Akay and B. Meenan, "Influence of target surface degradation on the properties of rf magnetron-sputtered calcium phosphate coatings," *Surf. Interface Anal.,* vol. 35, no. 2, pp. 188-198, 2003.

[307] R. F. Cooper, J. B. Fanselow and D. B. Poker, "The mechanism of oxidation of a basaltic glass: chemical diffusion of network-modifying cations," *Geochim. Cosmochim. Acta,* vol. 60, no. 17, pp. 3253-3265, 1996.

[308] M. Jamesh, S. Kumar and T. S. Narayanan, "Electrodeposition of hydroxyapatite coating on magnesium for biomedical applications," *J Coat Technol Res,* vol. 9, pp. 495-502, 2012.

[309] A. Rasooli, M. S. Safavi and M. K. Hokmabad, "Cr2O3 nanoparticles: A promising candidate to improve the mechanical properties and corrosion resistance of Ni-Co alloy coatings," *Ceramics International,* vol. 44, pp. 6466-6473, 2018.

[310] M. S. Safavi and A. Rasooli, "Ni-P-TiO2 nanocomposite coatings with uniformly dispersed Ni3Ti intermetallics: Effects of TiO2 nanoparticles concentration," *Surface Engineering,* vol. 35, pp. 1070-1080, 2019.

[311] P. Duchyene, Comprehensive Biomaterials, Amsterdam: Elsevier, 2015.

[312] H. Maleki-Ghaleh and J. Khalil-Allafi, "Characterization, mechanical and in vitro biological behaviour of hydroxyapatite-titanium-carbon nanotube composite coatings deposited on NiTi alloy by electrophoretic deposition," *Surface Coating Technology,* vol. 363, pp. 179-190, 2019.

[313] E. Mohseni, E. Zalnezhad and A. R. Bushroa, "Comparative investigation on the adhesion of hydroxyapatite coating on Ti-6Al-4V implant: A review paper," *Int J Adhes Adhes,* vol. 48, pp. 238-257, 2014.

[314] H. X. Wang, S. K. Guan, X. Wang, C. X. Ren and L. G. Wang, "In vitro degradation and mechanical integrity of Mg-Zn-Ca alloy coated with Ca-deficient hydroxyapatite by the pulse electrodeposition process," *Acta Biomaterialia,* vol. 6, pp. 1743-1748, 2010.

[315] R. Drevet, F. Velard, S. Potiron, D. Laurent-Maquin and H. Benhayoune, "In vitro dissolution and corrosion study of calcium phosphate coatings elaborated by pulsed electrodeposition current on Ti6Al4V substrate," *J Mater Sci Mater Med,* vol. 22, pp. 753-761, 2011.

[316] M. I. Coskun, I. H. Karahan and Y. Yucel, "Optimized electrodeposition concentrations for hydroxyapatite coatings on CoCrMo biomedical alloys by computational techniques," *Electrochimica Acta,* vol. 150, pp. 46-54, 2014.

[317] Y. Li, J. Huang, G. Zhu, L. Cao and X. Zeng, "Influence of ethanol on the HAp coatings prepared by hydrothermal electrodeposition on C/C composites," *J Coat Technol Res,* vol. 7, p. 67, 2010.

[318] J. Fornell, Y. P. Feng, E. Pellicer, S. Surinach, M. D. Baro and J. Sort, "Mechanical behaviour of brushite and hydroxyapatite coatings electrodeposited on newly developed FeMnSiPd alloys," *Journal of Alloys and Compounds,* vol. 729, pp. 231-239, 2017.

[319] D. Gopi, J. Indira and L. Kavitha, "A comparative study on the direct and pulsed current electrodeposition of hydroxyapatite coatings on surgical grade stainless steel," *Surface Coating Technology,* vol. 206, pp. 2859-2869, 2012.

[320] S. Shadanbaz and G. J. Dias, "Calcium phosphate coatings on magnesium alloys for biomedical applications: A review," *Acta Biomaterialia,* vol. 8, pp. 20-30, 2012.

[321] C. Vasilescu, P. Drob, E. Vasilescu, I. Demetrescu, D. Ionita, M. Prodana and S. I. Drob, "Characterisation and corrosion resistance of the electrodeposited hydroxyapatite and bovine serum albumin/hydroxyapatite films on Ti-6Al-4V-1Zr alloy surface," *Corrosion Science,* vol. 53, pp. 992-999, 2011.

[322] D. Y. Lin and X. X. Wang, "Electrodeposition of hydroxyapatite coating on CoNiCrMo substrate in dilute solution," *Surface Coating Technology,* vol. 204, pp. 3205-3213, 2010.

[323] S. Dorozhkin, "History of calcium phosphates in regenerative medicine," in *Advances in Calcium Phosphate Biomaterials,* Berlin, Springer, 2014, pp. 435-483.

[324] S. Ahmadi, I. Mohammadi and S. Sadrnezhaad, "Hydroxyapatite based and anodic titania nanotube biocomposite coatings: Fabrication, characterization and electrochemical behaviour," *Surface Coating Technology,* vol. 287, pp. 67-75, 2016.

[325] Kamath and P. V, "Novel electrosynthetic route to calcium phosphate coatings," *J Mater Chem,* vol. 8, pp. 405-408, 1998.

[326] P. Zhu, Y. Masuda and K. Koumoto, "The effect of surface charge on hydroxyapatite nucleation," *Biomaterials,* vol. 25, pp. 3915-3921, 2004.

[327] Q. Yuan and T. D. Golden, "Electrochemical study of hydroxyapatite coatings on stainless steel substrates," *Thin Solid Films,* vol. 518, pp. 55-60, 2009.

[328] T. Dobbelaere, P. M. Vereecken and C. Detavernier, "A USB-controlled potentiostat/galvanostat for thin-film battery characterization," *HardwareX,* vol. 2, pp. 34-49, 2017.

[329] M. Saremi and B. Golshan, "Microstructural study of nano hydroxyapatite coating obtained by pulse electrodeposition process on Ti-6Al-4V," *Trans IMF,* vol. 85, pp. 99-102, 2007.

[330] M. Saremi, S. Mohajernia and S. Hejazi, "Controlling the degradation rate of AZ31 magnesium alloy and purity of nano-hydroxyapatite coating by pulse electrodeposition," *Mater Lett,* vol. 129, pp. 111-113, 2014.

[331] J. Xue, A. Farris, Y. Wang, W. Yeh, C. Romany, J. K. Guest, W. L. Grayson, A. S. Hall and T. P. Weihs, "Electrodeposition of hydroxyapatite on a metallic 3D-woven bioscaffold," *Coatings,* vol. 10, p. 715, 2020.

[332] Z. Seyedraoufi and S. Mirdmadi, "Effects of pulse electrodeposition parameters and alkali treatment on the properties of nano hydroxyapatite coating on porous Mg-Zn scaffold for bone tissue engineering application," *Mater Chem Phys,* vol. 148, pp. 519-527, 2014.

[333] Y. Han, T. Fu, J. Lu and K. Xu, "Characterization and stability of hydroxyapatite coatings prepared by an electrodeposition and alkaline-treatment process," *J Biomed Mater Res,* vol. 54, pp. 96-101, 2001.

[334] F. Marashi-Najafi, J. Khalil-Allafi and M. Etminanfar, "Biocompatibility of hydroxyapatite coatings deposited by pulse electrodeposition technique on the Nitinol superelastic alloy," *Mater Sci Eng C,* vol. 76, pp. 278-286, 2017.

[335] B. Dhandayuthapani, M. T. Yoshida and D. S. Kumar, "Polymeric scaffolds in tissue engineering application: A review," *Int J Polym Sci,* p. 290602, 2011.

[336] B. P. Chan and K. W. Leong, "Scaffolding in tissue engineering. General approaches and tissue-specific considerations," *Eur Spine J,* vol. 17, pp. 467-479, 2008.

[337] M. V. Risbud and M. Sittinger, "Tissue engineering: Advances in in vitro cartilage generation," *Trends Biotechnol,* vol. 20, pp. 351-356, 2002.

[338] E. L. Nyberg, A. L. Farris, B. P. Hung, M. Dias, J. R. Garcia, A. H. Dorafshar and W. L. Grayson, "3D-printing technologies for craniofacial rehabilitation, reconstruction and regeneration," *ANN Biomed Eng,* vol. 45, pp. 45-57, 2016.

[339] T. Hayakawa, M. Yoshinari, H. Kiba, H. Yomamoto, K. Nemoto and J. A. Jansen, *Biomaterials,* vol. 23, pp. 1025-1031, 2002.

[340] M. Yoshinari, Y. Oda, T. Inoue, K. Matsuzaka and M. Shimono, *Biomaterials,* vol. 23, pp. 2879-2885, 2002.

[341] J. I. Ong, K. Bessho, R. Cavin and D. L. Carnes, *Journal of Biomedical Materials Research,* vol. 59, pp. 184-190, 2002.

[342] C. Wen, S. Guan, L. Peng, C. Ren, X. Wang and Z. Hu, "Characterization and degradation behaviour of AZ31 alloy surface modified by bone-like hydroxyapatite for implant applications," *Applied Surface Science,* vol. 255, pp. 6433-6438, 2009.

[343] M. B. Kannan and L. Orr, "In vitro mechanical integrity of hydroxyapatite coated magnesium alloy," *Biomed Mater,* vol. 6, p. 045003, 2011.

[344] H. Wang, S. Guan, X. Wang, C. Ren and L. Wang, "In vitro degradation and mechanicla integrity of Mg-Zn-Ca alloy coated with Ca-deficient hydroxyapatite by the pulse electrodeposition process," *Acta Biomaterialia,* vol. 6, pp. 1743-1748, 2010.

[345] H. Wang, S. Guan, Y. Wang, H. Liu, H. Wang, L. Wang and e. al, "In vivo degradation behaviour of Ca-deficient hydroxyapatite coated Mg-Zn-Ca alloy for bone implant application," *Coll Surf B,* vol. 88, pp. 254-259, 2011.

[346] E. C. Meng, S. K. Guan, H. X. Wang, L. G. Wang, S. J. Zhu, J. H. Hu and e. al, "Effect of electrodeposition modes on surface characteristics and corrosion properties of fluorine-doped hydroxyapatite coatings on Mg-Zn-Ca alloy," *Applied Surface Science,* vol. 257, pp. 4811-4816, 2011.

[347] Y. Zong, J. L. Niu, L. Mao, X. B. Zhang, G. Y. Yuan and W. J. Ding, "Improvement of corrosion performance in simulated body fluid solution of Mg-Nd-Zn-Zr alloy coated with hydroxyapatite by pulse electrodeposition," *Corr Prot,* vol. 32, pp. 430-437, 2011.

[348] Y. Song, D. Shan and E. H. Han, "A novel biodegradable nicotinic acid/calcium phosphate composite coating on Mg-3Zn alloy," *Mater Sci Eng C,* vol. 33, pp. 78-84, 2013.

[349] M. B. Kannan, "Improving the packing density of calcium phosphate coating on a magnesium alloy for enhanced degradation resistance," *J Biomed Mater Res A,* vol. 101A, pp. 1248-1254, 2013.

[350] M. Erinc, W. H. Sillekens, R. Mannens and R. J. Werkhoven, "Applicability of existing magnesium alloys as biomedical implant materials," *Magnesium Technology,* pp. 209-214, 2009.

[351] M. S. Hasan, I. Ahmed, A. J. Parsons, G. S. Walker and C. A. Scotchford, "Material characterisation and cytocompatibility assessment of quinternary phosphate glasses," *J Mater Sci: Mater Med,* vol. 23, pp. 2531-2541, 2012.

[352] D. H. Lee and N. Cho, "Assessment of surface profile data acquired by a stylus profilometer," *Measurement Science and Technology,* vol. 23, no. 10, 2012.

[353] G. Pintori and E. Cattaruzza, "XPS/ESCA on glass surfaces: A useful tool for ancient and modern materials," *Optical Materials X,* vol. 13, p. 100108, 2022.

[354] D. N. G. Krishna and J. Philip, "Review on surface-characterization applications of X-ray photoelectron spectroscopy (XPS): Recent developments and challenges," *Applied Surface Science Advances,* vol. 12, p. 100332, 2022.

[355] G. Major, V. Fernandez, N. Fairley, E. Smith and M. Linford, "Guide to XPS data analysis: Applying appropriate constraints to synthetic peaks in XPS peak fitting," *Journal of Vacuum Science & Technology A,* vol. 40, no. 6, p. 063201, 2022.

[356] M. P. Seah, Quantification of AES and XPS in Practical Surface Analysis by Auger and X-ray Photoelectron Spectroscopy, Chichester, UK: John Weley & Sons, 1983.

[357] *ISO 10993-5 Biological Evaluation of Medical Devices. Part 5: Tests for in Vitro Cytotoxicity.,* 2009.

[358] E. J. Catanzaro, T. J. Murphy, E. L. Garner and W. R. Shields, "Absolute Isotopic Abundance Ratios and Atomic Weight of Magnesium," *Journal of Research of the National Bureau of Standards,* vol. 70A, 1966.

[359] B. W. Stuart, G. E. Stan, A. C. Popa, M. J. Carrington, I. Zgura, M. Necsulescu and D. M. Grant, "New solutions for combatting implant bacterial infection based on silver nano-dispersed and gallium incorporated phosphate bioactive glass sputtered films: A preliminary study," *Bioactive Materials,* vol. 8, pp. 325-340, 2022.

[360] B. Wopenka and J. D. Pasteris, "A mineralogical perspective on the apatite in bone," *Materials Science and Engineering C,* pp. 131-143, 2005.

[361] E. Sassoni, "Hydroxyapatite and Other Calcium Phosphates for the Conservation of Cultural Heritage: A Review," *Materials,* vol. 11, p. 557, 2018.

[362] C. D. Wagner, A. V. Naumkin, A. Kraut-Vass, J. W. Allison, C. J. Powell and J. R. J. Rumble, "NIST Standard Reference Database 20," http:/srdata.nist.gov/xps/, 2003.

[363] G. Beamson and D. Briggs, "Jigh Resolution XPS of Organic Polymers - The Scienta ESCA300 Database," Wiley Interscience, 1992.

[364] B. P. Chakraborty, S. Al-Saadi, S. Harandi and R. Singh, "Magnesium Implants: Prospects and Challenges," *Materials (Basel),* p. 136, 2019.

[365] J. Park, D. Lee, K. Oh, Y. Lee, K. Kim and K. Kim, "Bioactivity of calcium phosphate coatings prepared by electrodeposition in a modified simulated body fluid," *Materials Letters,* vol. 60, no. 21, pp. 2573-2577, 2006.

[366] M. S. Safavi, F. C. Walsh, M. A. Surmeneva, R. A. Surmenev and J. Khalil-Allafi, "Electrodeposited hydroxyapatite-based biocoatings: Recent progress and future challenges," *Coatings,* vol. 11, p. 110, 2021.

[367] N. Monasterio, J. L. Ledesma, I. Aranguiz, A. Garcia-Romero and E. Zuza, "Analysis of electrodeposition process to obtain calcium phosphate layer on AZ31 alloy," *Surface & Coatings Technology,* vol. 319, pp. 12-22, 2017.

[368] X. Sun, H. Lin, C. Zhang, J. Jin and S. Di, “Electrochemical studies of CaP electrodeposition on three dimensional surfaces of selected laser melted titanium scaffold,” *Coatings,* vol. 9, p. 667, 2019.

[369] W. Tato and D. Landolt, “Electrochemical determination of the porosity of single and duplex PVD coatings of titanium and titanium nitride on brass,” *Journal of the Electrochemical Society,* vol. 145, pp. 4173-4181, 1998.

[370] P. R. Dev, C. P. Anand, D. S. Michael and P. Wilson, “Hydroxyapatite coatings: a critical review on electrodeposition parametric variations influencing crystal facet orientation towards enhanced electrochemical sensing,” *Advanced Materials,* vol. 3, pp. 7773-7809, 2022.

[371] S. A. Yaseen, G. A. Yiseen and Z. Li, “Elucidation of calcite structure of calcium carbonate formation based on hydrated cement mixed with graphene oxide and reduced graphene oxide,” *ACS Omega,* vol. 4, no. 6, pp. 10160-10170, 2019.

[372] A. P. Dementjev and K. I. Maslakov, “Possibilities of C 1s XPS and N(E) C KVV Auger spectroscopy for identification of inherent peculiarities of diamond growth,” *Applied Surface Science,* vol. 253, pp. 1095-1100, 2006.

[373] M. Makiewicz, R. A. Wach and K. Nawrotek, “Investigation of Paramteres Influencing Tubular-Shaped Chitosan-Hydroxyapatite Layer Electrodeposition,” *Molecules,* vol. 26, pp. 104 - 119, 2021.

[374] M. Kumar, H. Dasarathy and C. Riley, “Electrodeposition of brushite coatings and their transformation to hydroxyapatite in aqueous solutions,” *Journal of Biomedical Materials Resources A,* vol. 45, no. 4, pp. 302-310, 1999.

[375] P. Jayaweera, S. Hettiarachchi and H. Ocken, “Determination of the high temperature zeta potential and pH of zero charge of some transition metal oxides,” *Colloids and Surfaces A,* vol. 85, pp. 19-27, 1994.

[376] V. Smoluchowski, Handbuch des electrizitat und des magnetismus, Leipzig: Graetz, X, 1914.

[377] X. Shen, J. Wang and G. Xin, “Effect of Zeta Potential on the Corrosion Resistance of Electroless Nickel and PVDF Composite Layers Using Surfactants,” *ACS Omega,* vol. 6, pp. 33122-33129, 2021.

[378] R. Rojaee, M. Fathi, K. Raeissi and M. Taherian, “Electrophoretic deposition of bioactive glass nanopowders on magnesium based alloy for biomedical applications,” *Ceramics International,* vol. 40, pp. 7879-7888, 2014.

[379] S. W. Jiang, L. Yang, J. N. Pang, H. Lin and Z. Q. Wang, “Electrodeposition of Ni-Al2O3 composite coatings with combined addition of SDS and HPB surfactants,” *Surface & Coatings Technology,* vol. 286, pp. 197-205, 2016.

[380] E. Fujii, M. Ohkubo, K. Tsuru, S. Hayakawa, A. Osaka, K. Kawabata, C. Bonhomme and F. Babonneau, "Selective protein adsorption property and characterization of nano-crystalline zin-containing hydroxyapatite," *Acta Biomaterialia,* vol. 2, no. 1, pp. 69-74, 2006.

[381] D. Noviana, D. Paramitha, M. F. Ulum and H. Hermawan, "The effect of hydrogen gas evolution of magnesium implant on the postimplantation mortality of rats," *Journal of Orthopaedic Translation,* vol. 5, pp. 9-15, 2016.

[382] M. Esmaily, J. E. Svensson, S. Fajardo, N. Birbilis, G. S. Frankel, S. Virtanen, R. Arrabal, S. Thomas and L. G. Johansson, "Fundamentals and advances in magnsium alloy corrosion," *Progress in Materials Science,* vol. 89, pp. 92-193, 2017.

[383] S. V. Dorozhkin, "Calcium orthophosphate coatings on magnesium and its biodegradable alloys," *Acta Biomaterialia,* vol. 10, no. 7, pp. 2919-2934, 2014.

[384] T. S. Narayanan, I. S. Park and M. H. Lee, "Surface modification of magnesium and its alloys for biomedical applications: Modification and coating techniques," *Elsevier,* 2015.

[385] Z. Zhao, G. Zhang and H. Li, "Preparation of calcium phosphate coating on pure titanium substrate by electrodeposition method," *Journal of the Central South University of Technology,* vol. 11, pp. 147-151, 2004.

[386] P. T. Nam, T. D. Lam, H. T. Huong, N. T. Phuong, N. T. Thu Trang, T. Hoang, N. T. Thanh Huong, L. B. Thang, C. Drouet, D. Grossin, E. Kergourlay, G. Bertrand, D. Devilliers and D. T. Mai Thanh, "Electrodeposition and Characterization of Hydroxyapatite on TiN/316LSS," *Journal of Nanoscience and Nanotechnology,* vol. 15, pp. 9991-10001, 2015.

[387] Y. Cheng, X. Luo, J. Betz, S. Buckhout-White, O. Bekdash, G. F. Payne, W. E. Bentley and G. W. Rubloff, "In situ quantitative visualization and characterization of chitosan electrodeposition with paired sidewall electrodes," *Soft Matter,* vol. 6, pp. 3177-3183, 2010.

[388] E. B. Caldona, A. C. C. de Leon, J. D. Mangadlao, K. J. A. Lim, B. B. Pajarito and R. C. Advincula, "On the enhanced corrosion resistance of elastomer-modified polybenzoxazine/graphene oxide nanocomposite coatings," *Reactive and Functional Polymers,* vol. 123, pp. 10-19, 2018.

[389] A. Simchi, F. Pishbin and R. Boccaccini, "Electrophoretic deposition of chitosan," *Materials Letters,* vol. 63, pp. 2253-2256, 2009.

[390] A. A. Abdeltawab, M. A. Shocib and S. G. Mohamed, "Electrophoretic deposition of hydroxyapatite coatings on titanium from dimethylformamide suspensions," *Surface Coatings Technology,* vol. 206, pp. 43-50, 2011.

[391] C. Wang, J. Ma, W. Cheng and R. Zhang, "Thick hydroxyapatite coatings by electrophoretic deposition," *Materials Letters,* vol. 57, pp. 99-105, 2002.

[392] E. Charriere, S. Terrazzoni, C. Pittet, P. Mordashini, M. Dutoit, J. Lemaitre and P. Zysset, "Mechanical characterization of brushite and hydroxyapatite cements," *Biomaterials,* vol. 22, pp. 2937-2945, 2001.

[393] M. S. A. Johnsson and G. H. Nancollas, "The role of brushite and octacalcium phosphate in apatite formation," *Critical reviews in Oral Biology and Medicine,* vol. 3, pp. 61-82, 1992.

[394] P. Ducheyne, C. S. Kim and S. R. Pollack, "The effect of phase differences on the time-dependent variation of the zeta potential of hydroxyapatite," *Journal of Biomedical Materials Resources,* vol. 26, pp. 147-168, 1992.

[395] X. Pang and I. Zhitomirsky, "Electrodeposition of composite hydroxyapatite-chitosan films," *Materials Chemistry and Physics,* vol. 94, pp. 245-251, 2005.

[396] I. Zhitomirsky and L. Gal-Or, "Electrophoretic deposition of hydroxyapatite," *Journal of Materials Science: Materials in Medicine,* vol. 8, pp. 213-219, 1997.

[397] K. Zielinska, A. Stankiewicz and I. Sczcygiel, "Electroless deposition of Ni-P-nano_ZrO2 composite coatings in the presence of various types of surfactants," *Journal of Colloid Interface Science,* vol. 377, pp. 362-367, 2012.

[398] J. Lincks, B. D. Boyan, C. R. Blanchard, C. H. Lohmann, Y. Liu, D. L. Cochran, D. D. Dean and Z. Schwartz, "Response of MG63 osteoblast-like cells to titanium and titanium alloy is dependent on surface roughness and composition," *Biomaterials,* vol. 19, pp. 2219-2232, 1998.

[399] R. Drevet and H. Benhayoune, "Electrodeposition of Calcium Phosphate Coatings on Metallic Substrates for Bone Implant Applications: A Review," *Coatings,* vol. 12, p. 539, 2022.

[400] G. Yang, F. He, J. Hu, X. Wang and S. Zhao, "Biomechanical comparison of biomimetically and electrochemically deposited hydroxyapatite-coated porous titanium implants," *Journal of Oral Maxillofacial Surgery,* vol. 68, no. 2, pp. 420-427, 2010.

[401] S. Yen and C. Lin, "Characterization of electrolytic AlO/CaP composite coatings on pure titanium," *Journal of the Electrochemical Society,* vol. D79, p. 149, 2002.

[402] C. Montero-Ocampo, D. Villegas and L. Veleva, "Controlled potential electrodeposition of calcium phosphate on Ti6Al4V," *Journal of the Electrochemical Society,* vol. C692, p. 152, 2005.

[403] X. Yang, X. Lu, Q. Zhang, X. Zhang, Z. Gu and J. Chen, "BCP coatings on pure titanium plates by CD method," *Material Science & Engineering C,* vol. 27, no. 4, pp. 781-786, 2007.

[404] K. Rogers, S. Etok and R. Scott, "Structural characterisation of apatite coatings," *Journal of Material Science,* vol. 39, no. 18, pp. 5747-5754, 2004.

[405] J. Redepenning, G. Venkataraman, J. Chen and N. Stafford, "Electrochemical preparation of chitosan/hydroxyapatite composite coatings on titanium substrates," *Journal of Biomedical Materials Resources A,* vol. 66, no. 2, pp. 411-416, 2003.

[406] P. Peng, S. Kumar, N. Voelcker, E. Szili, R. Smart and H. Griesser, "Thin calcium phosphate coatings on titanium by electrochemical deposition in modified simulated body fluid," *Journal of Biomedical Materials and Resources A,* vol. 76, no. 2, pp. 347-355, 2006.

[407] J. Xie, C. Riley, M. Kumar and K. Chittur, "FTIT/ATR study of protein adsorption and brushite transformation to hydroxyapatite," *Biomaterials,* vol. 23, no. 17, pp. 3609-3616, 2002.

[408] J. Kuemmerle, A. Oberle, C. Oechslin, M. Bohner, C. Frei, I. Boecken and B. von Rechenberg, "Assessment of the suitability of a new brushite calcium phosphate cement for cranioplasty - an experimental study in sheep," *Journal of Craniomaxillofacial Surgery,* vol. 33, no. 1, pp. 37-44, 2005.

[409] F. Theiss, D. Apelt, B. Brand, A. Kutter, K. Zlinsky, M. Bohner, S. Matter, C. Frei, J. A. Auer and B. von Rechenberg, "Biocompatibility and resorption of a brushite calcium phosphate cement," *Biomaterials,* vol. 26, no. 21, pp. 4383-4394, 2005.

[410] R. Narayanan, S. Seshadri, T. Kwon and K. Kim, "Calcium phosphate based coatings on titanium and its alloys," *Journal of Biomedical Materials and Resources B Applied Biomaterials,* vol. 85, no. 1, pp. 279-299, 2008.

[411] V. Uskokovi and D. P. Uskokovi, "Nanosized hydroxyapatite and other calcium phosphates: chemistry of formation and application as drug and gene delivery agents," *Journal of Biomedical Materials Resources B Applied Biomaterials,* vol. 96, no. 1, pp. 152-191, 2011.

[412] M. Kumar, J. Xie, K. Chittur and C. Riley, "Transformation of modified brushite to hydroxyapatite in aqueous solution: effects of potassium substitution," *Biomaterials,* vol. 20, no. 15, pp. 1389-1399, 1999.

[413] Y. Song, D. Shan and E. Han, "Electrodeposition of hydroxyapatite coating on AZ91D magnesium alloy for biomaterial application," *Materials Letters,* vol. 62, no. 18, pp. 3276-3279, 2008.

[414] C. Zhang, "Preparation of calcium phosphate coatings on Mg-1.0 Ca alloy," *Transactions of Nonferrous Metals Society of China,* vol. 20, no. 2, pp. 655-659, 2010.

[415] I. Ahmed and e. al, "Phosphate glasses for tissue engineering: Part 1. Processing and characterisation of a ternary-based P2O5-CaO-Na2O glass system," *Biomaterials,* vol. 25, no. 3, pp. 491-499, 2004.

[416] I. Ahmed and e. al, "Cytocompatibility and effet of increasing MgO content in a range of quaternary invert phosphate-based glasses," *J Biomater Appl,* vol. 24, no. 6, pp. 555-575, 2010.

[417] I. Ahmed, A. J. Parsons, C. D. Rudd, S. N. Nazhat, J. C. Knowles, P. Gerry and M. E. Smith, " Comparison of phosphate-based glasses in the range 50P2O5–(50-x)CaO-xNa2O prepared using different precursors," *Glass Technology,* vol. 49, no. 2, pp. 63-72, 2008.

[418] R. Muller, E. D. Zanotto and V. M. Fokin, "Surface crytallization of silicate glasses: nucleation sites and kinetics," *Journal of Non-Crystalline Solids,* vol. 274, no. 1, pp. 208-231, 2000.

[419] P. W. Levy, "Shaping or figuring ceramic surfaces by ion-beam bombardment," *The Science of Ceramic Machining and Surface Finishing,* pp. 155-168, 1970.

[420] K. S. Sree Harsha, Principles of physical vapor deposition of thin films, Great Britain: Elsevier, 2006.

[421] S. Berg and I. V. Katardjiev, "Preferential sputtering effects in thin film processing," *Journal of Vacuum Science & Technology a-Vacuum Surfaces and Films,* vol. 17, no. 4, pp. 1916-1925, 1999.

[422] G. E. Stan and e. al, "Bioactive glass thin films deposited by magnetron sputtering technique: the role of working pressure," *Applied Surface Science,* vol. 256, no. 23, pp. 7102-7110, 2010.

[423] M. Z. Hossain, M. S. Hasan, R. Felfel and I. Ahmed, "Development of phosphate-based glass fibers for biomedical applications," in *Hot Topics for Biomaterials,* London, Future Science Ltd, 2014, pp. 104-115.

[424] T. Okano, N. Yamada, M. Okahura, H. Sakai and Y. Sakurai, "Mechanism of cell detachment from temperature-modulated, hydrophilic-hydrophobic polymer surfaces," *Biomaterials,* vol. 16, pp. 297-303, 1995.

[425] H. Orimo, "The mechanism of mineralization and the role of alkaline phosphatase in health and disease," *Journal of Nippon Medical School,* vol. 77, pp. 4-12, 2010.

[426] I. R. Orriss, T. R. Arnett and R. G. G. Russell, "Pyrophosphate: a key inhibitor of mineralisation," *Current Opinion in Pharmacology,* vol. 28, pp. 57-68, 2016.

[427] T. Kasuga, Y. Hosoi, M. Nogami and M. Niinomi, "Apatite formation on calcium phosphate invert glasses in simulated body fluid," *Journal of the American Ceramics Society,* vol. 84, pp. 450-452, 2001.

[428] M. Navarro, M. P. Ginebra and J. A. Planell, "Cellular response to calcium phosphate glasses with controlled solubility," *Journal of Biomedical Materials Resources A,* vol. 67, pp. 1009-1015, 2003.

[429] M. B. Tosic, J. D. Nikolic, S. R. Grujic, V. D. Zivanovic, S. N. Zildzovic, S. D. Matijasevic and S. V. Zdrale, "Dissolution behaviour of a polyphosphate glass into an aqueous solution under static leaching conditions," *Journal of Non-Crystalline Solids,* vol. 362, pp. 185-194, 2013.

[430] H. W. Hassan, M. Rahmati, A. Barrantes, H. J. Haugen and P. Mirtaheri, “In vitro monitoring of magnesium-based implants degradation by surface analysis and optical spectroscopy,” *International Journal of Molecular Science,* vol. 23, no. 11, p. 6099, 2022.

[431] W. F. Neuman, M. W. Neuman, A. G. Diamond, J. Menanteau and W. S. Gibbons, “Blood:Bone Disequilibrium. VI. Studies of the solubility characteristics of brushite: Apatite mixtures and their stabilization by noncollagenous proteins of bone,” *Calcified Tissue International,* vol. 34, pp. 149-157, 1982.

[432] P. Panjan, A. Drnovsek, P. Gselman, M. Cekada and M. Panjan, “Review of Growth Defects in Thin Films Prepared by PVD Techniques,” *Coatings,* vol. 10, no. 5, p. 447, 2020.

[433] X. Li, B. Bakhit, M. P. J. Joesaar, L. Hultman, I. Petrov and G. Greczynski, “Toward energy-efficient physical vapor deposition: Routes for replacing substrate heating during magnetron sputter deposition by employing metal ion irradiation,” *Surface and Coatings Technology,* vol. 415, p. 127120, 2021.

[434] M. A. Ahmed, S. F. Mansour, S. I. El-dek, S. M. Abd-Elwahab and M. K. Ahmed, “Characterisation and annealing performance of calcium phosphate nanoparticles synthesized by co-precipitation method,” *Ceramics International,* vol. 40, pp. 12807-12820, 2014.

[435] I. A. Khlusov, Y. Dekhtyar, Y. P. Sharkeev, V. F. Pichugin, M. Y. Khlusova, N. Polyaka, F. Tyulkin, V. Vendinya, E. V. Legostaeva, L. S. Litvinova, V. V. Shupletsova, O. G. Khaziakhmatova, K. A. Yurova and K. A. Prosolov, “Nanoscale electrical potential and roughness of a calcium phosphate surface promotes the osteogenic phenotype of stromal cells,” *Materials,* vol. 11, no. 6, p. 978, 2018.

[436] D. D. Deligianni, N. D. Katsala, P. G. Koutsoukos and Y. E. Missirlis, “Effect of surface roughness of hydroxyapatite on human bone marrow cell adhesion, proliferation, differentiation and detachment strength,” *Biomaterials,* vol. 22, pp. 87-96, 2000.

[437] H. Peltoniemi, “Biocompatibility and fixation properties of absorbable miniplates and screws in growing calvarium: An experimental study in sheep,” University Central Hospital, Helsinki, 2000.

[438] A. Lapa, M. Cresswell, P. Jackson and A. R. Boccaccini, “Phosphate glass fibres with therapeutic ions release capability - A review,” *Advanced Applied Ceramics,* vol. 119, pp. 1-14, 2019.

[439] P. V. Giannoudis, T. A. Einhorn and D. Marsh, “Fracture healing: the diamond concept,” *Injury,* vol. 38, no. 4, pp. S3-S6, 2007.

[440] S. W. Wiesel and J. N. Delahay, Essentials of Orthopedic Surgery, Springer, 2007.

[441] L. Tian, N. Tang, T. Ngai, C. Wu, Y. Ruan, L. Huang and L. Qin, “Hybrid fracture fixation systems developed for orthopaedic applications: A general review,” *Journal of Orthopaedic Translation,* vol. 16, pp. 1-13, 2019.

[442] J. Li, L. Qin, K. Yang, Z. Ma, Y. Wang, L. Cheng and D. Zhao, “Materials evolution of bone plates for internal fixation of bone fractures: A review,” *Journal of Materials Science & Technology,* vol. 36, pp. 190-208, 2020.

[443] J. E. Gray-Munro and M. Strong, “The mechanism of deposition of calcium phosphate coatings from solution onto magnesium alloy AZ31,” *Journal of Biomedical Materials Research A,* vol. 90, no. 2, pp. 339-350, 2009.

[444] M. Peuster, P. Wohlsein, M. Brugmann, M. Ehlerding, K. Seidler, C. Fink, H. Brauer, A. Fischer and G. Hausdorf, “A novel approach to temporary stenting: Degradable cardiovascular stents produced from corrodible metal - results 6-18 months after implantation into new zealand white rabbits,” *Heart,* vol. 86, no. 5, pp. 563-569, 2001.

[445] N. I. Zainal Abidin, A. D. Atrens, D. Martin and A. Atrens, “Corrosion of high purity Mg, Mg2Zn0.2Mn, ZE41 and AZ91 in hank's solution at 37C,” *Corrosion Science,* vol. 53, no. 11, pp. 3542-3556, 2011.

[446] C. B. Chng, D. P. Lau, J. Q. Choo and C. K. Chui, “A bioabsorbable microclip for laryngeal microsurgery: Design and evaluation,” *Acta Biomaterialia,* vol. 8, pp. 2835-2844, 2012.

[447] D. H. Tsuji, L. M. Nita, A. Hachiya, R. Imamura and L. U. Sennes, “T-shaped microstructure: a new suture technique for laryngeal microsurgery,” *Journal of Voice,* vol. 23, pp. 739-742, 2009.

[448] A. Haenzi, A. Metlar, M. Schinhammer, H. Aguib, T. C. Luth, J. F. Loffler and P. J. Uggowitzer, “Biodegradable wound-closing devices for gastrointestinal interventions: degradation performance of the magnesium tip,” *Materials Science and Engineering C,* vol. 31, pp. 1098-1103, 2011.